SYNTHESIS AND CHARACTERIZATION OF SILVER OXIDE/TITANIUM (IV) OXIDE SUPPORTED ON KAOLIN NANO-FILTER FOR TREATMENT OF MINING WASTEWATER

BY

AJALA, Mary Adejoke
PhD/SEET/2017/920

DEPARTMENT OF CHEMICAL ENGINEERING
FEDERAL UNIVERSITY OF TECHNOLOGY
MINNA.

MAY, 2023

SYNTHESIS AND CHARACTERIZATION OF SILVER OXIDE/TITANIUM (IV) OXIDE SUPPORTED ON KAOLIN NANO-FILTER FOR TREATMENT OF MINING WASTEWATER

BY

AJALA, Mary Adejoke
PhD/SEET/2017/920

A THESIS SUBMITTED TO THE POSTGRADUATE SCHOOL, FEDERAL UNIVERSITY OF TECHNOLOGY, MINNA, NIGERIA IN PARTIAL FULFILMENT OF THE REQUIREMENTS FOR THE AWARD OF THE DEGREE OF DOCTOR OF PHILOSOPHY (PhD) IN CHEMICAL ENGINEERING

MAY, 2023

ABSTRACT

This study has developed a nanocomposite filter from kaolin base material with Ag_2O, and TiO_2 nanoparticles, for the treatment of mining wastewater. The kaolin clay was beneficiated using a sedimentation technique for 24 h to obtain slurry which was sundried, pulverized and sieved with a <150 μm mesh size. The beneficiated clay was activated with 98% H_2SO_4 for 2 h and was then washed, filtered, and oven-dried at 100^oC for 2 h to obtain acid-activated clay (AAC). Green syntheses of Ag_2O and TiO_2 nanoparticles were investigated by *Parkia biglobossa* leaves extract using bulk silver trioxonitrate (V) and titanium isopropoxide solution respectively. The nanoparticles of Ag_2O and TiO_2 with AAC were incorporated in different proportions onto each other to obtain different adsorbents of Ag_2O-TiO_2, Ag_2O-clay, TiO_2-clay, and Ag_2O-TiO_2-clay nanocomposites. Other adsorbents that were also considered for the mine wastewater treatment are TiO_2 nanoparticles, beneficiated clay and AAC. Each of the adsorbents was characterised for its functional groups, optical band, morphology/elemental composition, disparity, phase identification, surface area, and oxidation state. The mining wastewater was collected from an abandoned mine site in *Chanchaga* Local Government, Minna, Niger state. The wastewater was analysed for its metal ions composition and was found to have a high concentration of heavy metals such as Mn (II) (4.29 mg/L), Fe (III) (20.01mg/L), Pb (II) (0.98 mg/L), and Cu (II) ions (0.31 mg/L). Other physicochemical characteristics present in the wastewater are turbidity, low pH, TDS, colour, microbes, electrical conductivity, sulphate, BOD, and COD which are above the WHO/NIS permissible limit for drinkable water. The adsorbents were tested for the removal of the heavy metals by investigating the effects of time (20-180 min), adsorbent dosage (0.1-1.0 g), and temperature (30-70℃) on the batch adsorption process. Various models of kinetics, isotherms, and thermodynamic parameters of the best adsorbent from the study were evaluated. The adsorbent with the highest percentage removal of all the metal ions was built into a water filter which was composed of 60% clay, 40% sawdust, and 0.042/2.46 $mg.g^{-1}$ of Ag_2O/TiO_2 nanoparticles respectively. The results obtained revealed improved crystallite size of the clay from 16.65 nm to 14.92 nm and 8.08 nm for beneficiated and activated clay respectively. The nano-synthesis of TiO_2 by *Parkia biglobossa* leaves extract yielded rutile TiO_2 with 3.45 nm crystallite size. The immobilised Ag_2O/TiO_2 on the AAC developed as adsorbents revealed the presence of hydroxyl groups at 3697.62 cm^{-1}, Si-O-Si band at 1000.68 cm^{-1}, TiO_2 band at 869.92 cm^{-1} and Ag_2O band at 461.29 cm^{-1}. The optical bands of the adsorbents confirmed the presence of Ag_2O and TiO_2 doping on the AAC with Ag and Ti in the +1 and +4 oxidation states respectively. The morphology of Ag_2O-TiO_2-clay adsorbents and nanocomposite revealed well-intercalated flat plates structure, with hemispherical edges and porosities that encourage maximum adsorption of heavy metals and other pollutants.The batch adsorption process justified the characterisation of the Ag_2O/TiO_2-clay nanocomposite as the most effective, among the adsorbents with percentage removal of 96.59, 99.66, 40.26 and 96.12 for Mn (II), Fe (III), Pb (II) and Cu (II) respectively. From among the isotherm models studied, Jovanovic was the best-fitted experimental data as such, the surface adsorption was homogeneous with mono-layer coverage. Also, the pseudo-second-order was the most suitable kinetic model for the experimental data, confirming multiple adsorption systems. The thermodynamic parameters justified that the adsorption process was endothermic ($+\Delta H^\circ$), spontaneous ($-\Delta S^\circ$), and feasible ($-\Delta G^\circ$). The fabricated filter showed a better performance than the adsorbents with percentage removal of 99.5, 100, 100, and 100 for Mn (II), Fe (III), Pb (II), and Cu (II) respectively. Therefore, Ag_2O/TiO_2-clay nano-filter is suitable and efficient for the sequestration of pollutants from the mining wastewater.

TABLE OF CONTENTS

Content **Page**

CHAPTER THREE

LIST OF TABLES

Table **Page**

LIST OF FIGURES

Figures **Page**

LIST OF PLATES

Plates **Page**

ABBREVIATIONS

Ag_2ONps	Silver oxide nanoparticles
AgNps	Silver nanoparticles
A_T	Temkin equilibrium binding constant
B and A	Harkin-Jura constants

B_T	Temkin isotherm constant
C_e	Equilibrium concentration (mg/L)
C_i	Initial concentration of adsorbate (mg/L),
k_1	Rate constant for the pseudo-first-order sorption (min-1)
k_2	Rate constant of the pseudo-second-order kinetic equation ($g/mg.min^{-1}$)
K_d	Distribution coefficient
K_e	Elovich equilibrium constant (L/mg)
K_F	Freundlich isotherm constant (mg/g)
K_{int}	Intraparticle diffusion model rate constant
K_J	Jovanovic isotherm constant (L/mg)
M	Mass of adsorbent (g)
Nps	Nanoparticles
NPs	Nanoparticles
pm	Picometer
q_e	Amount of adsorbate in the adsorbent at equilibrium (mg/g)
Q_m	Maximum monolayer adsorption capacity (mg/g)
q_t	Quantity of adsorbate adsorbed at time t (mg/g)
R	Universal gas constant (8.314 J/molK)
T	Temperature (K)
t	Time (min)
TiO_2Nps	Titanium (IV) oxide nanoparticles
V	Volume of aqueous solution (L)
ΔG	Change in Gibbs free energy (kJ/mol)
ΔH	Change in enthalpy (kJ/mol)
ΔS	Change in entropy (J/molK)
ε	Dubinin-Radushkevich isotherm constant

CHAPTER ONE

1.0 INTRODUCTION

1.1 Background to the Study

Access to quality water for human survival and sustenance remains a serious challenge to citizens living in rural and urban areas across the globe (Luo *et al.*, 2020; WHO, 2019). Additionally, pollution of water bodies through different point and non-point sources such as flooding, poor agricultural practices, industrial activities, and urbanisation amongst others contributed in no small measures to the deterioration and degradation of water resources (Baluch and Hashmi, 2019; Russo *et al.*, 2020). These activities are responsible for the generation and presence of thousands of organic, inorganic and microbial constituents in the water bodies (Chetty and Pillay, 2019).

United Nations report between 2018 to 2020, submitted that water pollution kills more people than all other forms of violence including wars. Therefore, now is the time to secure the well-being of people, economies, societies and the planet (UNESCO, 2020). In developing countries including Nigeria, approximately 2.2 million people under the age of 5 years die of water-related diseases (Foroutan *et al.*, 2019), occasioned by poor wastewater management systems (Abhishek *et al.*, 2014; Balali-Mood *et al.*, 2021). Among the anthropogenic sources of water pollution, is mining, which contributes a substantial amount of quantity to the wastewater problem in the environment.

Mining involves the extraction of valuable minerals or other geological materials from the earth, usually from an ore body, lode, vein, seam, reef or placer deposit (Acheampong and Ansa, 2017). This usually involves rock mass fragmentation that dramatically increases the surface area and consequently the rate of acidic water production through various reactions.

The acidic water increases the solubility of aluminium and other heavy metals such as Zn, Cd, Cu and Ni depending on the types of ores and solvents used for washing (Acheampong and Ansa, 2017). These heavy metals are highly mobile, non-biodegradable, recalcitrant and toxic at low concentrations and their continuous presence in the environment can cause physiological disturbances to both plants and animals (Balali-Mood *et al.*, 2021; Cobbina *et al.*, 2015).

For instance, exposure to Lead (Pb), even at low concentrations in the environment can cause severe dysfunction in the renal, reproductive and central nervous systems of humans (Bodrud-Dozaa *et al.*, 2016). The volume of indigenous mining wastewater generated globally was estimated between 17-27 billion gallons of water per year (Sumi and Gestring, 2013), the volume from each site is dependent on the size of the excavated area of sulphide and seasonal changes per site (Okolo *et al.*, 2018). A particular mining site wastewater is noted to affect areas more than 8 km from the exact location due to flows and underground leaching (Anawar, 2015). Therefore, there is a need to treat mining wastewater before releasing it into the environment.

There are several methods employed in the treatment of mining wastewater, these include; chemical disinfection with chlorine and its derivatives (Ghernaout *et al.*, 2019), ozonation (Ren *et al.*, 2019), UV disinfection, solar disinfection, reverse osmosis (Aguiar *et al.*, 2016), adsorption on activated carbon (Shukla *et al.*, 2020), ion exchange resin, chemical precipitation, electrochemical treatment, filtration/ultrafiltration processes (Lam *et al.*, 2018). However, these technologies have different drawbacks, for instance, the use of chemical disinfectants such as chlorine and iodine. This leads to the formation of disinfection by-products (DBPs) which are carcinogenic and therefore harmful to consumers (Ghernaout *et al.*, 2019).

Ozonation and UV disinfection require a high cost of equipment and energy to implement (Prasse *et al.*, 2015). Solar disinfection and boiling are time-consuming and can only treat small quantities of water at a time (García-Gil *et al.*, 2021), reverse osmosis is costly and the use of more energy is a disadvantage. Commercial activated carbon and ion exchange resins are costly (Shukla *et al.*, 2020) with great demand for regeneration, chemical precipitation and electrochemical treatment generating a large volume of sludge needing secondary treatment. The use of ordinary ceramic filters is hindered by low flow rates and virus penetration (Shivaraju *et al.*, 2018).

These factors make the application of these systems difficult. On the contrary, the adsorption technology is often used compared to others due to its relative simplicity, ease of design, affordability, availability of nano-adsorbents, regeneration, environmental friendliness and low cost of operation (Khan *et al.*, 2019). Hence, it is imperative to develop sustainable, effective and cheaper materials for wastewater treatment, an example of such materials is nano-adsorbent via a nanotechnology approach. Water treatment has gained prominence in recent times and many nanomaterials such as; Fe_2O_3, ZnO, TiO_2, WO_3, MWCNTs, Ag_2O and their composites have been used as nano-adsorbent to selectively remove organic and inorganic species in wastewater (Yadav *et al.*, 2017).

These nanomaterials are considered all-encompassing, due to their antimicrobial properties and non-production of harmful disinfection by-products (DBPs) like conventional chemical disinfectants (Sushman and Richa, 2015). Among the nanomaterials, Titanium dioxide (TiO_2) is widely used as a photocatalyst and nano-adsorbent for water and air purification. This is due to its low cost, relative abundance, non-toxicity and insolubility in water and resistance to most chemicals, such as acids, bases or solvents (Ani *et al.*, 2018; Nadeem *et al.*, 2018; Ortega-Dıaz *et al.*, 2020).

The TiO_2 nanoparticles have been employed for the mineralization and degradation of organic compounds and dyes in water remediation processes (Anirudh *et al.*, 2018). Despite its uniqueness, the low surface area of TiO_2 limits its industrial applications as a nano-adsorbent. Also among the nanomaterials, silver and silver oxide nanoparticles (AgNPs/Ag_2ONPs) are nanoscale clusters of metallic silver atoms, with several important applications in the field of bio-labelling, sensors, antimicrobial agents and filters (Christopher *et al.*, 2015). The Ag_2ONPs can destroy different pathogenic bacteria by altering the cell membrane structure and functions in the manner of a degrading agent (Christopher *et al.*, 2015; Singh *et al.*, 2020).

The Ag_2ONPs have been observed to possess anticancer characteristics, wastewater purification ability, and demonstrated excellent catalytic performance in the degradation of anthropogenic pollutants present in the environment (Arya *et al.*, 2018). Whenever Ag_2ONPs are incorporated into materials or placed on adsorbent supports, they release silver ions at concentrations, which are harmful to bacteria on the support surface, thereby making the incorporated material reactive instead of acting like a simple physical barrier, thus performing multiple functions in one unit.

Meanwhile, the AgNPs and Ag_2ONPs have been previously successfully used to disinfect organisms in wastewater (Trinh *et al.*, 2020). This was achieved by incorporating them into materials such as; polyurethane foams, carbon and polymeric nanofibres, and fabric (Harifi and Montazer, 2014; Kyomuhimbo *et al.*, 2019; Rajabi *et al.*, 2019). These depicted good disinfection ability on wide varieties of microorganisms. Hence, any combination of silver with other metal nanoparticles such as Zinc oxide, Aluminium oxide, Titanium dioxide, and Boron can enhance the adsorption capacity for wastewater treatment and limit the presence of microbial matter (Yadav *et al.*, 2017).

In addition, a possible combination of clay with metal nanoparticles is expected to perform multi-functionality such as adsorption, catalysis, disinfection, and ion exchange within the ceramic matrix system during the treatment of wastewater (Shivaraju *et al.*, 2018).

Clays possess desired properties of a good starting material for wastewater treatment and nano filter production. These properties include high cation exchange capacity and ease of surface modification to obtain the desired functionality required of a good adsorbent (Awasthi *et al.*, 2019). Clays of different origins, compositions and modifications have been used as adsorbents and as filter support for nanoparticles to treat wastewater (Foroutan *et al.*, 2019). The incorporation of nanoparticles into clay matrix has been reported to enhance the adsorptive capacity and efficiency of the nanocomposite for complex wastewater treatment (Guillaume *et al.*, 2018; Hajjaji *et al.*, 2018). However, the use of silver-immobilised titanium oxide nanocomposite supported on clay has not been reported for mining wastewater treatment.

Nigeria as a country is greatly endowed with natural resources and this has led to active mining activities in the country. The sector is underdeveloped as about 85% of mining activities carried out are artisanal and illegal, leading to the continuous release of deleterious mining wastewater freely into the environment (Hassan *et al.*, 2019). Hence, the wastewater must be treated. Therefore, this study focuses on the treatment of mining wastewater using silver-immobilised titanium oxide nanocomposite supported on clay to act as an adsorbent and nano filter to remove heavy metals, microbial, and chemical constituents in mining wastewater.

1.2 Statement of the Research Problem

The discharge of mining wastewater into the environment without treatment has contributed to the distortion of the ecosystem and the spread of diseases.

The volume of mining wastewater generated globally was estimated between 17-27 billion gallons of water per year. The volume generated in Nigeria arises majorly from the outrageous activities of illegal miners, encouraged by unfavourable government policies and the underdevelopment of the mining sector. Mining wastewater has; low pH, specific colour, turbidity, foul odour, microorganisms and contains heavy metals like; Cd, Pb, Ni, Cu, Cr, Mn, Fe, Al, Co and Zn.

Exposure to lead has been reported to cause; mental retardation, hyperactivity, kidney damage, dermatitis, and encephalopathy (Hussain and Ali, 2021). Exposure to the Cd causes; pulmonary fibrosis, cancer of the lungs and birth defects. Chromium exposure can cause; skin rashes, respiratory problems, acute renal failure, weakened immune systems, kidney and liver damage, alteration of genetic material, lung cancer, and pulmonary fibrosis (Kumari and Mishra, 2021; Wang *et al.*, 2021). Nickel can also cause lung, nose and bone cancer, headache, dizziness, nausea and vomiting, chest pain, and rapid respiration. Other effect includes; cirrhosis of the liver, thyroid dysfunction, skin peels, diarrhoea, stunted growth, and a lower reproduction rate (Balali-Mood *et al.*, 2021). The mining wastewater causes low yield and death of tender plants when used for irrigation due to its low pH.

Several wastewater treatment techniques such as reverse osmosis, and activated carbon adsorption exhibited low adsorption efficiency, generate toxic sludge and occupy space. Synthesis of nanoparticles using physical methods generates particles with low surface area, while the use of chemical synthesis methods uses toxic and expensive chemicals. The use of individual metallic oxide nanoparticles such as TiO_2 and Ag_2O agglomerate easily during synthesis which results in low surface activity and possess post-separation problems (Akinnawo, 2019). Thus, need to be immobilised on a support such as clay.

Clay alone as an adsorbent is not capable of removing microorganisms that may be present in wastewater. Hence the need to prepare an effective and efficient nano-adsorbent to remove colour, odour, heavy metals and microorganisms in a single-stage process.

1.3 Justification for the Research

Treating mining wastewater with TiO_2/Ag_2O nanoparticles is expected to destroy the bacteria resident in the artisanal gold mining wastewater, trap the metals present and bring the pH of the wastewater to the permissible level as stated by standard organisations. Immobilisation of TiO_2 and Ag_2O nanoparticles on kaolinite clay will increase the surface area of the adsorbent. Also, the incorporation of silver with titanium nanoparticles will create synergy by enhancing the surface area, surface activity and increasing the adsorptive capacity of the nanomaterials. This is because nanoparticles are easily subjected to aggregation in an aqueous solution; so they need to be either surface modified or anchored on other substrates (like clay) to avoid agglomeration, improve removal efficiency and overcome post-separation problems of nanoparticles. The Ag_2O and TiO_2 nanoparticles doped clay filter is expected to ensure that filtration and disinfection of wastewater are decoupled.

1.4 Aim and Objectives of the Study

The study aimed to develop Ag_2O/TiO_2 kaolinite nano-filter for the treatment of mining wastewater. This aim was achieved through the following objectives:

(1) Beneficiation, activation and characterisation of raw kaolinite clay, sourced from Ilorin, Kwara State, Nigeria.

(2) Investigation of the influence of synthesis parameters; temperature, the concentration of reducing agent, stirring speed and synthesis time on the particle size of Ag_2O and TiO_2, using 2^n factorial design.

(3) Preparation of different proportions of Ag_2O/TiO_2 nanoparticles and the kaolinite clay.

(4) Characterisation of the Ag_2O/TiO_2 nanoparticles and kaolinite clay composites for their physical and chemical properties using UV-visible spectrophotometer, BET, FTIR, XRD, HRSEM/EDS, HRTEM/SAED, and XPS.

(5) Analysis of the physico-chemical properties and selected heavy metals (Fe(III), Mn(II), Cu(II) and Pb(II)) of the mining wastewater sample before and after adsorption studies.

(6) Evaluation of the removal efficiency of selected heavy metals and other water quality parameters by the Ag_2O/TiO_2/clay nano-adsorbent via batch adsorption process.

(7) Fabrication of Ag_2O/TiO_2/clay nanocomposites filter and its performance evaluation on the mining wastewater.

1.5 Scope of the Research

This study is limited to the development of Ag_2O/TiO_2 nanoparticles supported on kaolinite clay as a nanocomposite for the treatment of mining wastewater via batch adsorption process. It also involves the fabrication of nano filters for mining wastewater treatment.

CHAPTER TWO

2.0 LITERATURE SURVEY

2.1 Mining Wastewater and their Environmental Impacts

Mining is an economic activity that involves excavations of the earth's surface and rocks, to reach the minerals beneath the surface. Rocky surfaces are frequently blasted to reach mineral reserves within and create permanent scars on the landscape resulting in negative environmental consequences (Dontala *et al.*, 2015). Mining activities can wreak havoc on landscapes, leaving blotches behind which may be irreplaceable once the process is complete (Merem *et al.*, 2017).

The mining process is a significant threat to biodiversity due to large-scale habitat losses as a result of exposure to unprocessed materials, putting fauna and flora at risk (Dontala *et al.*, 2015; Pretty and Odeku, 2017). Meanwhile, mineral resources that are often exploited are bauxite, coal, copper, gold, silver, diamonds, iron, precious metals and lead. Others are limestone, magnetite, nickel, phosphate, oil shale, rock salt, tin, uranium and molybdenum which have contributed to the economic growth of the nation. The explorations of these mineral resources generate large amounts of highly concentrated wastewater due to contact between water and various types of minerals.

Contaminated wastewater is generated as rain infiltrated the mining tailings, causing oxidation, hydrolysis, and washing due to contact between the minerals and water. A typical example of this is acid mine drainage which is usually generated from gold and coal mining activities (Bwapa *et al.*, 2017). The composition of mining wastewater generally includes sulphate, phosphate, nitrate, low pH, high turbidity, TDS, and heavy metal ions. Typical examples of heavy metal ions in mining wastewater are Fe, Mn, Al, Zn, Cu, Ni, Pb, As, and Cd which are toxic to both plants and animals (Ali *et al.*, 2018; Okolo *et al.*, 2018).

The concentrations of these heavy metal ions are different based on mining sites, minerals explored, area of exploration, rate of reactions, and seepages of the pollutants to the environment (Ojonimi *et al.*, 2019) with examples are shown in Plate I.

Plate I: Typical acid mine drainage and its effects

Cobbina *et al.* (2015) reported 0.038 and 0.064 (Hg), 0.031 and 0.002 (As), 0.250 and 0.031 (Pb), 0.034 and 0.002 (Zn), and 0.534 and 0.023 (Cd) in mg/L, for Nagodi and Tinga community in Ghana respectively. While 0.008 to 3.355 mg/L (Cu), 0.058 to 0.349 mg/L (Pb), 0.035 to 0.476 mg/L (Ni), and 0.006 to 0.022 mg/L (Cr) were reported for Dabaoshan mining site in South China (Xie *et al.*, 2018).

Also, in the Abare Artisanal Gold mining site in Zamfara State, Nigeria, the average values (mg/L) of Pb, Hg, Cd, Cr, Cu, and Fe in the wastewater samples are 0.832, 7.278, 0.004, 2.277, 0.062, and 45.908 respectively (Muhammad *et al.*, 2013). All the aforementioned heavy metal concentrations are above the permissible levels in useable water as specified by standard organisations (WHO, 2019).

These make the discharge of mining wastewater pose serious consequences to flora, fauna, and the ecosystem, especially due to the toxicity of heavy metals present in it.

2.2 Heavy Metals and Their Toxicity

The presence of heavy metals in mining wastewater has been responsible for several diseases and the eventual death of plants, animals, and human beings (Balali-Mood *et al.*, 2021). These elements are found in abundance throughout the earth's crust and are non-biodegradable. While a handful plays important roles in bio-systems when at permissible amounts. A larger concentration of these heavy metals can cause toxicity, danger, and other health problems as a result of their bioaccumulation (Bashir *et al.*, 2019). More than 14000 deaths daily have been attributed to various degrees of heavy metal contamination (Okolo *et al.*, 2018).

The acute heavy metal congestion in the human body has been attributed to altering several functions in the central nervous system (CNS), causing dysfunctions and other anatomical imbalances. Serious exposure to these heavy metals has been reported to be responsible for many degenerative diseases and liability to cancerous cells. Tables 2.1a and b summarised the toxicity of heavy metals found in typical mining wastewater and their permissible level according to WHO. The values shown in the table reveal that the presence of contaminants in the mining wastewater can result in various health conditions, hence, requiring removal.

2.3 Wastewater Treatment Methods

The techniques that are employed in mining wastewater treatment are broadly classified into two namely; passive (bioremediation) and conventional methods. The conventional method includes; filtration (ultra and nano), chemical precipitation, reverse osmosis, electrodialysis, ion exchange coagulation, flocculation, and floatation.

Table 2.1a: Heavy metals in mining wastewater, permissible level, and toxicity

Heavy metals	Source/Use	Permissible level (mg/L)	Toxicity	Reference
Pb	Earth's crust as minerals, used in the extraction of gold	0.010	CNS injury, lung dysfunction, Liver damage, encephalopathy.	Balali-Mood *et al.* (2021); Mohd-Noor *et al.* (2019)
Cd	Occurs naturally in soil and minerals such as sulfide, sulfate, carbonate, chloride, and hydroxide salts as well as in water	0.003	Degenerative bone disease, kidney dysfunction, liver damage, and lung injuries.	Nishijo *et al.* (2017); Wang *et al.* (2021)
Hg	Earth's crust as minerals, used in the extraction of gold, has wide industrial applications	0.010	Renal dysfunction, chromosome damage, hepatoxicity, and gastrointestinal ulceration	Chen *et al.* (2019)
As	Natural occurrence. Used as a metalloid substance and medicinal product.	0.010	Liver damage, skin and hair changes, cardio-vascular dysfunction, CNS injury.	Balali-Mood *et al.* (2021)
Cu	Naturally occurring in sea and soil. Used in the manufacturing of several products like; canned foods, hormonal pills, pesticides, insecticides; fungicides and copper cooking pots	1.000	Sleeplessness, ovarian cyst, mental imbalance, bone problems, rheumatoid arthritis; schizophrenia, autism, postpartum psychosis, liver inflammation, leukaemia, and heart damage.	Taylor *et al.* (2020)
Mn	Naturally occurring, used in steel, battery, and food industries	0.200	Degenerative brain disorder, manual dexterity, and impairments in children.	Rudi *et al.* (2020)

Table 2.1b: Heavy metals in mining wastewater, permissible level, and toxicity

Heavy metals	Source/Use	Permissible level (mg/L)	Toxicity	Reference
Cr	Naturally occurring in the earth's crust and seawater, a trace amount of Cr (III) for natural lipid and protein metabolism	0.100	Lungs and upper respiratory cancers.	Pavesi and Moreira (2020)
Ni	Naturally occurring, used in silver refineries, electroplating, zinc base casting and storage battery industries.	0.020	Hasty respiration, dermatitis**,** dizziness, nausea, vomiting myocarditis**,** encephalopathy, pulmonary fibrosis**,** lungs, nose and bone cancer	Hussain and Ali (2021)
Fe	Occurs in nature, used in metallurgical and pharmaceutical industries.	0.300	Gastrointestinal (GI) mucosal irritant, respiration inhibition	Ponka *et al.* (2015)
Co	A hard, silvery grey, and ductile metal element, exists in nature. Used in paints, inks, and dyes	0.300	Heart failure, hearing, and visual problems, cough, difficulty in breathing, and interstitial lung disease.	Leyssens *et al.* (2017)

2.3.1. Passive method

The passive or bioremediation method of wastewater treatment involves the use of microbes and cells by channelling the effluent through natural or constructed wetlands (Bwapa *et al.*, 2017). The microbes or cells that are used to treat wastewater passively are anaerobic and aerobic as well as various algae strains. This method offers advantages like; non-polluting, easy manipulation, low cost, landfill generation, and biomass for potential biofuel production (Edmunson and Wilkie, 2013; Sharma and Khan, 2013).

Park *et al.* (2013) noted that a high level of Fe can be detrimental to algae growth and lipids accumulation, thereby limiting the treatment ability of algae biomass when dealing with AMD. The review of Ben and Baghour (2013) also showed that individual species have shown to be 'hyper-accumulators' and 'hyper-absorbents' with high selectivity for different metals. A long time and large span of area are other demerits of the passive or bioremediation method. Therefore, this is not the ultimate solution for mining site wastewater treatment, as they are still used alongside secondary treatment methods (Bwapa *et al.*, 2017). Conventional methods are better used for mining wastewater because they can produce suitable water for optimal reuse.

2.3.2 Conventional/ advanced wastewater treatment methods

Coagulation/Flocculation

Coagulation is a water purification process that occurs when a chemical or coagulant is added to wastewater or polluted water to remove its pollutants. Some factors such as sources, composition, electrical conductivity, particle size, and density of wastewater are considered in choosing a coagulant (Prakash *et al.*, 2014). The coagulants permit the colloidal materials to form aggregates, change in size, and settle. Among the various coagulants used are alum, iron (III) chloride, and iron (II) sulphate (Prakash *et al.*, 2014). Other coagulants are known as the pre-polymerised type which includes poly aluminium chloride, polysilicates, and composite coagulants. The drawback of coagulation/flocculation methods of wastewater treatment is the generation of a large amount of sludge, which its disposal could be another environmental concern (Mohd-Noor *et al.*, 2019). Ferromagnetite, alum, and eggshells and their hybrids were used as coagulants for the treatment of industrial wastewater by Sibiya *et al.* (2021).

In the research, turbidity, total suspended solid and colour were treated in the wastewater, and the results of the findings showed that the coagulants were effective for the wastewater treated (Sibiya *et al.*, 2021).

Also, Tetteh *et al.* (2017) used polyacrylamide as a coagulant for the treatment of industrial mineral oil wastewater and was effective to remove more than 70% of pollutants. However, the application of these coagulants is limited because they are not easily biodegradable and have less dispersal in water due to their molecular structure.

Chemical precipitation

Chemical precipitation is another technique of wastewater treatment which has been widely used. As it involves the removal of metal ions and other inorganic ions, suspended solids, fats/oils, greases, and some other organic substances from wastewater. The process requires that the contaminants are either dissolved or suspended in the solution which is made to settle as a solid precipitate (Younas *et al.*, 2021). Thereafter, separated from the liquid phase by sedimentation or filtration and the treated water is decanted and appropriately discharged or reused. This method is usually adopted to treat wastewater containing a high concentration of heavy metal ions but it is ineffective when the metal ion concentration is low. Oncel *et al.* (2013) used chemical precipitation for the sequestering of some heavy metals which includes; Fe, Al, Ca, Mg, Mn, Sr, B, Pb, Cr and As present in a coal mining wastewater using sodium hydroxide. The result of their finding has removal efficiencies between 28.4% to 99.96% under varied conditions (Oncel *et al.*, 2013). However, this process produces a large amount of metallic sludge that needs further disposal, making metal recovery difficult. Also, the chemical precipitation of metal sulphides has the demerits of the low solubility of metal sulfides, high sensitivity of the process precipitation agent dosage, and emission of toxic hydrogen sulfide during the process (Lakherwal, 2014; Pohl, 2020).

Ultrafiltration

Ultrafiltration is a separation method that primarily removes pollutants from an aqueous solution by a size exclusion mechanism. This process uses a separation membrane with a pore size in the range of 0.1 to 0.001 mm to remove pollutants (Lakherwal, 2014).

It usually removes high molecular weight substances, colloidal materials, and organic and inorganic polymeric molecules. The membranes merely serve to separate or fractionate wastewater components into more useful and/or less polluting streams, but cannot break down or chemically alter the pollutants (Awaleh and Soubaneh, 2014).

Ultrafiltration as a wastewater treatment technique was employed for the treatment of metal finishing industry effluent, the process removed between 91.3% and 99.8% of the contaminants which includes; suspended solids, nickel, ammonium nitrogen, sulphate nitrogen, chemical oxygen demand, and biochemical oxygen demand. The result of the findings also showed that concentrations in the permeate complied with acceptable limits by standard organisations (Petrinic *et al.*, 2015). This method has high efficiency for heavy metal ions removal from wastewater. Nevertheless, its high cost, process complexity, membrane fouling, and low permeate flux have been major challenges in its deployment for wastewater treatment (Mohd-Noor *et al.*, 2019).

Electro-dialysis

Electro-dialysis is another conventional wastewater treatment method where metal ions are separated using semi-permeable ion-selective membranes (Gurreri *et al.*, 2020). Electrodes are usually used as an ion-selective membrane as there is an electrical potential between two electrodes. This causes a separation of cations and anions in the polluted water, thus cells of concentrated and dilute salts are formed (Younas *et al.*, 2021). A semi-empirical mass transfer model, describing the ions and water transport across the ion-exchange membranes was researched by Mitko *et al.* (2021), using mining wastewater from a coal mine. The result of the finding showed a prediction of maximum attainable chloride concentration in the industrial-scale electro-dialyzer implying that the electro-dialysis of the coal mine water can be applied as a method for the production of concentrated solution (Mitko *et al.*, 2021).

High operational costs due to membrane fouling, pre-treatment using nano-filtration/reverse osmosis and energy consumption are major challenges of the electro-dialysis method (Mitko *et al.*, 2021).

Ion-exchange

The ion exchange technique uses a reversible chemical reaction to remove heavy metals from wastewater, which is performed via ion exchange in the resin (Bashir *et al.*, 2019; Esmaeili and Foroutan, 2015). Because of their many advantages, such as high treatment capacity, high removal efficiency, and quick kinetics, ion-exchange techniques have been widely utilised to remove heavy metals from wastewater. Many heavy metal ions can be sequestered with a variety of resins for a variety of purposes. Synthetic organic resins and inorganic gels are frequently employed in ion exchange because of their ability to be custom-made for specific applications. They are also resilient under more extreme physical conditions and so, have been explored for the removal of heavy metals (Esmaeili *et al.*, 2019; Esmaeili and Foroutan, 2015). In recent research, a unified process of ion exchange resins and activated carbon was used for the treatment of condensate water (Li *et al.*, 2021).

The fixed bed column used contains a pre-treated basic anion exchange resin, acidic cation exchange resin, mixed ion exchange resins and modified activated carbon. They were targeted for the removal of organic pollutants, ionic pollutants and pH adjustment of the water. The result of the findings showed that the treated water has pH between 5 and 8, conductivity lower than 5.0 μS/cm as well as a TOC content reduced to less than 70 ppm, demonstrating the efficiency of the ion exchange resins (Li *et al*., 2021). The disadvantages of the ion exchange process include the fact that not all ion exchange resins are suitable for metal ions removal, have short longevity and the process needs high capital cost (Esmaeili and Foroutan, 2015).

Adsorption process

The adsorption process for the removal of heavy metal ions from an aqueous solution provides advantages over other conventional methods of wastewater treatment. It involves the removal of contaminants on the adsorbent surface which is simple, economically effective, versatile, and easy to operate (Wazwaz *et al.*, 2019). The adsorption process has been used for mining wastewater treatment (Acheampong and Ansa, 2017).

2.3.3 Principles of the adsorption process

Adsorption is a surface phenomenon in which adsorptive (gas or liquid) molecules bind to a solid surface. However, in practice, adsorption is performed as an operation, either in batch or continuous mode, in a column packed with porous sorbents. Under such circumstances, mass transfer effects are inevitable. The principle of adsorption includes mass transfer and comprises up to five explicit process steps (Ho, 2006; Sarma *et al.*, 2019) namely:

Step 1: Transportation of the adsorbate from the bulk of the solution to the liquid film surrounding the solid adsorbent.

Step 2: Diffusion of adsorbate across the liquid film surrounding the solid adsorbent particles to the bare solid surface.

Step 3: Diffusion of adsorbate from the liquid film into the pores of the solid adsorbent (for a porous solid) through intraparticle diffusion (IPD).

Step 4: Adsorption of the adsorbate on the adsorbent surface either by surface reaction or by physical processes.

Step 5: Desorption of the adsorbate from the solid adsorbent surface (in case of reversible adsorption).

The adsorption process can be subdivided into physical adsorption (or physisorption) and chemical adsorption (or chemisorption). Physisorption occurs when the adsorbate adheres to the surface because of physical forces due to Van der Waals interactions, which are attractive forces that occur between molecules due to weak electrostatic interactions (Liley *et al.*, 2017).

If the adsorbate molecules hit the surface with low energy, this can be dissipated as heat by the vibration of the lattice of the solid; hence, they can be trapped on the surface. However, if the molecules hit the surface with too much energy, this cannot be dissipated by the adsorbent, and they bounce away. On the other hand, chemisorption which is chemical adsorption occurs when the adsorbate is chemically bound to the adsorbent's surface (Shooto *et al.*, 2016). It involves stronger forces, whereby the adsorbate forms a real chemical bond (usually covalent) with the adsorbent's surface. The chemical adsorption is usually accompanied by an energy (enthalpy change, ΔH), the change in enthalpy is greater compared to that of physisorption, that is, from 40 to 400 kJ/mol, and it is always negative due to the spontaneous nature of the adsorption process (Ayawei *et al.*, 2017).

The chemisorption can be an activated process as it requires that the adsorbate has minimum energy to be sorbed. This depends on the presence of an energetic barrier between the physisorbed and chemisorbed state. If this barrier is higher than the energy of the free molecules, the adsorbate would be chemically bonded to the adsorbent (Figure 2.1a), otherwise, it would be desorbed. In case the barrier is lower than the energy of free molecules, all the molecules attached to the surface can quickly form a chemical bond with the adsorbent making chemisorption occur rapidly (Figure 2.1b) (Barbato and Bruno, 1996).

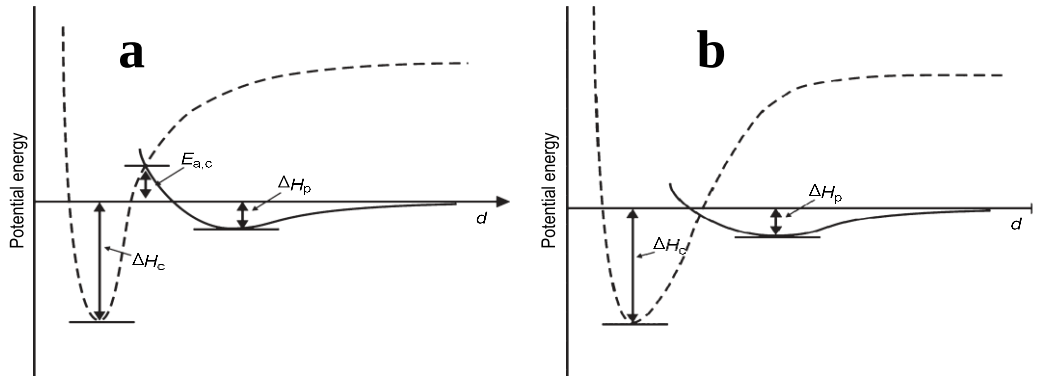

Figure 2.1: Diagram of the energy of adsorption (a) Physisorption (b) Chemisorption

From the figure, the solid line is for physisorption, involving low enthalpy (H_p), while the dashed line is for chemisorption, which involves higher energy (H_c). On the left is the case of activated chemisorption: $E_{a,c}$ is the activation energy for chemisorption. The mechanism of adsorption processes is widely explained by the adsorption isotherms (Ayawei *et al.*, 2017).

2.3.4 Adsorption isotherms

There are several types of adsorption isotherms used to describe the adsorption mechanism and the most used are Langmuir and Freundlich adsorption isotherms (Awasthi *et al.*, 2019). Other isotherms include Jovanovic, Harkin-Jura, Dubinni-Raduskevich, Redlich-Peterson, and Elovich, among several others.

Langmuir Isotherm

Langmuir principle which was primarily designed to describe gas-solid phase adsorption is now employed to quantify and contrast the adsorptive capacity of various adsorbents (Ayawei *et al.*, 2017). Hence, the following assumptions were considered to propose the Langmuir model:

1. The adsorption to be energetically uniform,
2. All the vacant sites are of equal size and shape on the surface of the adsorbent,
3. A dynamic equilibrium exists between the absorbed gaseous molecules and the free gaseous molecules.

The Langmuir theory then applies to homogeneous adsorption where the adsorption of each adsorbate molecule onto the surface has equal sorption activation energy. The linear form of this isotherm is represented by Equation 2.1:

$$\frac{1}{q\mathrm{e}} = \frac{1}{q\mathrm{m}K\mathrm{L}C\mathrm{e}} + \frac{1}{q\mathrm{m}} \qquad (2.1)$$

where q_e (mg/g) and C_e (mg/L) are the amounts of adsorbed adsorbate per unit weight of adsorbent and un-adsorbed adsorbate concentration in solution at equilibrium respectively.

The constant K_L (L/g) is the Langmuir equilibrium constant and q_m is the theoretical monolayer saturation capacity. The essential feature of the Langmuir isotherm can be expressed in terms of a dimensionless constant called separation factor (R_L) which is also known as the Equilibrium parameter and defined by Equation 2.2:

$$R\mathrm{L} = \frac{1}{1+K\mathrm{L}C\mathrm{o}} \qquad (2.2)$$

where C_o (mg/L) is the initial adsorbate concentration.

The value of R_L indicates the shape of the isotherms to be either unfavourable ($R_L > 1$), linear ($R_L = 1$), favourable ($0 < R_L < 1$) or irreversible ($R_L = 0$) (Miyah *et al.*, 2017).

Freundlich isotherm

Freundlich isotherm applies to adsorption processes that occur on heterogeneous surfaces. This isotherm gives an expression that defines the surface heterogeneity, exponential distribution of activities and their energies (Shooto *et al.*, 2016). According to Ayawei *et al.* (2017), the most important multi-site adsorption isotherm for heterogeneous surfaces is the Freundlich which has the linear form of the model expressed as shown in Equation 2.3:

$$\mathrm{Log}\ q_e = \mathrm{Log}\ K_F + \frac{1}{n}\mathrm{Log}\ Ce \qquad (2.3)$$

Where K_F is adsorption capacity (L/mg) and $1/n$ is adsorption intensity; it also indicates the relative distribution of the energy and the heterogeneity of the adsorbates.

Dubinin-Radushkevich isotherm

Dubinin-Radushkevich isotherm model is an empirical adsorption model that is generally applied to express the adsorption mechanism with Gaussian energy distribution onto heterogeneous surfaces. This isotherm is only suitable for intermediate-range of adsorbate concentrations because it exhibits unrealistic asymptotic behaviour and does not predict Henry's laws at low pressure. The model is a semi-empirical equation in which the adsorption follows a pore-filling mechanism. It presumes a multilayer character involving Van der Waal's forces, applicable for physical adsorption processes, and it is a fundamental equation that qualitatively describes the adsorption of gases and vapours on microporous sorbents. It is usually applied to differentiate between the physical and chemical adsorption of metal ions. A distinguishing feature of the Dubinin-Radushkevich isotherm is the fact that it is temperature-dependent.

This implies that the adsorption data at different temperatures are plotted as a function of the logarithm of the amount adsorbed against the square of potential energy to obtain relevant parameters. Dubinin-Radushkevich isotherm is thus expressed in Equation 2.4;

$$\ln q_e = \ln q_m - \beta E^2 \qquad (2.4)$$

Harkin-Jura isotherm

The Harkins-Jura adsorption isotherm was initially applied to gas-solid systems and later adapted to liquid-solid systems by assuming that the adsorbed film is of the condensed type. The isotherm also assumes the prospect of multilayer adsorption on the surface of adsorbents having heterogeneous pore distribution. This model is expressed in Equation 2.5:

$$\frac{1}{{q_e}^2} = \left(\frac{B_H}{A_H}\right) - \left(\frac{1}{A_H}\right) log C_e \quad (2.5)$$

where B and A are Harkin-Jura constants that can be obtained from plotting $\frac{1}{{q_e}^2}$ against log C_e (Ayawei *et al.*, 2017). The model has been reported to show a better fit to the adsorption data than Freundlich, Halsey, Langmuir, Dubinin–Radushkevich and Temkin isotherms in an investigation of the adsorptive removal of reactive black onto Bentonite clay pollutants from wastewater (Amin *et al.*, 2015a).

Jovanovic isotherm

The Jovanovic isotherm is hinged on the assumptions contained in the Langmuir model but in a modified approach. The model specifies the possibility of some mechanical contacts between adsorbate and adsorbent (Ayawei *et al.*, 2017). The linear form of the Jovanovic isotherm is expressed in Equation 2.6:

$$ln q_e = ln q_{max} - K_J C_e \quad (2.6)$$

where q_e is the amount of adsorbate in the adsorbent at equilibrium (mg g^{-1}), q_{max} is the maximum uptake of adsorbate obtained from the plot of ln q_e versus C_e, and K_J is Jovanovic constant.

Meanwhile, Mustapha *et al.* (2020b) reported the application of various isotherms to model the treatment of tannery wastewater using kaolinite clay. Their findings showed that the best prediction of retention capacity was obtained by applying the Jovanovic isotherm model. Therefore, it can be suggested that the Jovanovic isotherm could be most preferred among other isotherms for the modelling of wastewater treatment by the adsorption process.

Elovich isotherm

Elovich isotherm based its mechanism on chemical reaction as a factor that is responsible for the adsorption of heavy metals or dyes onto the adsorbent (Batool *et al.*, 2018).

The equation that defines this model is based on a kinetic principle that assumes that adsorption sites increase exponentially with adsorption, this implies multilayer adsorption. The linear forms of the Elovich model are expressed in Equation 2.7:

$$Q_t = \frac{1}{\beta}\ln(\alpha\beta) + \frac{1}{\beta}\ln(t) \quad (2.7)$$

Elovich's maximum adsorption capacity and Elovich constant can be calculated from the slope and intercept of the plot of ln ln $\left({}^{q_e}/_{C_e}\right)$ versus q_e.

Rania and Yousef (2015) reported the use of the Elovich isotherm model in the equilibrium and kinetic studies of the adsorption of copper (II) ions using a prepared natural adsorbent. The result of their investigation showed that the value of the regression coefficient (R^2) and other adsorptive parameters was higher and more suitable for the Elovich model than that of the Langmuir isotherm model; therefore the adsorption of copper (II) onto Chitin was best described by the Elovich isotherm.

2.3.5 Adsorption kinetics

Adsorption kinetics describes the reaction pathways and the time needed to reach the equilibrium (Pintor *et al.,* 2018). Whereas, chemical equilibrium gives no information about pathways and reaction rates. Adsorption kinetics shows a large dependence on the physical and chemical characteristics of the adsorbent material which also influences the adsorption mechanism that can either be film or pore diffusion or a combination of both, depending on the system hydrodynamics.

Pseudo-first and second-order kinetic model

The pseudo-first-order of Lagergren is given as Equation 2.8:

$$\frac{\mathrm{dq}}{\mathrm{dt}} = k_1(q_e - q_t) \quad (2.8)$$

Where q_t and q_e are the amounts of impurities adsorbed at the time (t) and equilibrium (mg/g), respectively, and k_1 $\left({}^{1}/_{min}\right)$ is the pseudo-first-order rate constant for the adsorption process.

The integration of Equation 2.8 with the initial condition (q_t = 0 at t = 0) leads to Equation 2.9:

$$\log(q_e - q_t) = \log q_e - \frac{K_1}{2.303} t \tag{2.9}$$

The pseudo-second-order chemisorption kinetic rate equation is expressed as Equation 2.10:

$$\frac{dq}{dt} = (k_2\ (q_e -\ q_t)^2 \tag{2.10}$$

The linear form of the pseudo-second-order model can be expressed in Equation 2.11:

$$\frac{1}{q} = \frac{1}{q_e} + (\frac{1}{K_{qe}^2})\frac{1}{t} \tag{2.11}$$

Where k_2 $({}^{g}/_{mg.min})$ is the rate constant of pseudo-second-order adsorption and kq_e^2 is the initial adsorption rate $({}^{mg}/_{g.min})$.

Intra-particle diffusion model

In some cases, pseudo-second-order and elovich kinetic models could not identify the diffusion mechanism. Therefore, the kinetic results could be analyzed using the intra-particle diffusion model to obtain the diffusion mechanism. The initial rate of intra-particle diffusion is then determined by Equation 2.12:

$$q_t = k_i t^{1/2} + C \tag{2.12}$$

where C is the intercept and k_i is the intra-particle diffusion rate constant $\left({}^{mg}/_{g.min^{1/2}}\right)$.

According to this model, the plot of uptake q_t versus the square root of time ($t^{1/2}$) should be a linear graph if intra-particle diffusion is involved in the adsorption process. Also, if the line passes through the origin then intra-particle diffusion is the rate-controlling step. When the plots do not pass through the origin, this is indicative of some degree of boundary layer control. This further shows that the intra-particle diffusion is not the only rate-limiting step, other kinetic models may control the rate of adsorption, all of which may be operating simultaneously.

2.3.6 Adsorption thermodynamics

Thermodynamics parameters such as ΔG^o, ΔH^o and ΔS^o were determined to investigate the feasibility, spontaneity, and nature of the interaction using Equation 2.13;

$$\Delta G^o = -RT \ln K_L \tag{2.13}$$

Where K_L is the Langmuir constant, T is the temperature in kelvin and R is the gas constant. A plot of $\ln K_L$ against $1/T$ was used to obtain ΔH^o and ΔS^o values. The activation E_a energy values were also obtained using the equation.

With the aforementioned parameters, the adsorption process/technology is considered a good alternative to wastewater treatment, the process has been adjudged excellent using a nanotechnological approach.

2.4 Nanotechnological Approach to Wastewater Treatment

Nanotechnology is the making of very small constituents, components, or subsystems from bulk materials to gain greatly enhanced products with improved properties and functionality (Zekić *et al.*, 2018). It is an important field of modern research dealing with the synthesis and manipulation of particle structures ranging from approximately 1 to 100 nm in size (Awasthi *et al.*, 2019).

Within this size range, all the properties (chemical, physical and biological) change in such a way that the individual atoms/molecules and their corresponding bulk are affected (Zekić *et al.,* 2018). Novel applications of nanoparticles and nanomaterials are growing rapidly on various fronts due to their enhanced properties based on size, distribution, and morphology (Ismail *et al.,* 2018).

Nanotechnology is relevant in a large number of fields such as healthcare, cosmetics, biomedical, food and feed, drug-gene delivery, environment, health, mechanics, optics chemical industries, electronics, space industries, energy science, catalysis, light emitters, single-electron transistors, nonlinear optical devices, photo-electrochemical applications, and water treatment. The tremendous growth in these expanding technologies had opened applied frontiers and novel fundamentals with the use of nanomaterials (Ahmed *et al.*, 2016). The use of specific nanoparticles, either embedded in membranes or on other structural media has been reported to rapidly purify contaminants in unusable water (Durgalakshmi *et al.*, 2019).

Nanoparticles are extensively used for the removal of biological contaminants (such as bacteria), chemical contaminants, and heavy metals (Okhovat *et al.*, 2015). Examples of novel nanomaterials used in wastewater treatment are metallic oxides like CuO, SnO, ZnO, XO_3, Ag_2O, TiO_2, and their derivative composites. Among the metallic oxides, silver/silver oxide and titanium oxide nanoparticles are the most sought due to their vital characteristics.

2.4.1 Silver/silver oxide nanoparticles

Silver (Ag) is an element that belongs to the transition series on the periodic table. It is a malleable and ductile metal with a white metallic lustre appearance. Among other metals, silver has the highest electrical conductivity, thermal conductivity, lowest contact resistance, and high optical reflectivity.

Thus, widely used in many electrical applications (Singh *et al.*, 2016). It is stable in pure air and water and can be tarnished by the presence of ozone or hydrogen sulfide or sulphur in the air or water. Silver can exist in four different oxidation states as nanoparticles: Ag^0, Ag^+, Ag^{2+} and Ag^{3+}.

According to Thilagavathi *et al.* (2016), Ag^0 and Ag^+ are abundant and stable while Ag^{2+} and Ag^{3+} are unstable and usually found in aquatic environments. Silver oxide (Ag_2O) nanoparticles are the oxidized form of silver ion (Ag^+) which are formed when metallic silver is reduced physically, chemically, or biologically. In the process, the silver metal salt is first reduced to atoms, then nanoparticles utilising reducing agents from either green or chemical substances. The obtained atoms then agglomerate and form tiny clusters that grow into Ag_2O nanoparticles (Ravichandran *et al.*, 2016a). The Ag_2O is usually dark or grey and has wide industrial applications like in surgery fabrics, batteries, and biomedical engineering among others. It has good anti-bacterial activity, and such been used for wide applications (Singh *et al.*, 2016).

The Ag_2O nanoparticles have been proven resistant to strains of microbes and have effective antimicrobial activity at very low concentrations (Kyomuhimbo *et al.*, 2019). This is because it destroys many biological pathways in a cell and it would necessitate the microorganism to go through many concurrent transmutations to develop resistance (Ju *et al.*, 2018). Furthermore, silver oxide nanoparticles need a very short contact time to cause a very long and lasting cell growth inhibition (Liu *et al.*, 2019). However, the accumulation of silver and its oxide in the human body >10 g can have negative health outcomes like Argyria or DNA damage (Venis and Basu, 2020).

2.4.2 Titanium dioxide nanoparticles

Titanium dioxide (TiO_2) in either bulk or nanoparticle forms are white solid inorganic materials that have found application in a variety of industries.

These industries include plastics, cosmetics, automobiles, building coatings, textiles, pharmaceuticals, and food (Akinnawo, 2019). They are widely used and well-researched due to their appealing characteristics such as; stability in alkaline and acidic media, biocompatibility, non-toxicity, optical and electrical properties (Musial *et al.*, 2020).

Hence, titanium dioxide as bulk particles or nanoparticles has been reported for use in several fields, including sensors, solar cells, air cleaning, self-cleaning applications, photocatalysts and in wastewater treatment (Landage *et al.*, 2020). It had been modified with other relevant nanomaterials and has played significant roles in several processes, especially wastewater treatment applications due to its ability to demineralise toxic pollutants (Durgalakshmi *et al.*, 2019; Krishnan and Mahalingam, 2017). The TiO_2 (bulk or nanoparticles) exists in the crystalline forms of brookite, rutile, and anatase. Among the three crystalline forms, the anatase and rutile phases of TiO_2 are mostly demanded in industrial applications (Ajala *et al.*, 2021).

To obtain rutile, both anatase and brookite can be modified through thermal treatment at temperatures between 450 and 1200°C. The rutile form is the most stable of all the phases at all temperatures and pressures <60 kbar. It is worthy of note that the transformation of temperature to rutile is dependent on the synthesis conditions, nature, and structure of the precursor (Nyamukamba *et al.*, 2016). The crystalline phase transformations of TiO_2 nanoparticles are considered of utmost importance due to their efficient capability as a catalyst in several reactions and impactful in wastewater treatment processes (Oi *et al.*, 2016). The TiO_2 nanoparticles like Ag_2O nanoparticles are synthesised either physically, chemically, or biologically. Hence, the synthesis of nanoparticles is a novel technology that can be perused to obtain desired nanoparticles adjudged through various characterisation techniques.

2.5 Synthesis of Nanoparticles

There are two different approaches for the synthesis of nanoparticles which are the Top-down and Bottom-up approaches. These are further classified into methods, which include: chemical, physical, and biological synthesis methods (Ahmad *et al.*, 2021a). Figure 2.2 further elucidated the sub-techniques of synthesising nanoparticles.

2.5.1 Chemical methods

The chemical methods are used for the synthesis of nanoparticles such as Ag_2O and TiO_2 using organic and inorganic substances as reducing agents. Examples of chemical methods are microemulsion techniques, UV-initiated photoreduction, electrochemical reduction, solution irradiation, microwave-assisted synthesis and sonochemical method as presented in Figure 2.2 (Akinnawo, 2019; Ravichandran *et al.*, 2016a). The use of chemical methods for nanoparticle synthesis has the advantage of simple preparation in an aqueous solution. They are used as protective agents to stabilise the dispersion of the nanoparticles and avoid their agglomeration (Falk *et al.*, 2018). Examples of chemical-reducing agents reported in the literature for nanoparticle synthesis are citric acid, sodium citrate, borohydride, ascorbate, glucose, and hydrazine (Ijaz *et al.*, 2020; Satyanarayana and Reddy, 2018). Nevertheless, they are costly, and toxic to human cells and the environment, thereby making the chemical synthesis methods less desirable.

2.5.2 Physical methods

The physical methods include ball milling, thermal decomposition, ceramic heating, arc discharge technique, evaporation-condensation and laser ablation as presented in Figure 2.2 (Alaqad and Saleh, 2016). The evaporation-condensation and laser ablation are the most common physical methods for metal oxides nanoparticles synthesis. The methods have some advantages which include uniform distribution of nanoparticles and non-contamination of solvent in the prepared thin films (Satyanarayana and Reddy, 2018).

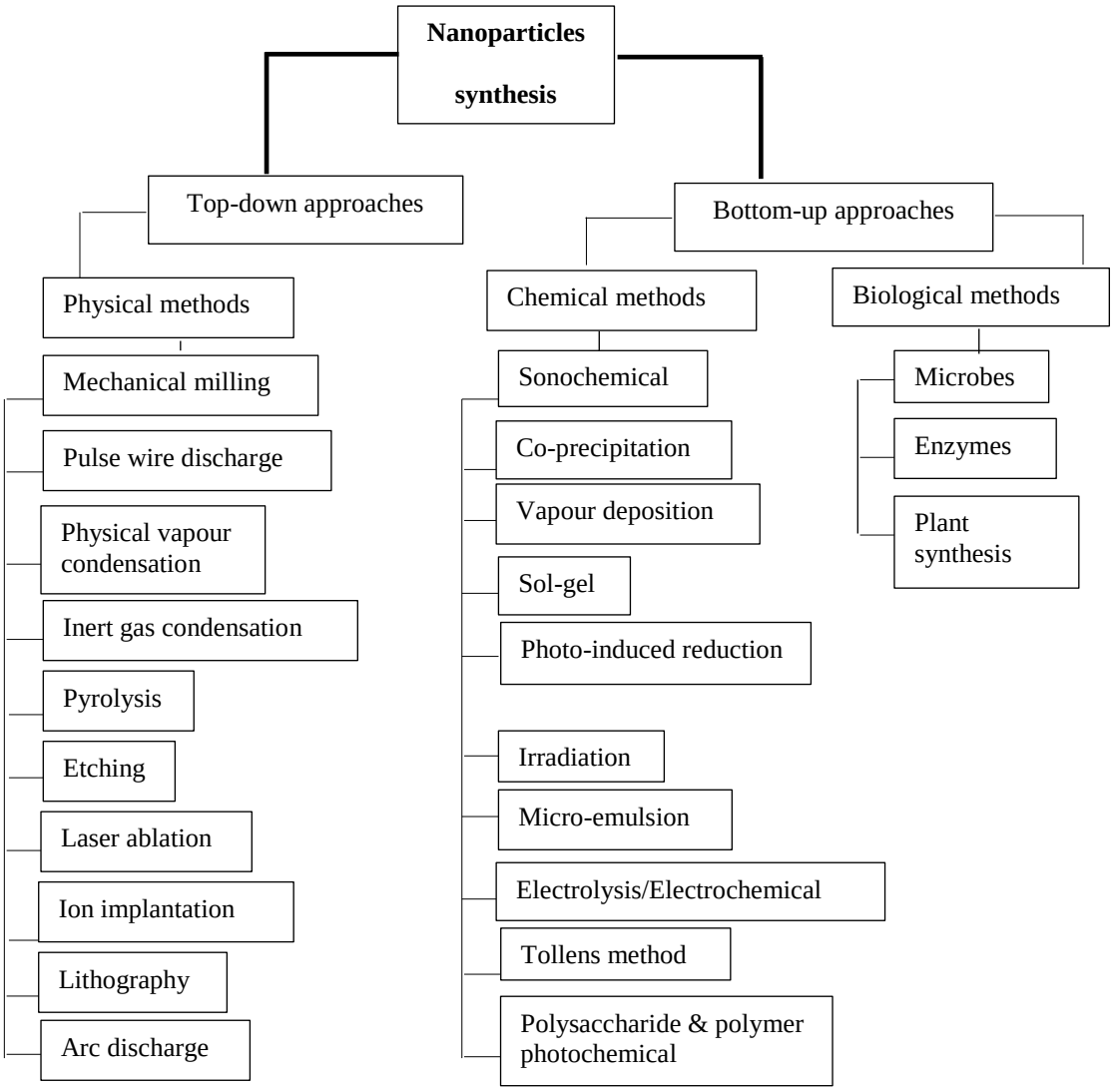

Figure 2.2: Schematic diagram of nanoparticles synthesis approaches

(**Source**: Akinnawo, 2019)

However, these methods require sophisticated equipment that is complex to operate, occupies space and is capital intensive. Also, they consume a great amount of energy to achieve the required temperature of the process and a lot of time to achieve thermal stability (Akinnawo, 2019).

In the case of the use of the laser ablation method for the synthesis of nanoparticles, several factors are usually considered. The factors are laser wavelength, duration of laser pulses, laser fluency, ablation duration, and effectiveness of liquid medium which sometimes could be with or without surfactants (Ijaz *et al.*, 2020).

These factors are difficult to manage and time-consuming, hence, the need for more friendly methods of nanoparticle synthesis such as biological methods.

2.5.3 Biological synthesis

Generally, nanoparticles are mostly produced by physical and chemical methods, however, there is a need for an alternate route due to high cost and toxicity respectively (Karunakaran *et al.*, 2016). These have inspired researchers to discover a more environmentally benign approach which is known as the biological method. The method has several advantages over the other methods, as it has ease of rapid synthesis, controlled toxicity and size, low cost, and eco-friendly (Sethy *et al.*, 2020).

The biological synthesis of nanoparticles has grown prominently to create novel materials that are stable with great importance in the wider applications of electronics, medicine, and agriculture (Kavitha *et al.*, 2013). Figure 2.2 presents some approaches under biological methods with the use of reducing agents from microorganisms, enzymes and plant extract. These reducing agents can be achieved for the synthesis of nanoparticles following the generalised cheaper pathways as presented in Figure 2.3.

The biological method of nanoparticle synthesis is a bottom-up approach that involves a reduction or oxidation reaction. The microbes or plant aqueous extract for nanoparticle synthesis contains antioxidant or phytochemical properties, which are responsible for the reduction of metal compounds into their respective nanoparticles. Plant sources such as *Carica papaya, Nelumbo nucifera, Aloe vera,* and *Musa paradisiaca* have been reported in the literature for the synthesis of metal oxide nanoparticles (Ahmed *et al.*, 2016). Also, microbes such as bacteria, yeasts, algae, fungi, and actinomycetes have been used for the biosynthesis of nanoparticles (Yadav *et al.*, 2017). The main drawback in the use of fungi and bacteria as antioxidants for nanoparticle synthesis is the longer incubation time to reduce the bulk particles.

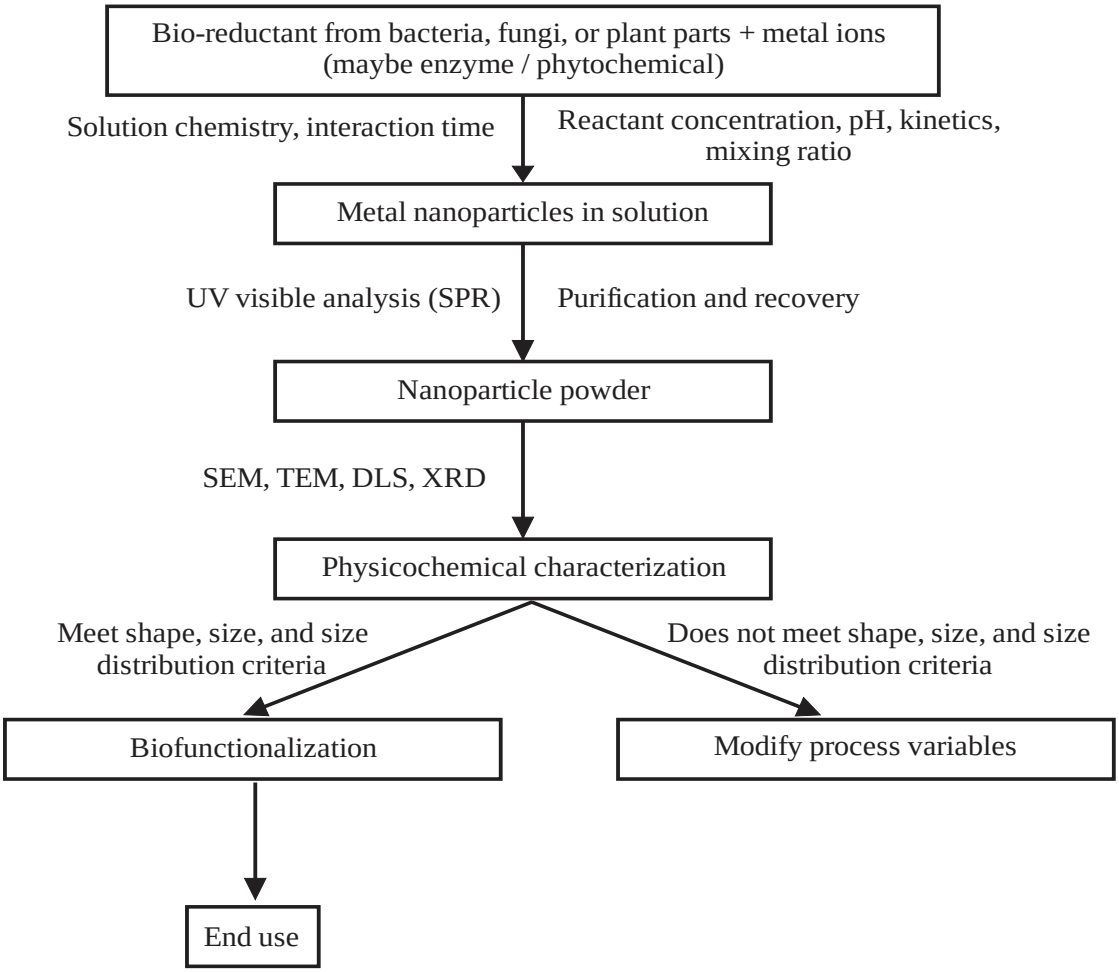

Figure 2.3: Generalised pathway for biological synthesis of nanoparticles

(**Source:** Yadav *et al.*, 2017)

As the phytochemicals (flavonoids, phenol, and tannin) in plant leaf extracts possess the potential to reduce metal ions in a much shorter time (Singh *et al.*, 2018). The green synthesis of nanoparticles by plants is more acceptable, preferable, and gaining importance nowadays due to its single-step biosynthesis, absence of toxicants, and presence of natural capping agents (Yadav *et al.*, 2017). In addition, the use of plant sources for the synthesis of nanoparticles is preferred to other biological processes. This is due to their ease of availability, safe to handle, and possess broad variability of metabolites that may aid in reduction. Several plants and plant parts have been used for the nano synthesis of metal oxides such as Ag_2O and TiO_2 nanoparticles.

Examples of such plants are *Syzygium cumini* leaves (Sethy *et al.*, 2020), *Bidens pilosa leaves* extract (Kyomuhimbo *et al.*, 2019), *Hyptis suaveolens* leaves extract (Lateef *et al.*, 2020), pod extract of *Cola nitida* (Azeez *et al.*, 2017), *Piliostigma thonningii* leaves extract (Shittu and Ihebunna, 2017a). Worthy of note is that *Parkia biglobossa* (Locust bean) leaves have not been reported in the literature for Ag_2O and TiO_2 nanoparticle synthesis, at least to the best of the author's knowledge.

Parkia biglobossa

Parkia biglobosa belongs to a sub-family of *Mimosoideae* and the family of *Fabaceae.* It is popularly known as the African locust bean tree and is a perennial tree legume, which grows in the Savannah region of West Africa up to the Southern edge of the Sahel zone at 13° (Dedehou *et al.*, 2016). The fruit is a slightly bent, brown indehiscent pod, 30 to 40 cm long and 2 to 3 cm wide producing up to 20 seeds per pod as shown in Plate II.

Plate II: *Parkia biglobossa* (Locust) plant

Parkia biglobosa is a medicinal plant widely used in traditional African medicine, particularly in Nigeria, Togo, and Cameroun, to treat a range of diseases. Studies have shown that it is non-toxic to humans, and contain phytochemical compounds such as tannins, saponins, flavonoids, terpenes, carbohydrate, and phenols (Ampitan, 2013; Udobi and Onaolapo, 2009). The bark, leaves, and roots are used to treat digestive disorders, wounds, hypertension, diabetes, abscess, and infections (Udobi and Onaolapo, 2009). The fermented seed is used locally as spices in food and delicacy soups (Dedehou *et al.*, 2016; Udobi and Onaolapo, 2009).

2.6 Synthesis, Characterisation and Applications of Ag_2O Nanoparticles using Plant Extract

The biological/green synthesis of Ag_2O nanoparticles has been reported to have some advantages over other methods (Kalaki *et al.*, 2018). Also, among the various methods of green synthesis of Ag_2O nanoparticles, varieties of plant extracts have gained prominence due to their cost-effectiveness, environmental compatibility and simplicity. Moreover, the plant extract possesses secondary metabolites that effectively reduce bulk silver salt to Ag_2O nanoparticles (Jayapriya and Lalitha, 2013).

Recently, Ghotekar *et al.* (2020) reported the use of plant extracts to facilitate the development of Ag_2O nanoparticles and obtained well-dispersed products. Kyomuhimbo *et al.* (2019) synthesised Ag_2O nanoparticles using an aqueous plant extract of *Bidens pilosa* in the presence of silver nitrate salts to produce hand-sanitizing antiseptics. Their characterisation result showed a silver nanoparticle formation at a peak between 408 - 411 nm using a UV-visible spectrophotometer. The formulated handwashing antiseptic was found active against wide pathogens. Karunakaran *et al.* (2016) developed Ag_2O nanoparticles using a biological method at maximum absorbance of 450 nm to obtain cubic face-centred shape particles of 40 nm size.

The Ag_2O nanoparticles demonstrated good anti-bacterial activity against selected gram-positive and gram-negative bacterial strains in an aqueous solution. In another study by Jalees *et al.* (2018), the Ag_2O nanoparticle was successfully synthesised using Mango peel extract at 436 nm wavelength of Uv-visible spectroscopy. The formation of the Ag_2O nanoparticles was confirmed by the XRD and TEM characterisations to have particle sizes between 3-20 nm. The obtained Ag_2O nanoparticles were of cubic face-centred shape which could be recommended for pharmaceutical and medical applications.

Mukul *et al.* (2022) synthesised Ag-AgO-Ag_2O nanocomposite using $AgNO_3$ as a precursor to obtain particle sizes between 15-40 nm. The as-synthesised nanocomposite was characterised and showed properties of an efficient anti-cancer antioxidant agent in biomedical practice. The green synthesis of Ag_2O nanoparticles using leaf extract of *Callistemon lanceolatus* was also reported by Ravichandran *et al.* (2016a). They found out that the leaf extract successfully synthesized hexagonal-shaped Ag_2O nanoparticles with sizes ranging from 3-30 nm. The leaf extract of the medicinal plant *Pavetta indica* Linn was also used successfully for the synthesis of Ag_2O nanoparticles. The possibility of the 49.8 nm particle-sized (distorted square-shaped) nanoparticles' outcome was attributed to the phytochemical constituents of the leaf extract used (Suresh *et al.*, 2018).

Another eco-friendly process was applied for the synthesis of Ag_2O nanoparticles using *Paeonia emodi* fresh leaves extract as a reducing agent (Shah *et al.*, 2019). The nanoparticles having a crystallite size of 38.29 nm were obtained by XRD and other characterisations such as SEM, TEM, and FTIR were also employed. The as-synthesised Ag_2O nanoparticles were tested active against gram-positive, gram-negative, and *Pseudomonas aeruginosa* bacteria.

Manikandan *et al.* (2017) reported the use of *Ficus benghalensis* prop root extract as a reducing and stabilizing agent for Ag_2O nanoparticle synthesis and evaluated it for its antibacterial activity against dental bacterial strains. The UV–vis absorption spectra showed an absorbance peak in the range of 430 nm. Also, the FTIR spectral peaks indicated that the phytochemicals in the extract were responsible for the formation of the Ag_2O nanoparticles. The HRTEM image, SAED, and XRD pattern confirmed the 42.7 nm particle size of the Ag_2O nanoparticles. Sharma and Srivastava (2020) also biogenically synthesized Ag_2O nanoparticles using leaves extract of *Artocarpus hetrophyllus*. The as-synthesized Ag_2O nanoparticles were spherical and 14 nm in size. In another study, a facile and green approach was used for the synthesis of Ag_2O nanoparticles using an extract from a wild plant called *Herniaria hirsuta*.

The UV-Vis, SEM, and XRD characterisations gave a surface plasmon resonance peak at 430 nm with a nearly spherical shape and crystallite size of 15.51 nm for the Ag_2O nanoparticles. The catalytic activity of Ag_2O nanoparticles was tested to remove methylene blue from an aqueous solution (El-Ghmari *et al.*, 2021). *Centella asiatica* and *Tridax* which were found to contain flavonoids and other phytochemicals were also used to successfully prepare Ag_2O nanoparticles (Rashmi *et al.*, 2020). The findings from the reviewed literature supported the claim that leaves extract gave good accounts for the successful synthesis of Ag_2O nanoparticles (Azeez *et al.*, 2017; Lateef *et al.*, 2020). The literature further reported that the Ag_2O nanoparticles could be used for the treatment of wastewater from different sources (Jerlin and Beula, 2017; Rajabi *et al.*, 2019; Shittu and Ihebunna, 2017a). Tables 2.2a and b further revealed several biologically synthesised Ag_2O nanoparticles for various applications in wastewater treatment.

Table 2.2a: Synthesis of silver and silver oxide nanoparticles and their applications

Materials	Precursor	Synthesising agent	Characterisation techniques	Particle size (nm) and shape	Applications	Shortcomings	Reference
Ag_2O	$AgNO_3$	*Pinus longifolia*	Uv-visible, SEM	1-100	Anti-bacteria	Wastewater was not treated	Khatun *et al.* (2015)
AgNPs	$AgNO_3$	*Bidens pilosa*	Uv-visible, XRD, EDS	-	Hand sanitising antiseptic	AgNPs not Ag_2O were synthesised	Kyomuhimbo *et al.* (2019)
Ag_2O	$AgNO_3$	*Nitrobacter sp.*	Uv-visible, FTIR, EDX, XRD	40	Biomedical	The synthesised Ag_2O was not with plant extract	Karunakaran *et al.* (2016)
AgNPs	$AgNO_3$	*Avicenna marina* leaf extract	Uv-visible, FTIR, EDX, XRD	10-30, spherical	Water treatment	AgNPs instead of Ag_2O were synthesised	Jerlin and Beula (2017)
AgNPs	$AgNO_3$	*Piliostigma thonningii* leaves extract	Uv-visible, FTIR, EDX, TEM	50-114, spherical	Heavy metal adsorption	Only heavy metals were removed	Shittu and Ihebunna (2017a)
Ag_2O	$AgNO_3$	Mango peels	UV-Vis, XRD, TEM and FTIR	3-20	-	Ag_2O was synthesised but not applied	Jalees *et al.* (2018)
AgNPs	$AgNO_3$	*Carallumma umbellate*	SEM, EDS, UV-Vis, XRD, TEM and FTIR	26	Antimicrobial	Mining wastewater was not involved	Anju *et al.* (2018)
AgNPs	$AgNO_3$	*Costus igneus leaves*	XRD, EDX	60-70	-	AgNPs synthesised were not applied	Chinnasamy *et al.* (2017)

Table 2.2b: Synthesis of silver and silver oxide nanoparticles and their applications

Materials	Precursor	Synthesising agent	Characterisation techniques	Particle size (nm) and shape	Applications	Shortcomings	Reference
AgNPs	$AgNO_3$	Pomengranate peel extract	FTIR, XRD	35	-	The synthesised AgNPs were not applied	Thilagavathi *et al.* (2016)
Ag-AgO-Ag_2O	$AgNO_3$	*Solanum elaeagnifolium* leaves	SEM, EDS, UV-Vis, XRD, TEM and FTIR	15-40	Anticancer	Mixed nanoparticles were obtained	Mukul *et al.* (2022)
Ag_2O	$AgNO_3$	*Pavetta indica*	XRD, Zeta potential, SEM, EDAX	49.8	Anti-inflammatory	The obtained Ag_2O was applied to a wound dressing	Suresh *et al.* (2018)
Ag_2O	$AgNO_3$	*P. emodi* leaves	XRD, SEM, FTIR	38.29	Antibacterial	Wastewater treatment was not considered	Shah *et al.* (2019)
Ag_2O	$AgNO_3$	*Ficus benghalensis*	UV-Vis, XRD, TEM, SAED, and FTIR	42.7	Antibacterial	No wastewater treatment	Manikandan *et al.* (2017)
Ag_2O	$AgNO_3$	*Centella asiatica*	XRD, UV-Vis, SEM, EDS, FTIR	11-12	-	The synthesised Ag_2O were not applied	Rashmi *et al.* (2020)
Ag_2O	$AgNO_3$	*Herniaria hirsute*	UV-Vis, XRD, TEM, and FTIR	15.51	Methylene blue	Heavy metals were removed	El-Ghmari *et al.* (2021)
Ag/Ag_2O	$AgNO_3$	*Artemisia Herba-Alba*	UV-Vis, XRD	10.7-36.8	-	Mixed nanoparticles were synthesised	Belaiche *et al.* (2021)

Worthy of note is that *Parkia biglobossa* leaves extract has not been reported for Ag_2O nanoparticles and the nanoparticles have not been reported for mining wastewater treatment, hence, the novelty of this study.

2.7 Mechanism of Ag_2O Nanoparticles Synthesis by Plant Extract

Silver oxide nanoparticles are an essential product in nanotechnology as it is widely used in the biomedical field and wastewater treatment. This is due to the Ag_2O nanoparticles' unique properties such as chemical stability, high catalytic activity, good electrical conductivity and exceptional antimicrobial activities (Bao *et al.*, 2021). The synthesis of Ag_2O nanoparticles using plant extracts has been reported in the literature (Chinnasamy *et al.*, 2017; Chinthalapudi *et al.*, 2021; El-Ghmari *et al.*, 2021; Kyomuhimbo *et al.*, 2019; Suresh *et al.*, 2018). This is because the plant extracts are composed of carbohydrates and proteins biomolecules that are readily available as reducing agents, promoting the formation of metallic nanoparticles. For instance, the proteins with functionalised amino groups ($–NH_2$) present in plant extracts actively participate in the reduction of metal ions. Also, functional groups such as –C–O–C–, –C–O–, –C=C–, and –C=O– in phytochemicals of plant extracts also aid the formation of metallic nanoparticles (Singh *et al.*, 2018).

Therefore, the mechanism of Ag_2O nanoparticle synthesis using plant extract involves three steps which are the reduction of ions, clustering and nanoparticle growth (Jain and Mehata, 2017). Each of these steps is affected by the following factors: the nature of the reducing agent, the concentration of precursor, pH, temperature, and concentration of the reducing agent (Chowdhury *et al.*, 2016). These factors could be varied to control the size, shape, general morphology, efficiency, and applicability of the synthesised nanoparticles.

The type and concentration of plant extract are also important factors in nanoparticle synthesis, as different plants comprise varying concentration levels of phytochemicals (Singh *et al.*, 2018). The main phytochemicals present in plants are flavonoids, terpenoids, sugars, ketones, aldehydes, carboxylic acids, and amides, which are responsible for the bioreduction of nanoparticles (Singh *et al.*, 2018).

The plant extract-mediated synthesis of Ag_2O nanoparticles entails the mixing of an extract with metal precursor solution at different reaction conditions. These conditions are responsible to control the rate of nanoparticle formation, yield and stability (Singh *et al.*, 2018). Therefore, plant leaf extracts are excellent and benign materials as a reducing agent for metal and metal oxide nanoparticle synthesis, that play a dual role by acting as both reducing and stabilizing agents to facilitate nanoparticle synthesis.

According to Jain and Mehata (2017), the reduction of silver ions to Ag_2O nanoparticles may be attained by dissociation energies of the O–H bond of –OH groups present in flavonoids. This was made possible as the -OH groups of flavonoids might have taken part in metal ion reduction. Also, sugars such as glucose and fructose in plant extracts can be responsible for the formation of metallic nanoparticles. As glucose was capable of participating in the formation of metallic nanoparticles of different sizes and shapes, whereas fructose-mediated Ag_2O nanoparticles are mono disperse in nature (Singh *et al.*, 2018). The mechanism proposed in the literature suggests that silver precursor in solution dissociates into silver ions (Ag^+) and nitrate ions (NO^{3-}). Then, flavonoids (quercetin) having hydroxyl and ketonic groups reacts with Ag^+ as an acid through reactive hydroxyl groups and attaches to the aromatic ring carbon atoms. This reduces the Ag^+ to Ag_2O nanoparticles and provides stability against agglomeration (Borodina and Mirgorod, 2014). The enzymes in the leaf extract also combine with the Ag^+ to form an enzyme-substrate complex with a charge transfer between quercetin and Ag^+.

This results in the formation of protein-capped Ag nanoparticles (Jain and Mehata, 2017). Thereafter, the atoms agglomerates form tiny clusters which then grow into Ag_2O nanoparticles. Figure 2.4 reveals the proposed mechanism of the Ag_2O nanoparticles synthesis from aqueous plant extract.

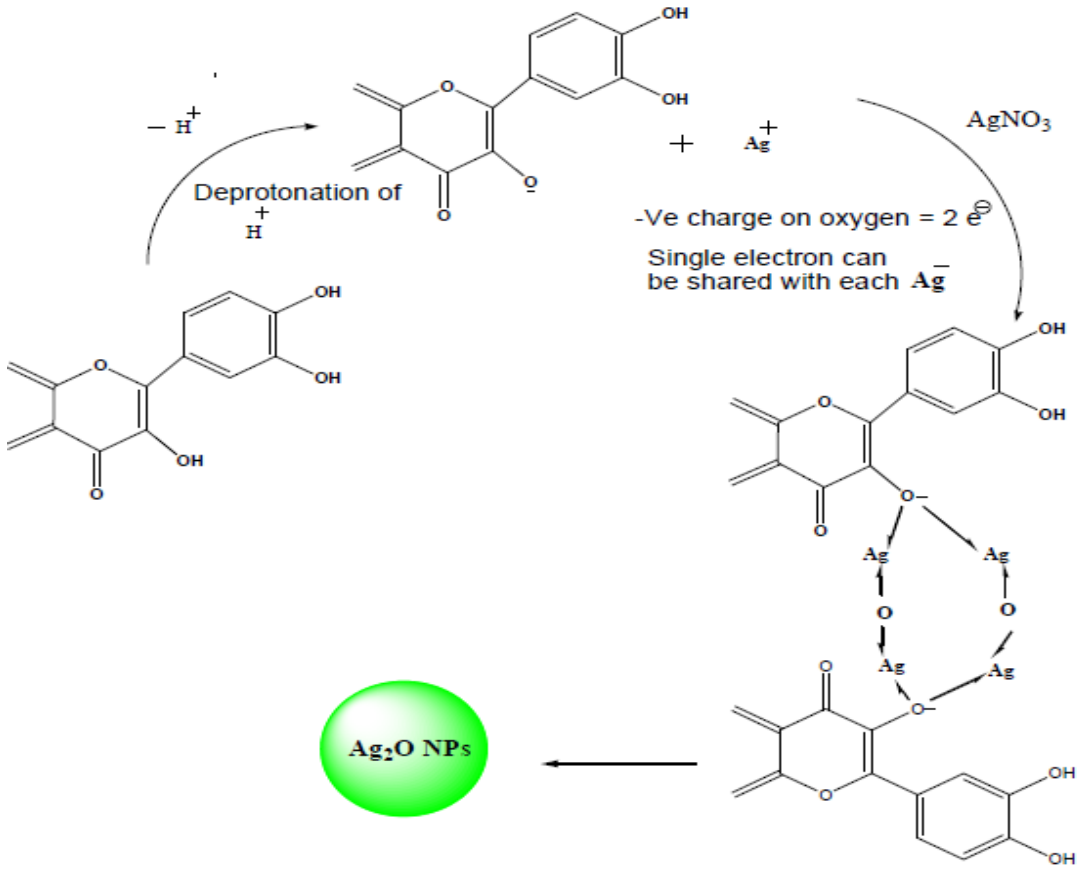

Figure 2.4: Mechanism of Ag_2O synthesis by green leaves extract

(**Source:** Ghotekar *et al*., 2020)

Available reports on suitable process variables in synthesizing Ag_2O nanoparticles are majorly on a one-factor-at-a-time approach. These methods have drawbacks; they are non-interactive enough and primarily focused on improving the production yield of nanoparticles (Chinnasamy *et al.*, 2017).

A research, optimisation study conducted by Chowdhury *et al.* (2016) discovered that the concentration of precursor ($AgNO_3$), and concentration of reducing agent significantly contribute to the yield of nanoparticles. While the stirring time of the process has no significant influence on the yield of nanoparticles. There is a paucity of information about the optimal process conditions for synthesizing silver nanoparticles from bio sources such as *Parkia biglobossa* leaves extract. Hence, the need for applying statistical optimisation techniques which include response surface methodology, to determine suitable factors that could improve the yield of nanoparticles.

2.8 Silver Oxide Binary and Ternary Composites in Adsorptive Applications

Silver oxide has been developed into composites of binary and ternary mixtures for wastewater treatment. Taha *et al.* (2020) reported the use of a ternary composite of silver oxide and zinc oxide loaded on activated carbon (Ag-ZnO/AC) for 4-nitrophenol degradation and antibacterial effects in an aqueous solution. Their findings showed that the Ag-ZnO/AC nanocomposites were proven effective for the 4-nitrophenol photo-degradation due to the facilitated electron transfer. This was attributed to the good dispersal of AgNPs on the surface of activated carbon. The nanocomposite also showed a great antibacterial effect as 8 out of 16 tested pathogens were successfully eliminated.

In another study by Ostovar *et al.* (2017), a binary nanocomposite of silver oxide and sawdust (Ag_2O/SD NC) was developed for the removal of Cr (VI) ions from aqueous solutions. The study indicated that the Ag_2O/SD NC was successfully utilised as an adsorbent for the removal of Cr (VI) ions from wastewater. The removal of phosphate from an aqueous solution using a binary composite of silver nanoparticles loaded on tea-activated carbon (AgNPs-TAC) was studied (Trinh *et al.*, 2020). Their findings showed that the composite was effective in the removal of phosphate from the wastewater.

Xu *et al.* (2018) developed a ternary nanocomposite from polyacrylonitrile (PAN) with TiO_2 and Ag_2O to form PAN-TA. The morphologies and structure of the nanocomposite were examined using different techniques and the findings revealed that the product contains adequate functional groups suitable for adsorption. An adsorptive experiment was conducted using the PAN-TA composite and the result showed high efficiency for the removal of methylene blue (MB) dye at a maximum adsorption capacity of 155.4 mg g^{-1}.

Eco-friendly composites of cellulose nanofiber (CNF) and silver nanoparticles (Ag NPs) as a binary nanocomposite (CNF-Ag NPs) were prepared for the adsorption of malachite green (MG) dye from wastewater (Chinthalapudi *et al.*, 2021). The adsorption study revealed that the maximum uptake of MG dye using CNF-Ag NPs composites was 142 mg/g. A ternary silver oxide-loaded bismuth oxybromide (Ag_2O/BiOBr) nanocomposite was synthesised for antibacterial applications (Bisht *et al.*, 2021). The as-prepared sample was characterised by different analytical techniques and showed the incorporated Ag in the +1 oxidation state as Ag_2O. The synthesised nanoparticles were subjected for 2 h to opportunistic human pathogenic bacteria such as; *Escherichia coli, Pseudomonas aeruginosa, Salmonella typhimurium, Klebsiella pneumonia, and Aeromonas salmonicida*. The nanocomposite was found to have a potential bactericidal activity as it completely inhibited the growth of all the tested bacterial strains, therefore could be an alternative to the conventional antimicrobial agents currently used (Bisht *et al.*, 2021). Jiao *et al.* (2015) investigated the synthesis of a binary nanocomposite using graphene oxide (GO) and silver oxide. The synthesis of the nanocomposite was carried out in situ through the simultaneous reduction of GO and silver precursor within the GO gel matrix to form cross-linked nanosheets.

The binary nanocomposite was characterised and silver oxide was found to be homogeneously and uniformly dispersed on the surface of the reduced graphene-oxide nanosheets within the composite gel. The as-synthesized composite was used as a potential catalyst for removing organic dye (Rhodamine Blue and Methyl Blue) pollutants from an aqueous environment with adsorptive capacities of 13.51 mg/g and 33.59 mg/g. The as-prepared catalytic composite matrix structure was conveniently separated from an aqueous environment after the reaction due to the co-doping effects of the composite.

In another research, silver-doped titanium dioxide films were synthesized by sol-gel spin coating technique on the silicon substrates (Demirci *et al.*, 2016). The photocatalytic activities of the TiO_2 films having different Ag content were investigated for the degradation of methylene blue (MB) under UV light irradiation. The crystal phase structure, surface morphology, and chemical, as well as optical properties of Ag-doped TiO_2 films, were characterised using an X-ray diffractometer (XRD), scanning electron microscopy (SEM), and X-ray photoelectron spectroscopy (XPS), UV–vis spectrophotometer, and FTIR spectrophotometer.

The results obtained showed that the Ag-doped TiO_2 films calcined at 500◦C were of the anatase phase, crystalline, and with cracked surface morphology. The Ag substitution into the TiO_2 matrix did enhance the photocatalytic activity of TiO_2 films under UV light irradiation when compared with the undoped TiO_2 film. Also, the 0.7% Ag-doped TiO_2 film has better photocatalytic activity than compared to the undoped and other Ag-doped TiO_2 films. The study confirmed the suitability of Ag-doped TiO_2 films for the effective treatment of dissolved organic contaminants in water (Demirci *et al.*, 2016).

Also, silver-titanium oxide was doped on activated carbon for the removal of phenol from pharmaceutical wastewater and was found suitable to remove 9.86% (conc.0.3299 mg/L) at 3 h. 42 min. time, the temperature of 35°C, and the adsorbent dosage of 0.1 g/50 mL (Mustapha *et al.*, 2021).

In another study, the surface of TiO_2 nanotubes (TiO_2 NTs) was plated with an antimicrobial layer of nano zinc oxide particles (nZnO) and nano-hydroxyapatite (HA) to form a composite (Gunputh *et al.*, 2019). The composite was annealed at different temperatures of 350, 450, and 550°C and characterised using SEM and EDS. The result obtained showed that the nanocomposite annealed at 350°C temperature possessed the most uniform and nano-size porous coating product which was found effective against *S. aureus* as 60% was inhibited. It can be deduced from various literature reviews that either as binary or ternary nanocomposites, silver oxide-based nanocomposites are more effective for the removal of various pollutants including pathogens from wastewater, but still need to be improved for efficient treatment of wastewater. Therefore, it is important to modify silver oxide with other materials such as TiO_2, ZnO, SiO_2, activated carbon, and clay. This is to improve the efficiency of silver-based nanocomposite for the removal of a wide range of pollutants in wastewater treatment.

Applications of silver-based nanocomposites in wastewater treatment

Silver-based nanocomposites have been applied in wastewater treatment against pathogens, organic and inorganic pollutants. The nanocomposites of silver oxide with other materials have also been found to show enhanced antimicrobial activity against common microbes as compared to silver oxide nanoparticles (Liu *et al.*, 2019). This is because the properties of the hybrid are not just the sum of the individual advantages, however, the synergic interaction effect creates a new class of hybrid nanomaterials (Lu *et al.*, 2017).

The synergistic effects have been linked with the mass production of reactive oxygen species such as H_2O_2, which enhances the increased antimicrobial activity of hybrid nanocomposite (Kyomuhimbo *et al.*, 2019). Moreover, silver and silver oxide composites have been investigated for their ability to remove pollutants in water such as heavy metals (Al-Qahtani, 2017), phosphate (Trinh *et al.*, 2020) dyes (Yari *et al.*, 2021), antioxidant activity (Azeez *et al.*, 2017) amidst several others from aqueous solutions. Some researchers have loaded silver nanoparticles onto activated carbon to produce a new, inexpensive adsorbent for the removal of dye pollutants such as methylene blue, malachite green, and direct yellow (Choudhary *et al.*, 2021). These silver nanoparticle-modified materials had improved and more efficient application capacities, compared with others without silver or silver oxide nanoparticles (Trinh *et al.*, 2020).

2.9 Titanium Oxide Synthesis, Characterisation, and Applications

Titanium oxide nanoparticles have also been synthesised using several precursors and methods as shown in Tables 2.3a and b. The table also includes their methods of characterisation and various applications of TiO_2 nanoparticles. The properties of TiO_2 nanoparticles through unique, have limited applications due to some drawbacks, especially in adsorptive wastewater treatment. These drawbacks include; its wide band gap which is responsible for its low activity in the ultra-violet region of the solar spectrum. Others are low surface area and porosity which make it less suitable for effective adsorptive decongestion of pollutants. It also tends to aggregate in an aqueous solution, forming a colloidal suspension in an aqueous solution, thereby making post-separation possibilities difficult. Several measures have been taken to overcome these limitations which include; elemental doping, metal and semi-conductor loading, and dye sensitization (Guan *et al.*, 2019).

Table 2.3a: Synthesis, characterisation and applications of titanium dioxide nanoparticles

Material	Precursors	Synthesis method	Characterisation	Size and shape	Applications	Shortcomings	Authors
TiO_2 NPs	TTIP	*Aegle marmelos* leaf extract	FTIR, SEM, X-ray	Spherical, 150 nm	Photochemical Degradation of Ornidazole	Undoped TiO_2 NPs Heavy metals were not removed	Ahmad *et al.* (2021b)
TiO_2 NPs	TTIP	Sol-gel	SEM-EDX, XRD, FTIR	Spherical and rod, 121 nm	Photocatalysis	Green synthesis was not carried out neither was adsorption	Ahmad *et al.* (2021b)
TiO_2 NPs	$TiCl_4$	Sol-gel	XRD, FTIR, SEM, DLS	Spherical, 68 nm	Antioxidant and Antibacterial properties	Absence of *Parkia biglobossa* leaves	Albukhaty *et al.* (2020)
TiO_2 NPs	TiO_2	Laser ablation of a titanium mineral pellet	FESEM, TEM, XRD	Spherical, 25 nm	Antibacterial properties	TTIP, Green synthesis and adsorption processes absent	Bahjat *et al.* (2021)
TiO_2 NPs	TTIP	Sol-gel	XPS, DRS, TEM	Spherical, 2.8-26.5 nm	Ex-vivo tissue imaging	Green synthesis and adsorption process absent	Barkhade *et al.* (2021)
TiO_2 NPs	TTIP	Solvothermal/Sol-gel	TEM, SEM, XRD, EDS	Agglomerated, 11 nm	Dye-sensitized solar cells (DSSCs)	Green synthesis and adsorption process absent	Dubey *et al.* (2019)

Table 2.3b: Synthesis, characterisation and applications of titanium dioxide nanoparticles

Material	Precursors	Synthesis method	Characterisation	Size and shape	Applications	Shortcomings	Authors
TiO_2 NPs	TTIP	*Staphylococcus aureus*	SEM, XRD, FTIR, AFM, TEM, Raman Spectroscopy	Spherical, 20 nm	Antimicrobial and anti-biofilm properties	Green leaves and adsorption process absent	Landage *et al.* (2020)
TiO_2 NPs	TTIP	Sol-gel synthesis	TEM, EDX, XRD, Raman Spectroscopy	Oval shape 10.48 nm	Self-cleaning application	Wastewater treatment was not involved	Lukong *et al.* (2022)
TiO_2 NPs	TTIP	Sol-gel	XRD, TEM, UV Vis-Spectroscopy, SEM, FTIR	Cubic, 6.85–14.85 nm	Photocatalysis	Absence of adsorption study	Samy *et al.* (2019)
TiO_2 NPs	TiO_2	*Moringa oleifera* leaf extract	SEM, XRD, EDX, FTIR	Irregula, 24.58 nm	Fungal diseases control	Use of undoped TiO_2	Satti *et al.* (2021)
TiO_2 NPs	TiO_2	Precipitation	XRD, PSA, UV Vis-spectroscopy, SEM	Spherical, 60-200 nm	Seed germination	TiO_2 was synthesised for agricultural study	Verma *et al.* (2020)
TiN nanoparticles	TiN target	Femtosecond laser ablation	SEM, EDS, DLS,	Spherical, 25 nm	Nanomedicine-based cancer treatment	Absence of TiO_2 nanoparticles and wastewater treatment	Zelepukin *et al.* (2021)

Recently, the use of carbon-based materials such as carbon quantum dots have also been employed for sensitisation and expansion of TiO_2 Nps' activity towards visible light (Zhang *et al.*, 2021). To enhance the adsorption capacity and reduce aggregation tendency, a wide variety of materials such as silica, activated carbon, zeolites, and clays have been used as supports for TiO_2 Nps (Ouyang *et al.*, 2019). The role of these support materials is to provide high surface area, porosity, and reactive sites on TiO_2 Nps.

The support materials also hinder the aggregation of TiO_2 Nps and enhance reusability, by making it easy to recover from the reaction mixture. Among these, clay of different types has been highly investigated as supports since they are cheap, easily available in the earth's crust, have low toxicity, and have high chemical stability, mechanical strength, and porosity (Khan *et al.*, 2019). Tables 2.4a and b presents the nanocomposite of TiO_2 with other materials for various applications. The co-doping of TiO_2 with other materials such as clay or metal oxide has been reported to successfully reduce the band gap in the TiO_2 Nps (Akinnawo, 2019). This allows the excitement of the photoelectron and creates a synergic effect by the co-doped element towards the targeted applications.

2.10 Clay Minerals

Clay or clay minerals are generally products of chemical weathering, originating from fine-grained sedimentary rocks called mud. Clay minerals are composed of about 40% minerals in sedimentary rock and are the main constituent of soils. They are used extensively in the ceramics industry and are thus important economic minerals. The clay minerals could be crystalline or amorphous based on internal layer structures (Gu *et al.*, 2019) and are divided into classes based on their structures and chemical compositions. These are; kaolinite/kandite, smectite/pyrophyllite, illite/muscovite, and chlorite (Han *et al.*, 2019).

Table 2.4a: Synthesis, Characterisation, and Applications of Titanium-dioxide Composites

Material	Precursors	Synthesis method	Characterisation	Size and shape	Applications	Shortcomings	Author
TiO_2/SnO_2	$TiCl_4$	Sol-gel	SEM/ EDX, XRD, TEM	Spherical, 8-15 nm	Photocatalysis	The adsorption study was not included	Bayan *et al.* (2020)
TiO_2/SnO_2	TTIP	A hydrothermal method in two ways: single-stage and two-stage methods.	X-ray fluorescence analysis, XRD, XPS.	4.0 -20.1 nm	Adsorption of methylene blue and Congo red	Only dyes and not heavy metal ions were removed. Absence of Ag_2O	Dontsova *et al.* (2020)
Ag- TiO_2	TTIP	Sol-gel	HRTEM, BET, XRD	16.4 nm	Photocatalysis and Antibacterial Application	Green synthesis was not involved, AgNPs not Ag_2O were synthesised	Eksangsri *et al.* (2021)
Fe^0/TNW	TiO_2	Alkaline hydrothermal method	TEM, XRD	Spherical, 56 nm	Adsorption of ciprofloxacin	Heavy metals adsorption absent	Falyouna *et al.* (2021)
$Fe_3O_4/SiO_2/TiO_2/CeVO_4$	Tetra normal buthyl titanate	Precipitation	TEM, XRD, EDS, FTIR	80-100 nm	Photocatalysis	Ag_2O were absent in the composite	Marsooli *et al.* (2019)
Ga_2O_3/TiO_2	$TiCl_3$	Hydrothermal synthesis	SEM, XRD, EDS, TEM, XPS, BET, AFM	Rod-shaped, 11-22 nm	Photocatalysis	Ag_2O and heavy metals adsorption were absent	Ramesh *et al.* (2021)

Table 2.4b: Synthesis, Characterisation, and Applications of Titanium-dioxide Composites

Material	Precursors	Synthesis method	Characterisation	Size and shape	Applications	Shortcomings	Author
PMMA/TiO_2	TTIP	Precipitation	NMR, XRD, FTIR, TEM, SEM-EDX, BET	Roughly spherical, 50 nm	Antioxidant and antibacterial properties	Green synthesis, Ag_2O and adsorption processes were absent	Singh *et al.* (2022)
Ag_2O/TiO_2	$AgNO_3$, TTIP	Precipitation	TEM	Spherical, 17 nm	Biomedical	Heavy metals adsorption was absent	Eldebany *et al.* (2021)
Fe_3O_4/MWCNT Nanocomposite-TiO_2 NPs	$TiCl_3$, Fe_3O_4/MWCNT	Co-precipitation	SEM, XRD, EDS, FTIR	Spherical, 19.43 nm	Energy application		Taufiq *et al.* (2020)

2.10.1 Kaolinite

Kaolinite belongs to the kandite clay group with the chemical formula of Al2Si2O5(OH)4 and structural formula as shown in Figure 2.5 (Gu et al., 2019). They are formed by weathering or hydrothermal alteration of aluminosilicate materials. Rocks rich in feldspar (Fe) are the most commonly weathered to kaolinite by the leaching of Fe ions to form other ions, usually favoured by acidic conditions. Other kandites with similar structures are the anauxite, dickite, nacrite, and halloysite; all having structures similar to the kaolinites. Kaolinite has a 1:1 layered structure that is composed of a tetrahedral SiO_2 sheet and an octahedral sheet with Al^{3+} as the octahedral cation.

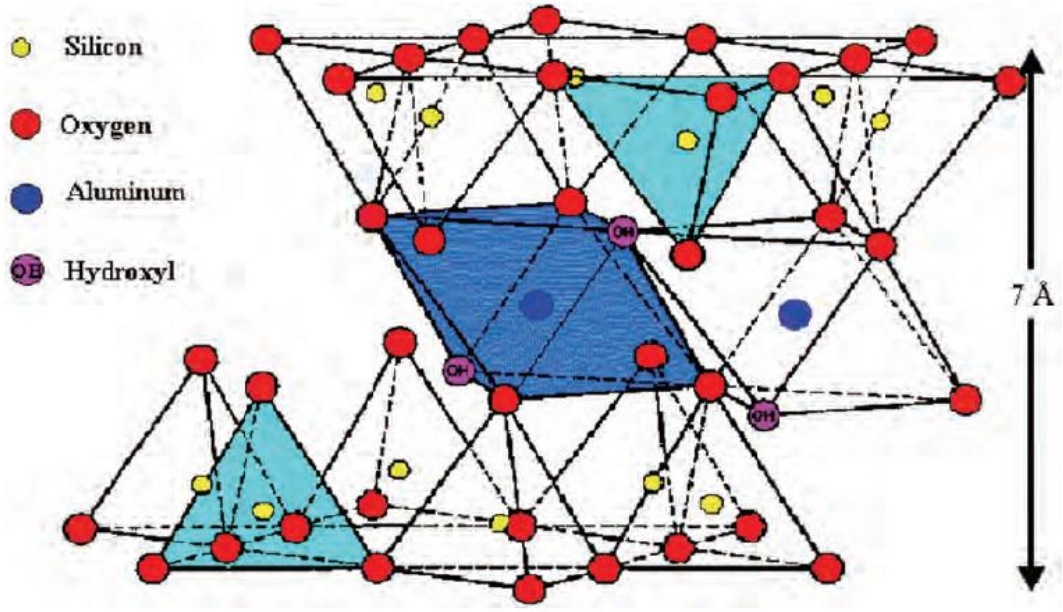

Figure 2.5: Structure of typical kaolinite clay

(**Source:** Awasthi *et al.,* 2019)

The hydroxyl groups situated below and above two Al atoms make a central hexagonal distribution in one single plane in the range of an octahedral sheet. Furthermore, there is a small net negative charge at the broken edges of the kaolinite crystals, despite the neutral surface charge. Also, kaolinite neither absorbs nor expands when in contact with water, thus its preference in the ceramics industry. It is also applied in the paper, medicine, and cosmetic industries (El-Sherbiny *et al.*, 2015).

Due to its chemically inert structure, fine particle size and white colour, kaolinite clay is a suitable raw material for ceramics, catalysts, adhesives and as an adsorbent for water treatment (Awasthi *et al.*, 2019). Dawodu and Akpomie (2014) reported the use of un-modified kaolinite clay as a low-cost adsorbent for the removal of Ni(II) and Mn(II) ions from a binary aqueous solution. Their findings concluded that the adsorbent efficiently removes both the Ni(II) and Mn(II) ions at maximum adsorption capacities of 166.67 mg/g and 111.11 mg/g, respectively.

Mustapha *et al.* (2019) reported the use of kaolinite clay as a low-cost adsorbent for the removal of several pollutants in tannery wastewater. Their results established that the kaolinite clay was a suitable and effective adsorbent for treating tannery wastewater. Worthy of note is that no report in the literature, at least to the best of the author's knowledge, utilised kaolinite clay for the treatment of pathogens in wastewater. Therefore, to effectively employed kaolinite clay as an adsorbent for a wide range of wastewater treatments including antibacterial activity, it must be modified with other substances such as TiO_2 and Ag_2O.

2.10.2 Smectite/Montmorillonite/Bentonite

The smectite is a sedimentary rock comprised largely of clays, with a typical 2:1 layer structure and high concentrations of Na^+, Ca^{2+}, Li^+, Mg^{2+}, and Fe^{2+} ions. The ions are located between their layers in such a way that it substitutes into octahedral and tetrahedral sheets as shown in Figure 2.6 (Han *et al.*, 2019; Uddin, 2017). The octahedral and tetrahedral sheets are in such a pattern that the tips of the tetrahedral in each silica sheet and one of the hydroxyl layers in the octahedral sheet constitute a single layer. The smectite group has the ability for H_2O molecules to be absorbed between their T-O-T (2:1) sheets, causing the volume of the minerals to increase when in contact with water. Thus, the smectites are called expanding clays.

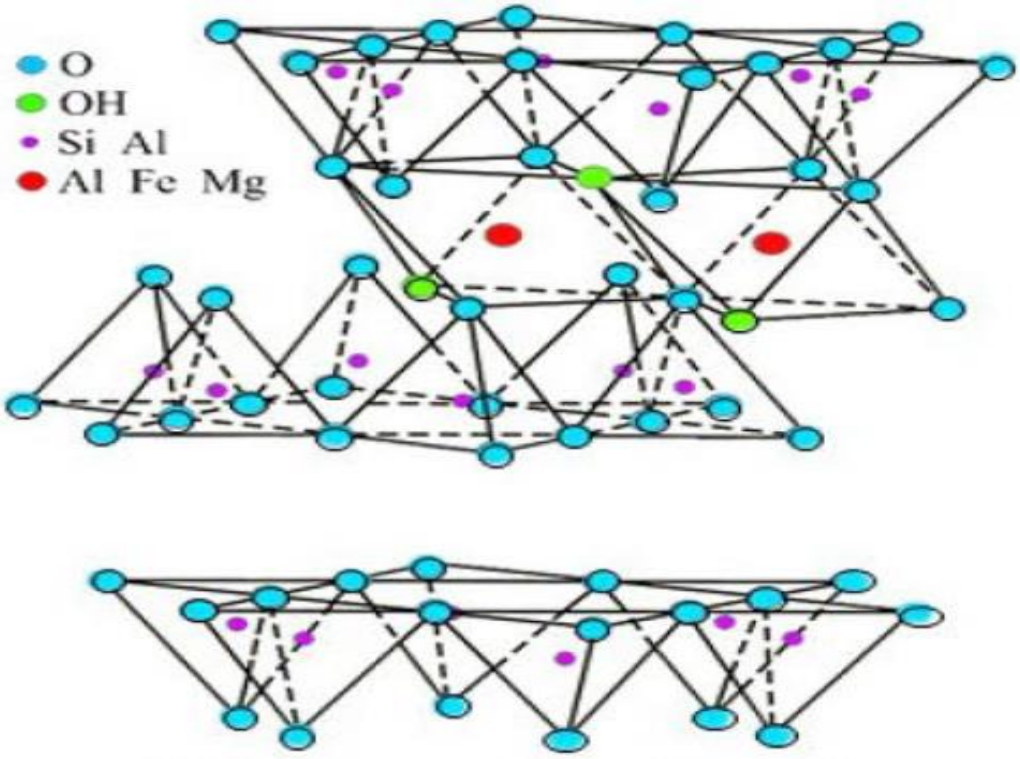

Figure 2.6: Structure of typical montmorillonite clay

(**Source:** Awasthi *et al.,* 2019)

Examples of smectite clay minerals are montmorillonite, beidellite, hectorite, saponite, and bentonite among others. Montmorillonite is the most common in this group with the molecular formula of $(0.5Ca, Na)(Al, Mg, Fe)_4(Si, Al)_8O_{20}(OH)_4 \cdot nH_2O$. Montmorillonite is the main constituent of bentonites, usually derived by the weathering of volcanic ash, they are aluminium phyllosilicate adsorbents in impure form (Liu, 2019). Laponites are synthesised from montmorillonite, containing alumina silicate mineral layers, and possesses negative charges which made them have excellent cationic adsorption property and significant surface area (Cao *et al.,* 2017). Montmorillonite can expand by several times its original volume when in contact with water. This makes it useful for drilling mud and plugging leaks in soil, rocks, and dams. However, it is a dangerous type of clay to encounter if found in tunnels or road cuts. This is because of its capability to immobilise water molecules between the sheets, which results in remarkable expansion and may lead to serious slope or wall failures (Gu *et al.*, 2019).

Due to these and many other properties, montmorillonite clay are useful in different applications such as food additives, desiccants, emulsion and as an adsorbent in wastewater treatment (Awasthi *et al.*, 2019). Choudhary *et al.* (2021) developed a montmorillonite/silver nanocomposite (MMT/Ag nanocomposite) adsorbent for the decongestion of methylene blue (MB) from industrial wastewater. The result obtained shows a low adsorption capacity for MB, however, it was effective for the antimicrobial purpose. Alandis *et al.* (2019) investigated the possibility of adsorbing Ag(I) and Cu(II) ions from aqueous solutions onto montmorillonite clay. The report concluded that the clay was efficient and suitable for the adsorption process, however, its effect against pathogens was not reported. It could therefore be inferred, that the montmorillonite clay is not efficient for organic pollutant sequestering and its un-modified form may not be suitable as an antimicrobial agent.

2.10.3 Other clay materials

The Illite-type clays are formed from weathering of potassium and aluminium-rich rocks under high pH conditions. Illite is a secondary mineral precipitate, and an example of a phyllosilicate, or layered alumino-silicate. Its structure is a 2:1 sandwich of silica tetrahedron – alumina octahedron – silica tetrahedron layers as shown in Figure 2.7. They are formed by the alteration of minerals such as muscovite and feldspar and are the main constituent of ancient mudrocks and shale. The Illite clays have a structure similar to that of Muscovite, however, they are typically deficient in alkalis with less Al substitution for Si. Thus, the general formula for the illites is $K_yAl_4(Si_{8-y}, Al_y)O_{20}(OH)_4$ with $y < 2$ due to possible charge imbalance, Ca and Mg can also sometimes substitute for K. The K, Ca, or Mg interlayer cations prevent the entrance of H_2O into the structure, thus, the illite clays are non-expanding (Kumari and Mohan, 2021).

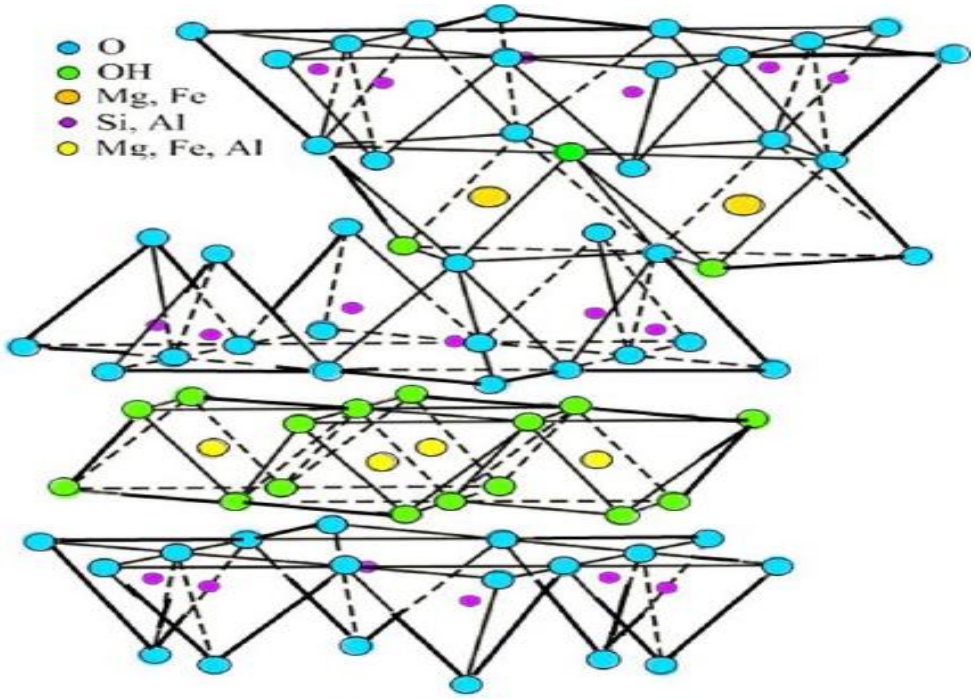

Figure 2.7: Structure of typical illite clay

(**Source:** Awasthi *et al.*, 2019)

Another example of a clay mineral is chlorite which belongs to the 2:1:1 silicate group that comprises iron, magnesium silicates, and some aluminium atoms. The typical chlorite clay is similar to the vermiculite clay mineral alternated with the magnesium-dominated tri-octahedral sheet, which gave rise to the 2:1:1 ratio. Worthy of note is the fact that all the octahedral positions in chlorite are occupied by magnesium ions. Chlorite has negative charges that are lesser than that of smectite or vermiculites, however, they are similar to that of fine-grained mica. It has no water adsorption between its layers, therefore it is a non-expanding clay with the chemical formula $Al_{4.33}(Si_3Al)O_{10}(OH)_8$. Other examples of chlorite are sudoites and cookeites (Kumari and Mohan, 2021). Through the search of the literature, there is a paucity of information on the use of both illite and chlorite as adsorbents either in pure or modified form for wastewater treatment. This may be due to their deficiency in alkali and possibly charge imbalance (Kumari and Mohan, 2021).

2.10.4 Desirable properties of clay minerals

The most common properties associated with clay are; high chemical stability, plasticity and ion exchange capacity (Hızal and Yılmazoğlu, 2021). Clays become plastic when combined with water and the degree of plasticity could be linked to interstitial materials during weathering. Shrinkage is another factor that determines the plasticity of clay as the greater the shrinkage the more the plasticity of clay material. The plasticity of clay determines its suitability as a raw material for ceramic and water filters. Also, to improve the physical properties (thermal stability, and mechanical stability) of any clay materials for their suitability for ceramic and water filter applications, purification, and modification processes are usually carried out. These processes involve sedimentation and activation treatment, before surface modification using water, acid, base, salts, and heat (Karimi and Salem, 2011).

The sedimentation process is carried out to remove unwanted materials from the clay's structure using Stokes' law while the activation process purifies the clay (Alaya-Ibrahim *et al.,* 2019). Whenever clays are heated at elevated temperatures (sintered), they attain a new form of clay that cannot return to their original physical and chemical properties (Khan *et al.,* 2019). These properties made clay materials suitable for the adsorption process in which their features for industrial application are dependent on their chemical compositions, sizes, and surface layers. Clays are also used in the decolourisation of oils, drug manufacturing, pulp and paper production, and adsorption. In adsorption, modified clays are reported to enhance the adsorption of pollutants in wastewater treatment, however, in membrane technology, kaolinite clay is most preferred due to its non-expansive nature and alkaline sufficiency. The hydroxyl and oxygen atoms in clays' structure are reported as being responsible for their physical adsorption due to van der Waals interaction, chemisorption, and catalytic capacity (Bel'chinskaya *et al.,* 2016).

Every adsorption process by a given clay is usually influenced by parameters such as contact time, pH, initial concentration, dosage, and temperature of the reaction.

2.10.5 Clays in wastewater adsorptive treatments

Several researchers have employed unmodified and modified clays for the adsorptive treatment of wastewater. This application includes the removal of physicochemical parameters such as dyes, heavy metals, BOD, COD, and other pollutants. A few examples of such are presented in Tables 2.5a and b.

2.10.6 Clays, Ag_2O, and TiO_2 nanoparticles as new frontiers in wastewater treatment

Clay materials have been reported as a support for the immobilisation of metal oxide nanoparticles through viable technology in the adsorption process. This is to enhance the adsorptive capability of metal oxide nanoparticles such as Ag_2O and TiO_2 for wastewater treatment (Mishra *et al.*, 2018). It is also to overcome the challenges due to the aggregation of Ag_2O and TiO_2 in an aqueous solution which minimizes the surface area and reduces the activity of the adsorbent. The clay as a support material provides high surface area, porosity, and adsorptive sites to the Ag_2O and TiO_2 nanoparticles in adsorption technology. The development of clay-Ag_2O-TiO_2 nanocomposites enhances the reusability of the adsorbent in wastewater treatment.

Meanwhile, clay as an adsorbent may not be effective for the treatment of a wide range of wastewater, hence it can be pillared with Ag_2O and TiO_2 nanoparticles. This is to functionalised, activate, and enlarge the surface area of clay for effective adsorption in a wide range of wastewater treatment. Also, the immobilisation of Ag_2O and TiO_2 Nps on clay has been proposed as a solution to overcome the post-separation and recovery problems of the metal oxide nanoparticles in an aqueous solution (Akinnawo, 2019).

Table 2.5a: Clay composites for adsorptive pollutants removal

Adsorbent	Characterisation technique	Pollutants removed	Adsorptive conditions	Research outcome/Shortcomings	Reference
Natural bentonite Clay	BET (47 m^2/g)	Cu^{2+}, Cd^{2+} and Pb^{2+}	Time, concentration, dosage	The natural bentonite removed 30.99, 48.20, 83.02, mg/g of Cu^{2+}, Cd^{2+} and Pb^{2+} following the PFO kinetics and Langmuir Isotherm. Absence of kaolin clay and nanoparticles.	Budsaereechai *et al.* (2012)
Acid-activated bentonite clay	BET (74 m^2/g)	Cu^{2+}, Cd^{2+} and Pb^{2+}	Time, concentration, dosage	The activated clay has enhanced surface area for heavy metal adsorption. Absence of kaolin clay and Ag_2O/TiO_2 nanoparticles.	Budsaereechai *et al.* (2012)
Kaolinite clay	FTIR, XRD, SEM (13.41 m^2/g)	Ni, Mn	Time, concentration, dosage	The kaolinite clay has a high adsorptive capacity for both ions investigated, following the Elovic and Freundlich models. Absence of nanoparticles.	Dawodu and Akpomie (2014)
Bentonite from Jeddah, Saudi Arabia	XRD, BET, XRF	Cu, Ni	Temperature	Metal ion adsorption increased with an increase in temperature. The adsorption process was endothermic. Absence of kaolinite clay and nanoparticles.	Aljlil and Alsewailem (2014)
Montmorillonite clay	SEM (42 m^2/g), EDS, BET	Cu^{2+}, Fe^{3+}	Time, temperature	Cu^{2+} and Fe^{3+} ions were removed over a long contact time of 42 h, explained by the Langmuir equilibrium model. Absence of kaolin clay, nanoparticles and mining wastewater.	Korolkova *et al.* (2020)
Verde-lodo Bentonite	XRD, BET	Cu^{2+}, Ag^{+}	Concentration, time, dosage, temperature	There are no significant changes in the morphology, crystal structure, functional groups, and thermal stability of clay after adsorption with equilibrium data explained by the Langmuir-Freundlich isotherm and EMTR kinetics model. Absence of green synthesis, kaolin clay and nanoparticles.	Freitas *et al.* (2017)

Table 2.5b: Clay composites for adsorptive pollutants removal

Adsorbent	Characterisation technique	Pollutants removed	Adsorptive conditions	Research outcome/Shortcomings	Reference
Raw Montmorilonite clay	BET	Methylene blue	Dose, time, conc	The MB adsorption study showed that raw MMT has the potential for the removal of MB dye due to its wide surface area of 77.23 m^2/g	Choudhary *et al.* (2021)
Kaolin	XRD, SEM	Methylene blue, Orange (II)	Time, initial concentration	There was rapid sorption of 90% dye at 20 min, fitted by Langmuir isotherm. Absence of Ag_2O and TiO_2 nanoparticles.	Hajjaji *et al.* (2018)
Kaolin and Bentonite	-	Cationic polymer	pH, dosage, ionic strength	The increase in pH facilitates the removal of cationic xylan copolymer. Heavy metals were not removed.	Konduri and Fatehi (2017)
Calcareous clay	BET, SEM, XRD	Pb (II), Cd (II), Cu (II) and Zn (II)	Time, concentration, and pH	The number of calcium carbonates in the clay influenced the amount of heavy metal removed. Absence of Ag_2O/TiO_2 nanoparticles.	Sdiri *et al.* (2012)
Bentonite	XRD, BET, FTIR, TGA, XPS	Reactive dye	Contact time, pH, initial Concentration	The isotherm fitted well by Langmuir and Redlich-Peterson models. The adsorption occurred due to the interaction of silanol groups with anion and hydroxyl/sulphonic groups.	Aguiar *et al.* (2017)
Bentonite	XRD, SEM	Cd^{2+}	Time, dosage, concentration, and pH	The bentonite clay has a 13.5 mg/g adsorption capacity explained by the Langmuir model. Absence of kaolinite and nanoparticles.	Khan *et al.* (2018)
Saudi montmorillonite clay	BET, SEM	Ag (I) and Cu (II)	Time, dosage, pH	Ordinary Saudi clay was a suitable adsorbent for Ag (I) and Cu (II) removal from aqueous solutions compared with other adsorbents.	Alandis *et al.* (2019)
Bentonite	XRF, FTIR, BET	Pb^{2+} and Cu^{2+}	Time, pH, conc., dosage	The bentonite clay had an affinity for Pb (II) than Cu (II). Absence of nanoparticles.	Hussain and Ali (2021)
Bentonite	-	Cu^{2+}, Cd^{2+}, Co^{2+}	Time, pH, conc, dosage	Adsorption of the three metals onto natural clays was pH-dependent and well explained by PSO kinetics and Langmuir isotherm.	Mnasri-Ghnimi and Frini-Srasra (2019)
Saudi clay	XRF, XRD, SEM	Ni, Cd	pH, Time, conc,	An increase in pH facilitates the removal of Cd from the aqueous solution, up to 97. 5, 99.5% of Ni and Cd ions were removed. Exclusion of Fe, Cu, Pb and Mn ions in the treated water.	Khan *et al.* (2019)

Tables 2.6a, b, c and d elucidated different nanocomposites of clay/Ag_2O/TiO_2 as adsorbents for sequestering various contaminants from wastewater. It was observed from Tables 2.5a and b that the clay/Ag_2O/TiO_2 nanocomposites of different types were effective for a wide range of heavy metal ions, colours, and microorganisms in wastewater treatment. However, there is a paucity of information on the synthesis and characterisation of Ag_2O/TiO_2-clay nanocomposites for mining wastewater treatment, hence, a research gap awaiting a solution. Although Liu *et al.* (2007) developed Ag–TiO_2/MMT for photocatalytic degradation of methylene blue, their study was only applicable to the adsorption of colour. The effectiveness of Ag–TiO_2/MMT against microbial activities was not ascertained as it was not reported.

Also, Ajenifuja *et al.* (2016) studied the adsorptive capacity of Ag-TiO_2-modified kaolinite ceramic adsorbents for copper and cobalt ions from highly polluted solutions. From their result, it was observed that the quantity adsorbed increased with a decrease in initial metal ion concentration in the aqueous solution. An electrospun nano-fibrous composite was also synthesised from silver oxide, titanium oxide and polyacrylonitrile (PAN) (Xu *et al.*, 2018). The metal oxide nanoparticles were well-dispersed on the PAN to form PAN-TA and were characterised by FTIR, XRD, and SEM. The effects of chemical modification, solution pH, temperature, dosage, contact time, and initial concentration of the dye were considered in the adsorption process. The result of the findings revealed that methylene blue (MB) dye was completely removed within 20 min at room temperature of 25ºC with a high maximum retention capacity of 155.4 mg g^{-1}. The obtained results indicated that the prepared adsorbent possesses excellent regeneration ability toward the removal of methylene blue dye.

Table 2.6a: Clay/Ag_2O and clay/TiO_2 composites for adsorptive pollutants removal

Adsorbents	Characterisation technique	Pollutants removed	Adsorptive conditions	Research Outcome	Shortcomings	Reference
Silver oxide-Kaolinite	XRD, XPS	Iodine-129	Concentration	20% concentration of $AgNO_3$ on clay was discovered most suitable for minimal loss and heat stability which was most effective for iodine retention	The limited characterisation was carried out	Sadasivam and Rao (2016)
AgNPs	Uv-vis, FTIR, SEM	Cd (II)	Dose, pH, time, concentration	Cd (II) ion removal depends on adsorption dosage, initial concentration of the metal ion, interaction time, pH, and agitation speed while the Freundlich isotherm-fitted equilibrium data	The adsorption process was not competitive, only a single component was removed	Al-Qahtani (2017)
MMT/Ag nanocomposite	Uv-vis, FTIR, FE-SEM, BET	Methylene blue	Dose, time, conc	A layered, sheet-like morphology of MMT/Ag nanocomposite was synthesised and was suitable for MB adsorption	Dye and not metal ions were removed. Absence of TiO_2 NPs	Choudhary *et al.* (2021)
Ag/kaolin nanocomposite	FTIR, XRD, TEM, BET	Acid cyanine 5R dye	Contact time, pH, and mass	Ag/kaolin nanocomposite with an average size of ~50 nm was synthesized and found suitable for 90% acid cyanine 5R dye (AC5R) removal from water.	Absence of TiO_2 nanoparticle and metal ions removal	Hashemian and Shahedi (2013)
Clay/CuO/Ag and clay/ZnO/Ag	Uv-vis, XRD, TEM FTIR, FE-SEM, BET	E. coli, S. aureus (antibacteria)	Time	The nanocomposite with a surface area of 6.46 m^2/g synthesized was found suitable for >90% E-coli removal from water at a shorter time. The Clay/CuO/Ag performed better than the others.	Adsorption studies were exempted, and TiO_2 absent in the composite	Asamoah *et al.* (2020)

Table 2.6b: Clay/Ag_2O and clay/TiO_2 composites for adsorptive pollutants removal

Adsorbents	Characterisation technique	Pollutants removed	Adsorptive conditions	Research Outcome	Shortcomings	Reference
Ag_2O/aquatic macrophytes	SEM	Cd (II), Ni (II)	Concentration, time, pH, dosage	The Ag_2O nano adsorbents were effective for the rapid removal and recovery of Cd and Ni ions from aqueous media.	Absence of TiO_2 in composite, only two metal ions were removed	Abdallah (2022)
Natural clay/TiO_2 (LAO-TiO_2)	XRD	Pb (II)	Temperature	Calcination temperature affects the basal spacing in the clay, the LAO-TiO_2 composite with anatase-rutile TiO_2 was suitable for Pb metal ion removal	Single component wastewater was treated and composite devoid of Ag_2O	Bijang *et al.* (2020)
TiO_2/Montmorillonite	XRD, SEM, FTIR, BET, TG-DTA	Methylene dye	Time	The TiO2 nanoparticles had large photocatalytic activity and the adsorbent for environmental remediation such as regeneration capability	Dyes and metal ions removed	Chen *et al.* (2014)
TiO_2/Polish halloysite	XRF, XRD, TEM, FTIR, BET	Chloro-aniline	Time	The presence of TiO_2 in the nanocomposites photo degraded aniline and chlorine derivatives greater than the commercial TiO_2 at reduced contact time.	Absence of Ag_2O nanoparticle, adsorption and metal ion removal	Szczepanik (2017)
TiO_2/Clay	XRD, FTIR, AFM, SEM	Methylene blue and Cadmium	Time	The TiO_2/Clay nanocomposites were highly crystalline which enhance their surface for the simultaneous removal of methylene blue	Bicomponent wastewater treated and photocatalysis employed	Guillaume *et al.* (2018)

Table 2.6c: Clay/Ag_2O and clay/TiO_2 composites for adsorptive pollutants removal

Adsorbents	Characterisation technique	Pollutants removed	Adsorptive conditions	Research Outcome	Shortcomings	Reference
TiO_2/Bentonite	FTIR, SEM, XRD, BET	Methylene blue and Rhodamine blue	Temperature	Hydroxyl radical formed from TiO_2 acts as the active site for a photocatalytic agent in the degradation of the dye	Absence of adsorption studies and heavy metal removal	Laysandra *et al.* (2017)
TiO_2/Sepiolite	RTEM, XRD, FESEM, EDX	Dyes	pH and time	The nanocomposites have photocatalytic properties for the photodegradation of organic pollutants	The study was limited to dyes removal	Liu *et al.* (2017)
TiO_2/Clay	SEM, XRD, TEM, EDX, BET	Methylene blue	Time	The clay exhibited good support for TiO_2 nanoparticles which serve as excellent photocatalytic performance and regeneration study	The composite was devoid of Ag_2O and was limited to dye removal	Wu *et al.* (2019)
TiO_2/Kaolin	XRD, FTIR, SEM, EDX, BET	Coomasie brilliant blue dye	Time, calcination temperature, concentration	The nanocomposites calcined at the lowest temperature have the best performance photocatalytic activity due to their high surface area and porosity. The TiO_2/Kaolin was recovered and reused in another three cycles.	The composite was devoid of Ag_2O and was limited to dye removal	Lopes *et al.* (2019)
Ce-TiO_2/clay	UV-vis, ICP-MS,BET, XRD, EDAX	E.coli	Time, stirring speed	The composite material efficiently adsorbs the bacteria in the dark for 30 mins and is degraded under illumination by photocatalysis.	The composite was devoid of Ag_2O and was limited to E.coli removal	Belver *et al.* (2020)

Table 2.6d: Clay/Ag_2O and clay/TiO_2 composites for adsorptive pollutants removal

Adsorbents	Characterisation technique	Pollutants removed	Adsorptive conditions	Research Outcome	Shortcomings	Reference
TiO_2/Sepiolite	XRD, SEM, EDX, FTIR, TGA	Eosin dye	Concentrations and pH	The efficiency of the catalyst to degrade up to 75% of dye was linked to the generation of radicals from the TiO_2 and the high specific surface area of the as-synthesized.	The absence of Ag_2O was limited to dye removal	Oliveira *et al.* (2020)
TiO_2/MMT	UV-vis, BET, XRD, IR	Methylene blue	Concentration and time	A large specific surface area leads to fast adsorption to the reactants and enriches enough methylene blue in contact with the catalytic activity sites of TiO_2. Ag_2O nanoparticles and kaolin are absent.	The authors do not use kaolin clay or Ag_2O nanoparticles	Liu *et al.* (2007)
Ag-TiO_2/MMT	UV-vis, BET, XRD, IR	Methylene blue	Concentration and time	Photooxidation activity because of its larger specific surface caused by pillaring and loading of silver for improving its light absorption. Adsorption study absent.	The authors do not use kaolin and removed dye	Liu *et al.* (2007)
TiO_2/Kaolinite	XRD, BET, XRF	MB, O(II) dyes	Temperature	Methylene blue removal was slow due to the complexity of the bonding of MB molecules. Almost 100% of O(II) was removed at 2 h explained by the Langmuir model. Absence of Ag_2O nanoparticles and metal ions removal.	The authors do not use Ag_2O nanoparticles and metal ions were not removed	Hajjaji *et al.* (2018)
Clay/TiO_2	XRD, FTIR	Cadmium	Conc, pH, dosage, Time	The adsorption process was exothermic and best explained by the Langmuir model. No Fe, Mn, Cu and Pb were removed. Ag_2O nanoparticles are absent.	Single-component wastewater was treated and characterisation limited	Sharififard *et al.* (2018)

It is worth mentioning that most of the literature reported did not investigate the antibacterial effect of the adsorbent in an aqueous solution. Mining site wastewater that was laden with Mn(II), Fe(III), Pb(II) and Cu(II) ions was not considered for their adsorption studies, hence, the novelty of this research work.

2.11 Ceramic Water Filters

Ceramic water filters are playing progressive and essential roles in the purification of industrial wastewater (Acosta *et al.*, 1995; Ihekweme *et al.*, 2020). This is due to their unique pore structures, high chemical, thermal and mechanical stabilities as well as hydrophilic surfaces, which made them a suitable candidate in wastewater treatment (Bories *et al.*, 2014; Zereffa and Desalegn, 2019). However, their method of fabrication is a factor that is responsible for their porosity to allow for the filtration of wastewater. Al-Naib (2018) identified and discussed some methods of ceramic filter fabrication which include partial sintering. The partial sintering method produces ceramic filters with low porosity (<50%) and significantly affects the pore size distribution. This method is not adequate for the fabrication of ceramic filters for wastewater treatment.

Honeycombs are another method of ceramic filter fabrication which has well-defined unidirectional channels. It is a more complex three-dimensional porous ceramic that can be rapidly made using prototyping techniques such as 3D printing. The deployment of this type of ceramic filter has not been reported in the literature for effective wastewater treatment. Apart from the reported method of ceramic filter fabrication, other distinguish types through different fabrication routes as presented by Al-Naib (2018) are shown in Figure 2.8. It is important to note that complete sintering is the commonly used fabrication technique for long-lasting and efficient ceramic water filters .

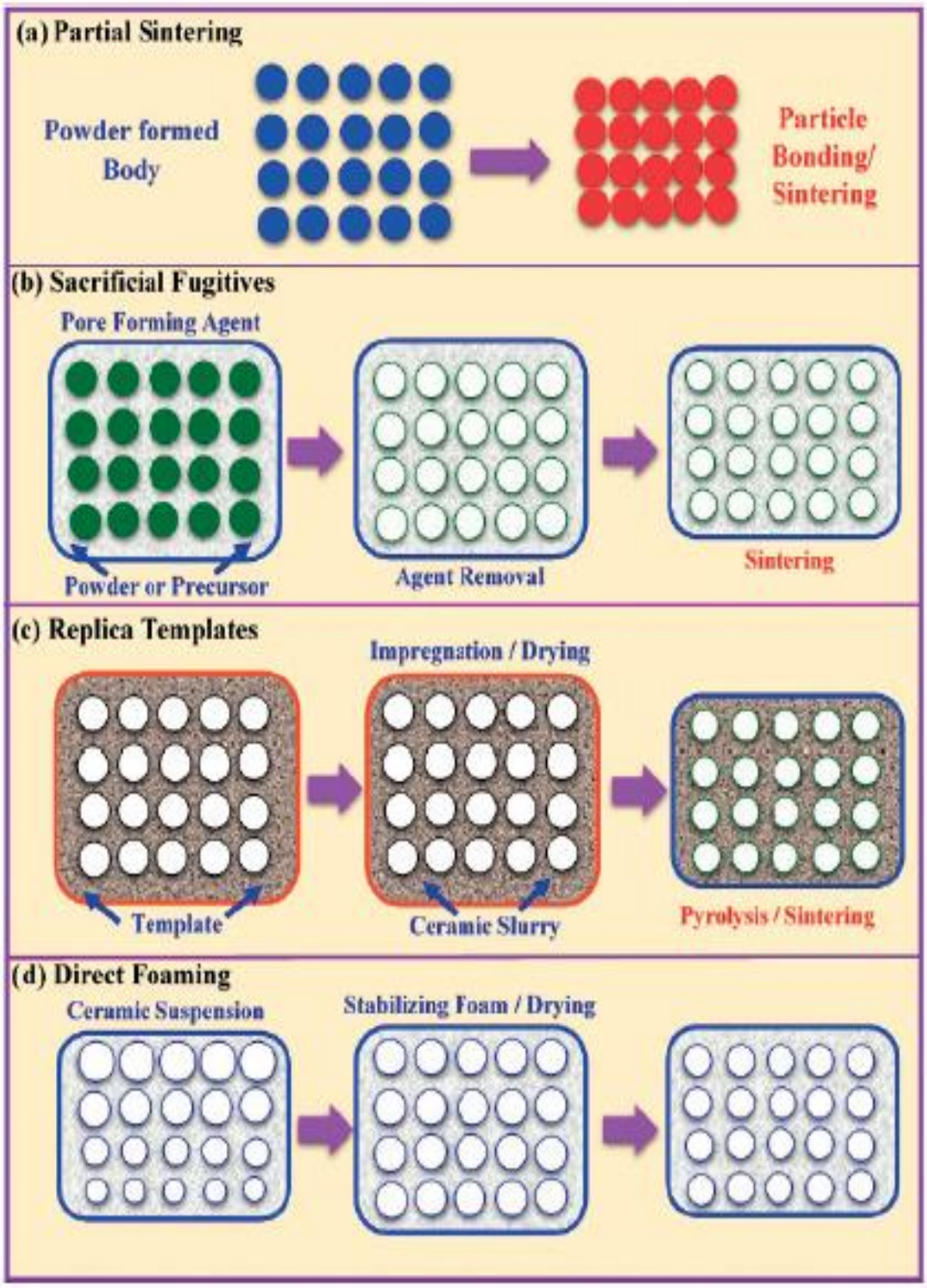

Figure 2.8: Schematic of porous ceramic processing methods: (a) partial sintering, (b) sacrificial fugitives, (c) replica templates, and (d) direct foaming

(**Source:** Al-Naib, 2018)P

According to Annan *et al.* (2016), complete sintering is carried out by heating the mixture of clay, water, and sawdust at a temperature above 800^{o}C in a kiln. During the sintering process of ceramic water filters, the carbonaceous material which is the sawdust is burned out, usually at a temperature in a range of 450–550°C. This process eventually leads to the formation of nano- or microporous structures in the ceramic water filter matrix. This can remove microorganisms and other pollutants from wastewater by geometrical occlusion/size exclusion process.

Also, to improve the performance of the filter against the targeted pollutants, it is essential to optimise the proportions of clay, and sawdust in the mixture and still maintain the mechanical properties without compromising flow. The nano- or microporous type of ceramic water filter has also been reported to allow for the regeneration of nanocomposites, and reduce toxicity, thereby giving room for industrial-scale production.

Furthermore, nano- or microporous ceramic water filter has been noted to have many advantages due to their lightweight, portability, low cost, and no chemicals requirements. It is simple to use and can be produced locally, using naturally available clay and other materials (Zereffa and Desalegn, 2019). Nanoparticles and nanocomposites in adsorbent development have been noted for their excellent adsorptive capacity for several pollutants in wastewater. However, the nano adsorbent is not always stable in an aqueous solution, thus may contribute to unavoidable health risks when leached into the treated water. As their presence in suspension may be difficult to recover and regenerate for an upward application. To overcome these challenges, the nano adsorbent is incorporated into clay as a framework to produce nano-based ceramic water filters for effective filtration technology.

The research efforts need to focus on the development of a nano-based ceramic water filter that is less energy-consuming, and easy to use, hence, this study. Tables 2.7a and b feature recent research work on ceramic water filters developed for wastewater treatments including findings, and gaps. Annan *et al.* (2018) identified that the effectiveness of ceramic water filters against microorganisms is due to mechanical screening and incorporation of colloidal silver. Worthy of note is that silver nanoparticles are effective in the "killing" of microorganisms. However, the method of silver impregnation into ceramic filter has been through coating which is carried out by dipping the filter or membrane in a colloidal solution of the particle or chemical. Spraying coating of silver on the ceramic filter is also envisaged inefficient, due to silver colloids not reaching the intrinsic sections of the filter membrane.

Therefore, it is important to properly incorporate Ag_2O and TiO_2 nanoparticles by adequately mixing them with other materials at the preparation stage. van Halem *et al.* (2017) reported the incorporation of bulk silver solution in their fabricated ceramic water filter. However, the filter was fabricated from a mixture of clay and risk husk with silver bulk particles and the application of the filter was only targeted at bactericidal activity. Also, Bulta and Micheal (2019) developed a ceramic water filter without incorporating either Ag_2O or TiO_2 nanoparticles. Their results showed that the mixture of clay and an increased amount of sawdust in the filter increases the porosity and flow rate at the expense of the removal efficiency of pollutants from the wastewater. In another study by Zereffa and Desalegn (2019), clay, grog, sawdust, and bone char was the composition of the ceramic water filter mixture. This revealed that Ag_2O/TiO_2 nanoparticles were not included in the fabricated ceramic.

Table 2.7a Clay-based Filters for Wastewater Treatment

Author(s)	Filters composition	Reaction conditions/Pollutants	Research findings	Research gaps
Grema *et al.* (2021)	50% clay, 50% sawdust	TDS, pH, turbidity	The filter type, 50:50 has the highest flow rate and was most suitable for turbidity removal than TDS and pH.	Metal ions were not treated and there was no nanoparticle in the filter.
Baosaree *et al.* (2018)	Zeolite: clay: rice husk 37.5: 37.5: 25 wt%	The physical and mechanical properties of the sintered specimens were examined.	The water absorption and open porosity of the filters increased with the increasing amount and size of rice husk charcoal, while the density and compressive strength decreases accordingly.	There is no wastewater treated, and no nanoparticles were introduced into the filters.
Efeovbokhan *et al.* (2019)	Sawdust: clay 6:80	TDS, conductivity, pH, heavy metals	The filters were effective for the purification of industrial and kitchen effluent.	There was no synthesis nor introduction of nanoparticles in the filter. Drastic reduction in flow rate after 30 min.
Zereffa and Desalegn (2019)	50 clay-15 sawdust-35 bone char	*E. coli*, nitrite and Fluoride	99.6% *E coli*, 81.17% nitrite, and 96.40% fluoride removal was achieved by the filter	Metallic nanoparticles were not introduced into the filter. No re-useability studies were carried out.
Ibeh and Nwadinobi (2021)	**C**lay, feldspar, silica, sawdust ratio 36:30:12:22	pH, total dissolved solids (TDS), total suspended solids (TSS)	The pH became 7.1, while 78.3% and 79.2% for the total dissolved solids (TDS) and total suspended solids (TSS)	Ceramic filter candles and not frustum shaped. There were no Ag_2O and TiO_2 nanoparticles incorporated into the filter composite
Soliman *et al.* (2020)	Local clay, sawdust, and demineralised the water weight ratio of 65%: 13%: 22%.	Micro-organisms	Repeated scrubbing resulted in a faster recovery of biofilms and associated log reductions of micro-organisms (protozoans and pathogens) but low performance on virus removal.	There was no incorporation of nanoparticles.

Table 2.7b Clay-based Filters for Wastewater Treatment

Author(s)	Filters composition	Reaction conditions/Pollutants	Research findings	Research gaps
van Halem *et al.* (2017)	30 kg clay, 9.7 kg rice husks, 1 kg of laterite, and 14.5 L of water	*E. coli*	The resident time of the wastewater in the ceramic filter and silver inclusion was an important parameter for microbial removal.	The silver included was neither green synthesised nor TiO_2 introduced.
Bulta and Micheal (2019)	80, 25 and 5% clay, sawdust, and grog	Turbidity, total coliform, *E. coli*, calcium, magnesium, sulphate, phosphate, iron, nitrite	The fabricated ceramic filter with the lowest porosity and flow rate has the best removal efficiency compared with others.	The nanoparticles of Ag_2O and TiO_2 were absent. No reusability test was carried out.
Yakub *et al.* (2012)	Clay: sawdust volume 50:50, 65:35 75:25.	-	The compressive strength of the filter samples was found to decrease linearly with increasing porosity.	Mechanical properties of porous clay ceramics were considered. No Ag_2O and TiO_2 nor water quality assessment was carried out.
Yakub *et al.* (2013)	Clay: Sawdust 50:50,65:35	*E. coli*	The *E. coli* removal of 99% in both filters was attributed to the geometrical occlusion provided by micron-scale pores and adsorption due to the high tortuous path created in the filter.	The nanoparticles of Ag_2O and TiO_2 were absent. No re-useability test was carried out
Haiyang *et al.* (2020)	Clay: combustible 90%:10%, 85%:15%, 80%:20%, and 70%:30%)	*E. coli*	Ceramic filter with 20% combustible exhibited the highest removal of the *E.coli*, the implication of pore size distributions in the filter.	Metallic nanoparticles of Ag_2O and TiO_2 were absent.
Zereffa and Bekalo (2017)	15% sawdust, 80% clay and 5% grog	Conductivity, pH, microbes, Fe, nitrite, and turbidity	The compositions of the various filters studied affected their removal efficiencies.	There were no nanoparticles of Ag_2O and TiO_2 absent. No re-useability test was carried out.

The efficiency of the ceramic filter was tested for *E*. coli (99.6%), fluoride (93.7%), and nitrite (90.13%) from the wastewater. Fabrication of ceramic water filter was also reported by Grema *et al.* (2021) using clay and sawdust without incorporation of any metal oxide nanoparticles, for the removal of turbidity and total dissolved solid in wastewater treatment. Their study did not investigate the removal of neither heavy metal ions nor microorganisms from an aqueous solution. In all the previous studies reported in this work, Ag_2O and TiO_2 nanoparticles were not incorporated into the ceramic water filter and the adsorption study was not reported for heavy metal ions that can be found in mining wastewater. This justifies the need for this study, therefore, the inclusion of Ag_2O and TiO_2 nanoparticles green synthesised in a ceramic water filter for mining wastewater treatment is novel.

2.12 Characterisation Techniques for nanoparticles and Nanocomposites

The suitability of prepared nanoparticles and nanocomposites for different applications is ascertained by their physicochemical, morphological, and structural properties. These are mostly determined by analytical techniques such as; Uv-visible spectroscopy, Fourier Transform Infrared Spectroscopy (FTIR), Thermo Gravimetric Analysis (TGA), Brunauer-Emmett-Teller BET, High-Resolution Scanning Electron Microscopy (HRSEM), X-Ray Diffraction analysis (XRD), and X-ray photo photoelectron spectroscopy.

Ultraviolet-visible Spectroscopy

The Principle of Ultraviolet-visible (UV-vis) Spectroscopy is based on the absorption of ultraviolet light or visible light by chemical compounds, which results in the production of results in the formation of different spectra. It uses ultraviolet and visible light in the wavelength range between 200 and 780 nm (Roberts *et al.*, 2018). The interaction of light and matter is the basis of spectroscopy, there is excitation and de-excitation as matter absorbs light, which results in the formation of a spectrum.

When matter absorbs ultraviolet light, the electrons inside it become excited. This leads them to transition from a ground state (an energy state with a relatively small quantity of energy) to an excited state (an energy state with a comparatively big amount of energy). It is worth noting that the difference in energy between the ground and excited states is significant in this technique. The Ultraviolet-visible (UV-vis) spectrophotometer provides information on the adsorption maximum which could be an indicator of particle size, it gives the quantitative analysis of specific materials. It can also be used to detect dyes, and phytochemicals such as; anthocyanins, phenolics, sugars, antioxidants and several particles (Roberts *et al.*, 2018). The technique is more effective for metallic particles, such as gold and silver than non-metallic ones. The UV-Vis method is also applicable in dissolution studies (Reidy *et al.*, 2013).

Fourier Transform Infrared Spectroscopy

Fourier Transform Infrared Spectroscopy (FTIR) provides information on the functional group composition of organic and inorganic samples. FTIR measurements are commonly used to identify biomolecules that may be involved in materials creation and to establish their involvement in nanoparticle reduction and stabilization. This spectroscopic approach detects and distinguishes small absorption bands of functional groups that have been covalently grafted onto functionally active sites and are specific to the material. This approach offers a high signal-to-noise ratio, is easy to repeat, and can deliver precision. The FTIR spectrometers have several advantages over other nanomaterial characterisation technologies. These include; non-invasive, collect data fast, produce strong and bold signals, have a good signal-to-noise ratio, and require very little sample heat-up. One of the key advantages of FTIR spectrometers over other methods of nanomaterial characterisation is that they are non-invasive, collect data quickly, have strong and bold signals.

The FTIR also have a high signal-to-noise ratio, and require very little sample heat-up (Dada *et al.*, 2018). The electromagnetic spectrum of the FTIR consists of different regions corresponding to different energy (E), frequency (ν), and wavelength (λ) range 4000 to 40 cm^{-1}. FTIR spectroscopy takes advantage of how IR light changes the dipole moments in molecules that correspond to a specific vibrational energy. The IR region is lying between the visible and microwave end of the electromagnetic radiation spectrum.

Since every functional group is composed of different atoms and bond strengths, vibrations are unique to functional groups, and classes of functional groups (O-H and C-H stretch appear around 3200 cm^{-1} and 2900 cm^{-1}, respectively). A correlation chart with various functional group vibrations is usually used to interpret the data obtained. In the interpretation, the collection of vibrational energy bands for each of the functional groups in a molecule is unique to each material analysed. Therefore these peaks can be used for identification using library searches of comprehensive sample databases (Jerlin and Beula, 2017).

Thermogravimetric Analysis

Thermogravimetric analysis (TGA) is a characterisation technique used to investigate the thermal decomposition behaviour/profiles of solid materials. The micrograph usually shows the percentage weight loss versus temperature under a nitrogen (inert) environment and constant heating rate to determine the suitability of the material for the as-prepared functions (Das *et al.*, 2014). The TGA device uses a very accurate, sensitive balance, the instrument measures the change in weight as a function of temperature. Other dynamic properties that can be obtained using the TGA include; the oxidative stability of materials, the composition of multi-component systems (no elemental data), the approximate lifetime of a product, decomposition kinetics of materials, the effect of reactive or corrosive atmospheres on materials, moisture and volatiles content of materials.

These properties are affected by parameters which include; the quantity of sample, heating rate and purge gas.

Brunauer-Emmett-Teller characterisation

Brunauer–Emmett–Teller (BET) theory is used to measure the surface area of solid or porous materials (Addy *et al.*, 2012). This characterisation technique gives important information on the physical structure and surface area of material, which affects how that solid will interact with its environment. Many properties such as dissolution rates, catalytic activity, moisture retention, and shelf life are often correlated to a material's surface area. Critical to the design and manufacture of solids, surface area analysis is one of the most widely used methods in material characterisation.

To determine the surface area, the solid sample is vacuum cooled, to cryogenic temperature using liquid nitrogen. Nitrogen gas (as a typical adsorbate) is applied to the adsorbent in controlled increments. After each dose of nitrogen gas, the relative pressure (P/P_0) is allowed to equilibrate, and the weight (W) of the nitrogen adsorbed is determined. The BET equation strictly describes a linear plot of $1/((P_0/P)-1)$ vs P/P_0 which for most solids, is restricted to a limited region of the adsorption isotherm, usually in the P/P_0 range of 0.05 to 0.35. From this plot, the weight of nitrogen (W_m) constituting a monolayer of surface coverage is determined. The total surface area of the sample can be calculated from the slope and intercept of the BET plot using the BET equation and the known molecular cross-sectional area of the nitrogen molecule.

$$\frac{1}{W}\left(\frac{P_0}{P}-1\right)=\frac{1}{W_mC}+\left(\frac{C-1}{W_mC}\right)\left(\frac{P}{P_o}\right) \qquad (2.14)$$

The BET constant C is related to the energy of adsorption in the first adsorbed layer and consequently, its value is an indication of the magnitude of the adsorbent/adsorbate interactions. To determine the pore volume and pore size distribution, the gas pressure is increased further incrementally until all pores are filled with nitrogen molecules.

Next, the gas pressure is reduced incrementally, evaporating the condensed nitrogen gas from the system. Evaluation of the adsorption and desorption isotherms reveals information about the pore volume and pore size distribution. The applications of BET include;

i. Surface area analysis of solid materials (such as carbon black, catalysts, batteries and ceramics),

ii. Simultaneous acquisition of surface area and pore size data,

iii. Non-destructive method,

While their limitation are;

iv. Closed pores are not accessible through the material surface. Therefore, gas adsorption cannot be used for their assessment.

High-Resolution Scanning Electron Microscope

High-Resolution Scanning Electron Microscope (HRSEM) is a characterisation technique used to determine the surface morphology of a material in terms of size, shape, and purity of powdered samples (Jerlin and Beula, 2017). The HRSEM generates a range of signals at the surface of solid specimens using a focussed beam of high-energy electrons. The signals generated by electron-sample interactions provide information on the sample's exterior morphology (texture), chemical composition, and crystalline structure and orientation of the materials that make up the sample, among other things. In most cases, data is collected across a specific area of the sample's surface, and a 2-dimensional picture is created to show spatial variations in these qualities. Using traditional SEM techniques, areas spanning in width from 1 cm to 5 microns can be scanned in a scanning mode (magnification ranging from 20X to approximately 30,000X, spatial resolution of 50 to 100 nm).

The SEM can perform analyses on a selected point in the prepared samples; this method is particularly useful for determining chemical compositions (using EDS).

It can also analyse crystalline structure, and crystal orientations in a qualitative or semi-quantitative manner (using Electron Backscatter Diffraction, EBSD). The HRSEM has a design and function that is quite the Electron probe microanalysis (EPMA), and the two instruments have a lot of capabilities in common.

High-Resolution Transmission Electron Micrograph

The High-Resolution Transmission Electron Micrograph (HRTEM) provides information on the morphological, surface characteristics, and lattice fringes of nanomaterials. HRTEM also gives information on the porosity and defects in the structure within crystals formed and their varied crystallinity. The functioning system of HRTEM is not the same as that of HRSEM but can give a similar type of information. The HRTEM generates images that are different from those of High-Resolution Scanning Electron Microscopy (HRSEM). In addition, the energy-dispersive X-ray (EDX) combined with the HRTEM equipment provides information on the elemental constituents of the nanomaterials.

It is noteworthy that, EDX expatiates on the parametric effects such as; pH calcination temperature and ageing time on the equivalent elemental compositions of nanoparticles investigated (Mustapha *et al.*, 2020).

X-Ray Diffraction analysis

X-Ray Diffraction analysis (XRD) is a technique used to measure the crystallinity and chemical composition of the structure of the nanocomposite/material. The sharp peaks and high intensity in the XRD pattern usually indicate the degree of crystallinity of the substance attributed to the reflection angle (Heydari *et al.*, 2016). The use of X-ray diffraction to determine the qualitative and quantitative properties of crystalline materials is extremely useful. It is used alongside the Debye Scherer formula to offer a rough

estimate of crystallite size, demonstrating the usefulness of this method for the successful structural analysis of nanoparticles and nanocomposites.

This flexible equipment is best known for measuring lattice constants and detecting the kind of phases in unknown solid samples, film thickness, stress-strain, and material crystallographic planes. X-ray diffraction also determines the structural arrangement of atoms packed together in the crystalline state from whence an X-ray beam is scattered from the electron (XRD). It facilitates the study of matter at the atomic level, which was previously difficult and made possible because of electromagnetic radiation wavelengths between gamma rays and ultraviolet. The diffraction penetrates the matter and produces a result that confirms the crystalline structure because the atomic distance in the matter is comparable to the wavelength of the X-ray (Motazedian *et al.*, 2019). The XRD results by Krishnan and Mahalingam (2017) showed that the developed composites; B-TiO_2, V-TiO_2, and R-TiO_2 are highly crystalline (63.9-82.1%) has structures composed of the tetragonal, anatase phase of TiO_2 mostly. Other identified phases are; the quartz and rutile phases of TiO_2 having crystallite sizes between 120.7 Å and 237.7 Å. The results further confirmed the chemical modifications of the materials linked to the synthesis technique.

X-ray Photoelectron Spectroscopy (XPS)

The XPS is a quantitative spectroscopic surface chemical analysis technique used to determine the oxidation state and energy level of the element present in a sample based on the photoelectric effect (Tijani *et al.*, 2017). It is also used to estimate empirical formulae of pure samples, the binding energy of electronic states, what elements and the number of elements within 10 nm of the sample surface, the electronic state, and the chemical state of the elements that exist within a material (Roos, 2017). The XPS is also known as electron spectroscopy for chemical analysis (ESCA).

The XPS plays a unique role in giving access to qualitative, quantitative/semi-quantitative, and speciation information concerning the sensor surface (Desimoni and Brunetti, 2015).

The XPS is performed under high vacuum conditions using X-ray irradiation of the nanomaterial that leads to the emission of electrons. The measurement of the kinetic energy and the number of electrons escaping from the surface of the nanomaterial gives XPS spectra (which is a plot of the number of electrons versus the binding energy of the varying identified electrons). The binding energy can be calculated from kinetic energy (Desimoni and Brunetti, 2015).

CHAPTER THREE

3.0 MATERIALS AND METHODS

3.1 Materials

Analytical grade chemicals used in this research study for reagent preparation (Appendix A) are shown in Table 3.1, while Tables 3.2a and b show the names and models of equipment employed to characterise the samples and heavy metals analysis.

Table 3.1: List of chemicals and reagents

S/N	Chemicals	% purity	Supplier
1.	$AgNO_3$	99%	Sigma Aldrich
2.	TTIP	97%	Sigma Aldrich
3.	NaOH	97%	JHD
4.	HCl	98%	JHD
5.	H_2SO_4	98%	Sigma Aldrich

Table 3.2: List of Analytical tools used for characterization

Equipment Specification	Uses	Manufacturer/Model	Locations
Ball Mill CAPCO Model 9 (Variable speed 0-350rpm 120mm x 100h. Ball diameters; 10, 12 and 20mm)	Size reduction of particles by high-energy milling	Soesterberg Holand/Kera Bv ball mill	Department of Material and Metallurgy Engineering, University of Ilorin.
Centrifuge	Classification of particle sizes by centrifugation method	Shimadu	Department of Chemical Engineering, University of Ilorin.
X-Ray Diffractometer (XRD)	(i) Detection of mineral phases and compounds in materials. (ii) Study of crystallinity of the mineral phases and compounds materials	Bruker AxSD8 Cu-K radiation	South Africa.
X-Ray Fluorescence (XRF) (Skyray EDX-3000)	Quantitative analysis of mineral phases and compounds in materials.		

Table 3.2b: List of Analytical tools used for characterization

Equipment Specification	Uses	Manufacturer/Model	Locations
High-Resolution Scanning Electron Microscope (SEM) + EDS	Determination of Surface morphology, Microstructure and Phase composition	Zeiss Auriga	Department of Physics, University of the Western Cape, South Africa.
BET Nitrogen Absorption Analyser	Surface area and pore size measurements and analysis of materials	Quantachrome, UK/NOVA 4200e	Department of Chemistry, Illinois Institute of Technology, Chicago, USA
Thermogravimetry Analyser (TGA)	Determination of physical properties of materials using their temperature characteristics	Perkin Elmer, USA/TGA 4000	FUT Minna STEP-B CoEx in Genetic Engineering and Biotechnology
pH meter	Measurement of hydrogen-ion concentration (acidity or alkalinity) of solutions	BDH, 1-14	Chemical Engineering Lab., Unilorin.
Magnetic Stirrer	For mixing liquids and slurries	Gallenkam, England/78HW-1 Constant	Chemical Engineering Lab., Unilorin.
Water Bath Shaker	For keeping mixtures to allow reactions to take place at desired temperature and speed.	Pye Unicam SP-9 Cambridge, UK.	Chemical Engineering Lab., Unilorin
Weighing Balance	Determination of the mass of a sample	Ohaus Corporation, NJ USA/Weda, T18	Chemical Engineering Lab., Unilorin
Atomic Adsorption Spectrophotometer (AAS)	Determination of metal ion concentration	Pye Unicam SP-9 Cambridge, UK.	Chemical Engineering Lab., Unilorin
XPS	Determination of oxidation state and energy level of elements	XPS PHI 5400	Department of Physics, University of the Western Cape, South Africa.

3.2 Sample Collection and Preparation

Kaolinite clay samples were randomly collected from different points in clay deposits at *Akerebiata*, Ilorin, Kwara State and mixed to form representative samples. The fresh leaves of Locust bean (*Parkia biglobossa*), Billy goat weed (*Ageratum conizoides*), Crowfoot grass (*Dactyloctenium aegyptum*), Spiny amaranth (*Amaranthus Spinosis*), Bristly foxtail grass (*Setaria barbata*) and *Sida carpinipolia* shown in Plate III, were obtained from different locations in Ilorin Metropolis.

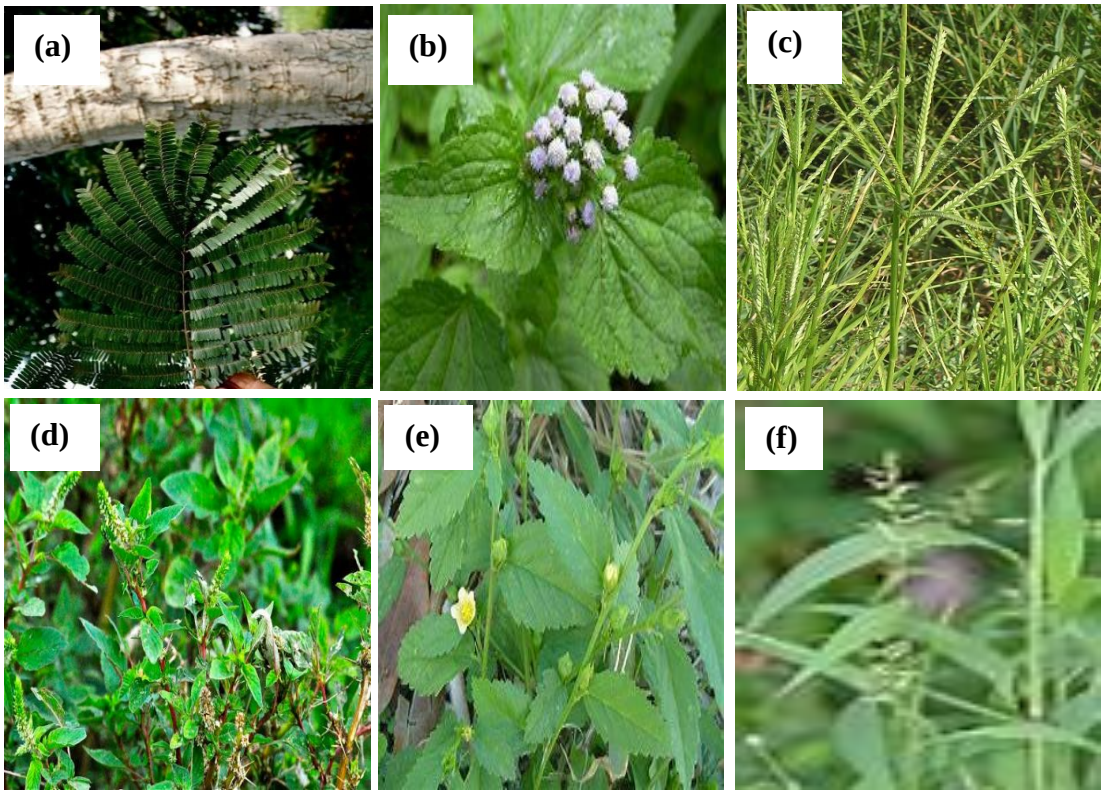

Plate III: Selected plant leaves collected for the synthesis of metal oxide nanoparticles (a) *Parkia biglobossa* L. (b) *Ageratum conizoides* L. (c) *Dactyloctenium aegyptum* L. (d) *Amaranthus Spinosis* L. (e) *Setaria Barbata* L. (f) *Sida carpinipolia* L.

The leaves were air-dried in the laboratory for 14 days and later pulverised before the phytochemical screening. Wastewater was collected from the mine site in the Chanchaga area of Minna, Niger State, Nigeria into a 100 L container, and subsequently transported to the laboratory, then stored in a refrigerator at 4^{o}C before analysis.

The physicochemical analysis for; Turbidity, pH, conductivity, phosphate, carbonate, dissolved oxygen, chemical oxygen demand (COD), biochemical oxygen demand (BOD), total coliform and heavy metal concentration (Co, Pb, Ni, Al, Cu, Cd, Fe, Mn and Zn) were carried out on the collected wastewater using standard methods.

3.2.1 Beneficiation of local kaolinite clay for nanoclay production

The raw clay shown in Plate IV(a) was beneficiated by the sedimentation technique to the fraction of < 2 µm hydrodynamic diameter according to Navier Stoke's equation as displayed in Equation 3.1 (Alaya-Ibrahim *et al.*, 2019). The beneficiation was carried out by measuring 50, 100, 150, 200, 250 and 300 g of milled clay samples, dispersed into different quartz crucibles. The clay was ground in a clean mortar and pestle to obtain homogeneous samples, then dispersed in different containers containing 5000 cm^3 of distilled water (Plate IV(b)). Each of the samples represents 1, 2, 3, 4, 5, and 6% w/w clay slurry in distilled water, labelled as LC1, LC2, LC3, LC4, LC5, and LC6 respectively.

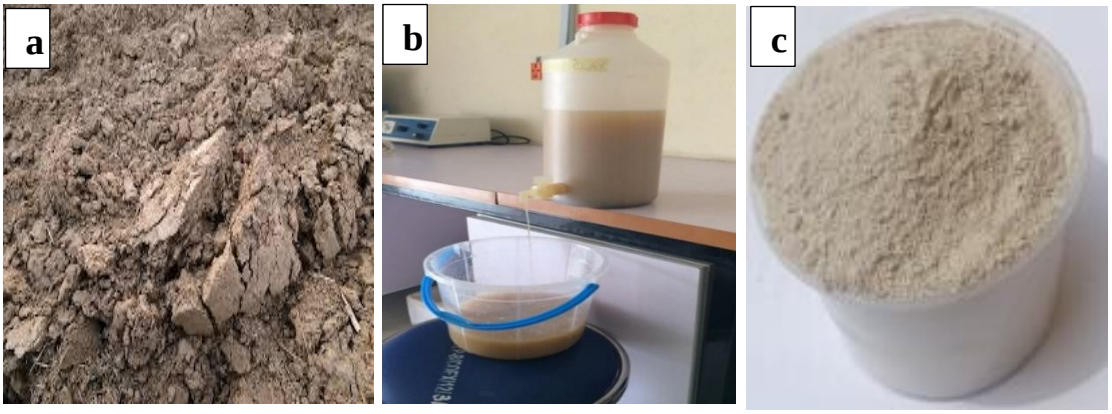

Plate IV: Beneficiation process (a) Raw clay (b) Sedimentation (c) Beneficiated kaolinite clay

The mixture was allowed to stay for 24 h for proper intercalation of the clay structure by water molecules. The beneficiation process aided in the removal of impurities present in the clay. The settling time of the clay was obtained using Equation 3.1:

$$r^2 = \frac{9\,\mu\,h}{2\,(\rho_1 - \rho_2)\,gt} \qquad (3.1)$$

Where; r = particle size (radius) of clay, assumed to be spherical,

μ = viscosity of fluid (distilled water),

h = settling height of fluid,

g = gravitational acceleration,

ρ_1 = density of clay,

ρ_2 = density of water, and

t = settling time

The clay suspension was stirred for 1 h, and the slurry was collected and poured into a 5000 cm^3 capacity aspirator bottle. The equation was used to calculate the settling time (nanoclay retrieval) by measuring the height of the slurry at 250 mm. The slurry was left freely settle and the supernatants were collected and discarded. The obtained slurry was sun-dried for 1 h and oven-dried at 100ºC until a constant weight was obtained. The dried beneficiated clay was ground with a cleaned porcelain pestle and mortar and sieved with <150 μm mesh size to obtain nanoclay as shown in Plate IV(c). The clay was kept in an airtight container and put in a desiccator, to prevent moisture inlet. The yield of the beneficiated nanoclay was calculated using Equation 3.2:

$$Y = \frac{Wr - Wp}{Wr} X\ 100\% \qquad (3.2)$$

Where; Y = Yield of purified clay,

W_r = Mass of raw clay, and W_p = Mass of purified clay.

3.2.2 Acid activation of kaolinite clay

The nanoclay of 50 g was weighed into a 500 cm^3 beaker, followed by the addition of 150 cm^3 of de-ionised water. The mixture was stirred to form a homogeneous solution and 100 cm^3 of 98% concentrated H_2SO_4 was added and stirred with a magnetic stirrer at 200 rpm for 2 h to prevent the content from forming mud.

The slurry was allowed to age for 3 h and washed with de-ionised water until a pH of 7 was attained and subsequently filtered and oven-dried at 100ºC for 2 h. The activated nanoclay was kept in a sample bottle.

3.2.3 Phytochemical screening of the plant leaves

Before the synthesis of nanoparticles, the selected leaves were identified by a Taxonomist at the Department of plant biology at the University of Ilorin. The leaves were then subjected to phytochemical screening, to select the most suitable leaves sample for the nanoparticle synthesis. The leaves were tested quantitatively for the presence of total tannins, total flavonoids and total phenolic contents.

Determination of total tannins

A mass of 0.2 g of the powdered leaves was measured into a 250 cm^3 beaker, 20 mL of 50% methanol was added and covered with foil and placed in a water bath shaker at 100 rpm maintained at 80°C for 1 h. Thereafter, the extract was filtered using a double-layered Whatan No.41 filter paper into a 100 cm^3 volumetric flask. Again, 20 mL of distilled water, 2.5 mL of Folin-Denis reagent and 10 mL Na_2CO_3 were each added to the filtrate and stirred. The mixture was made up to 100 mL with distilled water, mixed and allowed to stand for 20 min for the appearance of bluish-green colouration. The absorbance of the tannic acid standard solution and the bluish-green solution were taken using UV-spectrophotometer at a wavelength of 760 nm. Equation 3.3 was used to determine the equivalent concentration of the tannin in the leaves extract using a calibration curve of the tannin (De Silva *et al.*, 2017).

$$y = 0.5269x + 0.0602 \quad (3.3)$$

Where; y = Absorbance (nm), and x= concentration (mg/mL)

Determination of total flavonoids

Total flavonoids in the leaf extract were determined using the aluminium chloride colourimetric method (Roghini and Vijayalakshmi, 2018). 0.5 mL of the leaf extract was added into a test tube containing 1.5 mL of methanol. 0.1 mL of 10% aluminium chloride, 2.8 mL of distilled water and 0.1 mL sodium acetate solution were added to the leaves extract. The reaction mixture was incubated at room temperature for 30 min and absorbance of the reaction mixture was measured using the UV Spectrometer at 415 nm. Distilled water was used as a blank. Quercetin was used as a standard to establish the calibration curve. Total flavonoids were estimated using Equation 3.4:

$$y = 1.2766x + 0.0448 \quad (3.4)$$

Where; y = Absorbance (nm), and x= concentration (mg/mL).

Determination of total phenols

The number of total phenols in the leaves extract was determined as follows: 0.5 mL of the leaves extract was measured into a test tube, followed by the addition of 2.5 mL of 10% Folin Ciocalteau (FC) and 2.0 mL of 7.5% Na_2CO_3, one after the other to the extract. The mixture was heated at 45ºC for 40 min in a water bath and the absorbance of the mixture was measured at 765 nm wavelength using the UV spectrophotometer. Gallic acid was used as a standard to obtain a calibration curve (Roghini and Vijayalakshmi, 2018). The total phenols were estimated using Equation 3.5:

$$y = 0.5251x + 0.1661 \quad (3.5)$$

Where; y = Absorbance (nm), and x= concentration (mg/mL).

3.2.4 Preparation of leaf extract

Powdered leaves of 5 g were measured into a 250 cm^3 beaker, followed by the addition of 100 mL of deionised water. The mixture was stirred and heated at 70ºC for 15 min and later allowed to cool to room temperature.

The mixture was filtered using Whatman No. 1 filter paper and the filtrate (aqueous leaves extract) was stored in a refrigerator.

3.3 Synthesis of Silver Oxide Nanoparticles (Ag_2O Nps)

The preliminary synthesis of Ag_2O nanoparticles was carried out using the green method involving a variation of four parameters namely; the volume of $AgNO_3$ precursor (1-12 mL), the volume of aqueous leaves extract (1-10 mL), pH (2-12) and temperature (30-70ºC). The synthesis of Ag_2O nanoparticles was investigated using one factor at a time while other parameters remain constant to establish the optimum conditions. The modified method of Dhand *et al.* (2016) was used to synthesise the Ag_2O nanoparticles by measuring the appropriate volume of $AgNO_3$ precursor solution (1, 2, 4, 6, 8, 10 or 12 mL) into a 50 mL conical flask and other parameters; the volume of *Parkia biglobossa* aqueous leaves extract (1 mL), pH (8), reaction temperature (30ºC) were kept constant. The solution was stirred on a magnetic stirrer for 10 min at 100 rpm. A colour change from yellow to brown was observed which indicates the formation of silver oxide nanoparticles as shown in Plate V. The resultant solution was then scanned between 200 and 700 nm wavelength by UV-vis spectrophotometer.

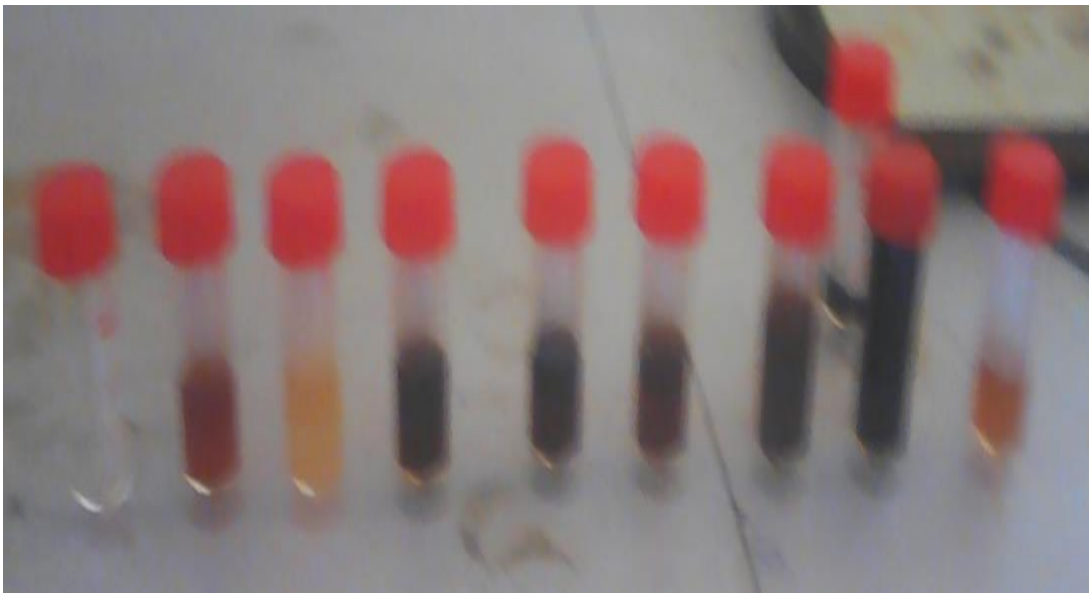

Plate V: Synthesised Silver oxide nanoparticles

The appearance of a peak with the highest intensity in the range of 400 – 500 nm was considered suitable for the formation of Ag_2O nanoparticles (Shittu and Ihebunna, 2017b). The synthesised Ag_2O nanoparticles were obtained by centrifugation and decantation, followed by freeze-drying. The optimisation of the synthesis parameters for the Ag_2O process was then investigated using a 2^4-factorial design with the variation of the following process variables: volume of $AgNO_3$ (7– 10 mL), the volume of aqueous leaves extract (1-3 mL), pH (6- 8) and reaction temperature (30 – 60ºC) as the minimum and maximum values.

The experimental design in Table 3.3 was used to generate Table 3.4 using the design expert and subsequently conducted sixteen experimental runs generated for the optimisation study. The first run of the optimisation experiment was carried out by measuring 10 mL of $AgNO_3$ precursor solution into a 50 mL conical flask, followed by a 1 mL volume of *Parkia biglobossa* aqueous leaves extract, the pH of the solution adjusted to 6. The solution was stirred on a magnetic stirrer for 10 min at 100 rpm, using the reaction temperature of 60ºC. Colour change from yellow to brown was also observed which indicates the formation of silver oxide nanoparticles. Other runs (2-16) were repeated using the conditions specified in Table 3.4.

Table 3.3: A factorial design for the synthesis of Ag_2O nanoparticles

Coded Variables	Actual Variables	Units	Low level	High Level
A	Precursor volume	mL	7	10
B	Volume of reducing agent	mL	1	3
C	pH	-	6	8
D	Temperature	ºC	30	60

Table 3.4: 2^4 Design matrices for Ag_2O nanoparticles synthesis for wavelength (nm) as a response

Exp. Runs	Precursor volume (mL)	Extract volume (mL)	pH	Temperature (ºC)
1	10	1	6	60
2	10	1	8	60
3	7	1	8	60
4	7	3	6	60
5	10	3	8	30
6	7	1	8	30
7	10	3	8	60
8	7	1	6	60
9	10	1	8	30
10	7	3	8	60
11	10	3	6	60
12	10	1	6	30
13	7	3	6	30
14	7	1	6	30
15	7	3	8	30
16	10	3	6	30

3.4 Synthesis of Titanium Dioxide Nanoparticles

The synthesis of TiO_2 nanoparticles was carried out using the modified method described by Zahir *et al.* (2015b). In this research, a 2^3-factorial experimental design was considered for the optimisation of TiO_2 nanoparticle synthesis using the Design-Expert software. The following process factors were considered; (A)-the volume of 0.5 M Titanium (IV) isopropoxide (TTIP) (5 – 50 mL), (B)-the volume of aqueous leaf extract (5 -50 mL), and (C)-stirring speed (100-200 rpm) as shown in Table 3.5, to give eight runs of the experimental matrix shown in Table 3.6. In carrying out the first run of titanium synthesis, 50 mL of precursor solution was measured into a 250 cm^3 conical flask and 50 mL of aqueous leaves extract was added, a light green colour was obtained.

Table 3.5: A factorial design for the synthesis of TiO_2 nanoparticles

Coded Variables	Actual Variables	Units	Low level	High Level
A	Volume of precursor	mL	5	50
B	Volume of plant extract	mL	5	50
C	Stirring speed	Rpm	100	200

Table 3.6. Design matrix for TiO_2 nanoparticles synthesis for crystallite size (nm) as a response

S/N	Stirring speed (rpm)	Volume of extract (mL)	Volume of precursor (mL)
1	100	50	50
2	200	5	50
3	100	5	50
4	100	5	5
5	200	50	5
6	100	50	5
7	200	50	50
8	200	5	5

Thereafter, the pH of the mixture was adjusted to 8 and the solution was then placed on the magnetic stirrer and stirred at 100 rpm for 2 h. After continuous stirring, the light green colour earlier observed changed to pale brown, which is an indication of the formation of TiO_2 nanoparticles (Madadi *et al.*, 2020). The absorption bands (peaks) developed due to the formation of TiO_2 nanoparticles were determined using the UV-visible spectrophotometer scanned in the wavelength range of 200 and 600 nm. The second run of the synthesis of TiO_2 nanoparticles was carried out by measuring 5 mL of TTIP precursor solution into a 250 cm^3 conical flask, followed by the addition of 50 mL of aqueous leaves extract.

This was accompanied by the formation of light green colour and thereafter the solution pH was adjusted to 8 and the mixture was placed on the magnetic stirrer maintained at 200 rpm for 2 h. The TiO_2 nanoparticles formed were filtered, washed severally with distilled water and allowed to age overnight. The TiO_2 cake was oven-dried at 100ºC for 1 h followed by calcination in a muffle furnace at 550ºC for 2 h. Other runs 3 to 8 were carried out according to the design matrix shown in Table 3.6. The calcined TiO_2 nanoparticles obtained from each run are shown in Plate VI.

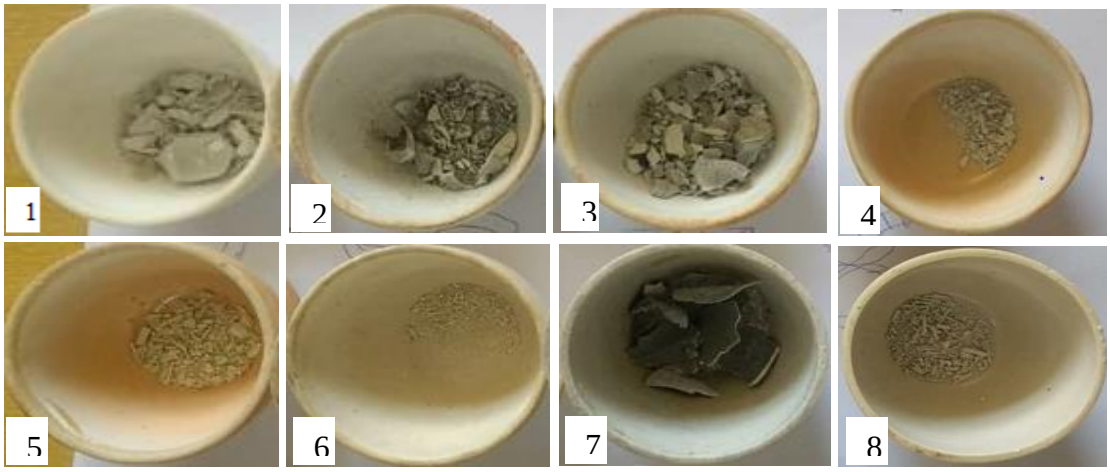

Plate VI: TiO_2 nanoparticles obtained from run (i) 1 (ii) 2 (iii) 3 (iv) 4 (v) 5 (vi) 6 (vii) 7 (viii) 8 the experimental runs of the factorial design

3.5 Synthesis of Silver Oxide-Titanium Dioxide (Ag_2O/TiO_2) Nanocomposite

The optimal conditions established in sections 3.3 and 3.4 were used to develop Ag_2O/TiO_2 nanocomposites via the green impregnation method. The effect of variation of concentration of $AgNO_3$ on the lattice layer of TiO_2 nanoparticles was investigated and the synthesis procedure describes as follows:

Twelve millilitres (12 mL) of different concentrations of $AgNO_3$ (0.01, 0.02 and 0.05 mol/L) were measured into three different 250 cm^3 beakers followed by the addition of 6 cm^3 of aqueous leaf extract. The solution pH was adjusted to 8 using 2 mol/L NaOH solution and 6 g of the prepared TiO_2 nanoparticles were added to the mixture. The mixture was stirred at 200 rpm on a magnetic stirrer for 2 h each.

The solution completely changed from pale white to dark grey which indicated the reduction of silver oxide-Titanium (IV) oxide nanocomposites. The mixture was left overnight to age and then oven-dried at 100°C for 1 h before calcination in a muffle furnace at 550°C for 2 hours. The AgO_2/TiO_2 nanocomposites obtained are shown in Plate VII.

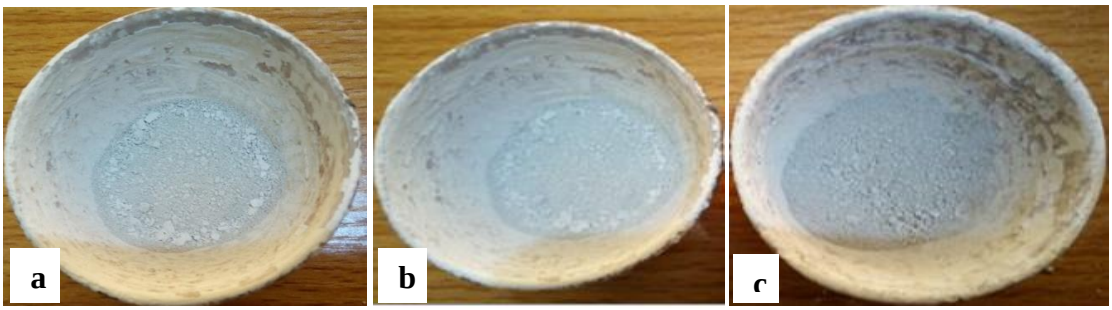

Plate VII: AgO_2/TiO_2 nanocomposites with different concentration of Ag_2O (a) 0.01 mol/L (b) 0.02 mol/L (c) 0.05 mol/L

3.6 Preparation of Binary Ag_2O/Acid-Activated Kaolinite Clay Nanocomposite

The Ag_2O/activated clay nanocomposites were prepared using the modified procedure described by Pessanha *et al.* (2014) and Jlassi *et al.* (2013) respectively. The optimum concentration of $AgNO_3$ precursor was employed to synthesise silver-doped activated clay nanocomposite. In this case, the optimal variables of 30 cm^3 of 0.05 mol/L $AgNO_3$, 5 mL of aqueous leaves extract, pH 8 and reaction temperature (30°C) were used for the preparation of Ag_2O/activated clay nanocomposites. 20 g of the acid-activated clay was added to 30 mL of 0.05 mL $AgNO_3$ solution in a 250 cm^3 conical flask, and then 5 mL of aqueous leaves extract also was added. The pH of the mixture was adjusted to 8 using 2 mol/L NaOH and then stirred in a thermostatic water bath shaker maintained at 30°C for 12 h. The obtained slurry was decanted, washed with deionized water and oven-dried at 50°C overnight to obtain silver oxide- acid-treated kaolinite clay composite (Ag_2O-clay) coded as Nc_1.

3.7 Preparation of Titanium-oxide Doped Activated Clay (Binary) Nanocomposite

The TiO_2/acid-treated kaolinite clay nanocomposites were prepared by mixing 50 mL of 0.5 M Titanium (IV) isopropoxide solution and 50 mL aqueous leaf extract with 20 g acid-treated kaolinite clay. The pH of the mixture was maintained at 8 and then stirred at 200 rpm, for the reaction time of 2 h. The resulting slurry was filtered, allowed to age for 12 h, oven-dried at 100ºC for 1 h and then calcined at 550ºC for 2 h to give Titanium (IV) oxide doped acid-treated kaolinite clay(TiO_2-clay) composite coded as Nc_2.

3.8 Preparation of Ternary Ag_2O/TiO_2 -Activated Treated Clay Nanocomposites

The ternary nanocomposites of Ag_2O/TiO_2-acid-treated kaolinite clay were prepared using the following ratio; 1:3 (25%:75%) as follows: 10 g of binary Ag_2O/TiO_2 nanocomposites obtained in section 3.5 was added to 30 g of the acid-treated kaolinite clay in a 500 cm^3 beaker under continuous stirring. The mixture was further stirred for 2 h after which the slurry obtained was filtered, oven-dried at 100ºC for 1 h and then calcined in a muffle furnace at 550ºC for 2 h and labelled as AgO_2/TiO_2-Clay (Nc_3). The procedures were repeated for (50%: 50%) and (75%: 25%) of Ag_2O/TiO_2-activated clay nanocomposites which represent (1:1) and (3:1) and labelled as Nc_4 and Nc_5 respectively, shown in plate VII. The nanocomposites Nc_1, Nc_2, Nc_3, Nc_4 and Nc_5 were then characterised using different analytical tools.

3.9 Characterisation of the Prepared Nano-Adsorbents

The beneficiated clay, activated clay, synthesised Ag_2O, TiO_2 nanoparticles, Ag_2O-acid-treated kaolinite clay, TiO_2-acid-treated clay, Ag_2O-acid-treated clay and Ag_2O/TiO_2-acid-treated clay nanocomposites were characterised using FTIR, Uv-Visible spectrometry, HRTEM, SAED, HRSEM/EDS, XRD, BET and XPS. The phytochemical constituents in the leaf extract were identified using GC-MS. The samples preparation and measurement conditions during the analysis are explained as follows:

Plate VII: Nanocomposites of (a) Ag_2O-clay, (b) TiO_2-clay, (c) Ag_2O/TiO_2 (75%)-clay (25%), (d) Ag_2O/TiO_2 (50%)-clay (50%), and (e) Ag_2O/TiO_2 (25%)-clay (75%)

3.9.1 Fourier transform infrared (FTIR) spectroscopy studies of samples

The FTIR analysis of the prepared samples was carried out using the Perkin Elmer 100 FT-IR spectrometer model "two". Before analysis, the FTIR probe was cleaned with ethanol and then baseline runs to avoid interference. 0.05 g of sample was placed directly under the probe and the scanning was done. The corresponding spectra for each sample were obtained as raw data in Excel format. The data were thereafter plotted to generate the FT-IR spectra. The operating parameters for the equipment are listed in Table 3.7.

Table 3.7: Operating Parameters for Perkin Elmer 100 FT-IR

Operating Parameter	Conditions
Force gauge	50
Scan wavelength	4000-400 cm^{-1}
Scan number	4
Unit	%Transmittance

3.9.2 UV-visible spectrophotometry measurements

The UV-visible absorption spectrophotometry was done using the UV-SPECTROMETER, (UV-1800) manufactured by SHIMADZU, Japan. A 2 mL of the liquid samples to be scanned was measured into the cuvette and the UV spectrometer was then connected to the computer. The de-ionised water was first scanned as the blank for the measurement before the sample to be read was scanned. For the de-ionised water, no peaks were formed, while peaks generated are plotted in graphical form and the data were obtained.

3.9.3 Gas chromatography-mass spectrophotometer (GC-MS) analysis

The GC-MS, model Agilent 7890A was used to further characterise the leaves extract of *Parkia biglobosa*. The carrier gas for the analysis was helium and the equipment was equipped with a triple-axis detector and auto-sampler injector. About 250 mg of the leaves extract sample was weighed into the sample bottle and placed in the sample tray for analysis. The injection of the sample into the GC-MS was done at a split mode of 50:1 through a highly polar Agilent 190925-433 capillary column of 30 m length. The spectra of the leaves extract were obtained and compared with the standard in the NIST 11 library.

3.9.4 High-resolution transmission electron microscopy (HRTEM) analysis

A Zeiss Auriga HRTEM, operated at 200 kV was used to examine the internal structure of the prepared Ag_2O, TiO_2 and Ag_2O/TiO_2 nanocomposite. Each sample was prepared by dissolving approximately 0.02 g of the synthesized samples in 10 mL ethanol, followed by ultrasonication for 5 minutes. A drop of the solution was placed on a holey-carbon copper grid and thereafter exposed to photo light for 3 minutes. After drying, the copper grids with samples were mounted into the electron microscope for HRTEM analysis.

3.9.5 Selected area electron diffraction (SAED) analysis

The SAED analysis was done using the sample grids from HRTEM analysis to determine the crystal nature of dispersity (either mono or poly). The SAED pattern was obtained using the same instrument for HRTEM and the patterns were recorded under the same instrumental set-up conditions.

3.9.6 High-resolution scanning electron microscopy (HRSEM) analysis

A Zeiss Auriga High-Resolution Scanning Electron Microscope (HRSEM) was used for this study. An approximate mass, of 0.05 g of each sample to be analysed was sprinkled on a sample holder having carbon adhesive tape on it. This was sputter-coated with Au-Pd Quorum T150T for 5 min before analysis. The samples were thereafter characterized at different magnifications. The microscope was operated at Electron High Tension (EHT) of 5 keV for imaging. For the determination of the elemental composition of the samples using Energy Dispersive Spectroscopy (EDS) measurements, the secondary electron mode was activated for imaging. A homogeneous region of the sample was identified and an electroscope operated at high tension (EHT) of 20 keV for EDS.

3.9.7 X-ray diffraction studies (XRD)

The X-Ray diffraction studies were done using the Bruker AXS D8 X-Ray Machine with CuKα radiation. 2 g each of the powdered samples to be analysed was placed in the holders and pressed with a clean glass slide to produce a flat surface. The loaded samples were scanned at the rate of 0.05°/sec under the applied measurement conditions: applied voltage 40 kV, and current 40 mA. The machine was calibrated using a pure silicon standard sample. After calibration, the sample was loaded into the machine for scanning. The X-ray diffraction patterns were recorded on the machine at room temperature within the range of 20 to 90° on the 2θ scale values.

At the end of the scan, the d spacing for each peak was calculated from the 2θ scale values. The interplanar spacing for the diffraction angle of each peak (d-spacing) was calculated using Braggs law as shown in Equation 3.6 and was compared using the search and match routine of the d-spacing of known materials with the d-spacing of unknown materials using the International Centre for Diffraction Data (ICDD), Powder Diffraction File (PDF).

$$n\lambda = 2d\sin\theta \tag{3.6}$$

Where; λ= wavelength of X-Ray= 1.5406Å.,

θ= Diffraction angle in radians

The unit cell parameters were calculated and indexed as h k l. The average crystallite size of the clay was calculated from the analysis of the peaks in the X-Ray diffraction pattern using Debye-Scherer's equation stated in Equation 3.7. The crystallite size (D) was used as a response and TiO_2 nanoparticles with the smallest size were considered.

$$D = \frac{K\lambda}{B Cos\theta} \tag{3.7}$$

Where; λ = wavelength of X-ray, K = Scherer's constant (0.9), B= Full Width at Half maximum (FWHM), θ =diffraction angle, D= Average crystallite size

3.9.8 Brunauer, Emmet and Teller (BET) nitrogen adsorption technique

The surface area and pore size and pore volume of the samples were determined using the Brunauer, Emmet and Teller (BET) Nitrogen adsorption-desorption technique on NOVA 4200e model equipment. 0.1 g of each sample was measured and put in a sample holder. The sample was degassed to open the pores and remove impurities at 200°C under vacuum (780 mmHg) for 1 h 30 min. The sample was thereafter analysed for the physisorption of nitrogen gas at a temperature of 273K. BET surface area, pore volume and pore size data were then obtained.

3.9.9 X-ray photoelectron spectroscopy (XPS) analysis

The XPS analysis was carried out with a PHI 5400 XPS spectrometer using a non-monochromatic Mg Kα X-ray source (1253.6 eV, 15 kV, 200 W) and a hemispherical sector analyser. The instrument work function was calibrated to give binding energy (BE) of 83.96 eV for the Au 4f7/2 line for metallic gold and the spectrometer dispersion was adjusted to give a BE of 932.67 eV for the Cu 2p3/2 line of metallic copper. The photoelectron take-off angle for all measurements was 45°. Survey scan analyses were carried out with a pass energy of 178.95 eV in steps of 0.25 eV and a scan rate of 5 eV/s. High-resolution analyses were carried out with a pass energy of 44.75 eV, a step size of 0.125 eV and a scan rate of 1.6 eV/s. For low concentrations and low sensitivity species, detailed energy regions were averaged over 20 sweeps. Charge correction was done using the adventitious carbon peak at 284.8 eV as a reference. Spectra were analysed using XPS PEAK 4.1 software. A Tougaard background was used for the Ag 3d fits. All other fit used a Shirley background. The XPS survey spectra were corrected for X-ray satellite peaks (present because a non-monochromatic Mg X-ray source was used) and smoothened. The analysis area was 3 x 10 mm^2 and the base pressure in the working chamber was < 5 x 10^{-9} Torr measured by a nude ionization gauge. The 0.5 g of powders were mounted on a vacuum-friendly carbon tape and stuck to a Mo specimen holder. All spectra were collected without cleaning by sputtering or chemical means and no special instrumentation was used for charge neutralization.

3.10 Physio-chemical Analysis of Mining Wastewater

The determination of the physicochemical parameters was carried out at the laboratory of the Upper River Niger Basin Minna, using American Public Health Association (APHA, 2017) methods before the adsorption experiment.

These include chemical oxygen demand (COD), biochemical oxygen demand (BOD), total organic carbon (TOC), dissolved oxygen (DO), coliform counts, conductivity, pH, alkalinity, phosphate, carbonates, sulphates, and nitrates in the collected mining wastewater

3.10.1 Determination of total organic carbon (TOC)

The level of TOC in the mining wastewater involved the measurement of two parameters; Total carbon (TC) and Total inorganic carbon (TIC). The difference between TC and TIC (TC-TIC) gave the TOC. TC and TIC were converted to carbon dioxide (CO_2) respectively via oxidation and acidification. Firstly, the inorganic carbon was removed via acidification of 15 mL of mining wastewater measured into a 50 cm^3 volumetric flask with 3 mL of 0.5% (v/v) H_3PO_4. Thereafter the solution pH was adjusted to 2 and maintained under continuous purging of purified O_2 for 10 min at a flow rate of 150 cm^3/min. The sample was later digested in an autoclave at 115°C for 2 h. Distillation of the digested sample was done by passing through 5 g CuO by a flow rate of 2-3 cm^3/min for 30 min to convert the volatile organic carbons while 0.05 g $K_2S_2O_8$ was equally added to decompose the non-volatile organic compounds. The TOC value was then determined from the amount of converted non-purgeable bonded carbon to CO_2 measured by a nondispersive infrared analyser (Tijani *et al*., 2017).

3.10.2 Determination of chemical oxygen demand (COD)

The determination of COD in the wastewater was carried out by pipetting 10 mL of wastewater into a round bottom flask, followed by the addition of 1 mL mercury sulphate ($HgSO_4$) and 5 mL potassium dichromate ($K_2Cr_2O_7$). The solution was mixed and 2 mL concentrated sulphuric acid was added in a controlled manner and subsequently digested at 150^{o}C for 2 h.

Distilled water was added through the condenser to cool it down and titrated with standard sulphate, 2-4 drops of ferroin indicator was added as an indicator and the amount of O_2 required was calculated from the quantity of oxidant consumed (Zhang *et al.*, 2018).

3.10.3 Determination of biochemical oxygen demand (BOD)

The measurement of BOD was done by firstly conditioning the wastewater (which included pH adjustment, and dilution followed by the addition of an appropriate amount of seed bacteria) to ensure a favourable growth for bacteria. Initial dissolved oxygen (DO) of 50 mL sample was recorded and then incubated for 5 days at 20°C. After 5 days, the sample was removed and the final DO was measured using a dissolved oxygen probe. BOD was calculated from the depletion of DO and volume of sample used as follows (Nimibofa and Bennett, 2022);

$$BOD_5 = BOD\ mg/L = [(DO_1\text{-}DO_5) - \text{seed correction}] \times \text{Dilution factor} \quad (3.8)$$

Where; BOD_5= at the end of day 5, DO_1 = at the beginning of day 1, DO_5 = at the end of day 5

3.10.4 Determination of pH

The pH of the mining wastewater was determined using a pH meter consisting of a glass electrode through which a small voltage was passed. A voltmeter measures the electronic impedance in the glass electrode and displays pH units instead of volts. The pH meter was calibrated before each use with buffers of pH 4 and pH 9. The measurement was done by submerging the probe into 10 mL of the mining wastewater until the reading was registered by the pH meter.

3.10.5 Determination of phosphate

To determine the amount of phosphate in the mining wastewater, 1 mL of the wastewater was measured into a 10 cm^3 flask, followed by 1 mL of ammonium molybdate and 0.4 mL of hydrazine sulphate.

The mixture was shaken for appropriate interaction and then made up to the mark with deionised water in the flask. The solution mixture was heated for 30 min in a water bath maintained at 60°C and accompanied by the formation of blue colouration, then the solution was cooled and its absorbance was measured at 830 nm using UV-spectrophotometer. The obtained absorbance was used to determine the equivalent concentration of the phosphate in the mining wastewater using a calibration curve of phosphates (Ganesh *et al.*, 2012).

3.10.6 Heavy metal analysis

The level of selected heavy metals such as Fe, Cd, Mn, Co, Cu, Zn, Pb, Cr and Ni in the raw and treated mining wastewater were determined using Atomic Absorption Spectrophotometer (Pye Unicam SP-9 Cambridge, UK). Standard samples of the metal ions to be analysed were prepared for the calibration of the AAS machine using 5 ppm, 10 ppm, 15 ppm and 20 ppm. A graph of absorbance against concentration was plotted to ensure proper calibration has been achieved. Once a straight line graph passing through the origin was obtained, the calibration was successful. For each metal ion to be determined, its cathode lamp was used for the elemental analysis. After taking the reading, the connected nozzle was purged with deionised water to avoid contamination of other samples whose readings were yet to be taken. The filtrate samples after the adsorption process were collected and stored in 100 mL sterile sample bottles. The metal ions present above standard organisation permissible limits were removed in batch adsorption processes.

3.11 Batch Adsorption Treatment of the Mining Wastewater

A generalised batch adsorption treatment of the mining wastewater was carried out using the following prepared materials; Acid treated clay, TiO_2 nanoparticles, Ag_2O-acid-treated clay, TiO_2-acid-treated clay, Ag_2O/TiO_2 and Ag_2O/TiO_2- acid treated clay.

This was done to identify the material with the highest adsorptive behaviour adopting the method of Abunah *et al.* (2019). The process was carried out at a constant temperature of 30^{o}C and 0.5 g/100 mL adsorbent dose. While contact time was varied between 20 - 180 min to study the adsorption equilibrium. For each of the nanocomposites, 0.5 g was measured into a 250 cm^3 flask with 100 mL of the mine wastewater (Abdallah, 2019). The mixture was corked and agitated at 125 rpm using the water bath shaker until equilibrium was reached. Sampling was done at an interval of 20 min and the resulting mixture was filtered using Whatman filter paper and the supernatant was analysed for heavy metal ions (Fe (III), Pb (II), Cu (II), Mn (II)) concentration by atomic Absorption Spectrophotometer (AAS). Also, the pH of the treated wastewater was monitored.

3.11.1 Effect of contact time

The influence of contact time on the adsorption process was investigated on the best adsorbent (Ag_2O/TiO_2/acid-treated kaolinite clay) for 120 minutes, at 20 minutes intervals. In doing this, a constant weight of Ag_2O/TiO_2/acid-treated kaolinite clay (0.5 g) was measured into five different conical flasks, 100 mL mining wastewater was thereafter added and agitated at 125 rpm and a temperature of 30^{o}C. A sample each was withdrawn for analysis after 20, 40, 60, 80, 100 and 120 minutes of continuous shaking. The supernatants were filtered and the filtrate was analysed for the residual concentration of the selected heavy metals in the mining wastewater using AAS.

3.11.2 Effect of adsorbent dosage

To determine the effect of adsorbent dosage on the adsorption process, adsorbent dosages of 0.1, 0.2, 0.3, 0.4, 0.5, 0.6, 0.7, 0.8, 0.9 and 1.0 g of Ag_2O/TiO_2-acid-treated kaolinite clay were measured into ten different conical flasks, 100 mL mining wastewater was also added, and temperature maintained at 30^{o}C.

The samples were withdrawn at the end of 120 minutes of constant contact time respectively. The supernatants were filtered and the filtrate was analysed for heavy metal ion compositions there present.

3.11.3 Effect of temperature

The effect of temperature on the adsorption of Fe (III), Pb (II), Cu (II) and Mn (II) ions onto the Ag_2O/TiO_2-acid-treated kaolinite clay adsorbent was tested by varying the temperature between 30^oC and 70 ^oC. In doing this, 0.5 g of the adsorbent was measured into a single conical flask, and 100 mL of mining wastewater was thereafter added and agitated at 125 rpm. The thermostatted water bath shaker temperature was maintained at 30^oC for 120 minutes before withdrawing the sample for filtration and analysis for the residual concentrations of the selected heavy metals. The experiment was repeated at 40, 50, 60 and 70^oC respectively.

3.11.4 Adsorption kinetic experiment

The kinetic study of the adsorption process was investigated with the Ag_2O/TiO_2-acid-treated kaolinite clay adsorbent, investigating the variation of the adsorption process with time. The adsorption kinetics data were fitted into pseudo-first-order (PFO), pseudo-second-order (PSO), intraparticle diffusion (IPD) and Elovic kinetics model.

3.11.5 Isothermal studies

The adsorption isotherm governing the adsorption process was determined using six isotherms equilibrium models: Langmuir, Freundlich, Temkin, Dubinni-Radushevich, Harkin –Jura and Jovanovic isotherms equations. Langmuir isotherm is based on the monolayer sorption of metal ions on the surface of the adsorbent.

3.11.6 Adsorption thermodynamics

The thermodynamics studies of Mn (II), Fe (III), Pb (II) and Cu (II) ions adsorption onto Ag_2O-TiO_2-Clay were carried out at temperatures; 30, 40, 50, 60 and 70$^{\circ}C$ respectively.

This was done to understand the influence of temperature on the removal efficiency of the metal ions from wastewater. Enthalpy change (ΔH°), Gibbs free energy change (ΔG°) and entropy change (ΔS) of the system during the adsorption process were evaluated.

3.11.7 Data analysis

The adsorption capacity (q_t, in mgg^{-1}) at a time (t) is calculated using Equation 3.9:

$$q_t = \frac{(C_o - C_t)V}{m} \qquad (3.9)$$

Where, C_o and C_t are the initial and the final metal ion concentration (mgL^{-1}) respectively; V is the water sample volume (L), and m is the mass of adsorbent used (g).

The adsorption at equilibrium, q_e (mgg^{-1}), was calculated according to Equation 3.10:

$$q_e = \frac{(C_o - C_e)V}{m} \qquad (3.10)$$

Where, C_o and C_e are the initial and the final (equilibrium) metal ion concentration (mgL^{-1}) respectively; V is the water sample volume (L), and m is the mass (g) of the adsorbent that will be used. The percentage of metal ion removal will be calculated using Equation 3.11 (Guillaume *et al.*, 2018):

$$\text{Removal (\%)} = \frac{C_o - C_t}{C_o} X\ 100\% \qquad (3.11)$$

Kinetics study of the adsorption process

The linearised pseudo-first-order, pseudo-second-order and intraparticle diffusion models are given used for the kinetics analysis are given in Equations 3.12, 3.13, 3.14 and 3.15 respectively (Guillaume *et al.*, 2018) as;

$$\ln(q_e - q_t) = q_e - k_1 t \qquad (3.12)$$

Where;

q_e and q_t depict the number of metal ions adsorbed at equilibrium ($mg.g^{-1}$) and time t respectively. k_1 is the rate constant for pseudo-first-order adsorption (min^{-1}). The pseudo-second-order kinetics equation is expressed in Equation 3.13;

$$\frac{dq_t}{dt} = k_2(q_e - q_t)^2 \quad (3.13)$$

Where; k_2 is the rate constant of pseudo-second-order adsorption ($g.mg^{-1}min^{-1}$).

For the boundary condition t = 0 to t = t and $q_e = q_t$ the integrated form of the equation becomes Equation 3.14;

$$\frac{1}{q_e - q_t} = \frac{1}{q_e} + k_2 t \quad (3.14)$$

Rearranging this equation, we have a linear form of Equation 3.15;

$$\frac{t}{q_t} = \frac{1}{k_2 q_e^2} + \frac{1}{q_e} t \quad (3.15)$$

The intraparticle diffusion model is expressed as Equation 3.16;

$$q_t = K_p t^{1/2} + C_p \quad (3.16)$$

Where K_p is the intra-particle diffusion rate constant ($mgg^{-1}min^{-1/2}$) and C_p (mg/g) is the intercept whose value gives information about the boundary layer thickness. The value of K_p and C_p are calculated from the slope and intercept of the linear plot of q_t versus $t^{1/2}$.

The Elovic equation is another kinetic model that describes the adsorption of adsorbate by a solid in an aqueous medium. The equation assumes a heterogeneous distribution of adsorption (chemisorption) or activation energies that vary continuously with surface coverage. The equation can be expressed as Equation 3.17;

$$Q_t = \frac{1}{\beta}\ln(\alpha\beta) + \frac{1}{\beta}\ln(t) \quad (3.17)$$

Where, α is the initial adsorption rate (mg/g min), and β represents the desorption constant, which is related to the extent of surface coverage and activation energy for chemisorption in g/mg. The Elovic coefficients were calculated from slopes (β) and intercept (α) of Q_t against ln t plots.

Isotherms of the adsorption process

The Langmuir equation is represented in Equation 3.18;

$$q_e = q_{max} \frac{K_L C_e}{1 + K_L C_e} \quad (3.18)$$

Where:

C_e (mgL^{-1}) and q_e ($mg.g^{-1}$) are the concentration (mg/L) of metal ions in solution at equilibrium and the amount of adsorbed metal at equilibrium, respectively, q_{max} (q_o) and K_L are Langmuir constants related to sorption capacity ($mg.g^{-1}$) and the energy of sorption (Lmg^{-1}) respectively. The linear form of Equation 3.18 can be written as;

$$\frac{C_e}{q_e} = \frac{1}{q_{max} K_L} + \frac{C_e}{q_{max}} \quad (3.19)$$

The essential characteristics of the Langmuir isotherm can be expressed in terms of a dimensionless equilibrium parameter R_L. Given as Equation 3.20;

$$R_L = \frac{1}{1 + b C_o} \quad (3.20)$$

Where:

b (K_L) is the Langmuir constant and

C_o is the highest metal ion concentration (mgL^{-1}).

The value of R_L indicates; unfavourable, if ($R_L > 1$), linear ($R_L = 1$), favourable, if ($0 < R_L < 1$) or irreversible, if ($R_L = 0$).

Freundlich isotherm describes the heterogeneous surface energies by multilayer sorption and is expressed by Equation 3.21 (Ogunleye *et al.*, 2014):

$$q_e = K_F C_e^{1/n} \quad (3.21)$$

Where: K_F (mg/L) $(1/mg)^{1/n}$ and n are the Freundlich constants related to sorption capacity and sorption intensity respectively.

The Freundlich isotherm has been derived by assuming an exponential decay sorption energy distribution. The linearized form of equation 3.21 gives equation 3.22.

$$\log q_e = \log K_F + \frac{1}{n} \log C_e \quad (3.22)$$

Temkin isotherm is based on the number of ions adsorbed during heating, which is due to the sorbate and adsorbent interactions, as represented in Equation 3.23 (Ayawei *et al.*, 2017).

$$q_e = B \ln A_T + B \ln C_e \quad (3.23)$$

Where:

$$B = \frac{RT}{b_T} \quad (3.24)$$

A_T is the equilibrium binding constant ($Lmol^{-1}$) corresponding to the maximum binding energy while constant B is related to the heat of sorption. A plot of q_e against C_e gives B as slope and $B \ln A_T$ as intercept from which the values of b_T and A_T are evaluated using R=8.314J/mol K.

The Dubinin-Radushkevich (D-R) model was used to estimate the characteristic porosity of the nano adsorbents and the apparent energy of adsorption. The non-linear form of the D-R isotherm equation is given in Equation 3.25:

$$q_e = q_o \, e^{-\beta \varepsilon^2} \quad (3.25)$$

The equation is linearized by taking the logarithm on both sides of the equation and is expressed as;

$$\ln q_e = \ln q_o - \beta \varepsilon^2 \quad (3.26)$$

Where q_e is the heavy metal amount that is adsorbed at equilibrium, per unit mass of nano adsorbent in mg g^{-1}; q_o is the maximum adsorption capacity in mgg^{-1}; $\beta \; or \; K_{ad}$ is the free energy of sorption per mole of the sorbate as it migrates to the surface of nano adsorbents from an infinite distance in the solution in mol^2 kJ^{-2}, and ε is the Polanyi potential (Egbosiuba *et al.*, 2019).

The Polanyi potential (ε) can be given as Equation 3.27;

$$\varepsilon = RT \ln(1 + {}^{1}/_{C_e}) \quad (3.27)$$

Where R is the gas constant in kJ.K^{-1}mol^{-1}, and T is the absolute temperature in K. Similarly, the value obtained was then used to estimate the mean free energy of adsorption; E is calculated using Equation 3.28;

$$E = \sqrt{\frac{1}{2\beta}} \tag{3.28}$$

Where E is the free energy change when one mole of ion is transferred to the surface of the adsorbent from infinity in the solution. The value is used to predict the sorption nature.

Harkin-Jura isotherm

The Harkin-Jura isotherm model is an isotherm that assumes the prospect of multilayer adsorption on the surface of adsorbents having heterogeneous pore distribution. This model is expressed as follows:

$$\frac{1}{{q_e}^2} = \left(\frac{B_H}{A_H}\right) - \left(\frac{1}{A_H}\right) log C_e \tag{3.29}$$

Where, B_H and A_H are Harkin-Jura constants that can be obtained from plotting $\frac{1}{{q_e}^2}$ versus log Ce. The Harkin-Jura isotherm model has been reported to show a better fit to the adsorption data than Freundlich, Halsey, and Temkin isotherm models (Foo and Hameed, 2010).

Jovanovic isotherm

The Jovanovic model is hinged on the assumptions contained in the Langmuir model, however, in a modified approach. The model specifies addition as the possibility of some mechanical contact between the adsorbate and adsorbent. The linear form of the Jovanovic isotherm is expressed in Equation 3.30:

$$ln q_e = ln q_{max} - K_J C_e \tag{3.30}$$

where qe is the amount of adsorbate in the adsorbent at equilibrium (mg g−1), $q$max is the maximum uptake of adsorbate obtained from the plot of ln qe versus Ce, and KJ is Jovanovic constant (Mustapha *et al.*, 2019).

Thermodynamics of the adsorption process

Enthalpy change (ΔH°), Gibbs free energy change (ΔG°) and entropy change (ΔS) of the system during the adsorption process were evaluated using Equations 3.31 and 3.32

$$\Delta G_{ads} = \Delta G° + RTln\ Q \tag{3.31}$$

The Gibbs energy change (ΔG, kJ/mol) of the metal ion(s) adsorption process was determined by Eq. (3.33) where Q describes the quotient of reaction and relates to the metal ion concentrations of a system that is not in equilibrium. However, at equilibrium $\Delta G_{ads} = 0$, hence Equation 3.31 is reduced to Equation 3.32:

$$\Delta G° = -RTln\ Kd \tag{3.32}$$

Where, $$Kd = \frac{q_e}{C_e} \tag{3.33}$$

$$\ln K_d = -\frac{\Delta G^0}{RT} = \frac{\Delta S}{R} - \frac{\Delta H^0}{RT} \tag{3.34}$$

Where K_d is the equilibrium parameter represented by Equation (3.33), q_e and C_e are the quantity of metal ion adsorbed at equilibrium and the equilibrium concentration of each metal ion in the solution. The values of ΔH° and ΔS° values were obtained from the slope and intercept of the Van't Hoff plots of In K_d against 1/T (Bankole *et al.*, 2019).

3.11.8 Analysis of error

To remove or minimise errors in the data obtained from each experiment, the analysis was duplicated and subjected to statistical analysis. The constants from the isotherm and kinetics studies were determined using Origin Pro software at a 95% confidence level. The linear determination coefficient (R^2), the non-linear Chi-square test (X^2) and the sum of square error (SSE) tests were performed to further choose the best-fitted isotherm and kinetic models. The mathematical equations are represented in Equations 3.35 and 3.36;

$$X^2 = \sum((q_{e,\ exp} - q_{e,cal})^2\ /q_{e,cal}) \tag{3.35}$$

$$SSE = \sum(q_{e,\ exp} - q_{e,cal})^2 \tag{3.36}$$

3.11.9 pH point of zero charges (pHPZC) determination for AAC and AAC-TiO_2

The pH point of zero charges (pHPZC) of the Ag_2O/TiO_2-clay, which is conveyed as the electrical balance between the adsorbent surface and metal ion adsorbate solution was determined. 100 mL of mining wastewater was measured into 12 separate Erlenmeyer flasks (in duplicates), and the initial pH (pH_i) was measured in the range of 2–12 (at 2.0 intervals) for the different flasks. A few drops of 2.0 M of HCl or NaOH were added to the mixture to control the pH of the solution using a pH meter (Eutech Instruments, Model Ecoscan Singapore).

The determined optimum dosage (0.5 g) of Ag_2O/TiO_2-clay was added into the 12 flasks separately and afterwards arranged on a shaker for 48 h to achieve balance charges between the surface of the adsorbent and the wastewater. The suspension was filtered after 48 h and the final pH at equilibrium (pH_f) of the filtrate was recorded. The pH_{PZC} of the adsorbent represents the meeting point between the pH_i curve against the pH_f curve.

3.12 Fabrication of Ag_2O/TiO_2-Clay Nanocomposites Filter for Mine Site Wastewater Treatment

The optimal mixing ratio of Ag_2O/TiO_2-acid-treated kaolinite clay nanocomposites found to effectively remove pollutants from the mine wastewater was adopted for the fabrication of a filter (0.5 g of 1:1 Ag_2O/TiO_2:Clay for 100 mL wastewater) from adsorption studies. The design drawing for the development of the filter pots was carried out using Corel-Draw Software. Production of the nano-based filter which contains Silver oxide and Titanium nanocomposites was carried out at the Ceramic Studios of the Industrial Design Department, The Federal University of Technology, Akure, Nigeria.

3.12.1 Preparation of materials

Grog was prepared from the beneficiated kaolinite clay, it was prepared to enhance stability and reduce linear shrinkage in filter samples. This was achieved by heating the dried beneficiated kaolinite clay to a temperature of 700^oC for 2 h in the muffle furnace.

The material was allowed to cool down in the furnace to room temperature before retrieval. This was stored until usage. Sawdust from the African birch tree (*Anogeissus Leiocarpus*) was collected from a Sawmill in Tanke, Ilorin. The sawdust oven-dried at a temperature of 110^{o}C for 1 h was milled to fine particle sizes and sieved using a < 300 μm mesh.

3.12.2 Preparation of test samples

Rectangular test samples were made in the dimension of 1 cm x 10 cm x 15 cm for shrinkage, water absorption and apparent porosity studies. The different mixing ratios of the kaolinite clay, grog and sieved sawdust were mixed in different test ratios and then bonded using about 50 mL of distilled water. Preliminary compounding of different aggregates of clay and sawdust (FC0-FC6), later clay and grog (FC7- FC8) was carried out to obtain suitable mixing formulas, the compounding ratios are presented in Table 3.8. The compounded aggregates were pressed into test filters, and these were marked at 8.0 cm to ascertain their degree of shrinkage.

The results obtained in Table 3.8 was used for further investigations on suitable mixing formulas, using various compositions of nanoclay, grog and sawdust (C1-C17) as shown in Table 3.9. The test samples were dried at room temperature until a constant weight was achieved thereafter oven-dried at 110^{o}C for 2 h. The dried samples were fired at a temperature of 800^{o}C in a muffle furnace for 1 h. The test samples were subjected to investigation on the effect of materials mixing ratios on the dried and fired linear and volumetric shrinkage, water absorption and apparent porosity of the nanoclay.

3.12.3 Determination of linear shrinkage

Test samples were moulded to determine linear shrinkage by drawing a 100 mm line (Lo) on each sample while it was in the green state. The samples were allowed to dry at ambient temperature until constant weights were obtained.

Table 3.8: Mixing ratio (v/v) of nanoclay, grog and sawdust of ceramic water filter test samples production

S/No	Sample identification	Nanoclay	Sawdust	Grog
1.	FC0	100	0	0
2.	FC1	90	10	0
3.	FC2	80	20	0
4.	FC3	70	30	0
4.	FC4	60	40	0
5.	FC5	50	50	0
6.	FC6	40	60	0
7.	FC7	20	80	0
8.	FC8	60	0	40
9.	FC9	50	0	50
10.	FC10	40	0	60

Table 3.9: Variable mixing ratio (v/v) of grog, nanoclay and sawdust for ceramic water filter production

S/No	Sample Name	Grog/Nanoclay	Sawdust
1.	C1	90	10
2.	C2	85	15
3.	C3	80	20
4.	C4	75	25
5.	C5	70	30
6.	C6	65	35
7.	C7	60	40
8.	C8	55	35
9.	C9	50	50
10.	C10	45	55
11.	C11	40	60
12.	C12	35	65
13.	C13	30	70
14.	C14	25	75
15.	C15	20	80
16.	C16	15	85
17.	C17	10	90

Thereafter, the samples were oven-dried at 110^{o}C for 2 h and Lo was re-measured as a new length (L_1). The Drying Shrinkage (DS) was then calculated using Equation 3.37:

$$DS = \frac{L_o - L_1}{L_o} \; X\; 100\% \tag{3.37}$$

For the determination of dried-to-fired shrinkage, L_1 was re-measured after firing at an elevated temperature to give firing length (L_f). Therefore, percentage shrinkage was calculated using Equation 3.38:

$$FS = \frac{L_1 - L_f}{L_1} \; X\,100\% \tag{3.38}$$

The green-to-fired shrinkage (TS) was determined for each sample using Equation 3.39:

$$TS = DS + FS \tag{3.39}$$

3.12.4 Determination of water absorption and apparent porosity

The water absorption and apparent porosity tests were done according to ASTM standard C 20 – 00 (ASTM, 2010). Each test sample was weighed and the weight was recorded as D. The test samples were then totally immersed and suspended in boiling water for 2 h. After boiling, the water was allowed to cool to room temperature with the samples still in suspension for another 12 h before further readings were taken. Each sample was thereafter weighed in water using a spring balance and the weight was recorded as S_1 (suspended weight). Alternatively, the suspended weight was also determined using the Archimedes principle. In doing this, each sample was immersed in a jar filled with distilled water. The weight of water displaced was measured using a weighing balance which was recorded as S_2. Comparisons were made and the average values were taken as S. The sample was removed from the water, excess water was cleaned from the surface and then weighed. The weight was recorded as W (saturated weight). The water absorption, A %, was calculated from Equation 3.40:

$$A\% = \left(\frac{W-D}{D}\right) X100 \tag{3.40}$$

The apparent porosity in percentage, P %, of each sample was also calculated from Equation 3.41:

$$P\% = \left(\frac{W-D}{W-S}\right) X100 \tag{3.41}$$

3.12.5 Fabrication of the small filters

After the characterisation of the various samples made from the mixtures of nanoclay, grog and sawdust, three samples which include NC6 (nanoclay: grog 1:1 with 35% sawdust), NC7 (nanoclay: grog 1:1 with 40% sawdust) and NC8 (nanoclay: grog 1:1 with 45 % sawdust) were chosen to produce the ceramic water filters. This was based on the studies of shrinkage, water absorption and apparent porosity tests.

To manufacture the small filters, a measured volume of clay and sawdust according to ratios 65:35, 60:40 and 55:45 were thoroughly mixed using mechanical sieves in ten cycles to accomplish uniform mixing and avoid the formation of clustered pores (Yakub *et al*., 2013) for about 40-60 min. About 1.6-1.9 litres of distilled water was added under continuous stirring to achieve a dough ball between 4.8 - 5.3 kg dough, sufficient to manufacture four pieces each of small filters. The doughs were kneaded and wrapped in clean polythene bags for 4 days; this was to allow the fermentation process to take place to improve the plasticity of the clay mix. A Jigger Jolly machine was used to mould the nano clay-based ceramic water filter using the dimensions shown in Figure 3.1.

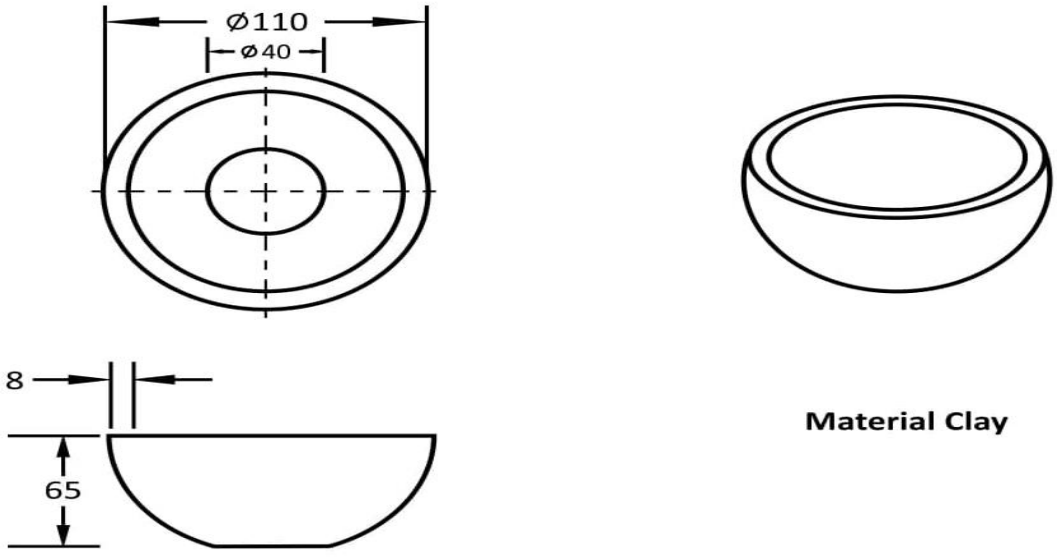

Figure 3.1: Design of Small Size Ceramic Filters

These moulded filters were dried at ambient temperature until a constant weight was recorded, they were also pre-heated in a gas kiln at 250^{o}C for 2 h. The pre-heating was carried out to remove the chemically combined water in the filter, which may cause sudden cracks in the filter. Thereafter, the filters were sintered in a gas kiln at a temperature of 850^{o}C for 2 h to produce a reticulated porous ceramic filter.

3.12.6 Determination of water flow rate

Each of the porous ceramic water filters was immersed in deionised water for 24 h to allow it to absorb water fully. The ceramic water filters were then placed in a container having the same diameter as the filters. A known volume of deionised water was poured into each of the filters. The filtered water was then collected in a beaker. The time for the total passage of water was noted. The flow rates for the water were then calculated using the relationship in Equation 3.42:

$$Q = \frac{V}{t} \tag{3.42}$$

Where Q = flow rate of water, V = volume of water and t = total time taken for the water to pass through.

The flow rate of the filters was evaluated to determine the most suitable from among the three fabricated filters. The adjudged best composition of the small filter was adopted for the fabrication of other small and bigger filters with the addition of Ag_2O-TiO_2 nanocomposites, using the dimensions shown in Figure 3.2 by the hydraulic press machine.

3.12.7 Fabrication of the big filters

The fabrication of the big filter was carried out to increase the rate at which wastewater is treated per time. This was carried out by measuring 60 volumes of clay and 40 volumes of sawdust (according to the best ratios 60:40 determined earlier) up to 12 kg each.

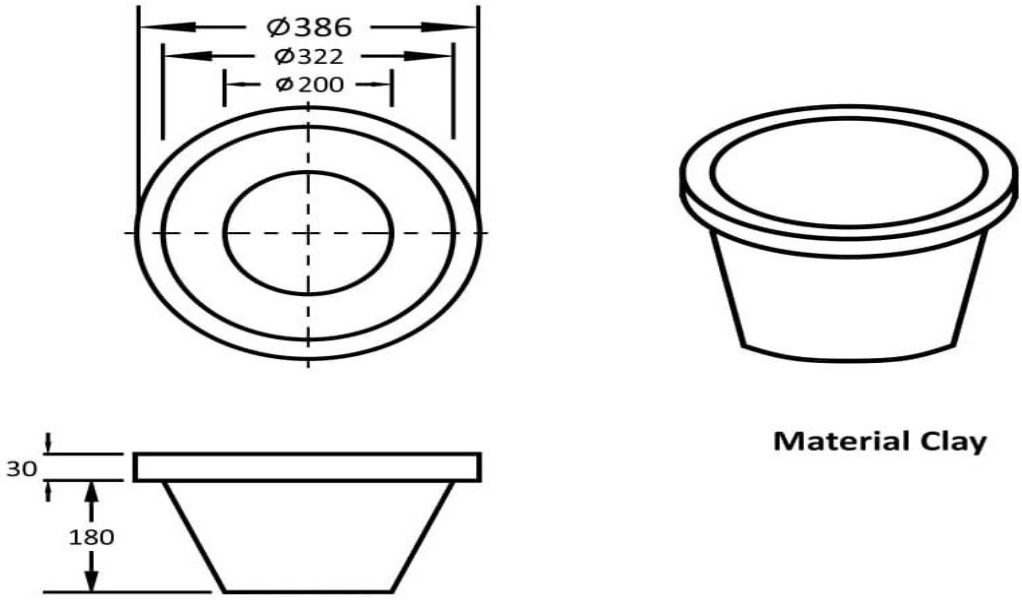

Figure 3.2: Design of Big-Size Ceramic Filter

These were thoroughly mixed using mechanical sieves in ten cycles to accomplish uniform mixing and avoid the formation of clustered pores (Yakub *et al.*, 2013) for about 40-60 min. Thereafter, 15 g of doped Ag_2O-TiO_2 was added based on the earlier calculation of 2 g Ag_2O-TiO_2 per 800 g, 60:40 clay: sawdust composite. The Ag_2O/TiO_2-clay was thoroughly mixed for another 40 min to allow proper interaction. About 3.2-3.8 L of distilled water was added to the composite mixture, under continuous mixing to achieve a thoroughly mixed clay-Ag_2O/TiO_2 composite dough ball. Other measurements were made according to specification and were mixed. About 4.8 - 5.3 kg dough, sufficient to manufacture four pieces of each of the small filters was kneaded and wrapped in clean polythene bags for 4 days; this was to allow the fermentation process to take place to improve the plasticity of the clay composite. Other known weights of the clay-Ag_2O/TiO_2 composite mixture (12 kg each) were kneaded and wrapped for fermentation. After four days of continuous kneading and fermentation, the doughs were thoroughly formed into a ball each, these were pressed tightly together to avoid visible cracks on their surface.

The fabrication was carried out in a two-piece aluminium mould (male and female), lined with a thick polythene bag to prevent the greenware (fermented clay) from sticking to the walls of the mould during pressing. The fermented mixture was then placed into the female part of the mould and a pressure of 120 kPa was applied to the male mould, using a 50-ton hydraulic press. After pressing into shape, the ceramic filter was dried at room temperature until a constant weight was achieved. Pre-heating of the dried pots was carried out in a gas kiln for 3 h, to a temperature of 300 ^{o}C. This was followed by heating to a sintering temperature of 850 ^{o}C for 2 h. The sintered ceramics were then allowed to furnace cool in the gas kiln for two days to room temperature before the withdrawal.

3.12.8 Principle of operation of the ceramic filter

The filter was operated as a single-stage process for the removal of selected heavy metals, turbidity, pH, colour, BOD, COD, sulphate and phosphate. The pre-filtered wastewater was then poured into the pot and allowed to filter through the pores in the ceramic filter under gravitational force as shown in Plate VIII. The filtered water was collected in the receptacle with a tap underneath the filter pot as shown in Plate VIIId and analysed for heavy metal composition and other physicochemical parameters.

3.12.9 Testing of the assembled filter

A known volume of raw mining wastewater (6 L) was used for the testing of the assembled filter. The raw mining wastewater was passed through the filter and the outlet tap was controlled for the collection of the samples at 5 ml/min. The treated water samples were taken inside 100 ml sterile sample bottles at an interval of 20 min for the first 1 hr, and then at 1 h interval of operation. The testing was done continuously for 24 h to certify the long-term performance of the filter over several cycles.

Plate VIII: Pictorial representation of (a) Assembled filter for the wastewater treatment, (b) residue, (c) mining wastewater, and (d) treated mining water

The samples were thereafter taken for heavy metal analysis using the AAS and water quality parameters, to determine the reduction level of contaminants that may be present in the mining wastewater.

3.12.10 Post-evaluation of filter

To determine the structural and morphological changes on the filter after its use for mining wastewater treatment, the XRD, HRSEM/EDS, stability and reusability tests were carried out on the used filter.

Mechanical properties of filters

The mechanical properties of the filter such as Compressive strength, Flexural strength and tensile strength were determined to know the behaviour of the fabricated filter when subjected to different kinds of forces per unit area.

Compressive strength

The compressive strength of the sintered clay-Ag_2O-TiO_2 filter bar was determined by a compression machine (Shimadzu Autograph, model AG-25TB). The compressive strengths of the sintered clay mixtures were obtained by compressive loading (1 kN) of a cylindrical rod with height = 54 mm and diameter = 56 mm. The tensile tester works by gradually increasing the pressure on the sintered clay mixtures.

Flexural strength

The flexural strengths or moduli of rupture (MOR) of clay-Ag_2O-TiO_2 (composite) filter bars were obtained by the bend testing of bars of width (W) 48 mm, and breadth (B), 10.500 mm. Two types of specimens were made due to the anisotropic nature of the porous clay ceramics. The bend testing was done under three-point bend loading at a test speed of 2.50mm/min and a loading span of 140 mm. The MOR was then evaluated from the expression in Equation 3.43;

$$MOR = \frac{3PS}{2B^2W} \tag{3.43}$$

Where S is the loading span, P is the applied load at the onset of failure, B is the breadth of the sample and W is the width of the rectangular specimen.

Tensile Strength

A tensile machine using a sample length of 100.00 mm, a width of 20.00 mm and a thickness of 9.70 mm under bend loading at test speed 2.00 mm/min and preload of 0.100 N/mm^2 carried out the tensile strength of the ceramic filter. The tensile tester works by gradually increasing the pressure on the sintered clay mixtures. The press is operated by the string principle. The string has one end created by the tip, which is pressing on the sintered clay mixtures. The pressure is gradually and carefully increased until the filter bar composite shatters.

Chemical stability test of the re-used nanofilter

The chemical stability/resistance test of the re-used filter was carried out in acidic, neutral and basic solutions. This was done by inserting 10% of the weight of the filter bar per volume of solution, in an acidic and basic aqueous medium with known pH of 1, 2, 3, 4, 5, 6, 7, 8, 9, 10, 11 and 12 respectively for 48 h. The solutions were adjusted with an aqueous solution of 1M HCl or 1M NaOH as required (Nguiamba *et al.*, 2019). The chemical resistance was computed by Equation 3.44:

$$\%R_c = \frac{M_1 - M_2}{M_1} X100\% \quad (3.44)$$

Where; $\%R_c$ is the percentage of chemical resistance or mass loss,

$M_1$is the mass of the filter before immersion in acidic, neutral or basic solution,

M_2 is the mass of the filter after immersion in acidic, neutral or basic solution.

3.13 Mechanism of Flow Through the Filter

3.13.1 Water flow experiment

The NC7 was saturated for 12 hours before the water flow experiment, by completely submerging it in a big bowl of distilled water to remove internal air bubbles. Purified water flow rates were then measured using the NC7 as the most appropriate synthetic water. Measurement of the volume of water discharged from the NC7 as a function of time yielded the flow rates. To reduce the risk of contamination and mass loss due to evaporation, the flow monitoring device was encased in a plastic container. The water-saturated NC7 was filled with roughly 6.8 L of filtered water and covered with a plastic lid at the start of the experiment. Without adding any water, the water was allowed to drain passively from the filter that was being tested. After 1 h the volume of water collected was measured. This experiment was repeated; by filling the water to different heights in the filter, experimental values were obtained to determine/model the flow rate at different heights.

3.13.2 Modelling of flow through the ceramic filters

To characterise the flow of water through the filters due to gravity, an analytical hydrodynamic model was created by modifying the method of Yakub *et al.* (2013). Flow proceeded until the filter had emptied to the point in which there was insufficient pressure head to overcome the membrane/resistance in the filter.

The main variables are labelled in Figure 3.3 of the water filter design. Darcy's law, provided by Equation 3.46, was considered to govern flow through the porous filters.

$$Q = \frac{KA}{\mu L}\Delta P \qquad (3.45)$$

Where; Q = flow rate; κ = permeability of the filter; A = surface area; L = thickness of the material; μ = dynamic viscosity of the fluid; and ΔP = pressure difference from the top to the bottom of the surface.

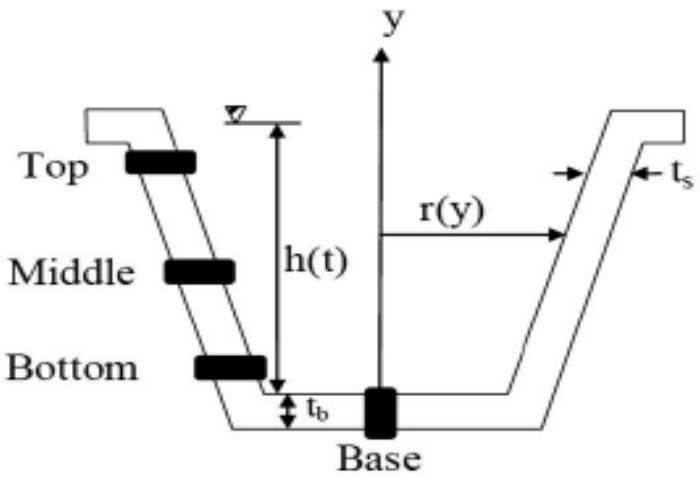

Figure 3.3: Schematic diagram of the filter showing key variables for modelling

The bottom and sides of the filter are considered individually (Qb and Qs, respectively) in this model, however, the corners are excluded. Because the flow is very slow, the pressure gradient between the surfaces is equal to the hydrostatic pressure of the water. As a result, a quasi-steady approach is adequate for the modelling. The change in pressure from the inside bottom surface to the outside bottom surface (the distance of porous medium through which the water flows) for flow through the bottom is equal to the fluid's hydrostatic pressure at the moment. Equation 3.46 provides this information.

$$\Delta P = \rho g h(t) \qquad (3.46)$$

Where; h(t) = height of water above the base of the filter at any given time; ρ = density of water; and g = acceleration due to gravity (9.8m/s^2). Additionally, the area at the bottom of the filter is given by;

$$A = \pi r_0^2 \tag{3.47}$$

Where r_0 is the radius of the base of the filter.

Equations 3.46 and 3.47 are substituted into Equation 3.45. As a result, the surface area on which the flow acts is the area at the bottom of the filter.

Permeable material has a thickness of L= t_b and permeability is assumed to remain constant. As a result, Equation 3.49 gives the flow rate through the bottom of the filter as:

$$Q_b = \frac{K\pi r_o^2 \rho g h(t)}{\mu t_b} \tag{3.48}$$

On the sides of the filter, the pressure is a function of the position y and is given by Equation 3.49;

$$\Delta P = \rho g(h(t) - y) \tag{3.49}$$

The area of the filter is also a function of y. The radius changes along with the filter height of the filter and is expressed as Equation 3.50.

$$r(y) = r_o + y tan\theta \tag{3.50}$$

Where θ is the angle of inclination between the base and the bottom of the filter.

The permeability coefficient is again considered to be constant and to be the same as on the bottom of the filter. Thus, Equation 3.51 gives the flow rate through the side of the filter.

$$Q_s = \int_0^{h(t)} \frac{K}{\mu} \frac{\pi \rho g(h(t)-y)}{t_s} 2(r_o + y tan\theta) dy \tag{3.51}$$

Integrating Equation 3.51 gives Equation 3.52 as;

$$Q_s = \frac{K}{\mu} \frac{\pi \rho g 2h^2(t)}{t_s} (\frac{r_o}{2} - \frac{h(t)}{3} tan\theta) \tag{3.52}$$

By adding Equations 3.48 and 3.52, the expression for the total mass flow rate is obtained as shown in Equation 3.53:

$$Q = \frac{K}{\mu}\pi\rho g h(t)(\frac{r_o^2}{t_b} + \frac{r_o h(t)}{t_s} - \frac{2h^2(t)}{3t_s} tan\theta) \quad (3.53)$$

Thus, an expression is derived for the flow rate through the NC_7 as a function of the height of water in the ceramic water filter. The values of h(t) were found from the following expression for the volume of water V(t), contained in the frustum-shaped fabricated water filter at any given time t as in Equation 3.54 and were compared with the experimental;

$$V(t) = \pi(R^2 h(t) + Rh(t)^2 \tan\Theta + \frac{h(t)^3 tan^2\theta}{2}) \quad (3.54)$$

The values of κ were used to fit Equation 3.53 to the experimental measurements of flow rate that were obtained using the methods described earlier.

3.13.3 Permeate flux

Permeate flux is one of the most critical parameters for evaluating membrane performance. Its evaluation is usually expressed as volume (or weight) per unit membrane area per unit of time. Permeate flux describes the quantity of the permeate produced during membrane separation per unit of time and membrane area. The flux is measured in volume per square meter per hour. It is a critical issue in the projection of scaling up from experience at the laboratory scale to pilot or industrial plants for a specific volume treatment requirement (Quezada *et al.*, 2021). Thus, it is a crucial task to forecast permeate flux in long-term operations. The permeate flux through the membrane was modelled by adopting the method of Álvarez *et al.* (2001). The permeate flux (J) is given by Equation 3.55:

$$J = \frac{M}{A_m \rho t} \quad (3.55)$$

Where M= permeate mass collected (L), A_m= membrane area (m^2),

t= permeation time (h), ρ =density of liquid.

Membrane separation performance was also assessed utilizing retention (also called rejection), given in Equation 3.56;

$$Retention\ (\%) = \left(1 - \frac{C_P}{C_F}\right) X100 \tag{3.56}$$

C_P = Concentration in the permeate

C_F= concentration in the feed.

3.13.4 Cake filtration

Cake filtration is the process in which the separation of particles from slurries or wastewater is effected using a medium, which is permeable to fluid flow but does not allow the passage of the particles in the wastewater. The particles retained at the surface of the medium form a cake, which separates unwanted particles from polluted water (Tien, 2006). This process is analysed using the volume-averaged continuity equation. In principle, the cake filtration analysis is carried out by satisfying several equations, including that of the Navier-Stokes equation for each point of the fluid and the equations of motion for each particle. Applying filtration's generalized volume-averaged equations given by Tien (2012) and expressed in Equation 3.57;

$$\rho_i \frac{\delta \varepsilon_i}{\delta t} = -\rho_i \nabla_i \varepsilon_i U_i + m_i \tag{3.57}$$

$$\rho_i \varepsilon_i \frac{D}{D_t} U_i = -S_i + W_i + F_{ji} \tag{3.58}$$

Where;

D/Dt = substantive derivative, the subscript (i) stands for fluid phase and S_i for particle phase. ε_i = the volume fraction of phase, U_i = mass-averaged velocity vector of phase i. S_i = force vector due to stress acting on phase i.

W_i= the body force vector acting on phase (i), F_{ji}=the interaction force vector in which phase j acts on phase i. $m_i$is the net mass transfer rate into phase i.

For one-dimensional cake filtration considered in this study;

$$\text{let } U_e = \frac{q_e}{\varepsilon} \text{ and } U_s = \frac{q_s}{\varepsilon_s} \tag{3.59}$$

U_e and U_s are the volume fractions of the void and particle phase, respectively (or porosity with $\varepsilon + \varepsilon_s = 1$).

q_e and q_s are defined as the superficial liquid and particle velocities. Equation 3.57 then becomes 3.60;

$$\frac{\delta \varepsilon}{\delta t} = -\frac{\delta q_e}{\delta x} \tag{3.60}$$

For 0<x<L(t), where L(t) is the cake thickness

$$\frac{\delta \varepsilon_s}{\delta t} = -\frac{\delta q_s}{\delta x} \tag{3.61}$$

From (3.61) and (3.62),

$$\frac{\delta (q_e + q_s)}{\delta x} = 0 \tag{3.62}$$

Where, $(q_e + q_s) = q_{em}$ and q_{em} is the instantaneous filtration velocity and is constant.

The schematic diagram of the filtration is given in Figure 3.4 and the section through the filter cake as Figure 3.5:

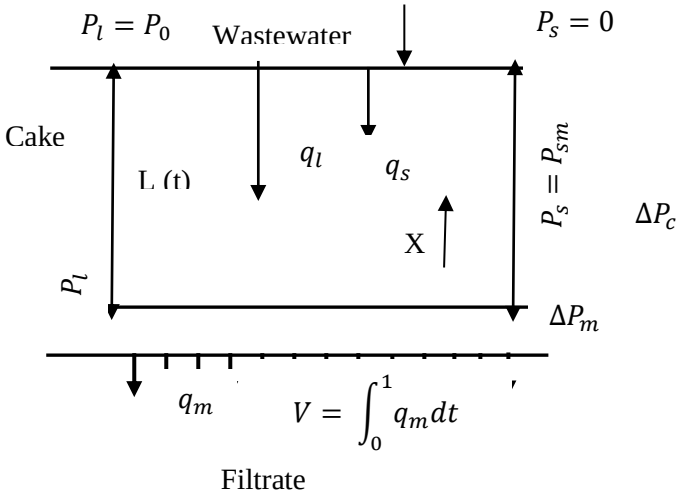

Figure 3.4: Schematic diagram of cake filtration

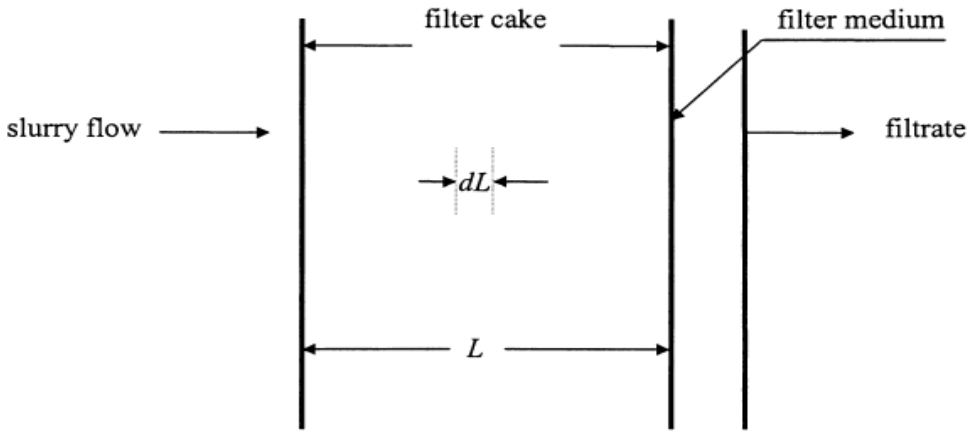

Figure 3.5: Section through the cake

The isotropic pressure terms, Pe and Ps, are the major ones of stress tensors in the one-dimensional cake filtering situation. Tien (2012), presents some of the most basic conceivable correlations between Pe and Ps, such as Equations 3.64 and 3.65;

$$\partial P_e - \partial P_s = 0 \tag{3.63}$$

$$(1 - \varepsilon_s)\partial P_e + \partial P_s = 0 \tag{3.64}$$

In the case of NC7 filter cake with $P_e = P_o$ at $x = L$, $P_e = \Delta P_m$ is the pressure drop across the medium. A general representation of the results given above is given in Equation 3.65;

$$\frac{\partial P_e}{\partial P_s} = f^1 \tag{3.65}$$

Where, f^1 can be -1 or -1/1-ε$_s$ or -ε$_s$/1-ε$_s$ or $\frac{(1-\varepsilon_s^o)P_o - P_s\partial\varepsilon_s}{(1-\varepsilon_s)^2\partial P_s} - \frac{\varepsilon_s}{1-\varepsilon_s}$

P_e at the downstream side of the medium is assumed zero**.**

As a result, Ergun's equation is used to model the velocity of flow through the filter cake, which is more generalized for pressure gradient and velocity of flow through the cake given as Equation 3.66;

$$U_c = \frac{1}{A}\frac{\partial v}{\partial t} = \frac{1}{5}\frac{e^3}{(1-e)^2} - \frac{\Delta P}{s^2\mu l} \tag{3.66}$$

Where;

A = Total cross-sectional area

S = specific surface of the particle (average particle size)

ΔP = change in applied pressure

For an incompressible cake, the resistance to flow is unaffected by the amount of pressure applied and the amount of voidage or voidage fraction is also consistent.

3.13.5 The liquid/particle relative velocity

The generalized Darcy's law expresses the liquid/particle relative velocity (q_{es}) for liquid flow through a medium undergoing compression, given as Equation 3.67 ;

$$\frac{q_{es}}{\varepsilon} = \frac{q_e}{\varepsilon} - \frac{q_s}{\varepsilon_s} = -\frac{1}{\varepsilon}\frac{K}{\mu}\frac{\partial P_e}{\partial x} \tag{3.67}$$

The equation (3.67) reduces to (3.68) when $q_s = 0$, at x = 0;

$$q_e + q_s = q_{em} = [-\frac{K}{\mu}\frac{\partial P_e}{\partial x}]_{x=o} = \frac{-P_{em}}{\mu R_m} \tag{3.68}$$

R_m=medium resistance (assumed to be 1)

P_{em}=filtrate pressure at x=0

The negative sign is to accounts for the fact that filtrate flows in the negative x-direction. Therefore, Equation 3.68 becomes ;

$$\frac{q_e}{\varepsilon} - \frac{q_{em} - q_e}{\varepsilon_s} = -\frac{1}{\varepsilon}\frac{K}{\mu}\frac{\partial P_e}{\partial x} \tag{3.69}$$

By re-arrangement and analysis, liquid/particle relative velocity becomes Equation 3.70;

$$q_e = -\varepsilon\frac{K}{\mu}\frac{\partial P_e}{\partial x} - (1 - \varepsilon_s)[\frac{K\partial P}{\partial x}]_{x=o} \tag{3.70}$$

3.13.6 Cake constitutive relationships

The filter cake constitutive relationship is the properties, which characterize the cake structure. These are; (i) cake solidosity ($-\varepsilon$), (ii) cake permeability (K), and (iii) specific cake resistance ($\propto$).

These three variables are inter-twined, analysed and assumed to be functions of the cake's compressive stress, which are expressed as Equation 3.71a:

$$\alpha = (K\varepsilon_s P_s)^{-1} \tag{3.71a}$$

Where P_s = cake compressive strength.

Specifically, the constitutive relationship may be expressed as ;

$$\varepsilon_s = \varepsilon_s(P_s) \tag{3.71b}$$

$$K = K(P_s) \tag{3.71c}$$

$$\alpha = K(P_{s)} \tag{3.71d}$$

Also, the following power-law expression may be used to represent the constitutive relationships of $\varepsilon_s vs\ P_s$, $K\ vs\ P_s$ and $\alpha\ vs\ P_s$ as;

$$\varepsilon_s = \varepsilon_s^o(1 + \frac{P_s}{P_A})^{\beta} \tag{3.71e}$$

$$K = K^o(1 + \frac{P_s}{P_A})^{-\delta} \tag{3.71f}$$

Therefore, the Equation 3.71a becomes 3.72

$$\alpha = \frac{1}{K\varepsilon_s P_s} = \frac{1}{\varepsilon_s^o K^o P_s}(1 + \frac{P_s}{P_A})^{\delta-\beta} = \alpha^o(1 + \frac{P_s}{P_A})^n \tag{3.72}$$

The symbols; $\varepsilon_s^o, K^o\ and\ \alpha^o$ denotes the $\varepsilon_s, K\ and\ \alpha$ values at zero-stress state (i.e P_s=0). P_A is the normalizing parameter of P_s and the exponents $\beta, \delta\ and\ n$ $(n = \delta - \beta)$ signify the compression effect due to P_s.

CHAPTER FOUR

4.0 RESULTS AND DISCUSSION

4.1 Beneficiation and characterisation of clay

Beneficiation of the clay was carried out to remove impurities and unwanted materials from the useable clay. The yield of the beneficiated clay was calculated using Equation 3.2 and the result of the clay beneficiation is presented in Table 4.1.

Table 4.1: Beneficiation result of raw kaolinite clay

Amount of raw clay (g)	Beneficiated clay Retrieved (Average, g)	Percentage yield (Y, %)
50	24.5	51±0.8
100	48	52±0.8
150	69	54±0.8
200	88	56±0.8
250	100	60±0.8
300	162	46±0.8

The number of each replicates minimum, n=5

According to Table 4.1, it was noticed that 50 g of raw clay produced only 24.5 g of beneficiated clay while 100 g of clay yields 48 g of beneficiated clay in 5 replicates (n = 5). This implies that there are substantial amounts of impurities/unwanted materials clogged together with clay in the clay's natural deposit which was removed during the beneficiation process. As the quantity of clay presented for beneficiation increase from 50 g to 300 g using the same volume of water, the amount of clay retrieved also increases. Also, the average yield per cent of the beneficiated clay (Equation 3.2) increased on progression from 51%, 52%, and 54% to 56% for 50, 100, 150, 200 and 250 g raw clay, but reduced at 300 g. The maximum yield of 60% purified clay was obtained with 250 g of beneficiated clay. This implies that interaction between clay and water up to 5% (w/w) of clay enhanced the optimum dispersion of clay in water to produce an optimum yield (60%) of beneficiated clay. This was due to the aggregation of clay particles and hence the settling of the clay particles as the clay content of the slurry increased.

The result suggests that the wet beneficiation process is suitable for obtaining a refined clay product with a selected particle size distribution of <2µm (from equation 3.1) and can be optimised using 5% w/w of clay and water. This result shows an improvement to Salahudeen *et al.* (2015), who obtained a 48% yield also with a wet beneficiation process though from a Kankara kaolin clay source (Salahudeen *et al.*, 2015). The difference may be attributed to location variation and the greater kaolin content of the clay used.

4.1.1 XRD analysis of clay

The beneficiated clay was treated with acid (activated), to improve its quality as described in section 3.2.2. The XRD pattern of (raw, beneficiated and acid-treated/activated clays) obtained are shown in Figure 4.1 a-c. From the figure, intense diffraction peaks were observed at 2Θ of 20.93º, 36.41º, 39.52º, 45.57º, 54.64º, 59.98º, 60.20º, 64.30º, 69.14º, 77.03º, 79.80º and 80.35º with the corresponding miller indices of (100), (110), (012), (021), (202), (211), (170) and (006) respectively.

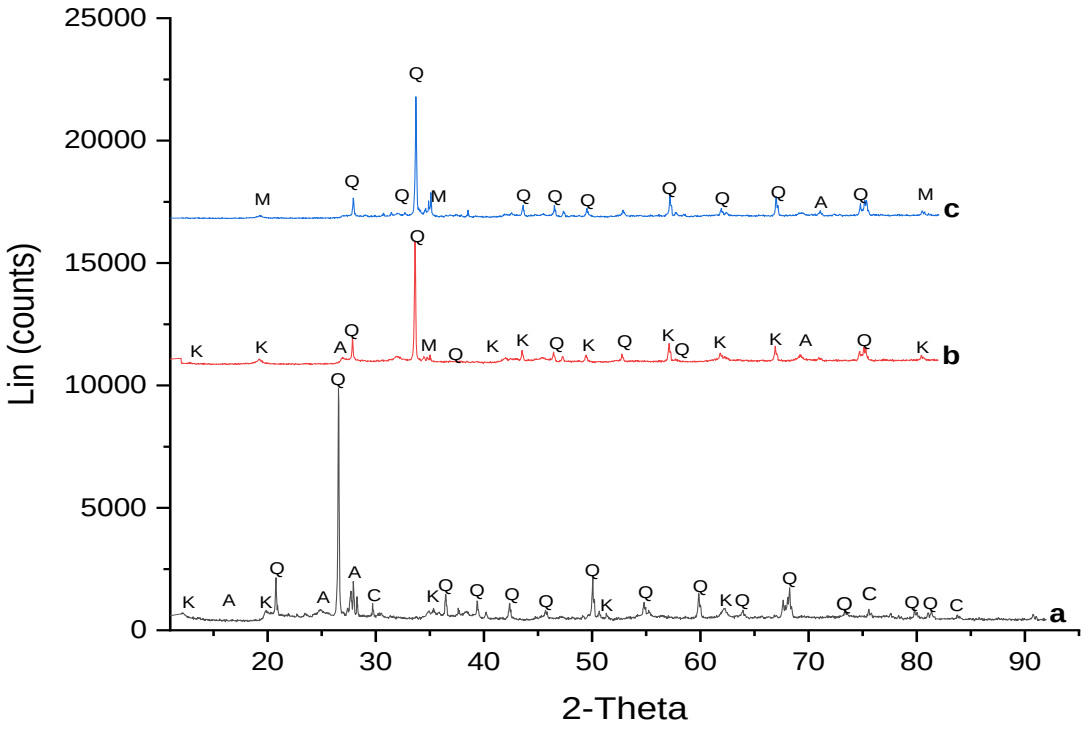

Figure 4.1: XRD spectra of clay (a) raw (b) beneficiated and (c) acid-activated clay

Keys: Q - Quartz, K – Kaolinite, A – Albite, C – Calcite, M – Microcline

These were indexed as quartz (SiO_2) with JCPDS number 083-0539. Few kaolinite clay peaks were observed at 2Ɵ angles of 35.86º (200), 36.67º (003), 51.42º, 62.34º (060) and 77.03 (170) respectively. A few low-intense peaks of Albite and Calcite were found to be present on the raw clay spectra (Figure 4.1a).

On the beneficiated clay (Figure 4.1b), several kaolinite peaks were observed, starting with a 2 theta value of 12.36º, which is characteristic of typical kaolinite clay. Other kaolinite peaks were found at 2Ɵ values of, 19.92º, 24.8º 35.91º, 38.4º, 62.34º, 66.81º, 69.24º and 80.46º which corresponds to the crystallographic orientations; (001), (020), (002), (-131), (-113) and (060) respectively with JCPDS number 01-079-1570. This further confirms that the clay is kaolinite in nature. XRD spectra of acid-activated clay show predominant phases of quartz peaks like that of the beneficiated clay. There was an absence of kaolinite clay on the activated clay (Figure 4.1c), this is linked to the acid activation, causing dehydration of the clay, and the eventual transformation of the kaolinite to other forms of clay. Increased Albite and Microcline peaks were observed in the acid-activated clay spectra as the new transformations but at very low percentages and intensities which may be linked to the acid activation process.

Other differences were observed in the intensity of the quartz peaks, as it was significantly increased in the activated clay compared to beneficiated and raw clay (Figure 4.1 a-c). Also, the crystallite sizes of the clay as calculated by the Debye-Scherer Equation were 16.65, 14.92 and 8.10 nm respectively. This shows that the beneficiation and acid activation treatment carried out on the clay imposed a reduction in the crystallite sizes of the kaolinite clay as treatment proceeded. Also, the reduction in crystallite size can be attributed to the removal of large particles, especially of impurities by the beneficiation process and the breaking down of large clay sizes by the acid activation process imposed on the clay.

Therefore, the obtained clay spectra showed predominant phases as kaolin and quartz, which is the common nature of kaolinite compositions and crystallite size reduction linked to impurities removal by beneficiation and acid treatment. Similar diffraction peaks on kaolinite clay were reported by Mustapha *et al.* (2019).

4.1.2 TGA/DTA analysis of the beneficiated clay

The thermogravimetric (TGA) and Differential Thermal Analysis (DTA) were conducted on the beneficiated clay, to examine the thermal stability and purity of the clay by observing the change in mass of the clay as a function of temperature and time. The TGA/DTA profile of the beneficiated clay sample is presented in Figure 4.2. Evidence of a single peak instead of multiple on the DTA curve (Figure 4.2B), implies purity and decomposition of the clay. A miniature decrease in weight of 3% was observed on the TGA (Figure 4.2A), between 50°C and 170°C linked to water loss from the clay surface. The TGA curve also showed that there is a 65% loss in weight of the clay at a temperature between 50°C and 270°C due to water loss and the burning of volatile and organic compost materials in the clay (Gu *et al.*, 2019).

Another decrease in weight of 3% was observed between the temperatures of 350°C and 400°C on the TGA, which may be due to the dehydroxylation of the clay into more reactive anhydrous amorphous clay as a result of exposure to increased temperature (El-Gaidoumi *et al.*, 2018). The DTA curve (Figure 4.2(B)), shows the presence of one major endothermic peak at T max = 274.8 °C, with a corresponding weight loss of 63%. At temperatures between 450°C and 950°C, the dehydroxylation phenomenon which involved the release of the OH group and transformation of clay into metakaolin occurred.

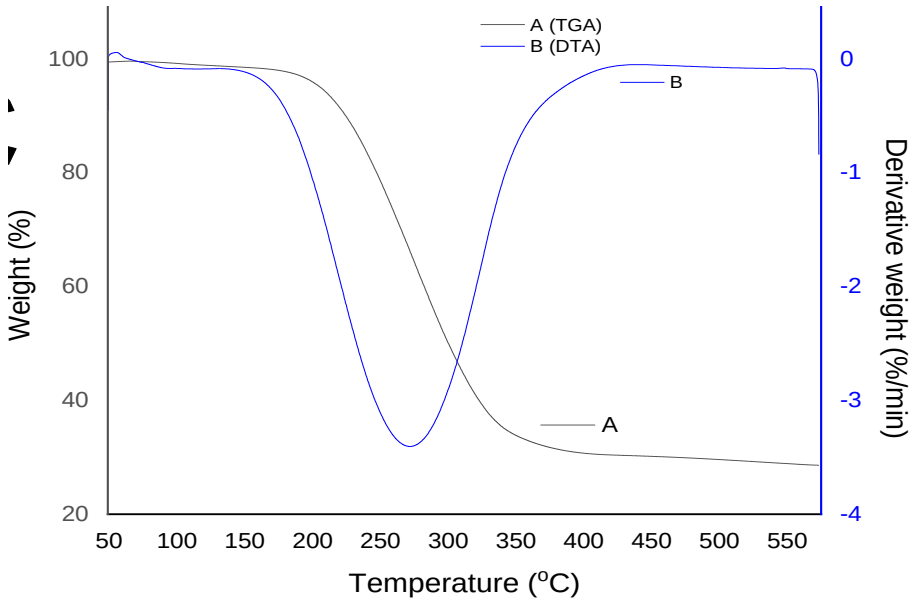

Figure 4.2: TGA/DTA of Beneficiated Local clay

A constant weight of 30 % was maintained over the range, this implies that, at elevated temperatures, the beneficiated clay is stable and can withstand high heat, cannot be easily degraded (Olaremu, 2015).

4.1.3 BET surface Area, Pore size and Pore volume of Beneficiated clay

The Brunauer- Emmet- Teller (BET) N_2 adsorption-desorption analysis was carried out on the beneficiated clay and the result is presented in Figure 4.3.

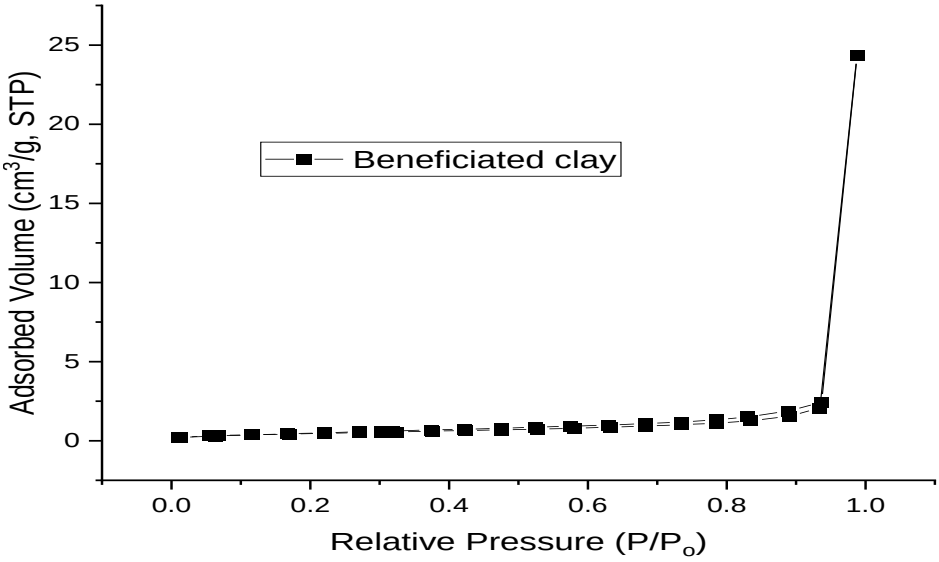

Figure 4.3: BET plot of Beneficiated clay

The result showed that the specific surface area of the clay was 13.942 m^2/g while the pore size and the pore volume were determined to be 2.955 nm and 0.016 cc/g respectively. The inert nitrogen gas adsorption-desorption isotherm of the beneficiated clay displays Type IV hysteresis isotherm. This result indicated that the beneficiated clay is mesoporous according to the IUPAC standard of pore classification (Sotomayor *et al.*, 2018). Therefore, from the clay's characterisation results, the clay is kaolinite in nature, can withstand heat and has a large surface area for effective deposition of nanoparticles and adsorption of pollutants.

4.2 Characterisation of Leaf

4.2.1 Phytochemical screening of plant leaves

The result of the phytochemical screening of the selected plant leaves is presented in Table 4.2. It was observed that all the six leaves (a) *Parkia biglobossa* L. (b) *Ageratum conizoides* L. (c) *Dactyloctenium aegyptum* L. (d) *Amaranthus spinosis* L. (e) *Setaria barbata* L. (f) *Sida carpinipolia* L. collected have considerable phytochemical contents of Phenols, Flavonoids and Tannins.

Table 4.2: Phytochemical analysis of leaves

Sample	Botanical name	English name	Tannin Content (mg/L)	Flavonoid Content (mg/L)	Phenolic Content (mg/L)
A	*Parkia biglobossa*	Locust leaf	0.85	10.39	1.91
B	*Ageratum conyzoides*	Billy goat weed	0.89	6.87	1.90
C	*Dactylotenium aegyptum*	Crowfoot grass	0.91	4.44	1.82
D	*Amaranthus spinosis*	Spiny amaranth	0.93	4.56	1.36
E	*Setaria barbata*	Bristly foxtail	0.92	4.71	1.74
F	*Sida carpinipolia*	Wire weed	0.97	3.69	1.31

The presence of the phenols, flavonoids and tannins in the six leaves is an indication of the fact that the six plants can be used for the synthesis of the nanoparticles. Studies have shown that these three phytochemicals' contents are in most cases responsible for the reduction of metals from their valence state to other states (Yusof *et al.*, 2018). This implies that the plant extract may behave similarly to commercial reducing agents such as citric acid, $NaBH_4$ and $LiAlH_4$ amongst others. Out of all the six leaves analysed, the locust leaf (*Parkia biglobosa*) was found to contain the highest quantity of phenolic content of 1.9095 mg/mL in contrast with other values as shown in the table. Noteworthy is that the phenolic and tannin contents have a great impact in acting as a reducing, capping and stabilizing agent for the reduction of metal salt precursors.

Parkia biglobosa leaf is therefore considered the most suitable out of the six leaves analysed for use. The confirmed phytochemicals present agree with the findings of Dedehou *et al.* (2016) and Yusof *et al.* (2018).

4.2.2 GC-MS analysis of *Parkia biglobosa* leaves

The GC-MS analysis of the *Parkia biglobosa* leaves is presented in Figure 4.4a.

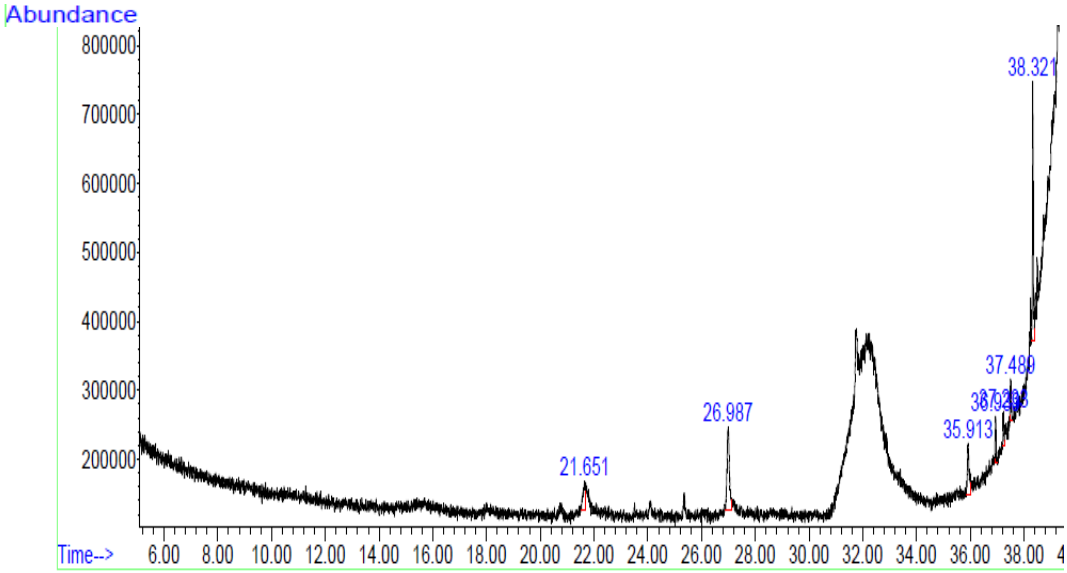

Figure 4.4a: GCMS spectra of *Parkia biglobosa* leaf

The figure reveals that the leaves are rich in phytol which is a phenolic group with peak areas of 38.32%. Other major chemical constituents identified are cyclodecasiloxane (peak area, 37.489), esters (peak area, 37.23%) and methyl palmitate (peak area, 36.94%). The cyclopentasiloxane was also identified at a peak area of 35.91%, and other siloxane compounds were observed at a peak area of 26.99%. The alkanoic acid/carboxylic acid group were observed at peaks area 26.99% and 21.65%, respectively. The presence of the aforementioned compounds in *Parkia biglobosa* leaf shows its potential as a reducing and capping agent in the syntheses of Ag_2O and TiO_2 nanoparticles (Zahir *et al.*, 2015a). This result confirms the presence of phytochemicals in *Parkia biglobosa* leaf as observed in Table 4.2. This corroborates other research works in the literature (Dedehou *et al.*, 2016; Sheeba and Viswanathan, 2014).

4.2.3 FTIR analysis of *Parkia biglobosa* leaf

The Fourier Transform Infrared (FTIR) spectra in Figure 4.4b shows different absorption peaks in the aqueous leaves extract of *Parkia biglobosa*, and the characteristic peak at 3417.98 cm^{-1} was assigned to O-H stretching vibration, a distinctive of phenol, an alcohol group (Yusof *et al.*, 2018). The peaks at 2862.46 cm^{-1} and 2746.73 cm^{-1} corresponds to H-C-H stretching vibrations of aldehydes and alkenes (Youssef *et al.*, 2015). The peaks noticed at 1728.28 cm^{-1} and 1627.97 cm^{-1} were attributed to C=O stretching vibrations of esters, ketones and aldehydes typical of methyl formate and acetones (Zahir *et al.*, 2015a). The absorption peaks noticed at 1373.36 cm^{-1} and 1327.07 cm^{-1} are assigned to the N=O bend of methylamine and nitromethane. The peak at 1026.16 cm^{-1} corresponds to C-O stretching vibrations of aromatics (Hari and Vandana, 2018). The peaks at 678.97 cm^{-1} represents =C-H bending vibration of diethyl ether.

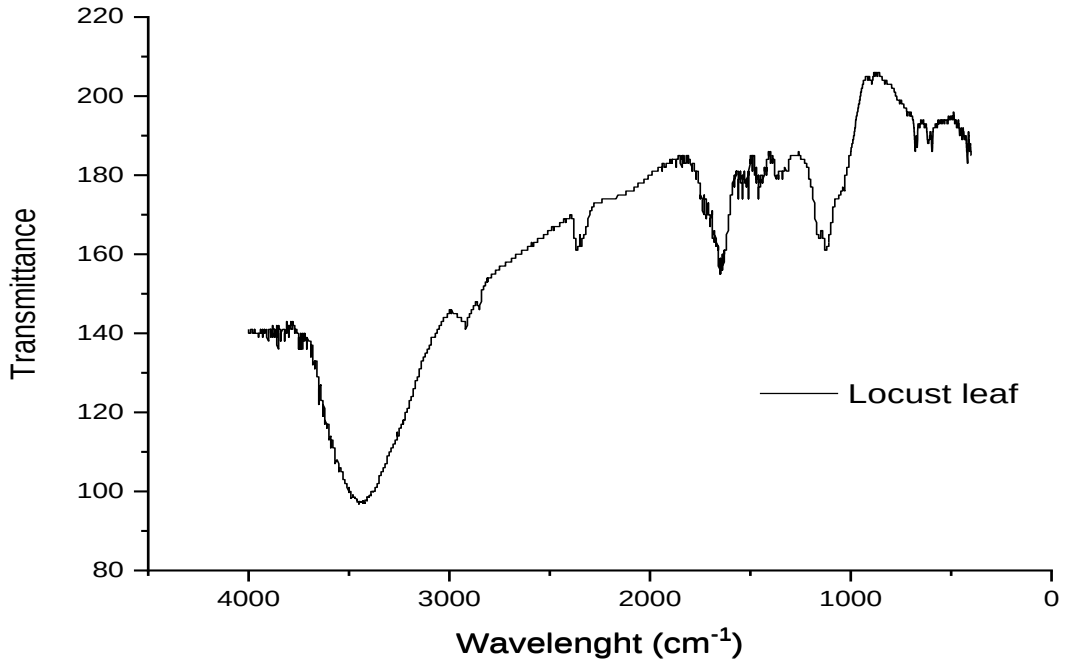

Figure 4.4b: FTIR Spectrum of *Parkia biglobosa* leaf

The shifting of several group peaks indicates that *Parkia biglobosa* has a high residue of alcohol (phenolic group), esters, and aldehydes (tannins and flavonoids). These can reduce metal salt precursors and stabilising nanoparticles similar to previous studies (Murali *et al.*, 2021; Shittu and Ihebunna, 2017a). The FTIR results further corroborate the results of phytochemical and GC-MS analyses.

4.3 Synthesis of Silver Oxide Nanoparticles (Ag_2O)

The effects of synthesis parameters (such as concentration of Ag salt precursor;1-12 mL, the volume of plant extract; 1-10 mL, solution pH; 2-12, and reaction temperature; 30-70ºC) on the nature of the synthesis of Ag_2O nanoparticles were examined, varying one parameter at a time. The UV-visible spectra shown in Figure 4.5 indicates a clear visible absorption peak in the wavelength in the range of 298- 450 nm evidence of strong surface plasmonic resonance of silver nanoparticles (Shittu and Ihebunna, 2017b). However, the formation of Ag_2O nanoparticles was found in the wavelength range of 406-450 nm (Dhand *et al.*, 2016).

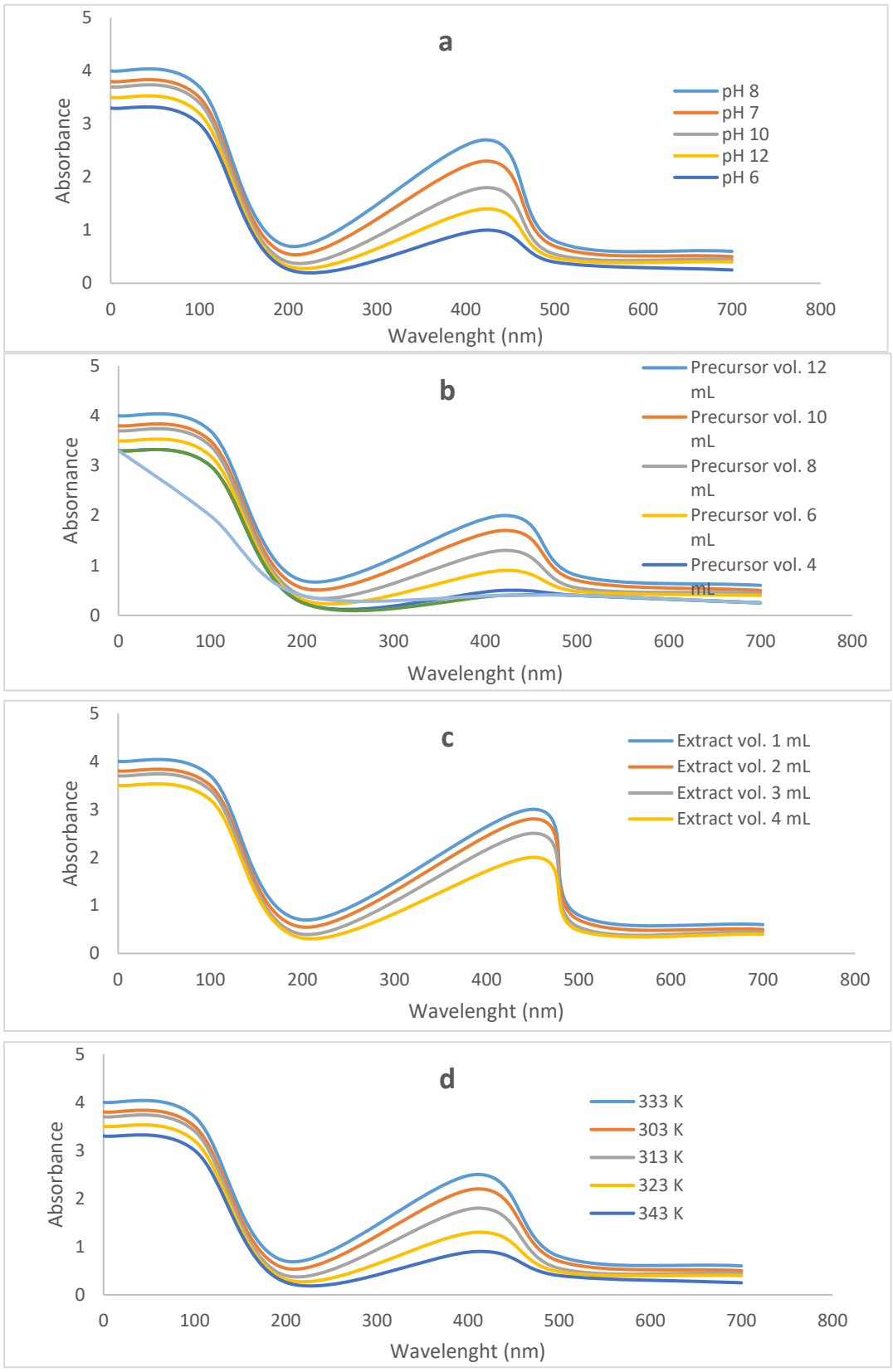

Figure 4.5: UV-Visible spectra of produced silver oxide nanoparticles based on effects of (a) pH (b) precursor volume (c) extract volume and (d) temperature

The highest wavelength of 450 nm among the other runs under investigation is similar to the result of Anju *et al.* (2018) who used *Caralluma umbellata* leaves extract for silver nanoparticle synthesis. The colour changes from yellow to brown were observed which indicates the formation of Ag_2O nanoparticles. The colour changes suggest the reduction of the Ag^+ salt complex in the mixture by the extract of *Parkia biglobossa* leaves (Ahmed *et al.*, 2016; Aritonang *et al.*, 2019; Banerjee *et al.*, 2014). The influence of various factors such as the solution pH, volume of precursor, volume of leaf extract and temperature on the formation of Ag_2O nanoparticles was investigated and the results obtained are as presented.

4.3.1 Effect of solution pH on the formation of Ag_2O nanoparticles

The effect of solution pH on the formation of Ag_2O nanoparticles was studied and the UV-visible spectrophotometer was used for the characterisation of the prepared samples. The result of the UV-Visible absorption spectra which revealed the formation of silver oxide nanoparticles is presented in Figure 4.5a. It was noticed that there was no formation of the silver oxide nanoparticles at acidic pH of 2 and 4 due to electrostatic repulsion between the Ag salt precursor and hydrogen ion. This corroborates the findings of Ndikau *et al.* (2017) who observed no formation of Ag_2O nanoparticles at pH < 5 and attributed the phenomenon to the non-stability of the nanoparticles at this pH. At the alkaline region, the formation of silver oxide nanoparticles was enhanced by the electrostatic attraction between the positive silver ions and the negative hydroxyl ions imposed by the alkaline pH on the reaction. Therefore, a pH between 6 and 8 best suited the synthesis of the Ag_2O nanoparticles. The chemical process is expressed, as shown in Equation 4.1:

$$2Ag^{+} + 2OH^{-} + Parkia\ b.complex \longrightarrow Ag_2O + H_2O + Parkia.b^{*} \quad (4.1)$$

This shows that solution pH plays a significant role in the formation and size of the Ag_2O nanoparticles (Ndikau *et al.*, 2017). The optimum absorbance wavelength of the synthesised Ag_2O nanoparticle was obtained at a pH of 8 with the formation of only one peak at 422 nm wavelength, an indication of a single-phase component. The peak also falls within this range for the synthesis of Ag_2O nanoparticles using plant extract as observed by Shittu and Ihebunna (2017a).

4.3.2 Effect of precursor volume on Ag_2O nanoparticles formation

The result of the effect of the volume of precursor on the synthesis of silver oxide nanoparticles using the leaves extract of *Parkia biglobossa* is presented in Figure 4.5b. The volume of aqueous $AgNO_3$ was varied between 1 and 12 cm^3 with constant leaves extract of 1 cm^3. The UV-Visible result shows a variation in the wavelength values for the different precursor volumes used. The values obtained when 1, 2 and 4 cm^3 were used (286, 362 and 390 nm) did not agree with the wavelength of silver oxide nanoparticles formation (were no shown as peaks on the spectral). The peaks at 362 and 398 nm as shown in Figure 4.5b may be due to quadrupole plasmon resonance corresponding to silver transition (Ravichandran *et al.*, 2016b). This shows that the absorbance wavelength is affected by precursor concentration. Lower precursor volume of 1 cm^3 to leaf extract of 1 cm^3 may have caused agglomeration of ionic silver due to excess reducing agent in leaves extract being made available, thus lower absorption wavelength (Gontijo *et al.*, 2020).

On the other hand, when a precursor volume of 6 cm^3 and leaves extract volume of 1 cm^3 were used, a shift in the absorption band to the wavelength of 400 nm was observed, which corresponds to the range for silver oxide nanoparticle formation. When 8, 10 and 12 cm^3 of Ag salt precursor was used, absorption peaks were noticed at the following wavelengths of 408, 426 and 408 nm respectively. This makes the obtained results at 8 cm^3 and 12 cm^3 comparable, with a preference for the lower. The precursor volume between 6 and 10 cm^3 was therefore preferred, being the optimum for the synthesis of the silver oxide nanoparticle because of the higher wavelength value. This is comparable with the results of Jalees *et al.* (2018), who obtained a wavelength value of 435 nm for silver oxide nanoparticles using the extract of mango peels and Belaiche *et al.* (2021) who also obtained a wavelength value of 435 nm for silver oxide nanoparticles in the research using the extract of *Artemisia Herba-Alba*, although excess precursor volume was used.

4.3.3 Effect of leaf extract volume on Ag_2O nanoparticles formation

The variation of volume of *Parkia biglobossa* leaves extract at a constant volume of Ag salt precursor produced Ag_2O nanoparticles with absorption peaks at different wavelengths as shown in Figure 4.5c. When the volume of the leaves extract was 1 cm^3, the absorption peak in the UV spectrum was noticed at wavelength 416 nm and an increase in the wavelength value to 421 nm was observed when the volume of extract was increased to 2 cm^3. The use of 3 cm^3 gave a wavelength of 450 nm while, the extract volume of 4 cm^3 gave a sharp rise up to 452 nm comprising other peaks and noise, which indicates the presence of other impurities and large-sized Ag_2O synthesis according to Mie's theory (Baset *et al.*, 2011). When the volume of the leaves extract was increased to 6 cm^3, 8 cm^3 and 10 cm^3, absorption peaks in the following wavelength (396 nm, 362 nm and 286 nm) were observed.

This shows a reduction in the wavelength as compared to the other reaction mixtures, signifying incomplete formation and absence (286 nm) of silver oxide nanoparticle synthesis. Therefore, a 1 - 3 cm^3 extract volume was considered suitable for the synthesis of the silver oxide nanoparticles.

4.3.4 Effect of reaction temperature on the formation of Ag_2O nanoparticles

The result of the influence of reaction temperature on the formation of Ag_2O nanoparticles represented in Figure 4.5d indicates that silver oxide formation was feasible at all reaction temperatures used. This is because there were no significant differences in the value of wavelength obtained at all temperatures (30ºC, wavelength of 416 nm), (40ºC, 410 nm), (50ºC, 410 nm), (60ºC, 417 nm), (70ºC, 411 nm). Several authors have successfully synthesised Ag_2O at different temperatures for instance, at 25ºC (Manikandan *et al.*, 2017), 40ºC (Khatun *et al.*, 2015) 65ºC (Shittu and Ihebunna, 2017b) and 90ºC (Liu, 2020). The result shows that the synthesis of Ag_2O nanoparticles may not necessarily depend on the reaction temperature. These results suggest that the synthesis of silver oxide nanoparticles is feasible at 60ºC temperature but enhanced by other synthesis parameters like the nature and volume of the leaf extract.

4.3.5 Optimisation study of silver oxide nanoparticle synthesis

It is worthy of note that, the conventional optimisation of varying one parameter and keeping other constants did not guarantee the synthesis of Ag_2O nanoparticles of desired sizes and morphology. This method also fails to establish the interactive effects among the synthesis variables. The response surface methodology based on the factorial design was employed to optimise the synthesis of silver oxide nanoparticles. A 2^4! equation of the design expert was used to fit the experimental data with the general equation as shown in Equation 4.2:

$$Y = \beta_0 + \beta_1 * x_1 + \beta_2 * x_2 + \beta_3 * x_3 + \beta_4 * x_4 + \beta_{12} * x_1x_2 + \beta_{13} * x_1x_3 + \beta_{14} * x_1x_4 + \beta_{23} * x_2x_3 + \beta_{24} * x_2x_4 + \beta_{34} * x_3x_4 + \beta_{123} * x_1x_2x_3 + \beta_{234} * x_2x_3x_4 + \beta_{1234} * x_1x_2x_3x_4 \quad (4.2)$$

Where;

β_0 is the value of the intercept,

$\beta_1, \beta_2, \beta_3, and\ \beta_4$ are the coefficients for the main effects of variables,

$x_1, x_2, x_3\ and\ x_4$ are the variables,

$\beta_{12}, \beta_{13}, \beta_{14}, \beta_{23}, \beta_{24}, and\ \beta_{34}$ are the coefficients for interactions between two variables,

$x_{12}, x_{13}, x_{14}, x_{23}, x_{24,}\ and\ x_{34}$ are the interactions between two variables,

β_{123}, β_{134} and β_{234} are the coefficient for interaction among the three variables,

$x_{123}, x_{134}, and\ x_{234}$ are the interaction among the three variables,

β_{1234} is the coefficient for interaction among the four variables, and

x_{1234} is the interaction among the four variables.

The equation is a semi-empirical relationship obtained by fitting the experimental data to give a solution equation. The 2^4 factorial design of the design expert generated 16 experimental runs, which were used to synthesise the Ag_2O nanoparticles and wavelength was used as the response. Table 4.3 shows the actual and predicted wavelengths with their respective experimental matrix from the design expert. Worthy of note is that the best plasmon resonance wavelength for Ag_2O nanoparticle formation is in the range of ~350 nm to 550 nm (Mahmood *et al.*, 2021). However, the closer the plasmon resonance wavelength to 450 nm, the smaller the particle size of Ag_2O nanoparticles formation as was reported by Ndikau *et al.* (2017). The experimental run 1, as shown in Table 4.3 gave wavelengths of 397 nm and 400.94 nm as plasmon resonance for Ag_2O nanoparticle formation, for actual and predicted values respectively.

Table 4.3: 2^4 factorial design for the synthesis of Ag_2O nanoparticles

Exp. Run	Precursor volume (cm^3)	Extract volume (cm^3)	pH	Temperature (^oC)	Actual wavelength (nm)	Predicted wavelength (nm)
1	10	1	6	60	397	400.94
2	10	1	8	60	450	445.44
3	7	1	8	60	410	414.19
4	7	3	6	60	250	255.94
5	10	3	8	30	408	410.69
6	7	1	8	30	421	426.44
7	10	3	8	60	392	398.94
8	7	1	6	60	402	398.44
9	10	1	8	30	416	410.94
10	7	3	8	60	243	236.44
11	10	3	6	60	396	389.69
12	10	1	6	30	350	355.69
13	7	3	6	30	300	303.69
14	7	1	6	30	406	399.94
15	7	3	8	30	298	294.94
16	10	3	6	30	394	390.69

Whereas, experimental run 2 under different operating conditions compared to experimental run 1 (Table 4.3) gave 450 nm (actual) and 445 nm (predicted). This showed that a pH of 8 favoured the Ag_2O synthesis of smaller nanoparticles compared to a pH of 6 (run 1). As run 2 has a wavelength of 450 nm, which is very high and similar to the literature where *Ocimum basilicum* was used for the silver oxide nanoparticle synthesis (Jayapriya and Lalitha, 2013). Comparatively, run 1 and run 2 revealed that the pH of the medium has a significant effect on nanoparticle synthesis.

The pH of 6 (run 1) which is an acidic medium, gave a plasmon resonance wavelength of 397 nm, resulting in the formation of silver nanoparticles rather than silver oxide nanoparticles formed at a pH of 8 (basic medium, run 2) at 450 nm wavelength when other operating conditions remained constant. This could be because of pH on the dissociation, agglomeration, isolation, interfacial free energy and net charge of a complexing agent as reported by Traiwatcharanon *et al.* (2017).

In the acidic medium of 6, there is a higher driving force for Ag_2O dissolution that balances the repulsive force to maintain the dispersion of the Ag_2O nanoparticles, resulting in smaller particle sizes of AgNps. While in the basic medium, sodium hydroxide dissociates in water to produce the negatively charged hydroxide ions (OH^-). The negative ions enhance the complete reduction of $Ag(OH)_2$ into Ag_2O nanoparticles. Therefore, at a higher ion density, Ag_2O nanoparticles tend to diffuse between adjacent adsorption sites on a surface and form bonds with nearest neighbour atoms via Brownian diffusion (Thilagavathi *et al.,* 2016). This is due to the high surface energy and thermodynamic instability of the nanoparticle surfaces, leading to the formation of Ag_2O nanoparticles formed at alkaline pH of 8.

Also, experimental runs 2 and 3 as shown in Table 4.3 presented that the precursor volume of 10 cm^3 and 7 cm^3 gave plasmon resonance wavelengths of 450 nm and 410 nm, respectively, when other operating conditions remained constant. This revealed that the precursor volume of 10 cm^3 favoured the Ag_2O nanoparticle synthesis better than AgNps, as the more the precursor volume, the larger the nanoparticle size formed. Experimental runs 5 and 7 showed the effect of temperatures of 30°C and 60°C on the Ag_2O nanoparticle synthesis, respectively, while other operating conditions remained constant. The different temperatures of 30°C and 60°C gave plasmon resonance wavelengths of 408 nm and 392 nm, respectively.

This revealed that the Ag_2O nanoparticles synthesis is affected by temperature change. Therefore, according to Stavinskaya *et al.* (2019), the reduction of $AgNO_3$ to Ag_2O nanoparticles is only slightly affected by the temperature of the process. Also, experimental runs 3 and 10 revealed that the leaves extract volume of 1 cm^3 and 3 cm^3 gave plasmon resonance wavelengths of 410 nm and 243 nm respectively, while other operating conditions remained constant.

Similar results were obtained for experimental runs 13 and 14 with the leaves extract volume of 3 cm^3 and 1 cm^3 given plasmon resonance wavelengths of 300 nm and 406 nm. This indicated that the extract volume of 1 cm^3 supported the nanoparticle formation of Ag_2O. As more leaves extract volume beyond 1 cm^3 can cause aggregation and agglomeration of the produced nanoparticles (El-Rafie *et al.*, 2014). Therefore, the optimal operating conditions for the synthesis of Ag_2O nanoparticles could be observed as 10 cm^3 precursor volume, 1 cm^3 of plant extract, solution pH of 8 and reaction temperature of 60°C, to give 450 nm plasmon resonance wavelength as shown in run 2 in Table 4.3. However, model and statistical analyses are required to support these findings.

Model fitting

Equation 4.3 is the coded solution to determine the significance of the parameters on the response (wavelength, nm).

$$Wavelenght\ (nm) = +370.81 + 29.56 * A - 35.69 * B + 8.94 * C - 3.31 * D + 32.81 * AB + 7.19 * AC + 11.69 * AD - 8.81 * BC - 11.56 * BD - 2.69 * CD \quad (4.3)$$

The coded parameters in the equation were used to make predictions about the response for given levels of each parameter where +1 was taken as the high levels and -1 as the low levels of the parameter. The coded equation is useful to identify the impact of the synthesis parameters by comparing the factor coefficients.

Equation 4.4 is the actual solution of the model to predict response in terms of wavelength (nm) for given levels of each variable. The equation shows the levels with specified original units for each parameter and cannot be used to determine the relative impact of each parameter as the coefficients are scaled to accommodate the units. The equations, therefore, consist of ten statistically significant variables, indicating that the individual effects of variables are sufficient to explain the wavelength of the Ag_2O nanoparticles.

$$Wavelenght\ (nm) = +828.52 - 80.96 * Precursor\ volume\ (cm^3) - 125.25 * Extract\ volume\ (cm^3) - 6.10 * pH - 1.84 * Temperature\ (℃) + 21.88 * Precursor\ volume\ (cm^3) * Extract\ volume\ (cm^3) + 4.79 * Precursor\ volume\ (cm^3) * pH + 0.52 * Precursor\ volume\ (cm^3) * Temperature\ (℃) - 8.81 * Extract\ volume\ (cm^3) * pH - 0.77 * Extract\ volume\ (cm^3) * Temperature\ (℃) - 0.18 * pH * Temperature\ (℃) \quad (4.4)$$

Equations 4.3 and 4.4 exhibit ten statistically significant terms and include linear terms (A, B, C and D,) and quadratic terms (AB, AC, AD, BC, BD and CD). The linear and quadratic terms contributed to the low wavelength of Ag_2O nanoparticles obtained. The model was justified by plotting the experimental data versus the predicted values as shown in Figure 4.6.

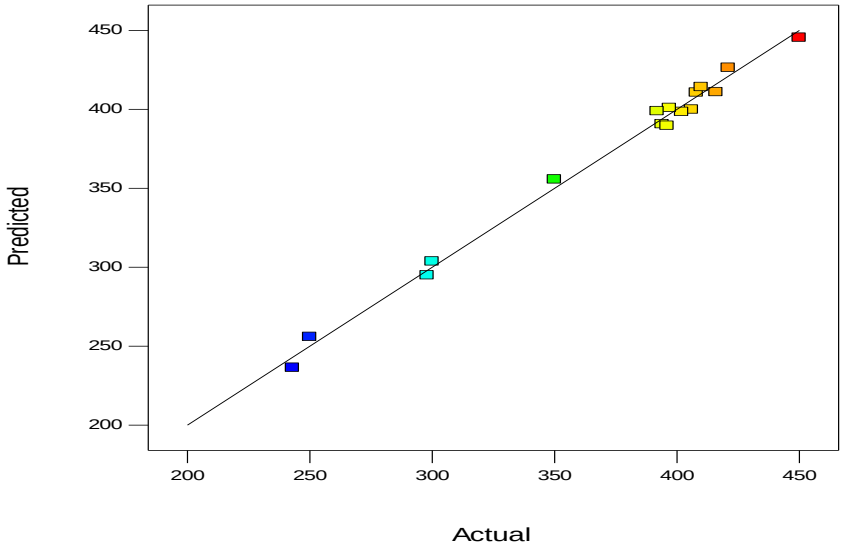

Figure 4.6: Plots of experimental versus predicted wavelength (nm)

The figure shows a regression coefficient of 0.993, an indication of a good correlation between the experimental and predicted values. To validate the model's performance, an analysis of variance was carried out to test the significance and adequacy of the model.

Analysis of variance (ANOVA) for Ag_2O nanoparticle synthesis

Table 4.4 is the ANOVA of the model used to analyse the effects of synthesis parameters on the wavelength (nm) of Ag_2O nanoparticles.

Table 4.4: ANOVA of factorial model for the wavelength (nm) of Ag_2O nanoparticles

Source	Sum of Squares	Df	Mean Square	F-Value	p-value Prob > F
Model	59550.13	10	5955.01	74.75	< 0.0001
A-Precursor volume (cm^3)	13983.06	1	13983.06	175.53	< 0.0001
B-Extract volume (cm^3)	20377.56	1	20377.56	255.80	< 0.0001
C-pH	1278.06	1	1278.06	16.04	0.0103
D-Temperature (^oC)	175.56	1	175.56	2.20	0.1978
AB	17226.56	1	17226.56	216.24	< 0.0001
AC	826.56	1	826.56	10.38	0.0234
AD	2185.56	1	2185.56	27.44	0.0034
BC	1242.56	1	1242.56	15.60	0.0109
BD	2139.06	1	2139.06	26.85	0.0035
CD	115.56	1	115.56	1.45	0.2823
Residual	398.31	5	79.66		
Cor Total	59948.44	15			
R^2 = 0.993	**Adjusted R^2 = 0.980**				
C.V. % = 2.41	**Predicted R^2 = 0.932**				

The Model F-value of 74.75 confidence interval implies a good fit of the model. The *p*-value (Prob. > F) less than 0.0500 indicates that the model terms are significant. From this study, A, B, C, AB, AC, AD, BC, and BD are significant model terms. However, the *p*-values greater than 0.1000 indicate insignificant terms D and CD. The Predicted R^2 of 0.9320 is in reasonable agreement with the Adjusted R^2 of 0.9801, hence, the model is acceptable for the prediction of the synthesis procedure.

Interactive effects of the combined variables

Figures 4.7(a-f) show the 3D plots of the combined effects of various parameters on the wavelength of Ag_2O nanoparticles developed. The "flag" (indicator) displayed on the top corner of each figure represents the point of attaining the best wavelength for Ag_2O nanoparticle synthesises. The optimum wavelength of 450 nm obtained is comparable with 430 nm reported by El-Ghmari *et al.* (2021) who employed aqueous leaves extract of *Herniaria hirsuta*. The wavelength of 440 nm reported by Mukul *et al.* (2022) who employed *Solanum Elaeagnifolium* leaves extract to prepare Ag_2O nanoparticles also compared well with the findings in this study.

Figure 4.7a shows the optimum wavelength at an $AgNO_3$ precursor volume of 10 cm^3 and plant extract volume of 1 cm^3, an indication that high precursor volume with the decrease in extract volume improved the formation of Ag_2O nanoparticles. Therefore, the lower extract volume of 1cm^3 used in this study was adequate to provide enough nucleation sites which allows the desired reduction to take place (Ndikau *et al.*, 2017).

Figure 4.7b presents interactive effects of the volume of $AgNO_3$ salt precursor and solution pH, respectively. The result obtained showed a favourable response at pH 8 (445 nm), compared to pH 6 (402 nm) which further points to the availability of a higher driving force for Ag_2O dissolution that balances the repulsive force to maintain the dispersion of the Ag_2O nanoparticles, resulting in smaller particle size. Also, the increase in pH to 8 may result in the homogeneity or regularity of the Ag_2O nanoparticles. This led to increase absorption, reduction of transmittance and formation of the desired Ag_2O nanoparticles and not AgNps observed at increased pH of 8, which compared favourably with the literature value (Aziz and Jassim, 2018). However, Traiwatcharanon *et al.* (2017) obtained Ag_2O nanoparticles at a pH of 6 which is different from the present study.

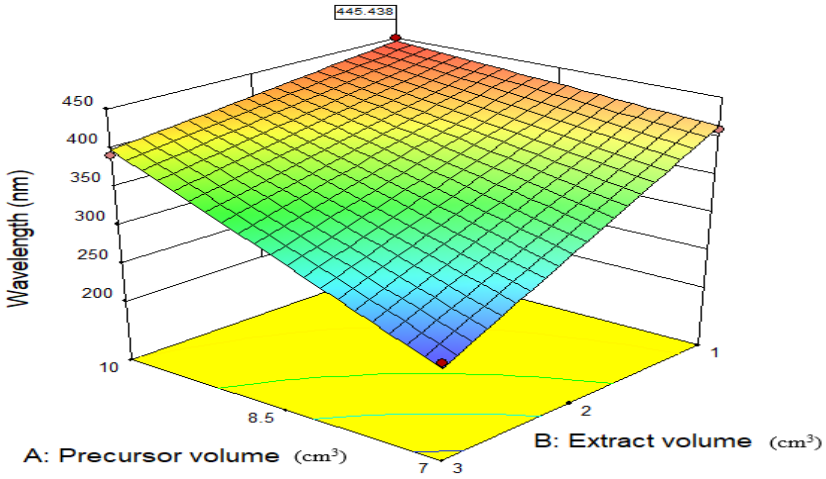

Figure 4.7a: 3D plot of A and B versus wavelength of Ag_2O at constant C of 8 and D of 60°C

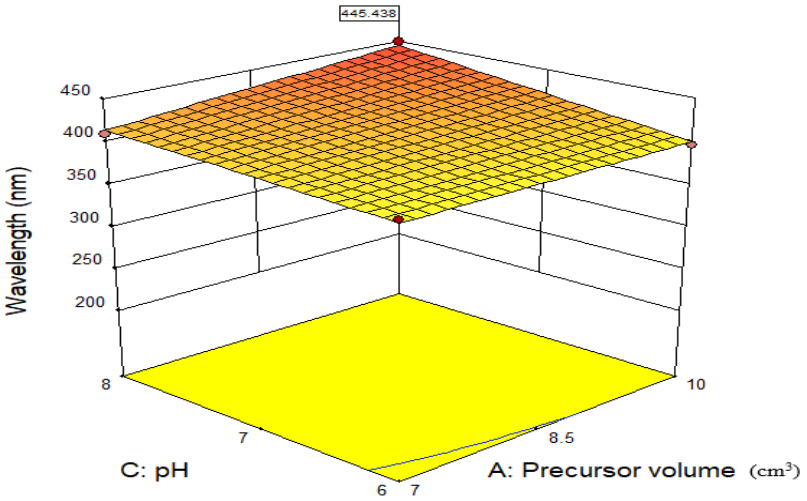

Figure 4.7b: 3D plot of A and C versus wavelength of Ag_2O Nps at B of 1.02 cm^3 and D of 60°C

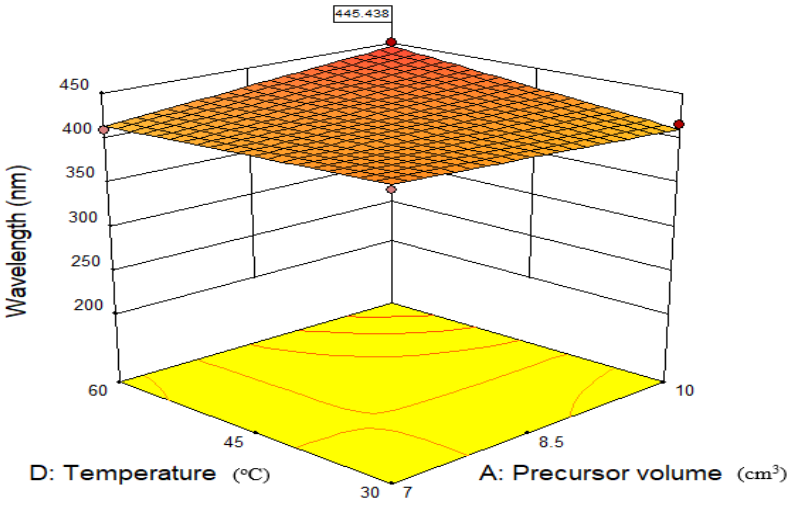

Figure 4.7c: 3D plot of A and D versus wavelength of Ag_2O Nps at constant B of 1 cm^3 and C of 8

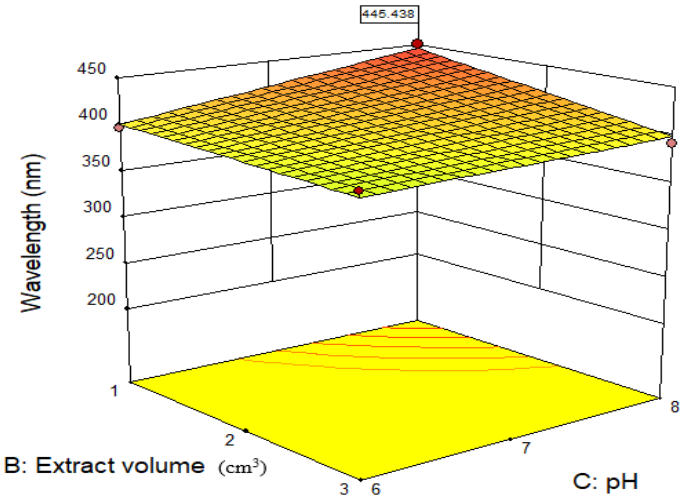

Figure 4.7d: 3D plot of B and C versus wavelength of Ag_2O Nps at constant A of 10 cm^3 and D of 60ºC

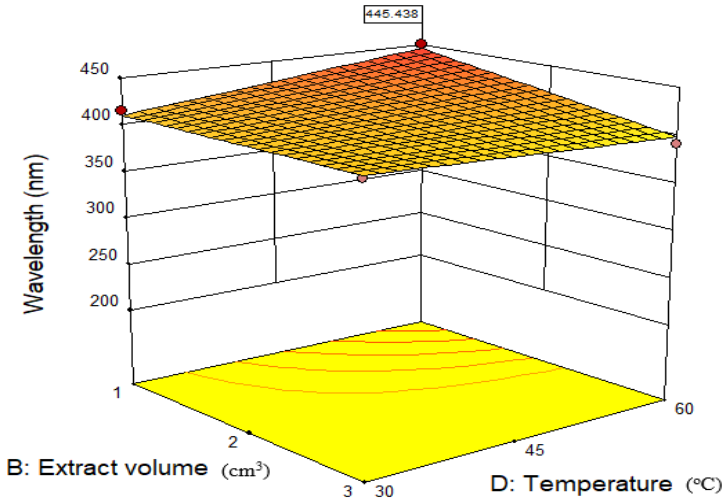

Figure 4.7e: 3D plot of B and D versus wavelength of Ag_2O Nps at constant A of 10 cm^3 and C of 8

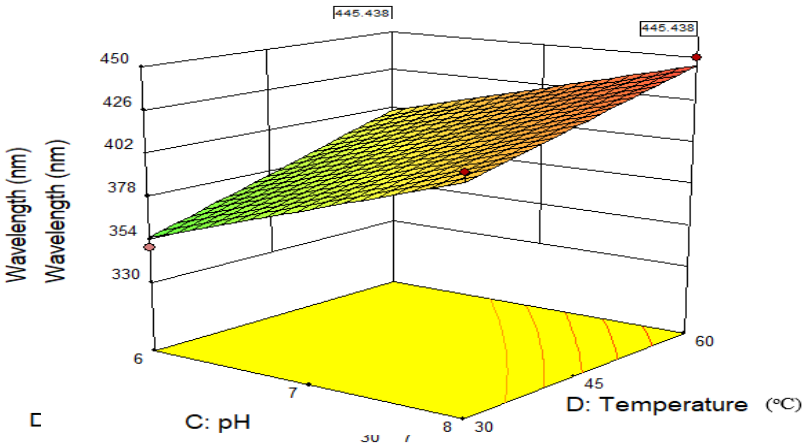

Figure 4.7f: 3D plot of C and D versus wavelength of Ag_2O Nps at constant A of 10 cm^3 and B of 1 cm^3

This difference in the optimum pH may be linked to the different leaf extract, different phytochemical constituents used and probably precursor volume considered. Figure 4.7c shows the combined effects of silver salt precursor volume and reaction temperature on the wavelength of Ag_2O nanoparticles synthesised. According to Figure 4.7c, the highest temperature of 60^oC and precursor volume of 10 cm^3 yielded a maximum wavelength of 450 nm. Similar trends were observed by Karunakaran *et al.* (2016) where an extract of *Nitrobacter sp.* extract was used to prepare Ag_2O and obtained a wavelength of 450 nm. This is because, at the high reaction temperature, the rate of reaction between the Ag^+ ions and OH^- ions in the solution was very fast, leading to the formation of $Ag(OH)_2$ that eventually yield Ag_2O nanoparticles.

Therefore, irrespective of temperature above room temperature, Ag^+ precursors nucleated and can form crystal nuclei faster to form Ag_2O, provided there is sufficient precursor volume at that temperature (Liu *et al.*, 2020). Figure 4.7d presents the interactive effects of extract volume and pH on the wavelength. The result reveals that 1 cm^3 extract volume and pH of 8 respectively, was enough to obtain a wavelength of 450 nm. The increase in pH indicates decreases in the bulk concentration of H^+ ions and results in a higher surface charge on the particle. Not only that, protonation and deprotonation surface reactions are responsible for the local surface charge that enhanced small-sized Ag_2O particle formation. The high pH activates many phenolic functional groups for Ag binding, leading to a higher number of Ag^+ ions in reaction, and resulting in a large number of nanoparticles formed with large particle diameters, while the basic pH activates the driving force for Ag_2O dissolution that balances the repulsive force to maintain the dispersion of the Ag_2O nanoparticles, and eventually resulted in Ag_2O particles formation (Ndikau *et al.*, 2017).

Figure 4.7e shows the combined effect of extract volume and reaction temperature on the wavelength of Ag_2O nanoparticles synthesised and reveals that the extract volume of 1 cm^3 and temperature of 60^oC yielded 450 nm of wavelength. This reaction temperature (60^oC) was sufficient to extract phenols from the smaller volume (1 cm^3) of the leaf extract used, coupled with interaction in a basic medium within a short time interval. Moreover, this reaction rate was faster and favoured by increasing the temperature, due to the effective collision between the phytochemical particles and the silver precursor solution leading to the formation of the Ag_2O nanoparticles.

Figure 4.7f presents the interactive effects of pH and temperature on the wavelength of Ag_2O nanoparticles developed. The figure shows an optimum wavelength of 450 nm at a pH of 8 and a temperature of 60^oC. This is because, at high pH, more hydroxyl ions were reacting with the ions in the solution. The rate of collision, nucleation and growth of Ag_2O is therefore enhanced at a slightly basic pH and high temperature, which may have promoted the formation of small particle-sized Ag_2O nanoparticles (Darroudi *et al.*, 2010).

Model optimisation and validation

The estimated coefficients obtained from the synthesis of Ag_2O nanoparticles using a design expert are shown in Table 4.5. It was noticed that the optimisation of synthesis variables with wavelength as response as predicted was at 95% CI (confidence interval) on low and high. This is put at a 95% level which means that 95 out of 100 is the true value of the parameter. The analysis concludes that optimal parameters of precursor volume (10 cm^3), extract volume (1 cm^3) pH (8), and temperature (60^oC), are based on the predicted wavelength of 445 nm. The validation test of the predicted optimal parameters was carried out to determine the actual value of wavelength which is 450 nm determined by the response.

Table 4.5: Estimated coefficient of the model and variables for the wavelength of Ag_2O nanoparticles formation

Factor	Coefficient Estimate	Df	95% CI Low	95% CI High
Intercept	370.81	1	365.08	376.55
A-Precursor volume (mL)	29.56	1	23.83	35.30
B-Extract volume (mL)	-35.69	1	-41.42	-29.95
C-pH	8.94	1	3.20	14.67
D-Temperature (^oC)	-3.31	1	-9.05	2.42
AB	32.81	1	27.08	38.55
AC	7.19	1	1.45	12.92
AD	11.69	1	5.95	17.42
BC	-8.81	1	-14.55	-3.08
BD	-11.56	1	-17.30	-5.83
CD	-2.69	1	-8.42	3.05

The percentage error was evaluated using the actual and predicted results to give 0.67%. The error is within the limit of <1% which confirms the validity of the result. Therefore, the model is considered suitable because the predicted value is close to the actual value for the wavelength (response).

4.4 TiO_2 Nanoparticles Synthesis Based on 2^3 Factorial Designs

During the synthesis, a colour change from greenish-brown of the leaf extracts of the *Parkia biglobossa* plant to a light brown solution was observed. This effect is known as the Tyndall effect which indicates the presence of nanoparticles in the solution (Shah *et al.*, 2015). The UV-visible spectrophotometer spectra of each experimental run 1 – 8 are shown in Figure 4.8. The figure indicates that peaks appear at the same region of wavelength for all the experimental runs with the highest peak at 358 nm. This implies that all the experimental conditions considered were suitable to study the formation of TiO_2 nanoparticles.

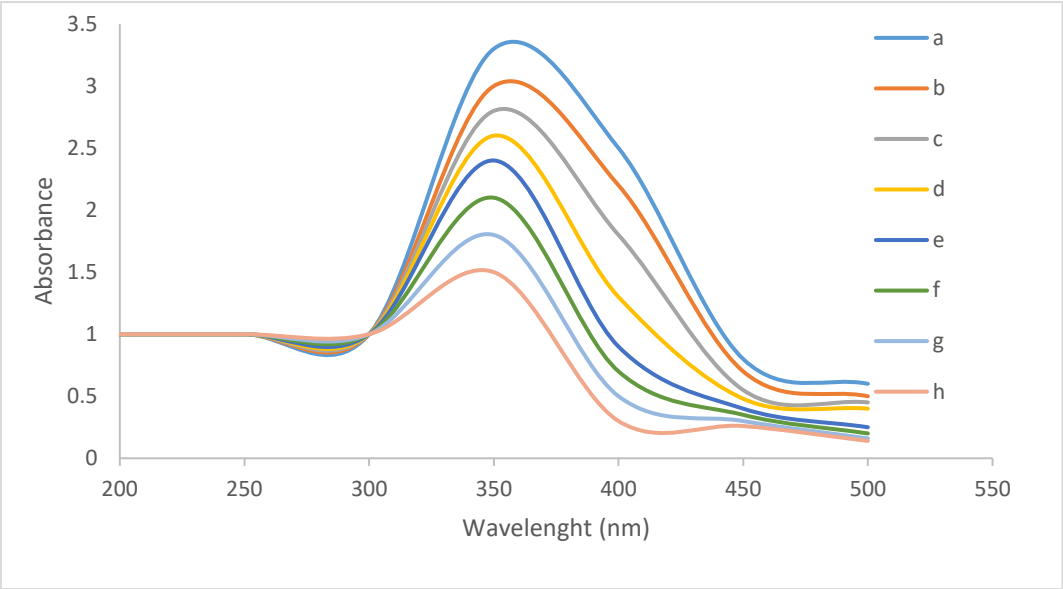

Figure 4.8: UV-Visible spectra of synthesised TiO_2 nanoparticles at various experimental conditions

The mechanism of TiO_2 nanoparticle synthesis has been proposed to follow the orders of hydrolysis, condensation and calcination processes. This is to produce the anatase, rutile and brookite phases of TiO_2 nanoparticles (Narayanan *et al.*, 2021). The hydroxyl group present in the *Parkia biglobossa* leaf extract serves as a base, which helped to hydrolyse the TTIP precursor. This is followed by the growth and agglomeration of the particles. In the hydrolysis process, Ti-OH moieties are formed by the substitution reaction of water with Ti-OR groups. The TTIP precursor undergoes condensation reactions to produce Ti-O-Ti by oxolation and Ti-OH-Ti bonds by olation (Islam *et al.*, 2017).

The condensate was filtered, allow to age overnight, oven dried to obtain constant weight and therefore calcined to obtain rutile TiO_2 nanoparticles in this study. The proposed overall mechanisms for the formation of TiO_2 nanoparticles using aqueous leaf extract of *Parkia biglobossa* are presented in Equation 4.5:

$$Ti(OCH(CH_3)_2)_4 + 2H_2O\ (P.biglobossa\ complex) * \rightarrow\ TiO_2 + 4CH_3 - CH - CH_3 - OH \quad (4.5)$$

The highest peak of 358 nm wavelength obtained is relatively close to 350 nm reported in the literature (Swathi *et al.*, 2019), where TiO_2 Nps were green synthesised with *Cassia fistula* leaves. The findings in this study show that green synthesis is as suitable as other methods for the synthesis of TiO_2 Nps. However, a peak at wavelength 450 nm was obtained by Subhapriya and Gomathipriya (2018) for TiO_2 Nps using Titanium oxy sulphate and *Trigonella foenum-graecum* leaf extract. The difference between the wavelength peaks might be due to the difference in precursor salt and the type of leaf extract used in this study.

4.4.1 Optimisation of process parameters to minimise crystallite size of the TiO_2 nanoparticles

To investigate the crystallite size and phase of TiO_2 formed in the 8 different experimental runs shown in Table 3.6, XRD analysis was employed. The crystallite size of each sample was calculated using Scherer's equation. Figure 4.9 (a-h) represents the XRD pattern of the as-prepared titanium nanoparticles for runs (a) to (h). The XRD pattern illustrates the presence of strong, sharp and relatively intense diffraction peaks at 2Ɵ values of 27.45º, 36.16º, 39.2º, 44.05º, 54.32, 56.64º and 69.79º.

These peaks aligned well with the crystal planes of (110), (200), (111), (210), (211), (220) and (112). The eight TiO_2 nanoparticles produced were all of the rutile phase of TiO_2 with JCPDS number 00-021-1276. The average crystallite sizes of each run range from 3.45 – 9.48 nm (actual and predicted) presented in Table 4.6. From the literature, smaller crystallite size has been attributed to a larger surface area (Gupta *et al.*, 2019) explained by the availability of numerous tiny, amorphous particles which may enhance the capability of adsorption by the nanoparticles. It could be observed in the literature that the uncommonly synthesised rutile-TiO_2 has large crystallite sizes which implies low surface area (Memarian *et al.*, 2020).

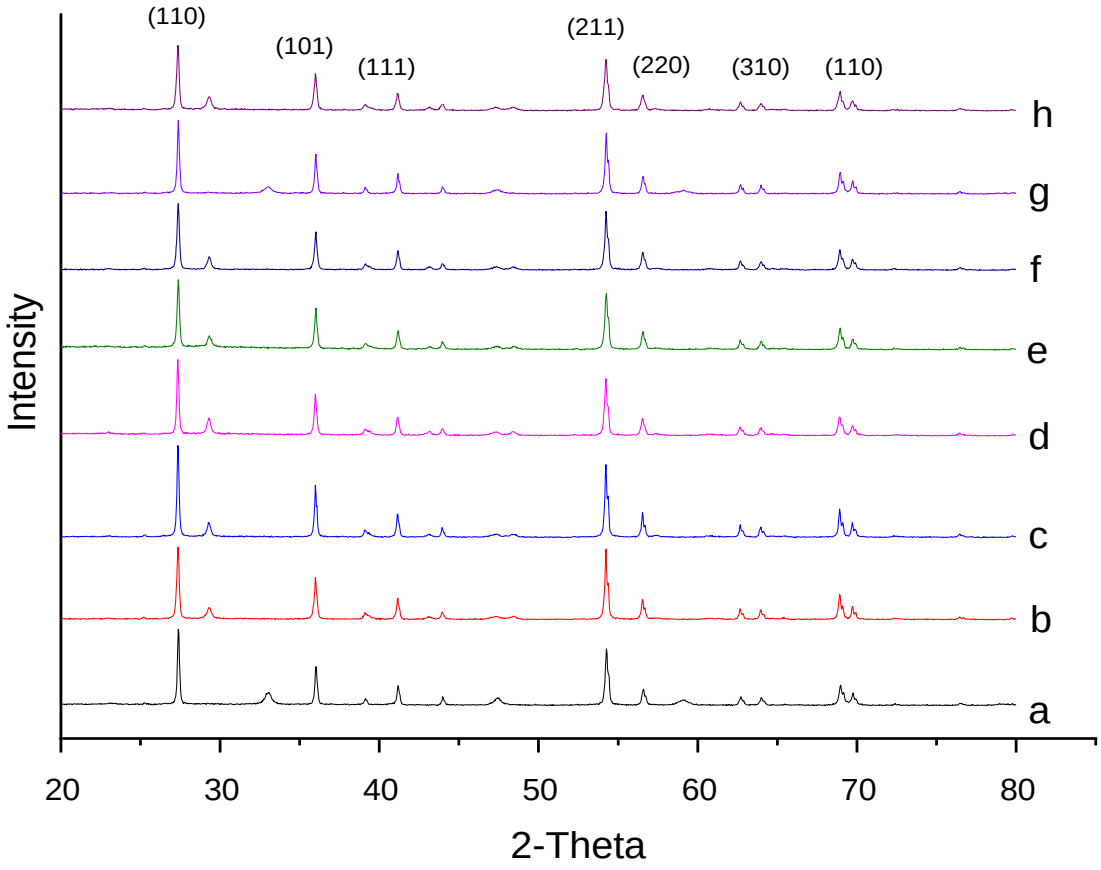

Figure 4.9: XRD patterns of synthesised TiO_2 nanoparticles at various operating conditions

Table 4.6: 2^3 factorial design matrix and response for the TiO_2 nanoparticles synthesis

				Crystallite size (nm)	
Exp. Run	**Precursor volume (cm^3)**	**Extract volume (cm^3)**	**Stirring speed (rpm)**	**Actual size**	**Predicted size**
A	5	50	100	9.52	9.48
B	5	50	200	5.51	5.55
C	5	5	200	8.49	8.45
D	50	5	200	8.59	8.63
E	5	5	100	6.41	6.44
F	50	50	100	5.01	5.05
G	50	50	200	3.49	3.45
H	50	5	100	4.32	4.28

Meanwhile, the commonly synthesised anatase phase TiO_2 has somewhat small crystallite sizes (Landage *et al.*, 2020; Myilsamy *et al.*, 2015). The pure rutile phased TiO_2 produced via the green synthesis observed in the present study irrespective of the synthesis conditions contradicts previous studies (Gupta *et al.*, 2019; Oi *et al.*, 2016).

For instance, the formation of rutile phase TiO_2 was reported at room temperature by Gupta *et al.* (2019) though with the co-precipitation method and $TiCl_3$ as a precursor. The research of Memarian *et al.* (2020) also synthesised a rutile phase TiO_2 with a crystallite size of 147.5 nm through a sol-gel synthesis method. Reported research with the production of rutile (sometimes mixed with anatase or brookite) titanium in the literature used varied precursor salts ($TiCl_3$, $TiCl_4$, Titanium butoxide), different reducing agents and varied synthesis temperatures. Goutam *et al.* (2017) green synthesised anatase phased TiO_2 from $TiCl_4$ using *Jatropha caucas* leaves at room temperature. Anwar *et al.* (2012) reported that hydrolysis temperature influences the crystal structure of TiO_2. The authors submitted that, when the temperature is less or equal to 50^oC, the TiO_2 sample always possesses a rutile structure.

Santhoshkumar *et al.* (2014) also synthesised rutile TiO_2 using low temperature/room temperature. Considering the synthesis temperature of 35^oC in this study, which falls within the surmised range. It may be deduced that the formation of the rutile titanium is favoured by the temperature used in this study. Also, the phase transformation depends on the nature, and structure of precursor and synthesis conditions, which are also transition temperature-dependent (Anwar *et al.*, 2012). Li *et al.* (2015) and Kumar *et al.* (1993) reported that titanium usually experiences phase transformation at calcination temperatures from 450^oC to 800^oC, especially, from anatase to rutile phase titanium. The findings in this study corroborate the 550^oC calcination temperature used in this research.

The crystallite size of 3.49 nm obtained is unusually small compared to those earlier obtained via green synthesis and other methods as shown in Table 4.7.

Table 4.7: Comparison of crystallite size and TiO_2 phase with various synthesis methods

Method of synthesis	Crystallite size (nm)	Phase	Reference
Biological	20	Anatase	Landage *et al.* (2020)
Hydrothermal/Sol-gel	5/10	Anatase	Sirichokthavasarp *et al.* (2020)
Solvothermal	5	Anatase-Rutile	Kobayashi *et al.* (2013)
Sol gel	12	Anatase	Naghibi *et al.* (2013)
Green (Pristine pomegranate peel)	92	Anatase	Abu-Dalo *et al.* (2019)
Sol-gel	7	Rutile	Bagheri *et al.* (2013)
Green	30	Anatase-Rutile	Subhapriya and Gomathipriya (2018)
Green (*Azadirachta indica*)	15	Anatase-Rutile	Thakur *et al.* (2019)
Green (*Glycyrrhiza glabra*)	24	Anatase	Madadi *et al.* (2020)
Hydrothermal	15	Anatase-Rutile	Dodoo-Arhin *et al.* (2018)
Sol-gel	11	Anatase	Gupta *et al.* (2019)
Co-precipitation	7	Rutile	Gupta *et al.* (2019)
Ball milling	60	Anatase-Rutile	Gupta *et al.* (2019)
Green (*Echinacea purpurea*)	120	Anatase	Dobrucka (2017)
Green (*Euphorbia prostata*)	12.82	Anatase	Zahir *et al.* (2015b)
Green (*Pithecellobium dulce* and *Lagenaria siceraria*)	7.5	Anatase	Kalyanasundharam and Prakash (2015)
Green (*Moringa oleifera*)	12.22	Anatase	Patidar and Jain (2017)
Green (Parkia biglobosa)	3.49	Rutile	**This study**

From the table, Landage *et al.* (2020) obtained an anatase phase of TiO_2 which has a 20 nm crystallite size using *S. aureus* for the synthesis. Also, *Glycyrrhiza glabra* leaves were used to synthesise anatase TiO_2 with an average crystallite size of 24 nm, and the obtained nanoparticles were calcined for 4 h, at 400˚C (Madadi *et al.*, 2020). The pure rutile phase of TiO_2 obtained by Bagheri *et al.* (2013), was by sol-gel method using egg white as a gelling agent and calcined at 500˚C for 5 h.

Gupta *et al.* (2019) reported that the smallest crystallite size (3.9 nm) for TiO_2 nanoparticles was prepared through the co-precipitation method, using $TiCl_3$ and HCl as titanium precursor and NH_4OH to carry out hydrolysis of $TiCl_3$. Subhapriya and Gomathipriya (2018) also obtained 30 and 25 nm crystallite sizes for TiO_2 prepared using *Trigonella foenum* for anatase and rutile phase TiO_2 synthesised. However, this study revealed a crystallite size of 3.49 nm when the green method was employed for nanoparticle synthesis. Also, 92 nm crystallite-sized anatase TiO_2 nanoparticles were obtained by Abu-Dalo *et al.* (2019) using Pristine pomegranate peel extract.

4.4.2 Effects of process parameters on the crystallite size during synthesis of the TiO_2 nanoparticles

The effects of titanium salt precursor volume (cm^3), plant extract volume (cm^3) and stirring speed (rpm) on the crystallite size of TiO_2 nanoparticles synthesised were investigated using XRD. Table 4.6 also shows the actual and predicted crystallite size (nm) of TiO_2 produced for experimental runs (a-h). The results from the table reveal that both the precursor and the extract volumes with the stirring speed have a combined influence on the particle size of TiO_2 formed. The instance of the run (a) and run (f) having all other conditions the same, except for the difference in precursor volumes of and 50 cm^3 respectively yielded a difference of 5.51 nm crystallite size. While maintaining the same precursor and extract volumes 50:50 (runs f and g) at increasing stirring speed from 100 to 200 rpm. There is a further reduction in the crystallite size by 1.53 nm from 5.01 o 3.48 nm, which is a clear indication of the interwoven influence of precursor, extract volumes and the stirring speed. The increase in stirring speed suppresses any form of coalescence during precursor and aqueous leaf extract stirring while on the magnetic stirrer.

Thus, providing sufficient volume for TiO_2 nanoparticles synthesis inside the individual precursor volume (Politova-Brinkova *et al.*, 2020). Also, the nucleation of particles in the appropriate volume is attributed to the formation of very small TiO_2 particles.

Model development for TiO_2 synthesis

A 2^3! equation of the design expert was used to fit the experimental data with general expression shown in Equation 4.6:

$$Y = \beta_0 + \beta_1 * x_1 + \beta_2 * x_2 + \beta_{12} * x_1x_2 + \beta_3 * x_3 + \beta_{13} * x_1x_3 + \beta_{23} * x_2x_3 + \beta_{123} * x_1x_2x_3 \quad (4.6)$$

Where; β_0 is the value of the intercept,

$\beta_1, \beta_2, and\ \beta_3$ are the coefficients for the main effects of variables,

$x_1, x_2, and\ x_3$ are the variables,

$\beta_{12}, \beta_{13}, and\ \beta_{23}$ are the coefficients for interactions between two variables,

$x_{12}, x_{13}, and\ x_{23}$ are the interactions between two variables,

β_{123} is the coefficient for interaction among the three variables, and

x_{123} is the interaction among the three variables.

The equation is a semi-empirical relationship obtained by fitting the experimental data to give solution equations.

Model fitting

Equations 4.7 and 4.8 are coded and actual model solutions, respectively, which were computed concerning the significant impact of variables on the response (crystallite size, nm).

$$Response\ (nm) = +6.42 - 1.06 * A - 0.53 * B + 0.10 * C - 0.57 * AB + 0.58 * AC - 1.49 * BC \quad (4.7)$$

$$Crystallite\ size\ (nm) = +3.91 - 0.09 * A + 0.21 * B + 0.02 * C - 1.12\ X\ 10^{-3} * A * B + 5.19\ X\ 10^{-4} * A * C - 1.32 * X\ 10^{-3} * B * C \quad (4.8)$$

Equation 4.7 can be used to predict response for given levels of each variable with high levels coded as +1 and low levels coded as -1. The coded equation is used to determine the relative impact of the variables by comparing the coefficients of the variable. The actual equation on the other hand is useful to predict response in terms of crystallite size (nm) for given levels of each variable. In this case, the levels are specified using the original units for each variable and the equation obtained should not be used to determine the relative impact of each variable. Since the coefficients are scaled to accommodate the units of each variable and the intercept is not at the centre of the design space. The equations, therefore, consist of three statistically significant variables, indicating that the individual effects of variables are sufficient to explain the crystallite size of the TiO_2 nanoparticles.

Equations 4.7 and 4.8 exhibit six statistically significant terms which include the main effect of A, B, and C, and the combined effects of AB, AC, and BC. The main and combined effects contributed to the synthesis of smaller crystallite sizes of TiO_2 nanoparticles. The model was established suitable by plotting the experimental data against the predicted values from models in Equations 4.6 and 4.7. The plots between the experimental and predicted crystallite size (nm) are shown in Figure 4.10 which gave a regression coefficient of 0.9997. This shows a good correlation between the experimental and predicted values. Further analysis was carried out on the model to validate its performance by analysis of variance, which tests the significance and adequacy of the model.

4.4.3 Analysis of variance (ANOVA) of the model

Table 4.8 shows the ANOVA statistical analysis of the factorial model, to determine the effects of synthesis variables on the crystallite size (nm) of TiO_2 nanoparticles produced. The high F-value of 483.47 and *p*-value of 0.0348 indicate the significance of the model.

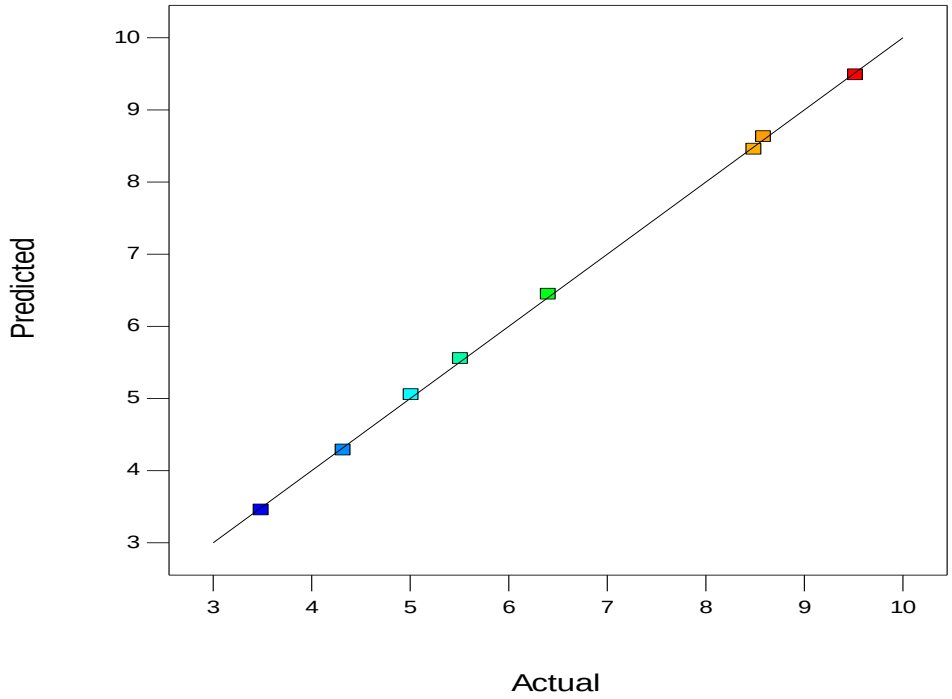

Figure 4.10: Plots of experimental versus predicted crystallite size (nm)

The *p*-values for the three main variables are 0.0230, 0.0459, and 0.2282 for the volume of titanium salt precursor, the volume of plant extract, and stirring speed, respectively. This shows that the precursor volume and extract volume is significant, as their values are less than the Prob > F of 0.05. Furthermore, the combined effects of the variables; AB, AC, and BC yielded *p* – values of 0.0431, 0.0419, and 0.0165 (Table 4.8), respectively. These values are also less than the Prob > F of 0.05 which indicates the significance of the combined variables (Souri *et al.*, 2018). The difference between adjusted R^2 and predicted R^2 values (0.0197) is far less than 0.2 which suggests a reasonable agreement between the two. Therefore, the ANOVA analysis suggests the applicability of the model to predict smaller crystallite size (nm) of TiO_2 nanoparticle synthesis.

Table 4.8: ANOVA of factorial model for the crystallite size (nm) of TiO_2 nanoparticles

Source	Sum of squares	Df	Mean square	F-value	*p*-value (Prob>F)
Model	34.40	6	5.73	483.47	0.0348
A - Precursor volume (cm^3)	9.07	1	9.07	764.85	0.0230
B - Extract volume (cm^3)	2.28	1	2.28	192.02	0.0459
C - Stirring speed (rpm)	0.084	1	0.054	7.12	0.2282
AB	2.58	1	2.58	217.85	0.0431
AC	2.72	1	2.72	229.70	0.0419
BC	17.66	1	17.66	1489.26	0.0165
Residual	0.012	1	0.012		
Total	34.41	7			
R^2 0.9997 **Adj. R^2** 0.9976 **Pred. R^2** 0.9779 **C.V. %** 1.70					

4.4.4 Interactive effects of the combined variables

Figures 4.11 (a-c) show the 3D plots of interactive effects of various variables under study, on crystallite size of TiO_2 nanoparticles synthesis.

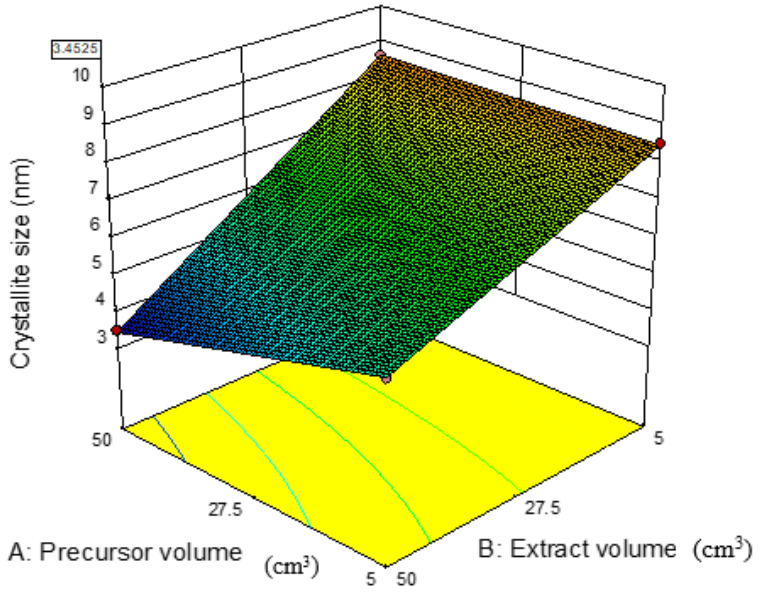

Figure 4.11a: 3D plot of A and B against crystallite size of TiO_2 Nps at constant 200 rpm

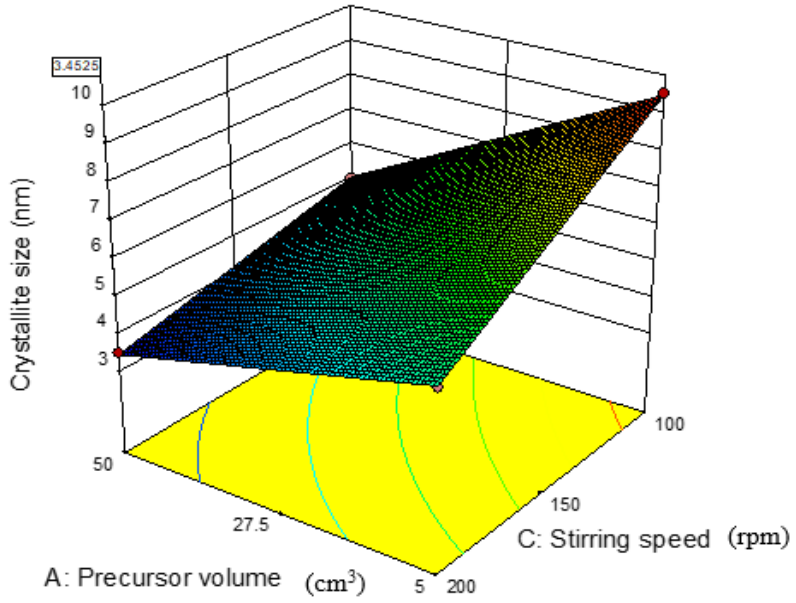

Figure 4.11b: 3D plot of A and C against crystallite size of TiO_2 Nps at constant B of 50 cm^3

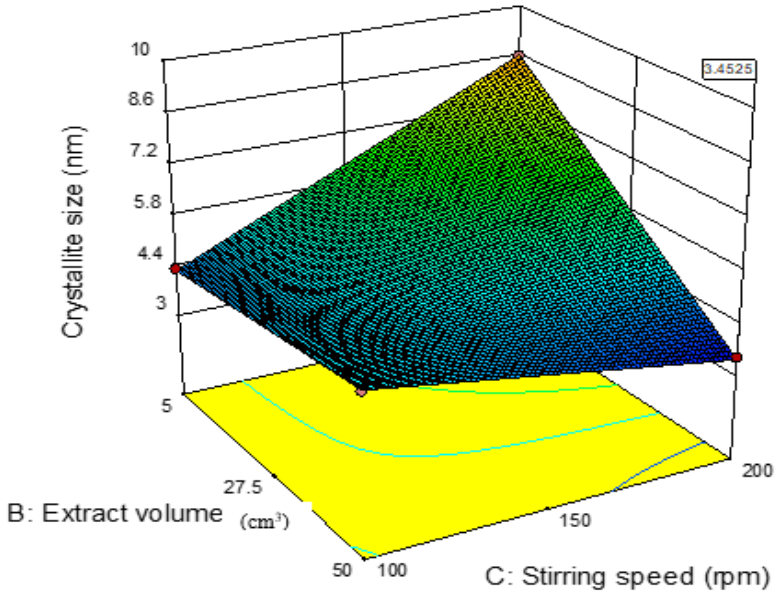

Figure 4.11c: 3D plot of B and C against crystallite size of TiO_2 Nps at constant A of 50 cm^3

The figures display the "flag" in the left top corner of the blue region which represents the optimised point of achieving a smaller crystallite size of 3.45 nm. As can be observed from Figure 4.11a, the crystallite size decreases with an increase in precursor volume and an increase in extract volume.

The increase in extract volume could have increased the number of phytochemical components such as flavonoids and phenolic that facilitated the formation of $TiO(OH)_2$ to TiO_2 nanoparticles from titanium (IV) isopropoxide salt (Aritonang *et al.*, 2019). The increase in the volume of leaf extracts may be responsible for the decrease in the crystallite size of the TiO_2 nanoparticles (Zahir *et al.*, 2015b). Figure 4.11(b) reveals a decrease in the crystallite size as the precursor volume and stirring speed increase due to an increase in the mass transfer of the phytochemical constituent of the leaf extract into the precursor titanium solution. This may also be linked to the increased stirring speed which resulted in the synthesis of smaller crystallite-sized TiO_2 nanoparticles. A similar trend was noticed in Figure 4.11c, where the smallest crystallite size (3.49 nm) of TiO_2 was observed when extract volume and the stirring speed were at the highest value considered.

4.4.5 Model optimisation and validation

The coefficients to optimise smaller crystallite size (nm) for the synthesis of TiO_2 nanoparticles using the design expert are shown in Table 4.9. From the table, optimisation shows that the value of response as predicted is 95% CI (Confidence Interval) for both low and high. This implies that the degree of certainty is at a 95% level, an indication that 95 out of 100 times contains true values of the variables. Based on this analysis, a precursor volume of 50 cm^3, extract volume of 50 cm^3, and stirring speed of 200 rpm gave a predicted smaller crystallite size of 3.45 nm as shown in Table 4.9. The result of the validation test (actual) for the crystallite size using the optimal variable is 3.48 nm. Comparatively, the percentage error between the actual and the predicted values of response for the crystallite size is 0.86% which is less than 1%, this implies the response value of the validation result was not significantly different.

Table 4.9: Estimated coefficient of the model and variables for crystallite size of TiO_2 nanoparticles

		Crystallite size (nm) of TiO_2 Nps	
Factors	**Coefficient estimate**	**95% CI Low**	**95% CI High**
Intercept	6.42	5.93	6.91
A	-1.06	-1.55	-0.58
B	-0.53	-1.02	-0.044
C	0.10	-0.39	0.59
AB	-0.57	-1.06	-0.079
AC	0.58	0.094	1.07
BC	-1.49	-1.97	-1.00

Therefore, the model is considered good since the predicted value is close to the actual value for the response (Qisti *et al.*, 2016). Hence, the obtained optimisation solution is validated using the predicted values of the variables by repeating the experiment.

4.5 Characterisation of the Prepared Nanomaterial

The kaolinite clay, Silver oxide, Titanium oxide, Silver oxide-Titanium oxide composites and Ag_2O/TiO_2-kaolinite clay nanocomposites were characterised using FTIR, HRTEM/SAED, HRSEM/EDS, XRD, BET and XPS to examine the functional groups, microstructure, optical structures, surface morphology, elemental composition, phase properties, textural properties and surface oxidation state of the prepared nanocomposites.

4.5.1. FTIR analysis

The Fourier Transform Infrared spectroscopic analysis of the raw clay, beneficiated clay and activated clay are presented in Figure 4.12(a-c). The result indicates the presence of several short absorption bands on the spectral of the raw clay (RC), at 3857.76 cm^{-1} and 3734.31 cm^{-1} and these are assigned to the O-H group stretch bonded to Si and Al (Figure 4.12a).

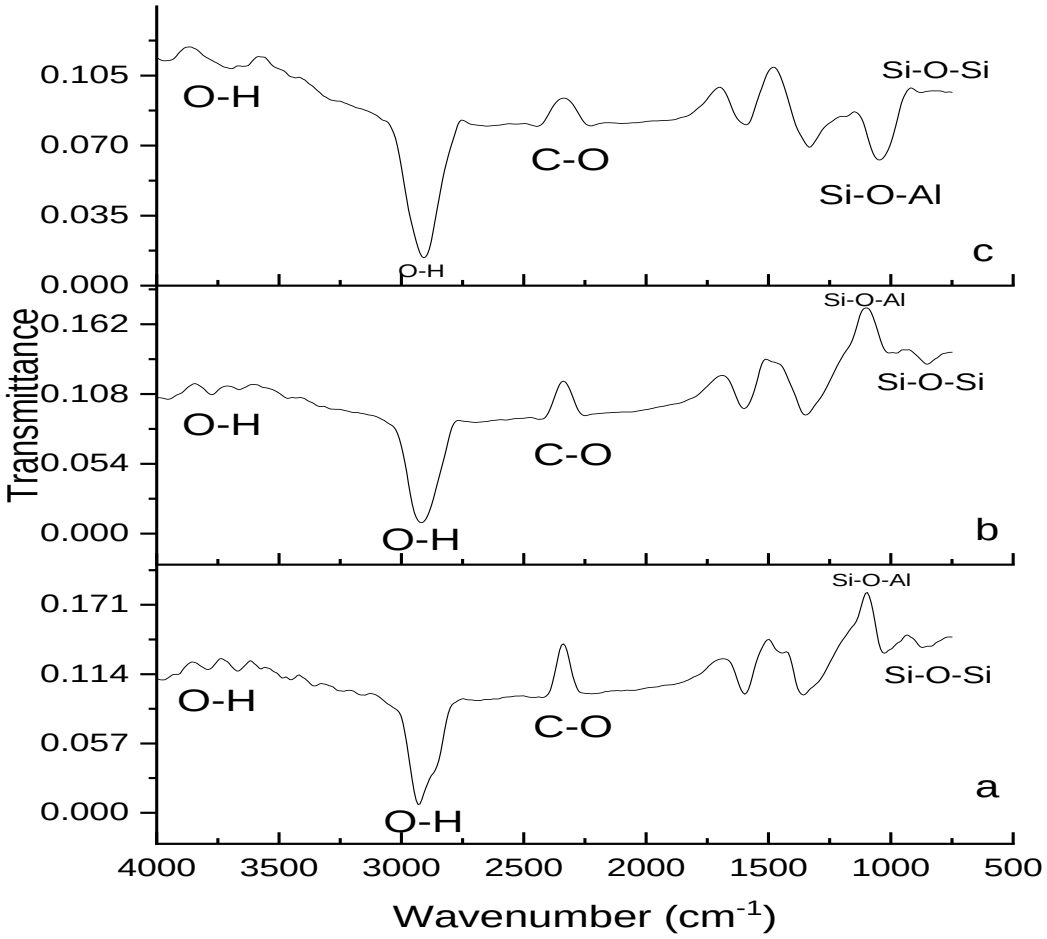

Figure 4.12: FTIR Spectra of (a) Raw (b) Beneficiated (c) Acid-activated Clay

The OH bridging hydroxyls in the kaolin cages were noticed at 3618.58 cm^{-1} which is bonded as Al-OH-Si like those observed in zeolite cages (Guillaume *et al.*, 2018). The peaks between 3417.98 cm^{-1} and 3217.37 cm^{-1} are indicative of the O-H-O stretch of water molecules (Krishnan and Mahalingam, 2017).

The peak at 2337.80 cm^{-1} may be attributed to adsorbed CO_2 while the peak at 1681 cm^{-1} is assigned to –OH bend in water molecules found in typical kaolin clays (Kenne-Diffo *et al.*, 2015). The bands noticed at 840.99 cm^{-1} and 768.84 cm^{-1} correspond to Si-O-Al and Si-O-Si bending respectively of typical kaolin quartz (Diko *et al.*, 2016). The spectrum of beneficiated clay in Figure 4.12b revealed peaks at similar points, although with a slight shift. This could be due to the washing away of alumina during the beneficiation process (Salahudeen *et al.*, 2015).

The peaks at 3842.23 cm^{-1}, 3711.14 cm^{-1}, 3610.86 cm^{-1} and 3417.98 cm^{-1} represent –OH stretch bonded to Si and Al as Al-OH-Si in Kaolin. The peaks on the beneficiated clay at 1689.70 cm^{-1}, 1512.24 cm^{-1} 1095.60 cm^{-1}, 949.01 cm^{-1} and 756.12 cm^{-1} became more visible with higher intensity when compared to that on the raw clay spectrum while peaks at 3556.85 cm^{-1}, 3325.39 cm^{-1}, 3124.79 cm^{-1}, 2623.28 cm^{-1}, 840 cm^{-1} on the raw clay disappeared completely from the beneficiated clay due to the removal of unwanted materials in the raw clay.

The FTIR spectrum of activated clay displayed in (Figure 4.12c) reveals the disappearance of a few peaks. However, the appearance of peaks at 3865.48 cm^{-1} is an improvement due to acid purification which increase the broadness of the bonded –OH functional group. Other peaks noticeable at 3664.87 cm^{-1} and 3587.72 cm^{-1} are Al–OH stretching of inner-surface hydroxyls, bonded to alumina of the kaolinite clay (Diko *et al.*, 2016). The spectrum band at 1095 cm^{-1} is assigned to the Si-O-Si bending vibration of the tetrahedral sheet while that at 918.84 cm^{-1} is attributed to the stretching vibration of Al-O-(OH)-Al, typical of kaolinite clay (Kenne-Diffo *et al.*, 2015). The shift of the peaks in the clay confirms the existence of functional groups capable of bonding with heavy metals and other pollutants in wastewater. The disappearance or decreased number of peaks also confirms the dissolution of other organic material caused by the acid treatment (activation) on the clay.

This also improved the porosity of the clay, as reported by Guillaume *et al.* (2018). Figure 4.13(a-c) presents the FTIR results of Ag_2O-clay, TiO_2-clay, and Ag_2O-TiO_2-clay, respectively. From Figure 4.13a, a band occurred at 3693.53 cm^{-1} due to the immobilisation of the Ag_2O on the well-ordered kaolinite structure of the clay. At the region of 3624.06 cm^{-1}, Al-O-H stretching of inner hydroxyl groups in kaolinites was also observed (Diko *et al.*, 2016; Krishnan and Mahalingam, 2017).

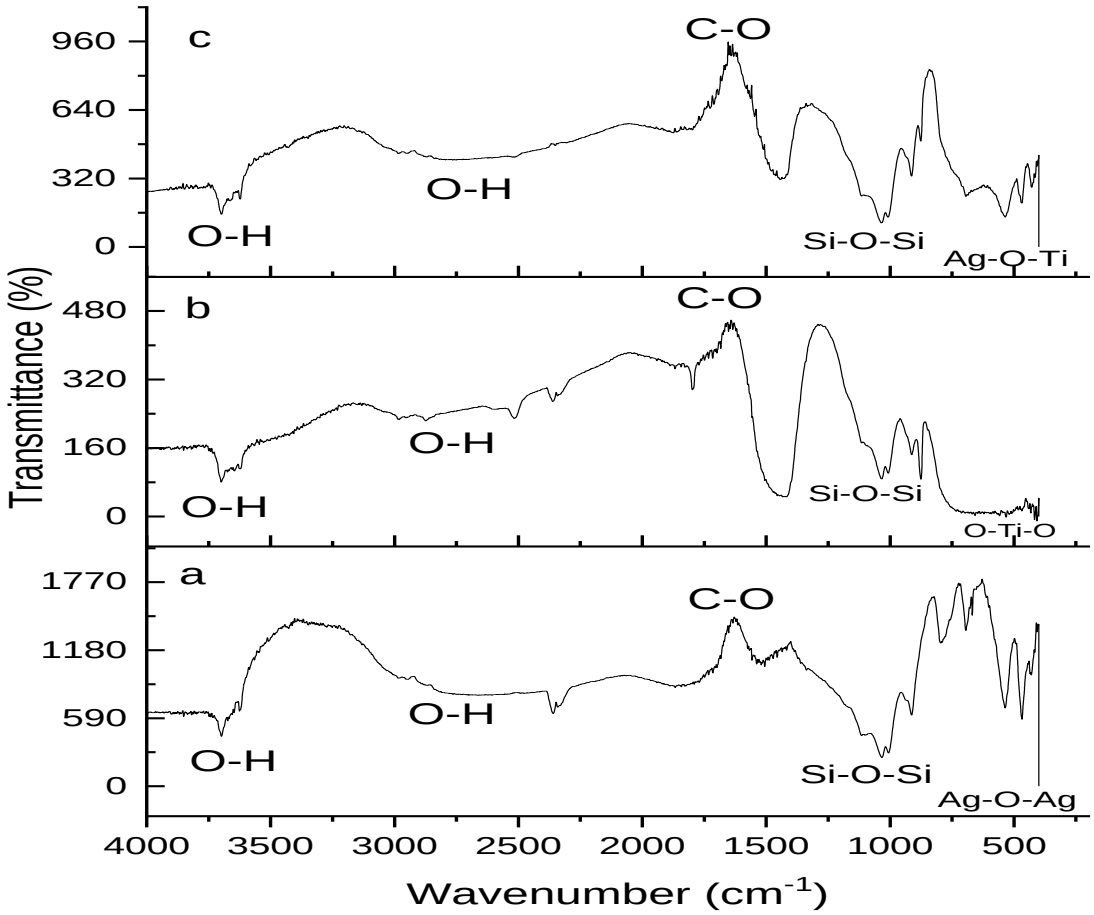

Figure 4.13: FTIR spectra of (a) Ag_2O-clay, (b) TiO_2-clay and (c) Ag_2O-TiO_2-clay nanocomposites

The same band of O-H group stretch appears on TiO_2-clay (Figure 4.13b), and Ag_2O-TiO_2-clay (Figure 4.13c). However, these bands were absent on the spectrum of the activated clay (Figure 4.12c) probably due to the absence of Ag_2O and TiO_2. The bands at 1822.02 cm^{-1}, 1519.64 cm^{-1} and 1119.18 cm^{-1} appear for Ag_2O-clay (Figure 4.13a), TiO_2-clay (Figure 4.13b) and Ag_2O-TiO_2-clay (Figure 4.13c) respectively. These bands are indicative of Ag_2O-kaolinite and TiO_2-clay (Krishnan and Mahalingam, 2017). The observed bands at 1033.37 cm^{-1} and 1000.68 cm^{-1} are assigned to the Si-O stretch, which is present in the three samples. The Si-O-Si bond is linked to the kaolinite and quartz composition of the beneficiated clay. Furthermore, peaks that appear at 914.87 cm^{-1}, 869.92 cm^{-1}, and 438 cm^{-1} are attributed to Ti-O-Ti bonded (Guillaume *et al.*, 2018).

This is evidence of TiO_2 within the clay matrix (Guillaume *et al.*, 2018). The peak noticed at 910.78 cm^{-1} is a deformed OH bond, while that at 788.20 cm^{-1} is a -OH deformation bond linked to Aluminium ions (Diko *et al.*, 2016). The bands observed at 686.04, 534.85, 461.29 and 432.69 cm^{-1} confirmed the presence of Si-O-Ag bonds (Guillaume *et al.*, 2018). The shifting of peaks observed on Ag_2O-clay (Figure 4.13a), TiO_2-clay (Figure 4.13b) and Ag_2O-TiO_2-clay (Figure 4.13c) indicates the presence of Ag_2O and TiO_2 nanoparticles embedded in the clay matrix.

Hence, the Ag_2O-TiO_2-clay nanoparticles spectra showed major changes in the clay structural network after immobilisation with the Ag_2O-TiO_2 nanoparticles. The shifts in the position of earlier peaks observed in Figure 4.12c (activated clay), Figure 4.13a (Ag_2O-clay) and Figure 4.13b (TiO_2-clay) as compared with those in Figure 4.13c (Ag_2O-TiO_2-clay) showed that the clay has interacted with the immobilised AgO_2-TiO_2 nanoparticles (Hadjltaief *et al.*, 2016; Krishnan and Mahalingam, 2017).

4.5.2 High-resolution transmission electron microscopy (HRTEM)/selected area electron diffraction (SAED)

The microstructural analysis of the Ag_2O, TiO_2 and Ag_2O/TiO_2 nanoparticles was carried out using HRTEM and the corresponding micrograph with particle size distribution shown in Plate IX. Plate IX a(i) revealed the formation of loosely packed spherical particles of Ag_2O in different sizes. The aggregation of Ag_2O nanoparticles confirmed that the synthesised particles were capped with the plant extract (Yusof *et al.*, 2018). This reveals a chemical interaction between the *Parkia biglobosa* leaf extract complex used and the Ag_2O nanoparticles formed having an approximate 5.00 nm average particle size as shown on Plate IX a(ii). This is close to the crystallite size of 5.79 nm obtained from the XRD.

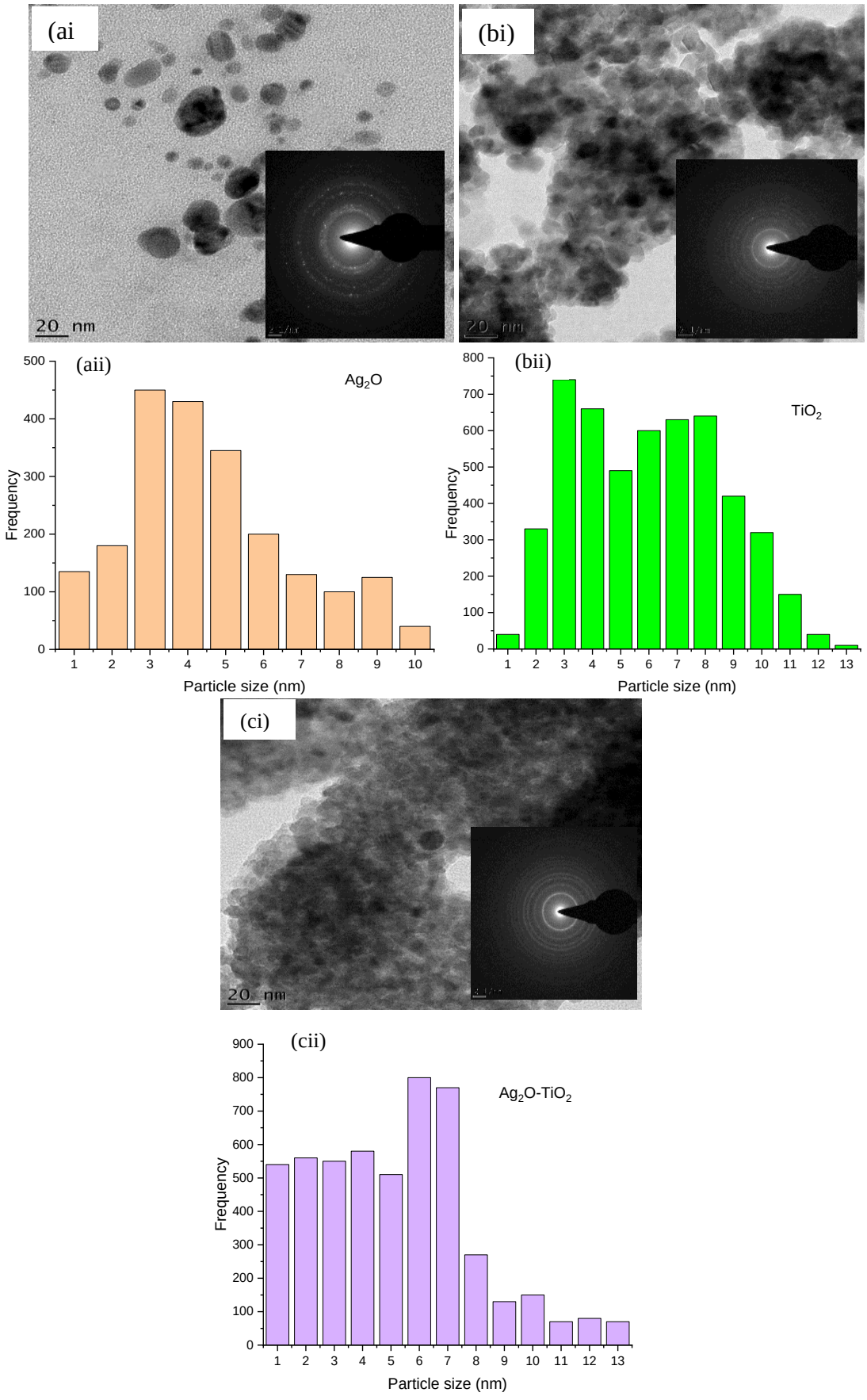

Plate 1X: HRTEM/SAED images of (a) Ag_2O (b) TiO_2 (c) Ag_2O/TiO_2 nanoparticles

A similar but densely packed aggregate was observed in the HRTEM of TiO_2 shown in Plate IX b(i). The particle size distribution of the TiO_2 Nps in Plate IX b(ii) revealed the effect of *P. biglobossa* extract. The synthesised TiO_2 Nps has the highest particle size distribution in the sub 4 nm, revealing a smaller size when compared to that of Ag_2O due to its atomic weight. The stability of the nanoparticles observed is due to stabilizing and capping agents around the nanoparticles formed on the HRTEM image in Plate IX a(i) and b(i). However, in Plate IX c(i) (Ag_2O/TiO_2), the nanoparticles became widely spread and more uniformly dispersed which indicates optimum intercalation of Ag_2O and TiO_2 on each other. The presence of uniformly dispersed dark spotted particles suggests the fusion of Ag_2O/TiO_2 Nps to form a single spherical particle with an average particle size of 7 nm (Kulkarni *et al.*, 2016). The doping of the Ag_2O with TiO_2 contributed to the slight increase in particle size of the combined nanoparticles. The SAED pattern also in Plate IX (a(i), and b(i)) reveals the existence of different bright spots along the crystal orientation of Ag_2O and TiO_2. The pattern revealed that the Ag_2O and TiO_2 arrangement are polycrystalline, which is in good agreement with the XRD results (Figure 4.9).

The SAED pattern in Plate IX a(i) shows Bragg reflections characteristic of crystalline Ag^o and Ag_2O (Pardha-Saradhi *et al.*, 2014). With crystal planes identified in the ring as follows; (110), (200), (111), (112), (210), (211) and (220). This confirms the face-centred cubic structure of the Ag_2O Nps which is similar to that of Liu *et al.* (2020), who used *C. camphor* leaf extract for Ag_2O synthesis. The bright spots were more scattered in the diffraction pattern in Plate IX c(i), which is that of Ag_2O/TiO_2. This signifies the doping of Ag_2O on the TiO_2 lattice. The doped Ag_2O/TiO_2 Nps reveal a slightly large grain size of nanoparticle when compared with Plate IX a(i), and Plate IX b(i). The defined ring arrangement with lattice fringes indicates an increasing upward intensity from that of Ag_2O to Ag_2O/TiO_2 Nps.

The intensity of the rings further confirms the crystalline and polydispersed nature of the Ag_2O and Ag_2O/TiO_2 nanoparticles. It was also observed that the doping effects of silver oxide on Ag_2O/TiO_2 may be responsible for the observed intense bright rings spot in the composite matrix (Karunakaran *et al.*, 2016; Krishnan and Mahalingam, 2017).

4.5.3. Higher resolution scanning electron micrograph (HRSEM) analyses

HRSEM of clays

The HRSEM image of the raw local clay, beneficiated clay and activated clay is presented in Plate X (a, b and c).

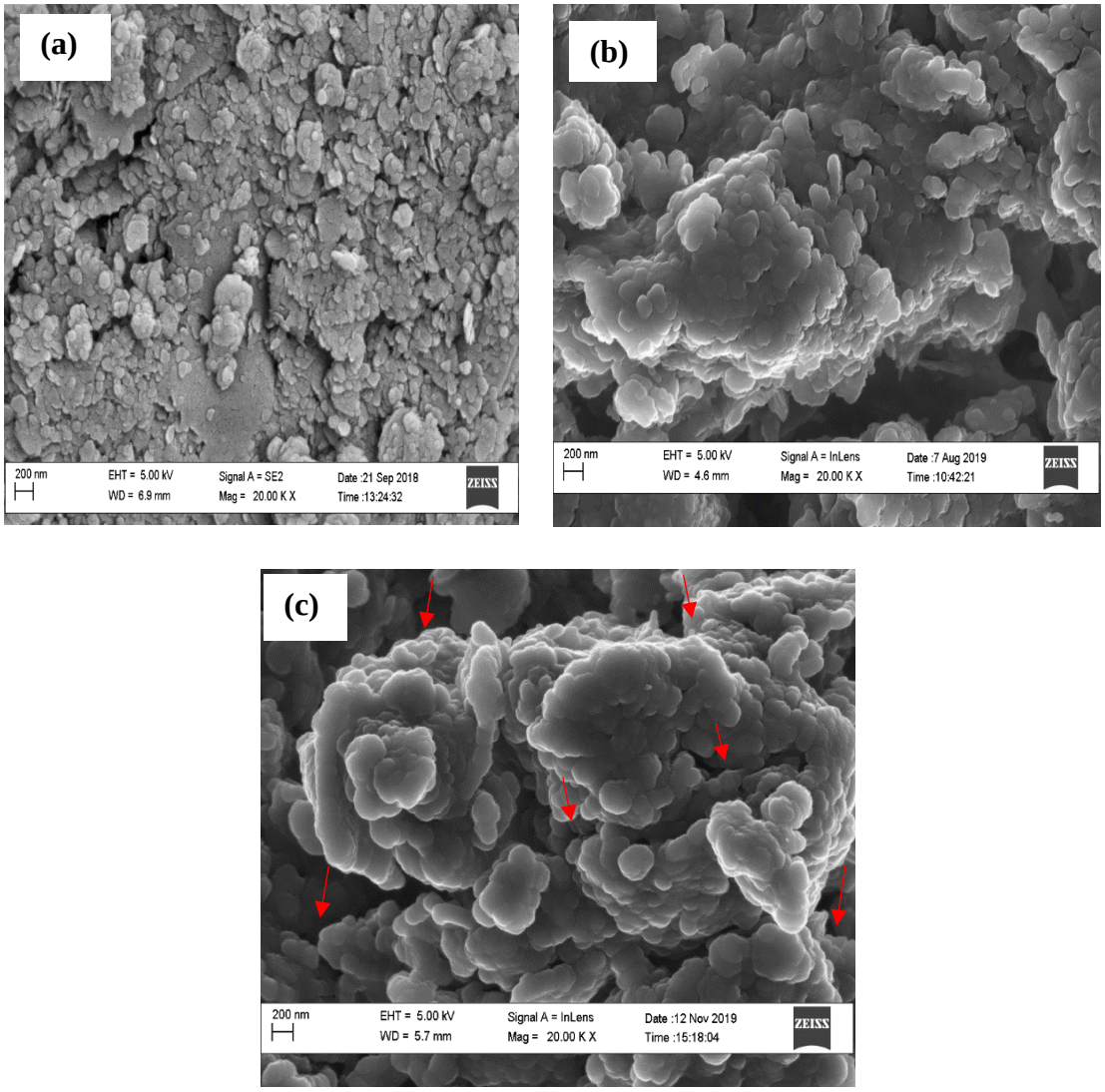

Plate X: HRSEM of (a) Raw clay, (b) Beneficiated clay (c) Activated clay

The morphology of the raw clay reveals an uneven interstitial arrangement of the clay lattice which consists of stacks of platelets structures of kaolinites (Mgbemena *et al.*, 2013; Mustapha *et al.*, 2019). The image in Plate Xa also reveals a stack disposition of an irregular plate-like network with broken edges crystals. The clay crystals show a hemispherical and uneven arrangement of the lattice revealing clusters of kaolin, arranged on each other. The irregularity in the arrangement of the kaolin surface structure suggested that the clay contains undesirable materials on the surface of the kaolinite. Plate Xb reveals the morphology of the clay after wet beneficiation. This shows also, hemispherical plates of kaolinites, porous, vividly and evenly arranged on each other, which is a better improvement when compared with the image on the Plate X a. This arose from the washing away of excess silica and other impurities clogged with the raw untreated clay.

Plate Xc, which is the morphology of the clay and after beneficiation and treatment with acid, reveals the presence of well-rounded, defined hemispherical edges of kaolinites with highly developed pores and voids. This confirmed the formation of kaolin with a definite and consistently rounded crystallographic arrangement of the grains. The difference in the HRSEM images from (a) to (b), then to (c) confirms improvement in the morphological disposition of the clay due to the wet beneficiation process, washing away of impurity, undesired soluble salt and the acid activation for optimum performance of the clay. The activated clay is seen with an improved clear surface and definite platelets arrangement (Mgbemena *et al.*, 2013; Salahudeen, 2018) an indication of suitable support for other metallic agents. This clay surface morphological improvement is like the results of the activation of clay achieved in literature (Kar *et al.*, 2013).

HRSEM of Ag_2O, TiO_2 and Ag_2O/TiO_2 nanoparticles

The morphological arrangement of the prepared nanoparticles is shown in Plate XI (a-d). The image of Ag_2O nanoparticles in Plate XIa shows a formation of densely packed agglomerated particles with few porosities.

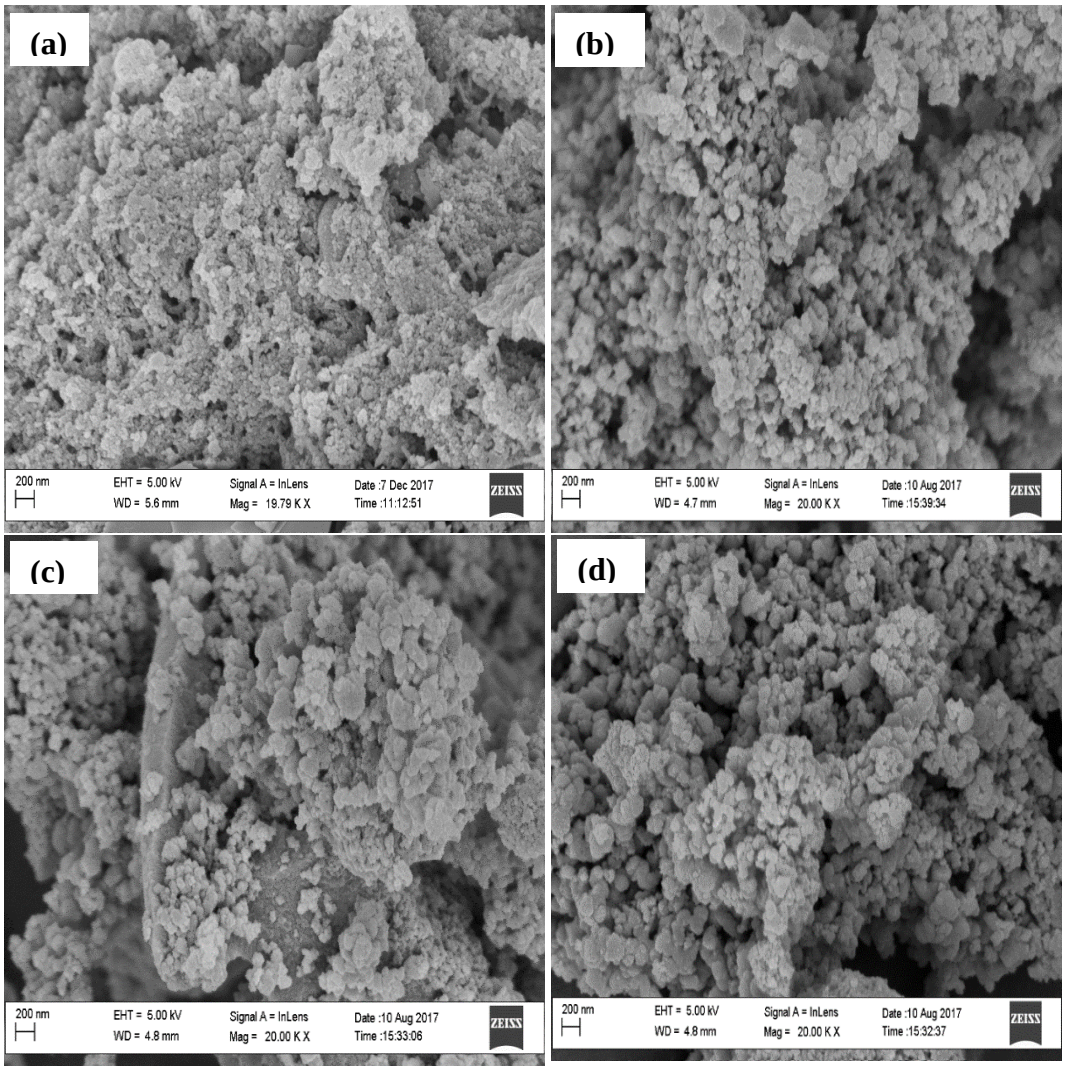

Plate XI: HRSEM of (a) Ag_2O (b) TiO_2 (c) 0.01mol/L Ag_2O/TiO_2 (d) 0.05mol/L Ag_2O-TiO_2 nanoparticles

The formation of the uniformly agglomerated particles in Plate XIa may be ascribed to the interaction between the *Parkia biglobossa* leaf extract and the Ag salt precursor. Agglomeration of Ag Nps in solution has been reported in the literature, whenever the nanoparticle is without support (Nersisyan *et al.*, 2003).

The HRSEM image of TiO_2 nanoparticles presented in Plate XIb shows a morphology that is marginally agglomerated. The morphology in Plate XIb exhibits a closely packed, agglomerated crystals arrangement with mild inter-particle gap and lattice stripe. This may be due to the interaction between the *Parkia biglobossa* leaf extract and Titanium (IV) isopropoxide. The morphological arrangement in Plate XIb showed better porosity when compared to Plate XIa, an indication that TiO_2 nanoparticles may adsorb more than Ag_2O nanoparticles. Plate XIc shows the morphological arrangement of the assemblage of Ag_2O/TiO_2. The particles of the doped nanoparticles are sparingly clustered together with more voids, showing a little deviation from Plates XIa and b, suggesting an improved porosity. The similarity of TiO_2 nanoparticles and Ag_2O/TiO_2 nanocomposite morphology indicates that the sample after modification with Ag maintains the original cage-bell structure of TiO_2 without destruction.

In addition, the HRSEM images of Ag_2O/TiO_2 nanocomposite present more pore voids, evidence of a high surface area than ordinary TiO_2 or Ag_2O surface area. The micrograph also showed that the Ag_2O is deposited and did not cause lattice distortion due to its greater ionic radius than TiO_2 (Pham and Lee, 2014). The image shown in Plate XId reveals uniformly distributed spherical particles of TiO_2 with improved pores when compared with Plate XIc due to a higher concentration of silver up to 0.05 mol/L.

It can then be concluded from Plates XIa and b that the single component nanoparticles of Ag_2O or TiO_2 nanoparticles exhibited closely packed agglomerated crystals arrangement with less lattice stripe. This is because no doping agent was added to the lattice layer of the nanoparticles. While more pores and voids fraction was observed in Plate XI (c) and (d) due to the incorporation of Ag onto the lattice layer of TiO_2. The creation of more space and channels may be responsible for the slight decrease in crystallite size as confirmed by XRD and HTEM.

This implies an increase in the specific surface area of Ag_2O-doped TiO_2. This would improve its adsorption performance compared to undoped TiO_2 nanoparticles (Figure 4.25). This suggests good dispersion of Ag_2O on the lattice layer of TiO_2. Comparing Plate XI (c) and (d), it can be concluded that Ag_2O particles were more readily dispersed and deposited in Plate XI (d) than in Plate XI (c). Thus, the doping effect influences the morphological arrangement, which will in turn influence the efficiency of the nanoparticles formed (Oguzhan *et al.*, 2016). The surface morphology of the Ag_2O-clay, TiO_2-clay, Ag_2O/TiO_2-clay (1:3), Ag_2O/TiO_2-clay (1:1), and Ag_2O/TiO_2-clay (3:1) nanocomposite samples are presented in Plate XII (a-e), respectively.

Plate XIIa reveals the presence of tiny, spherical particles of the Ag_2O on the surface of the nanoclay. There is the presence of voids due to the incorporation of Ag_2O onto the lattice layer of the activated clay similar to that of activated clay. Plate XII (b) represents the immobilization of TiO_2 onto clay structures which revealed evidence of evenly dispersed spherical crystals of TiO_2 on the clay structure. The hemispherical arrangement also suggests an even incorporation of TiO_2 nanoparticles on the clay structure.

Plate XIIc shows the morphology of Ag_2O/TiO_2 with a 1:1 mixing ratio, immobilised on (3) clay, which reveals the intertwining of disposition between the morphology presented in Plate XII a and b. The crystals remain spherical, sparsely dispersed and with an improvement in the pores formed, however, uneven interstitial and sandwiched arrangement of the nanocomposites were still observed. Plate XIId presents HRSEM of Ag_2O/TiO_2-clay (1:1). The disposition appears similar, however, the particles were more randomly distributed than that of Plate XIIc. The aggregated spherical and flake-like nanoparticles were seen dispersed on the surface of the nanocomposites. Plate XIIe shows composites of Ag_2O/TiO_2-clay (3:1) with observed spherical crystals, which are evenly distributed better than those of Plates XII (c) and (d).

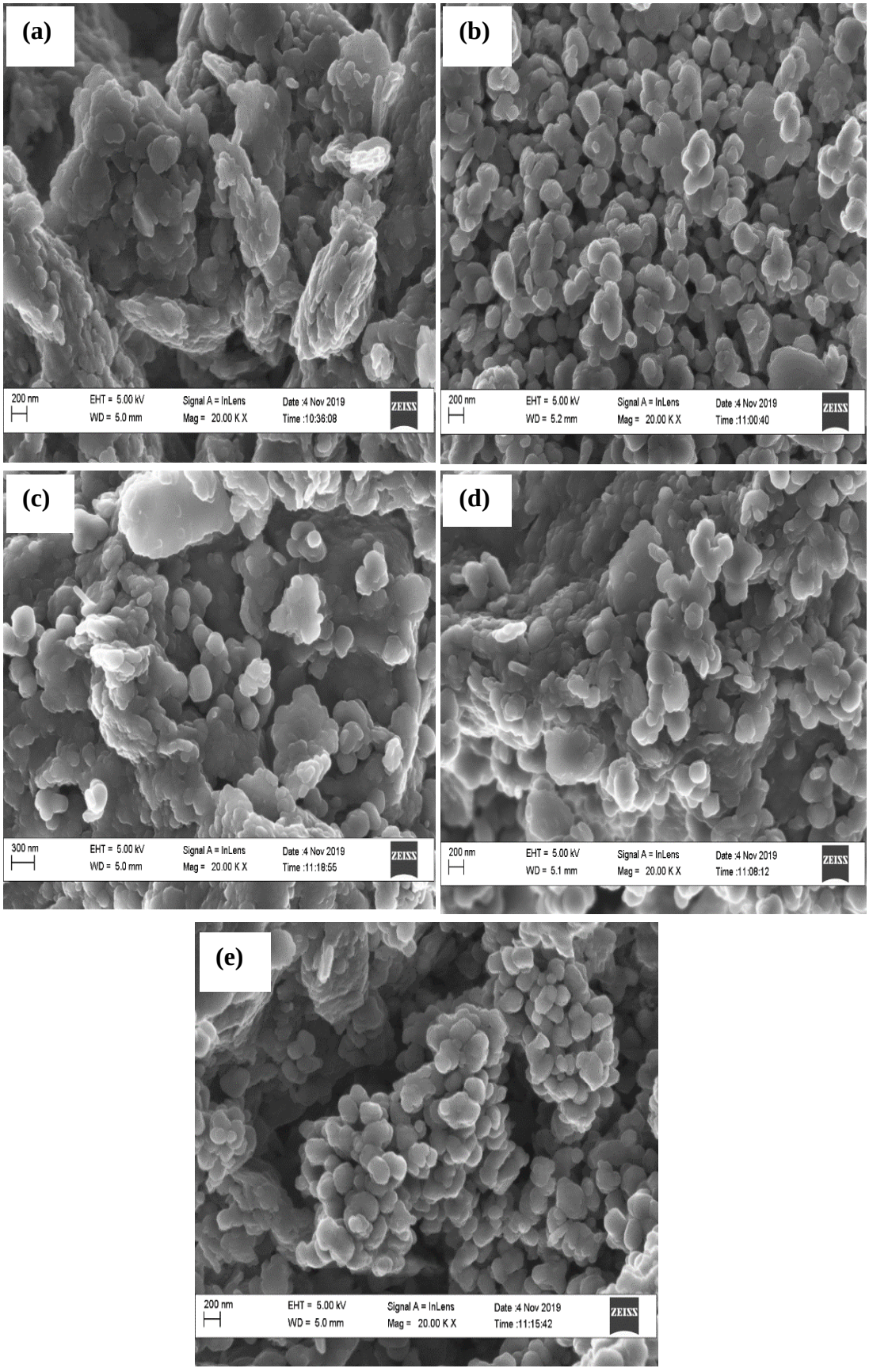

Plate XII: HRSEM micrographs of (a) Ag_2O-clay, (b) TiO_2-clay, (c) Ag_2O/TiO_2 /clay (1:3) (d) Ag_2O/TiO_2 -clay (1:1), and (e) Ag_2O/TiO_2-clay (3:1)

However, there is a slight disappearance of voids compared to Plate XII (d), due to a higher amount of Ag_2O/TiO_2 deposited or diffused onto the lattice of the clay matrix, thereby clogging the clay. Large agglomerates on the Ag_2O/TiO_2-clay nanocomposites, coupled with rugged and porous surfaces would provide more sites for the adsorption of heavy metals ion from an aqueous matrix (Ouyang *et al.*, 2019).

4.5.4 The EDS analysis

EDS analysis of clays

The elemental compositions of the raw clay, beneficiated clay and activated clay determined using EDS are shown in Plate XIII (a-c).

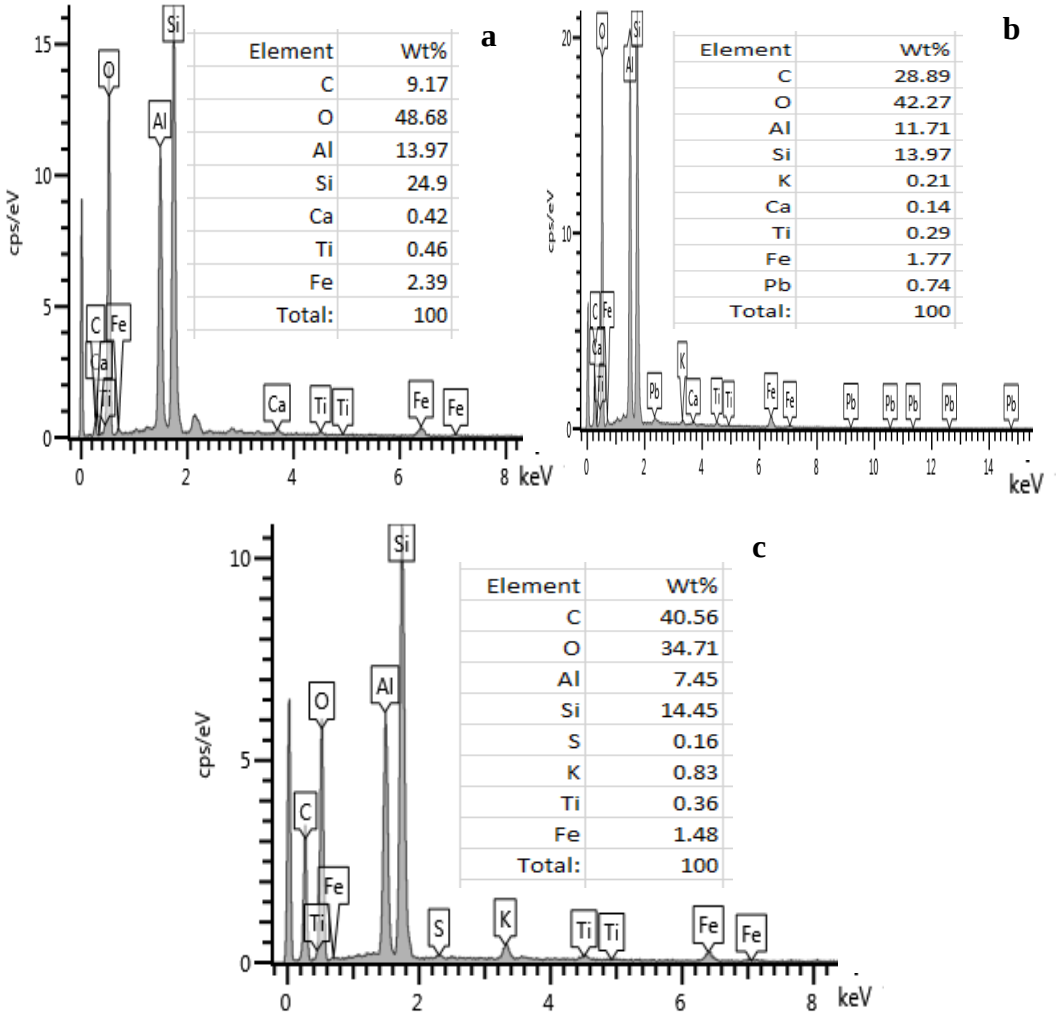

Plate XIII: EDS Spectrum of clay (a) raw (b) beneficiated and (c) activated

The Plate reveals the characteristic lines of C, O, Al, Si, Ca, Ti and Fe elements present in the three samples. From the EDS result obtained as shown in Table 4.10, the highest percentage of oxygen (48.68%) on (a) was due to the presence of oxides of the elements in the raw clay sample. While the oxygen reduction (48.68% to 42.27% and 34.71% respectively) may be due to the washing away by the beneficiation and acid activation processes. The element oxygen has the highest initial percentage composition followed by silicon with 24.9% composition, then aluminium (13.97%).

The percentage composition of aluminium was reduced to 11.71% and 7.45% in beneficiated and activated clay. Others are; iron, which reduced from 2.39% to 1.77% and 1.48%. Traces of titanium (0.46%), calcium (0.42%) and sulphur (0.16%) were observed in activated clay. The 0.74% Pb element was not evident in raw clay (XIIIa) but in beneficiated clay (XIIIb), probably be-clouded by other major elements. The lead ion (Pb) observed in beneficiated clay was absent in the activated clay elemental composition, as a result of being washed away by the acid activation process of the clay (XIIIc).

The EDS shows a decreased progression in aluminium content with silicon, due to the washing away of free silica during the beneficiation and activation reaction process. This result reveals that the clay is an alumina-silicate in nature, which depicts the composition of a typical kaolinite. It was also observed that the raw, beneficiated and activated clay are all composed of titanium oxide, though in small quantities. However, the presence of titanium oxide is desirous, as it can make a viable agent for bio-related applications.

Table 4.10: EDS Elemental composition of clays

Element	C	O	Al	Si	Ca	Ti	Fe	K	S	Pb	Total
Raw	9.17	48.68	13.97	24.90	0.42	0.46	2.39	-	-	-	100
Beneficiated	28.89	42.27	11.71	13.97	0.14	0.29	1.77	0.21	-	0.74	100
Activated	40.56	34.71	7.45	14.45	-	0.36	1.48	0.83	0.16	-	100

The EDS shows a decreased progression in aluminium content with silicon, due to the washing away of free silica during the beneficiation and activation reaction process. This result reveals that the clay is an alumina-silicate in nature, which depicts the composition of a typical kaolinite. It was also observed that the raw, beneficiated and activated clay are all composed of titanium oxide, though in small quantities. However, the presence of titanium oxide is desirous, as it can make a viable agent for bio-related applications.

EDS elemental composition of Ag_2O, TiO_2 and Ag_2O/TiO_2 nanoparticles

The EDS spectrum of the synthesised Ag_2O, TiO_2 and Ag_2O/TiO_2 nanocomposites are presented on Plate XIV (a-c).

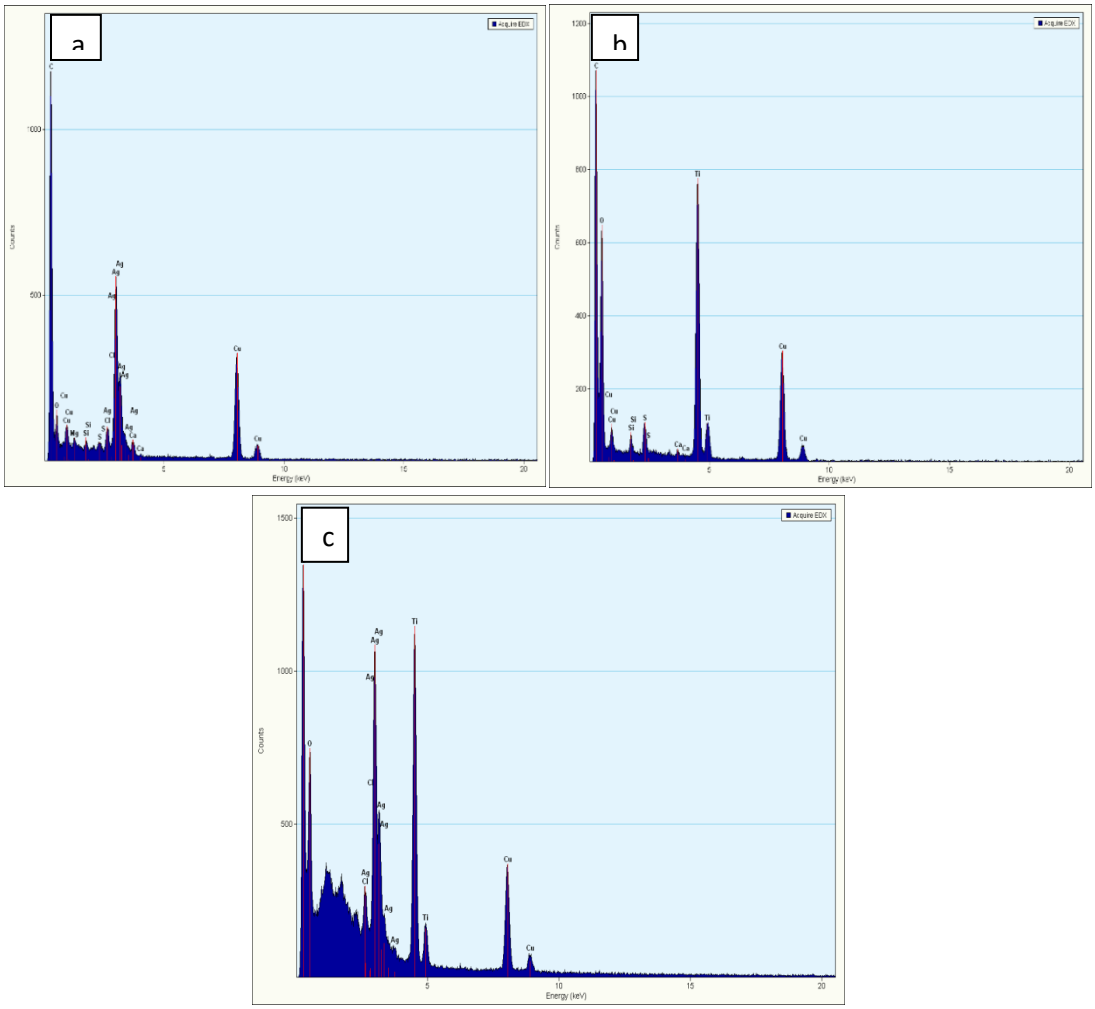

Plate XIV: EDS of (a) Ag_2O (b) TiO_2 (c) Ag_2O/TiO_2 nanoparticles

The Plates show the characteristic lines of Ag, Ti, O and other elements. The EDS spectrum of Ag_2O in Plate XIVa shows the presence of Ag as the dominant element having 58.2% composition, and 29.0% Oxygen combined as oxide. Magnesium and calcium presence can be attributed to other components of the leaves extract while the percentage composition of Cu is from the copper grid used for the analysis. The percentage composition of Ti (58.07%) was the highest in Plate XIVb for the TiO_2 nanoparticles as shown in Table 4.11 which is expected, as only TiO_2 was synthesised, other elements present are oxygen (40.3%) and calcium (1.63%). In the spectra of Ag_2O/TiO_2 nanoparticles, silver was also evident to be 8.40%, Ti of 55.28% as shown in Plate XIVc. Other elements present such as Si and Cu are traced to the analysis grid while the Ca content is from the leaf extract used in the synthesis.

The EDS analysis of nanocomposites

Plates XV (a-e) are the EDS of Ag_2O-clay, TiO_2-clay, Ag_2O/TiO_2-clay (1:3), Ag_2O/TiO_2-clay (1:1) and Ag_2O/TiO_2-clay (3:1) respectively. The elemental composition of the nanocomposites as shown in the Plates at binding energy between 0-20 keV revealed the presence of C, O, Al, Si, S, K, Ti, Fe, Ag, and Ca. The nanocomposites of Ag_2O-clay confirmed the existence of silver in the doped matrix. While that of TiO_2-clay also confirmed the significant amount of titanium in the alumina-silicate clay. It was observed that, for an increased clay ratio (75%) on Plate XV(d) and Table 4.12, the Ag was not detected.

Table 4.11: EDS Elemental composition of nanoparticles

Elements	O	C	Ti	Ag	Ca	Cu	Si	Total
Ag_2ONps	29.0	-	-	58.2	-	12.8	-	100
TiO_2Nps	40.03	-	57.05	-	1.63	1.09	0.20	100
Ag_2O/TiO_2	22.62	9.85	55.28	8.40	0.82	2.21	0.82	100

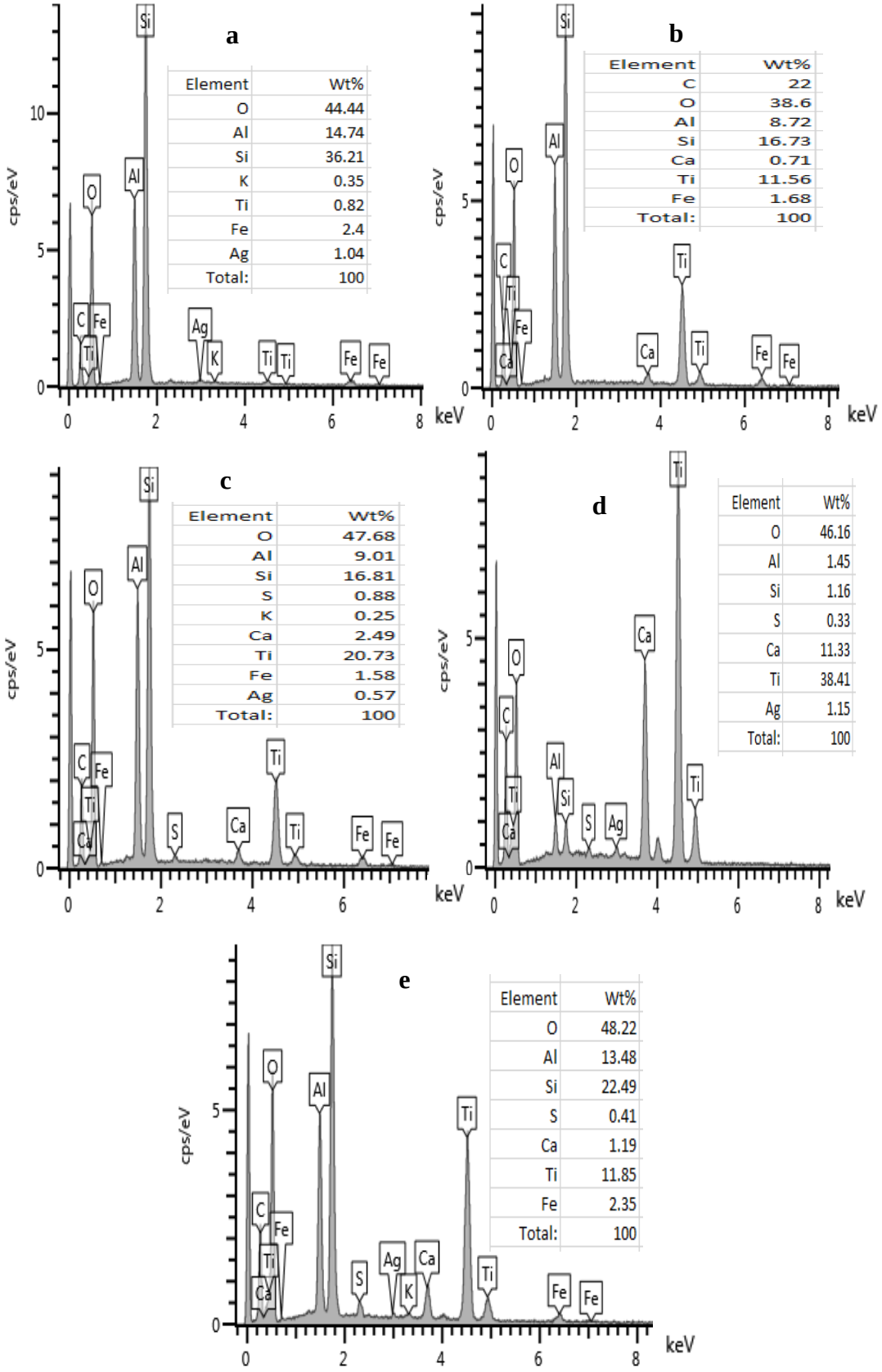

Plate XV: EDS micrographs of (a) Ag_2O-clay, (b) TiO_2-clay, (c) Ag_2O/TiO_2 (25%)-clay (1:1), (d) Ag_2O/TiO_2-clay (3:1), and (e) Ag_2O/TiO_2-clay (1:3)

Table 4.12: EDS Elemental composition of nanocomposites

Element	C	O	Al	Si	S	K	Ti	Fe	Ag	Ca	Total
NC1(a)	-	44.44	14.74	36.21	-	0.35	0.82	2.4	1.04	-	100
NC2 (b)	33.60	44.25	5.93	10.93	-	-	4.43	0.55	-	0.33	100
NC3 (c)	-	48.22	13.48	22.49	0.41	-	11.85	2.35	-	-	100
NC4 (d)	-	46.16	1.45	1.16	0.33	-	38.41	-	1.15	11.33	100
NC5 (e)	-	47.68	9.01	16.81	0.88	0.25	20.73	1.58	0.57	-	100

This indicates the overshadowing of Ag_2O by clay due to its low concentration. However, with an increase in Ag_2O loading onto the clay structure, Ag becomes visible in the doped titanium. In Plate XIV (a), Silicon (36.21%) was the most prominent element of the alumina-silicate clay due to the reaction with tetraoxo sulphate (VI) acid (H_2SO_4) and the washing away of the aluminium content. The 2:1 ratio of silicon to aluminium composition in each nanocomposite (a-d), as observed in the table, showed that the kaolinite nature of the clay was still maintained irrespective of the nanoparticle type immobilised on it (Diko *et al.*, 2016).

The nanocomposite (d) has the highest titanium (38.41%) and silver (1.15%) loading composition as expected due to the large ratio of Ag_2O/TiO_2 immobilised on only 25% of clay. The presence of sulphur in nanocomposites c, d and e is from the acid activation process, and it was below the detectable limit in Ag_2O-clay and TiO_2-clay due to the small quantity of clay used in the nanocomposites a and b, while Ca and K content is traced to the leaves extract used for nanoparticles synthesis. The results presented revealed a significant interaction between the Ag_2O, TiO_2 and clay, evidence of doping and immobilisation on clay structure.

4.5.5 XRD analysis

XRD analysis of Ag_2O nanoparticles

The phase structure of Ag_2O nanoparticles examined using XRD and their corresponding diffraction pattern is shown in Figure 4.14. The XRD pattern shows the formation of a sharp intense peak, at a 2Ɵ value of 38.12º. Other peaks were noticed at 2Ɵ values of 44.53º, 64.61º, 77.62º and 81.78º. These peaks aligned well with the crystal planes of (110), (200), (111), (210), (211) and (220), corresponding to the face-centred cubic (FCC) structure with JCPDS 004-0784.

The result also revealed that the Ag_2O nanoparticles formed based on the interaction of Ag salt precursor with the aqueous leaves extract of *Parkia biglobosa* (Equation 4.1). The crystallite size (D) of the synthesised Ag_2O was found to be 5.79 nm using Scherer's equation (Equation 3.7). The crystallite size obtained in the present research is smaller when compared to the 26 nm reported by Anju *et al.* (2018).

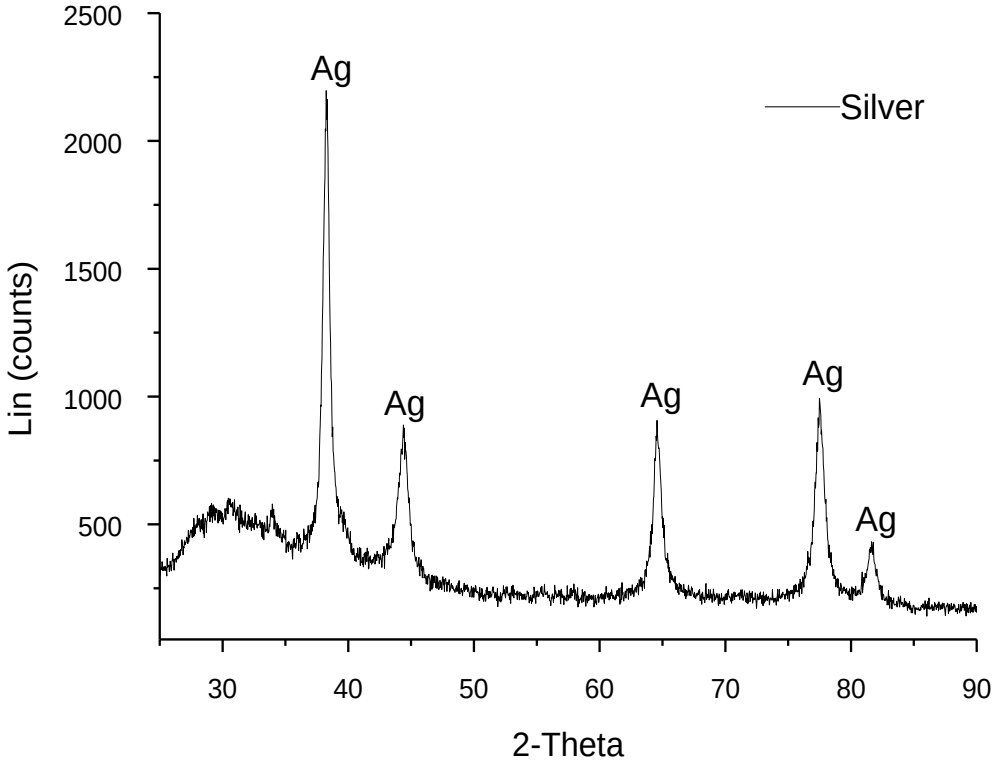

Figure 4.14: XRD pattern of unmodified silver nanoparticles

XRD analysis of TiO_2 nanoparticles

The XRD pattern of the various titanium dioxide nanoparticles is shown in Figure 4.15. The XRD spectra of Figure 4.15a with operating conditions in Table 3.6, demonstrated the presence of intense diffraction peaks at 2Θ values of 27.4°, 36.1°, 39.2°, 41.2°, 44.0°, 54.3°, 56.8°, 62.7° and 69.8° corresponding to crystal planes of (110), (101), (200), (111), (210), (211), (220), (002) and (112).

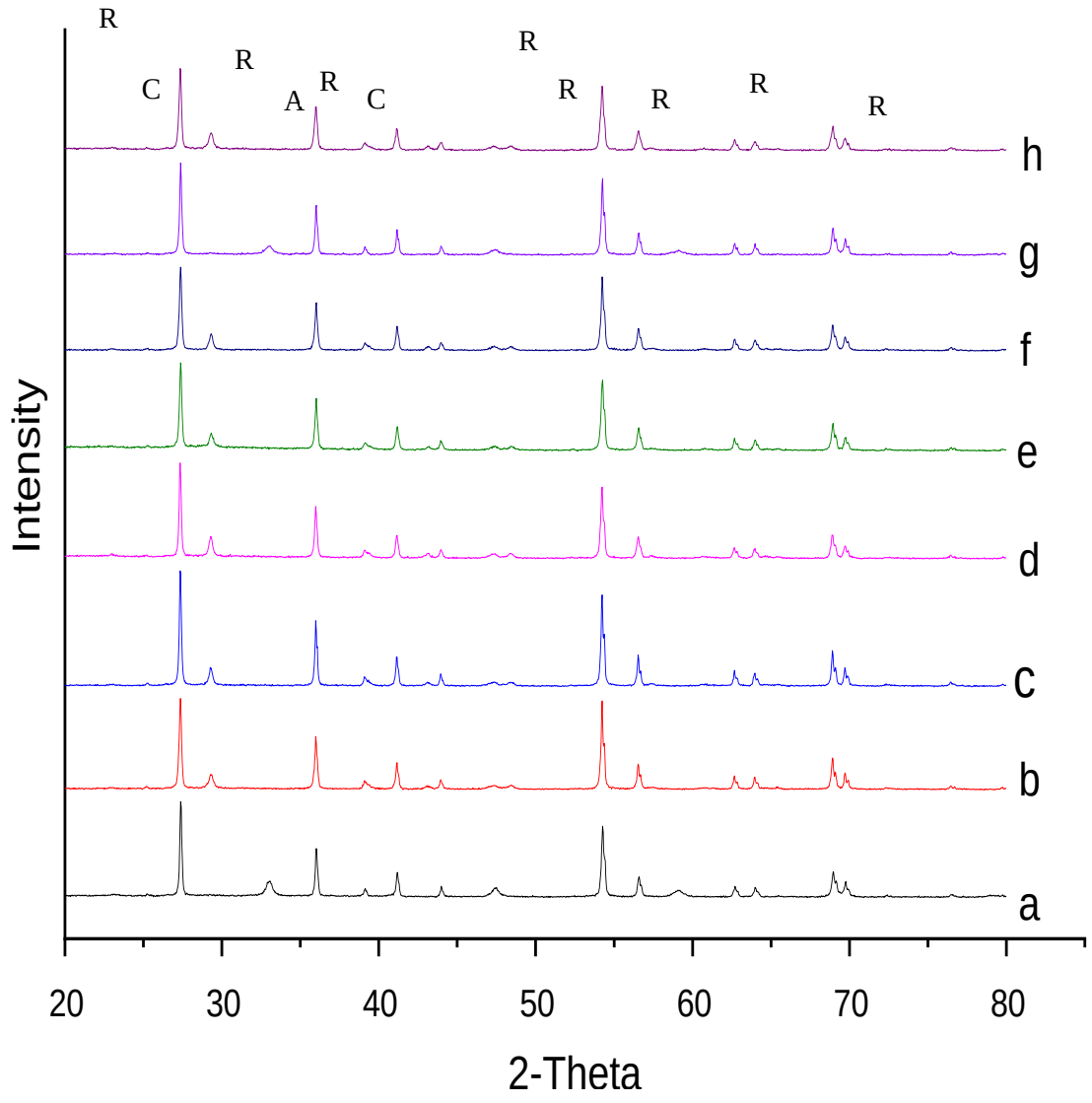

R-rutile, A- anatase, C-calcite

Figure 4.15: XRD patterns of synthesised TiO_2 nanoparticles at various operating conditions

The TiO_2 produced is tetragonal with the joint Committee on Powder Diffraction Standards (JCPDS) number 00-021-1276 for rutile phase titania. The intensity of the (110) and (211) facets was very much stronger than that of other facets in the spectrum. The presence of very few peaks of Perovskite ($CaO\text{-}TiO_2$) at 2Ɵ and crystal planes of 33.0° (110), 47.6° (018) and 60.9° (208) were noticed due to the calcium in *Parkia biglobossa* leaf extract used.

The run two (b) of the synthesised TiO_2 has more intense diffraction peaks than run one (a) with corresponding crystal planes at; 27.4° (110), 36.1° (101), 39.2° (200), 41.2° (111), 44.0° (210), 54.3°(211), 56.8° (220), 62.7° (002) and 69.8° (112) rutile, but with few peaks of calcite ($CaCO_3$), which may have resulted from leaf extract and analysis grid. The calcite peaks are at 23.2° (101), 44.1° (221) and 48.9° (230) respectively. The peaks of samples (a) and (g) shared a resemblance while those of samples (b), (c), (d), (e), (f) and (h) have different degrees of intensity.

It was also noticed that there was no peak shift in the diffraction pattern and no lattice distortion was observed, but the high intensity of rutile titanium was observed. The average crystallite size of the TiO_2 nanoparticle was 3.49 nm. The average crystallite size of the experimental run (a) is 9.52 nm while those of runs (b), (c), (d), (e), (f), (g) and (h) are 5.51 nm, 8.49 nm, 8.59 nm, 6.41 nm, 5.01 nm, 3.49 nm and 4.28 nm respectively. The large crystallite sizes obtained in runs (a), (c), (d) and (f) may be due to low stirring speed, because, a reduction in the stirring speed to 100 rpm causes low interaction which encourages coalescence during precursor and aqueous leaves extract stirring on the magnetic stirrer, thus making the volume aqueous leaves extract insufficient for TiO_2 precursor. This led to the formation of large-sized TiO_2 nanoparticles obtained in runs (a), (c), (d) and (f).

On the contrary, sufficient stirring speed, and volume of leaves extract to precursor volume make interaction sufficient. There was no coalescence of particles, thereby causing the formation of small-sized TiO_2 nanoparticles as observed in runs (b), (e), (f), (g), and (h) (Gunanto *et al.*, 2018). These results reveal that the run (g) has the smallest crystallite size which indicates a large surface area for the titanium. The figure reveals that all the eight TiO_2 nanoparticles synthesised at different conditions (Table 3.6) belong to the rutile phase.

XRD analysis of Ag_2O/TiO_2

Figure 4.16(a-c) represents the XRD pattern of Ag_2O-TiO_2 nanocomposites with varying concentrations of aqueous $AgNO_3$ solution. The XRD spectra of 0.01molL^{-1} Ag_2O doped TiO_2 as shown in Figure 4.16a demonstrates the presence of diffraction peaks at 2Θ values and corresponding crystal planes of 27.4° (110), 36.1° (101), 39.2° (200), 41.2° (111), 44.0° (210), 54.3°(211), 56.8° (220) and 69.8° (112).

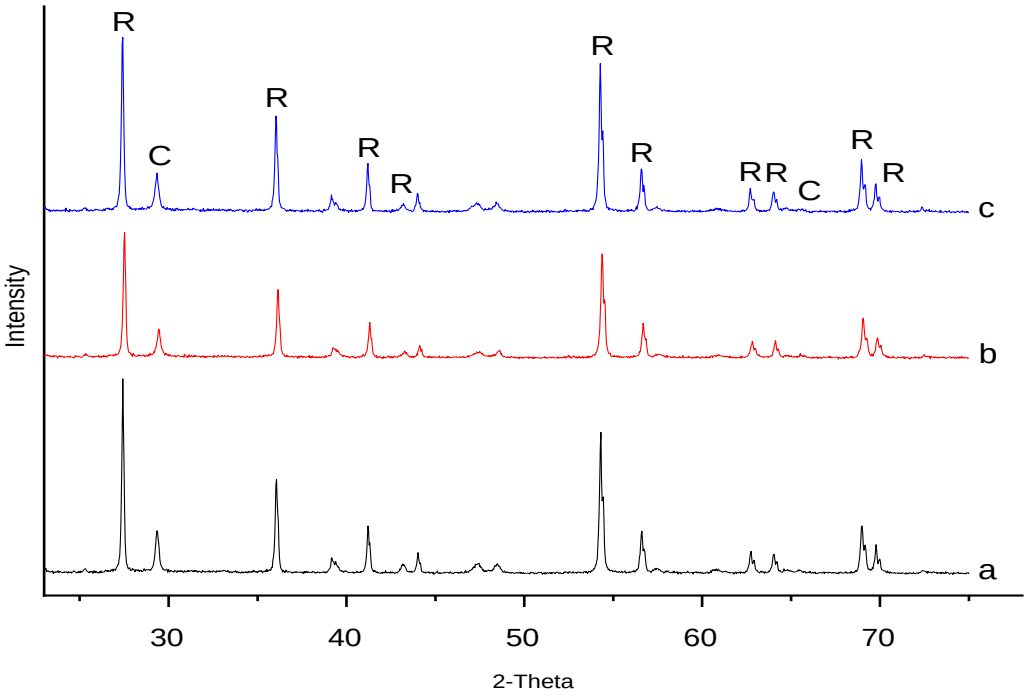

Figure 4.16: XRD patterns of synthesised Ag-TiO_2 nanoparticles at various concentrations of Ag_2O (a) 0.01 molL^{-1} (b) 0.02 molL^{-1} (c) 0.05 molL^{-1}

Keys: R= Rutile TiO_2 C= Calcite

These are assigned tetragonal titania, which agrees with the JCPDS number 00-021-1276 for the rutile phase. The XRD patterns indicate the formation of the pure rutile phase of TiO_2 despite the incorporation of Ag as a dopant. This implies that the addition of Ag_2O did not change the phase of TiO_2 nanoparticles. The average crystallite size calculated using Scherer's equation is 4.98 nm. Similarly, for the 0.02 $molL^{-1}$ Ag_2O doped TiO_2 (Figure 4.16b) and 0.05mol/dm^3 Ag_2O doped TiO_2 (Figure 4.16c), the diffraction peaks could be indexed to tetragonal rutile phase titanium oxide.

However, new peaks were formed due to an increase in silver loading, the new peaks may be linked to the change in colour from white TiO_2 nanoparticles to grey Ag_2O/TiO_2 nanocomposites. The new peaks discovered on nanocomposite (c) (0.05$molL^{-1}$ Ag_2O doped TiO_2) were more than those on (b) (0.02 molL-1 Ag2O doped TiO2). The average crystallite sizes of doped nanocomposites (Figure 4.16b and c) are 3.84 nm and 3.58 nm respectively. The decrease in the average crystallite size noticed can be linked to the higher concentration of silver in the former than in the latter. Therefore, it appears that the Ag loading did not significantly influence the crystalline structure and phase of TiO2, however, it slightly influenced the crystallite size. The Ag2O phase could not be detected by the XRD, due to its low concentration in the Ag-TiO2 matrix. Silver with an ionic radius (0.115 nm) greater than titanium (0.061 nm) did not diffuse onto the lattice layer of the TiO2 matrix, however, slightly caused a lattice distortion (Pham and Lee, 2014). A similar observation was also reported by Bagheri et al. (2015) for Ag-TiO2 powders. Non–detection of Ag_2O by the XRD may be due to insufficient Ag2O content in the composite (Petrik et al., 2012; Shameli et al., 2011). Therefore, the Ag2O did not influence the morphology and the phase of TiO2, corroborating the HRSEM and XPS results. Figure 4.17(a-e) show the XRD patterns of Ag_2O-clay, TiO_2-clay, Ag_2O/TiO_2-clay (3:1), Ag_2O/TiO_2-clay (1:1), and Ag_2O/TiO_2-clay (1:3) respectively.

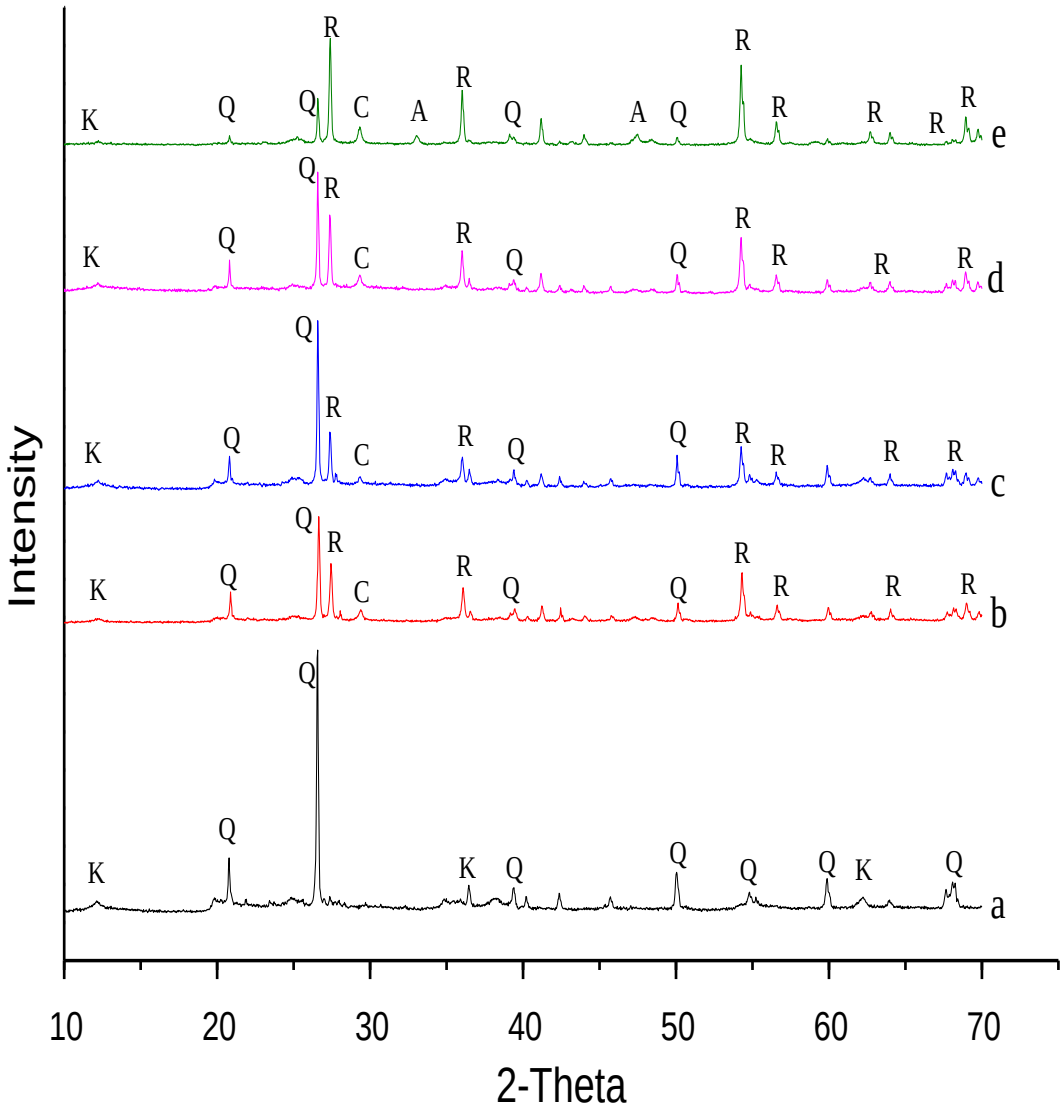

Figure 4.17: XRD pattern of (a) Ag_2O-clay, (b) TiO_2-clay, (c) Ag_2O/TiO_2-clay (3:1), (d) Ag_2O/TiO_2-clay (1:1) and (e) Ag_2O/TiO_2-clay (1:3)

Keys:Rutile-R, K-kaolin, Q-quartz, K-kaolin, C-calcite A-anatase

According to Figure 4.17a, diffraction peaks were observed at 2 theta values of 12.36º, 19.92º, 24.8º 35.91º, 38.4º and 62.34º with miller indices; (001), (020), (002), (-131), (-113) and (060) respectively which shows the presence of kaolinites type of clay (Dewi *et al.*, 2018). The presence of strong, sharp and relatively intense diffraction peaks at 2Θ values of 20.93º (100), 26.59º (101), 36.48º (110), 50.00º (112) and 68.57 (134) which agreed with the literature (JCPDS card no-083-0539), indicating the presence of SiO_2 on the Ag_2O-clay composite (Munasir *et al.*, 2018; Munasir *et al.*, 2015).

There are no diffraction peaks observed for Ag in the composite Ag_2O-clay due to low silver concentration (Bagheri *et al.*, 2015; Petrik *et al.*, 2012). However, EDS and XPS results confirmed the presence of Ag in the composite sample. Figure 4.17b which represents the XRD pattern of TiO_2-clay nanocomposite revealed the occurrence of sharp and intense diffraction peaks at 2Ɵ value and corresponding miller indices of 27.62º (110), 36.10º (101), 41.24º (111), 44.06º (210), 54.42º (211), 56.76º (220), 62.90º (002), 64.10º (310), 69.38º (301) and 70.14º (112). These peaks matched well with a typical rutile phase of TiO_2 nanoparticles with JCPDS number (00-021-1276). Whereas the diffraction peaks were observed at 12.43º (001), 26.59º (101), 34.90º (-130), 36.10º (110), 39.43º (012) and 40.42º (111) were associated with kaolinite and Quartz/SiO_2. These results further confirmed that the prepared rutile TiO_2 was well intercalated on the Kaolin surface.

Figures 4.17c, d and e present a similar pattern showing several intense peaks of rutile phase TiO_2, kaolinites and hexagonal SiO_2. The TiO_2 peaks were well intercalated between the peaks observed in the clay crystals. The intensity of the rutile phased TiO_2 was highest in Figure 4.17e, followed by that of Figure 4.17d, and the least was that of Figure 4.17c. The differences may be linked to the weight percentage loading of the nanoparticles onto the clay.

Therefore, XRD patterns of Figures 4.16 and 4.17, obviously show that the doping of Ag_2O on TiO_2 nanoparticles did not cause phase transformation from rutile to either anatase or brookite. The diffraction peaks earlier noticed on TiO_2 and Ag_2O/TiO_2 were also found on all the Ag_2O/TiO_2-clay nanocomposites. The crystallite sizes were calculated to be 5.79 nm (Ag_2O), 3.98 nm (TiO_2), 7.86 nm (Ag_2O/clay), 6.11 nm (TiO_2/clay), 7.24 nm (7.5% Ag_2O/TiO_2-clay), 6.29 nm (5% Ag_2O/TiO_2-clay) and 8.75 (2.5% Ag_2O/TiO_2-clay) nm respectively.

Comparatively, the peak intensity and crystallinity were enhanced by doping Ag_2O and TiO_2 on clay. This may also improve the adsorptive performance of nanocomposites.

4.5.6 BET analysis of Activated clay, Rutile-TiO_2, Ag_2O-clay, TiO_2-clay and Ag_2O/TiO_2-clay nanocomposites

The specific surface areas of the Activated clay, undoped rutile TiO_2, Ag_2O-clay, TiO_2-clay and the Ag_2O/TiO_2-clay ternary nanocomposites were measured using BET based on N_2 adsorption-desorption isotherms. The surface area and pore volume of each prepared catalyst value are given in Table 4.13 and the plot in Figure 4.18.

Table 4:13 BET surface area, pore diameter, pore volume of Activated clay, TiO_2, Ag_2O-clay, TiO_2-clay and the Ag_2O/TiO_2-clay ternary nanocomposites

Samples	BET surface area (m^2/g)	Pore volume (cc/g)	Pore diameter (nm)
Beneficiated clay	13.94	0.016	2.955
Activated clay	14.15	0.069	17.67
Synthesised R-TiO_2	10.23	0.093	4.09
Ag_2O-clay	11.59	0.18	3.55
TiO_2-clay	32.98	0.15	4.86
Ag_2O/TiO_2-clay	48.07	0.16	4.09

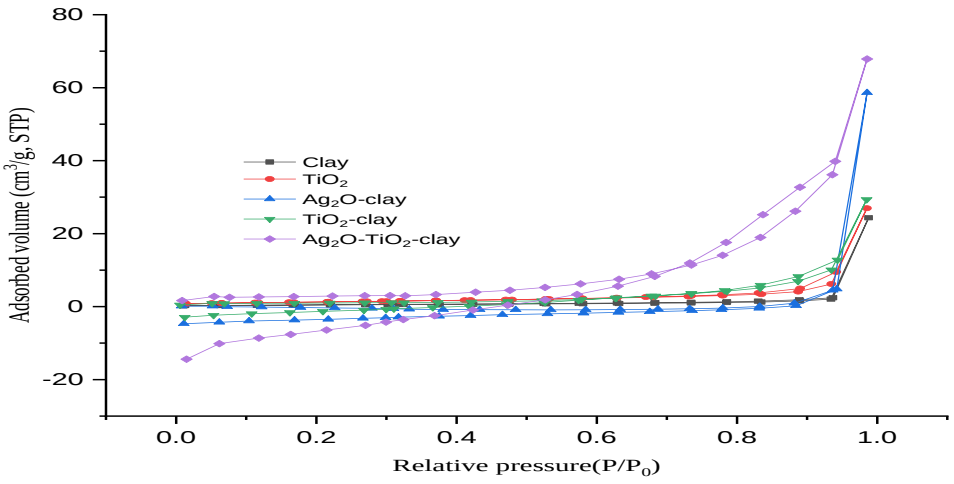

Figure 4.18: BET adsorption-desorption isotherm plots of (a) Activated clay (b) TiO_2 (c) Ag_2O-clay (d) TiO_2-clay (e) Ag_2O/TiO_2-clay

From the Table 4.13, Acid activated clay has a surface area of 14.15 m^2/g while TiO_2 has 10.23 m^2/g which shows that the former has a larger surface area than the latter. This claim is similar to the findings of Akinnawo (2019); Krishnan and Mahalingam (2017) who also reported low surface area for TiO_2. The Ag_2O-clay has a surface area of 11.59 m^2/g, the TiO_2-clay composite has 32.98 m^2/g while the ternary composite Ag_2O/TiO_2-clay has 48.07 m^2/g. The specific surface area of the Ag_2O-clay is observed lesser than that of undoped activated clay. This may be due to the deposition of the silver oxide nanoparticles on the pores of the clay, thereby causing a reduction in the surface area of the Ag_2O-clay nanocomposite.

However, the higher surface area of the TiO_2-clay was due to modification by the rutile-TiO_2 which agrees with the literature (Krishnan and Mahalingam, 2017). The specific surface area and pore volume of TiO_2-clay and Ag_2O/TiO_2-clay were significantly increased to 32.98 m^2/g, 0.15 cc/g and 48.07 m^2/g, 0.16 cc/g. This is due to the dispersed stacking of TiO_2 on the surface of the acid-activated clay and the synergistic interaction between the silver oxide and titanium (IV) oxide deposited on the surface of the ternary Ag_2O/TiO_2-clay composite. Also, the increase in surface area of Ag_2O/TiO_2-clay compared to Activated clay, TiO_2, Ag_2O-clay and TiO_2-clay may be linked to particle decrease in grain size of TiO_2 nanoparticles during the doping process.

The pore diameter of the prepared TiO_2-clay decreased after the modification by TiO_2. This is due to the in-situ deposition of the TiO_2 on the activated clay, which blocked some accumulated pores on TiO_2-AAC. On the other hand, the TiO_2-clay and Ag_2O/TiO_2-clay composite has a large specific surface area and pore volume. This is conducive for the removal and capturing of pollutant molecules from the aqueous matrix by the composite materials, with the Ag_2O/TiO_2-clay as the best.

According to the IUPAC classification (Sotomayor *et al.*, 2018), the samples demonstrated a Type IV adsorption isotherm of a typical mesoporous structure (Appendix G). This is similar to the one obtained by Malima *et al.* (2018). Besides, pure TiO_2 has a typical H1 hysteresis loop, which indicated the stacked mesoporous structure derived from the accumulated spherical particles.

Other samples display H3 hysteresis loops, which indicates that they have irregular mesopores and macropores. This is due to the irregular shape of particles and the composition of different components. The construction of a combined structure improves the particular surface area and pore volume of the Ag_2O/TiO_2-clay. The extensively constructed mesopores give the Ag_2O/TiO_2-clay significant adsorption capacity, which may enhance the adsorption ability of the Ag_2O/TiO_2-clay materials more than the other four materials (Xiang *et al.*, 2019). This study shows that the incorporation of silver-doped titanium (IV) oxide significantly improves the surface area of the activated clay and in addition, its adsorptive capability.

4.5.7 XPS studies

The XPS analysis was carried out to determine the surface oxidation state and orbital of each element present in the samples. Figure 4.19 (a-f) (Appendix B), shows the general survey spectrum of the prepared TiO_2, Ag_2O/TiO_2, clay, Ag_2O-clay, TiO_2-clay and Ag_2O/TiO_2-clay, respectively. Figure 4.19a revealed the presence of Ti (2s, 2p, 3s, and 3p) orbital at a binding energy of 568 eV, 460.1 eV, 80.3 eV, and 50.4 eV, respectively. A sharp narrow peak of oxygen (1s) was found at the binding energy of 529.7 eV while the binding energy for carbon (1s) was 284.8 eV. The titanium LMM Auger transition exhibits a sharp peak in the region of 880 eV and 760 eV which indicates the presence of the TiO_2 crystal. The binding energies obtained for titanium and oxygen agreed with the report of Krishnan and Mahalingam (2017).

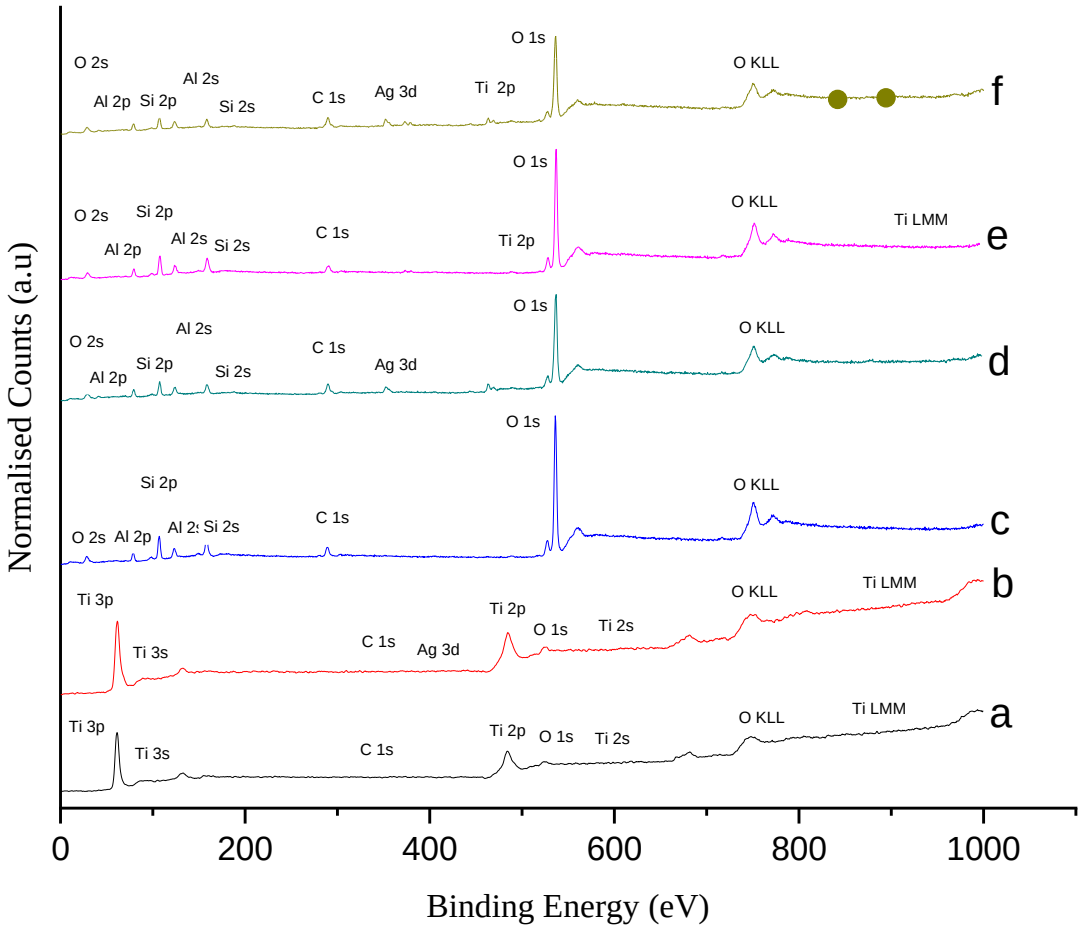

Figure 4.19: XPS Survey of (a) TiO_2 (b) Ag_2O/TiO_2 (c) activated clay (d) Ag_2O-clay (e) TiO_2-clay (f) Ag_2O/TiO_2-clay

Figure 4.19b shows the presence of titanium, oxygen, silver and carbon at different binding energies, revealing evidence of Ag_2O doping on TiO_2. Figure 4.19c which is the XPS of the activated clay sample, reveals the presence of Si (2s and 2p) at binding energies of 103.14(eV), C (1s) at 284.8 eV. A sharp narrow peak of oxygen (1s) was found at the binding energy of 529.7 eV. Figure 4.19d indicates the presence of silver (Ag), carbon (C), silicon (Si) and aluminium (Al) at different binding energies of 368.79, 284.80, 102.97 and 74.83 eV, respectively. The figure reveals the presence of Ag_2O doped on the alumina-silicate clay structure. This could not be seen in the XRD spectra in Figures 4.13 and 4.14. However, XPS confirms that the Ag_2O nanoparticles have been successfully immobilised on the clay due to its high sensitivity than XRD.

Figure 4.19e reveals the peaks of Ti, O, C, Ca, Si and Al, which demonstrate the existence of Ti and O on the surface of Ag_2O-clay nanocomposites. Figure 4.19f reveals the presence of Ti (2p), Ag (3d), Ca (2p), Si (2p), Al (2p), C (1s) and O (1s) orbitals at binding energies of 368.03, 347.07, 489.01, 107.07, 73.98 and 29eV, respectively. The presence of Ca ($2p^3$) peak observed in Figure 4.19c and d originates probably from the plant extract used during the synthesis of the TiO_2 nanoparticles. This is also confirmed by the XRD spectra.

Figure 4.19d is the XPS of the Ag_2O-clay showing Ag electrons belonging to the 3d orbital found at the binding energy of 368.79eV. This confirms that the Ag_2O nanoparticles were doped onto the alumina-silicate layer of the clay. The orbital level of Ti(2p) level shown in Figures 4.19c and d revealed a sharp narrow peak found around binding energies of 463.30eV and 458.34eV which depicts the presence of Ti $2p_{3/2}$ and Ti $2p_{1/2}$ respectively. This confirms the formation of pure Ti in the +4 oxidation state and further shows evidence of Ti^{+4} doping on the clay.

Figure 4.20 (a-d) is the deconvoluted XPS spectra of Ti 2p of TiO_2, Ag_2O/TiO_2, TiO_2-clay, and Ag_2O/TiO_2-clay samples, respectively. The figures show that Ti $2p_{1/2}$ and Ti $2p_{3/2}$ spin-orbital splitting photoelectrons in each of the four samples were located at similar binding energies. Figure 4.20a reveals the presence of two strong sharp peaks at binding energies of 459 and 465 eV respectively. These peaks are assigned to Ti $2p_{3/2}$ and Ti $2p_{1/2}$, which show a difference of 6 eV, an indication of the existence of Ti in the TiO_2 framework in the oxidation state of +4. This corroborates the reported values of Li *et al.* (2015). The Ti 2p peak deconvolution on Ag_2O/TiO_2 spectral (Figure 4.20b) shows the Ti $2p_{3/2}$ and Ti $2p_{1/2}$ in the binding energies at 458.7 and 464.5 eV, respectively.

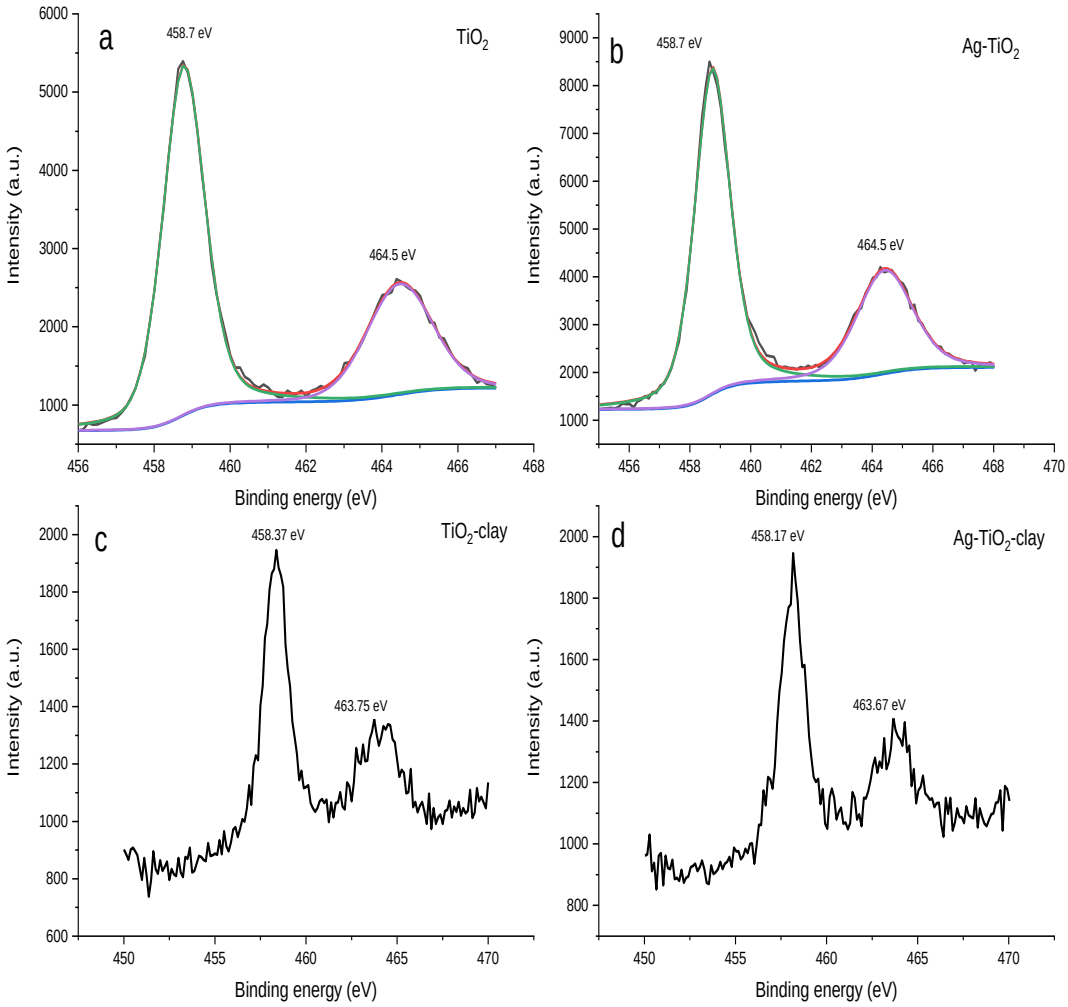

Figure 4.20: High resolution Ti 2p envelope and deconvoluted XPS spectra of TiO_2 in (a) TiO_2, (b) Ag_2O/TiO_2, (c) TiO_2-clay, (d) Ag_2O/TiO_2-clay

The value shows a slight decrease when compared to the 469 and 465 eV of the undoped TiO_2 nanoparticles. This is evidence of oxygen vacancies and the presence of defects in the TiO_2 lattice which was partly corrected by Ag. In addition, the excited electrons in TiO_2 nanoparticles were probably transferred to Ag_2O (Tijani *et al.*, 2017). Nevertheless, the +4 oxidation state (5.8 eV ~6 eV) was retained in the Ag_2O/TiO_2 nanocomposites supported by strong doublet peaks. Figure 4.20c presents the XPS of Ti in TiO_2-clay nanocomposites. Ti $2p_{3/2}$ and Ti $2p_{1/2}$ binding energies were further reduced to 458.37 and 463.75 eV when compared to that of TiO_2.

The decrease in binding energies is indicative of a reduction in the intensity of TiO_2 peaks in the TiO_2-clay sample and the formation of Ti-O-Si structure in the TiO_2 lattice through substitution reaction (substitution of transition metal ions) (Bharti *et al.*, 2016). This corroborates the HRSEM and XRD results displayed in Plate XIIb and Figure 4.17b.

Figure 4.20d represents the deconvoluted XPS spectra of Ti 2p for Ag_2O/TiO_2-clay. This revealed a further shift or reduction in the binding energies of TiO_2 on the surface of Ag_2O doped clay surface to 458.34 and 463.67 eV, when compared to 465 and 469 eV noticed for the pure TiO_2 only. This may also be attributed to the formation of Ti-O-Si, Al-O-Si, Ag-O-Ag, and Ti-O bend or chemical combination on the nanocomposite structure (Krishnan and Mahalingam, 2017). The observed shift in the deconvoluted spectra as shown in Figure 4.20 (b, and d) also indicates a strong interaction between Ti and Ag atoms and the absence of Ti^{3+} signals in any of the Ti 2p spectra (Bharti *et al.*, 2016). Figure 4.21 (a-c) is the deconvoluted XPS spectra of Ag in Ag_2O in the three samples (Ag_2O-TiO_2, Ag_2O-clay and Ag_2O-TiO_2-clay) respectively.

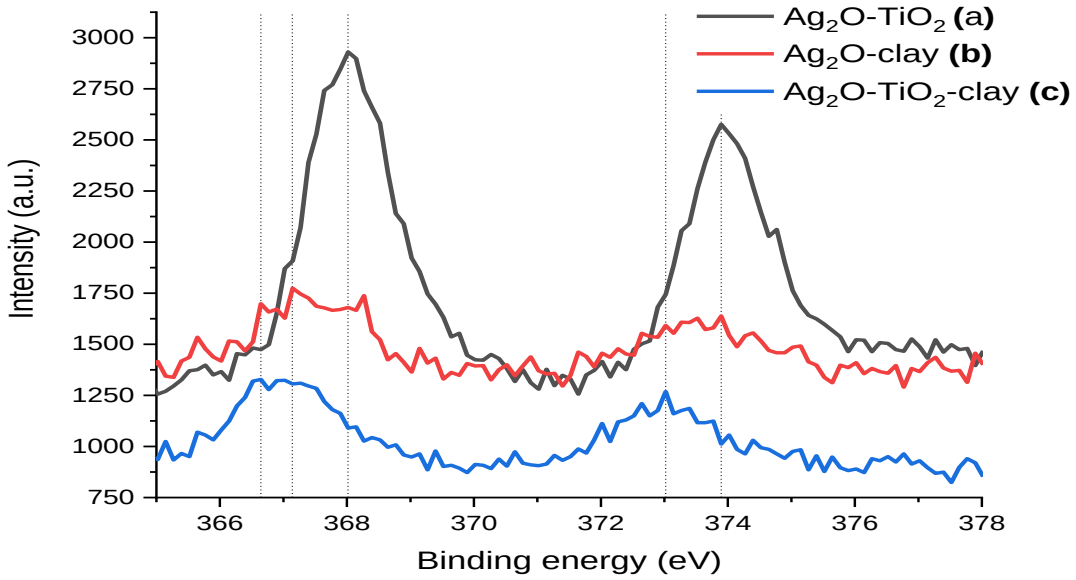

Figure 4.21. High-resolution Ag_2O (3d) envelope and deconvoluted XPS spectra of Ag in (a) Ag_2O-TiO_2 (b) Ag_2O-clay (c) Ag_2O/TiO_2-clay

Figure 4.21a reveals the presence of two sharp peaks at binding energies of 368.5 eV and 373.9 eV. The split peak observed was assigned to Ag $3d_{5/2}$ (368.5 eV) and Ag $3d_{3/2}$ (373.9 eV) respectively. The binding energy difference found between the split 3d doublet is approximately equal to 6.0 eV. This indicates that the oxidation state of Ag present on the surface of TiO_2 is zero. This is similar to the report of Krishnan and Mahalingam (2017). This implied that metallic silver from the $AgNO_3$ precursor has been reduced by the plant extracts and TiO_2 under visible light exposure. It is therefore evident that, despite the differences in the ionic radius of Ag (0.115 nm) and Ti (0.061 nm), some Ag in zero oxidation state species possibly penetrated the framework of TiO_2, suggesting a mutual interaction between the dopant and the TiO_2 matrix.

Figure 4.21b is the deconvoluted XPS spectra of Ag in Ag_2O-clay. The figure shows evidence of a reduction in the binding energies of Ag peaks observed at 367.14 and 373.89 eV in comparison with that of Ag in the Ag_2O/TiO_2. But with a wider difference of ~7.0 eV unlike that of Ag_2O/TiO_2 nanocomposites. This implies that Ag in the Ag_2O-clay composite exists in the form of Ag_2O in the Ag-Si framework (Sadasivam and Rao, 2016). Figure 4.21c presents the Ag deconvoluted in Ag_2O/TiO_2-clay nanocomposite. The figure shows two peaks of low intensity similar to the shift in the binding energies (366.65 and 373.02 eV) noticed for Ag in Ag_2O/clay composite which represents Ag_2O nanoclusters. This formation suggests a partial replacement of one oxygen in the TiO_2 lattice structures.

Contrary to the observed trend in the case of Ag-doped TiO_2 where Ag exists in a zero oxidation state, it was noticed that Ag exists in the form of Ag_2O in the Ag-O-Ti nanocomposites co-doped with the clay. The XPS analysis revealed that the dopants (silver and silicon) have different interactions with the TiO_2 nanoparticles. In the case of Ag, there was evidence of chemical bonding of Ag^0 or Ag_2O onto TiO_2.

This implies that either Ag^{o} or Ag^{+} was anchored onto the superficial surface of TiO_2. Therefore, the incorporation of Ag, Ti and Si did not change the electronic state of Ti from Ti^{4+} to Ti^{3+} and as such, the phase structure of TiO_2 was not affected or destroyed as evident in the XRD result shown in Figure 4.15.

Figure 4.22 (a-d) shows the deconvoluted XPS spectra of aluminium in the samples of activated clay, Ag_2O-clay, TiO_2- clay and Ag_2O/TiO_2-clay, respectively. The results obtained for the valence Al 2p for these samples show a shift to lower binding energies within the interval of 1 eV. The activated clay (Figure 4.22a) shows a single peak located at 74.93 eV which indicates the existence of Al in the +3 oxidation state. The value is similar to the report observed for Al 2p by Djebaili *et al.* (2015). The peak on the Ag_2O-clay shifted to 74.82 eV, while that on TiO_2- clay shifted to 74.10 eV, and that on Ag_2O/TiO_2- clay is located at 73.98 eV.

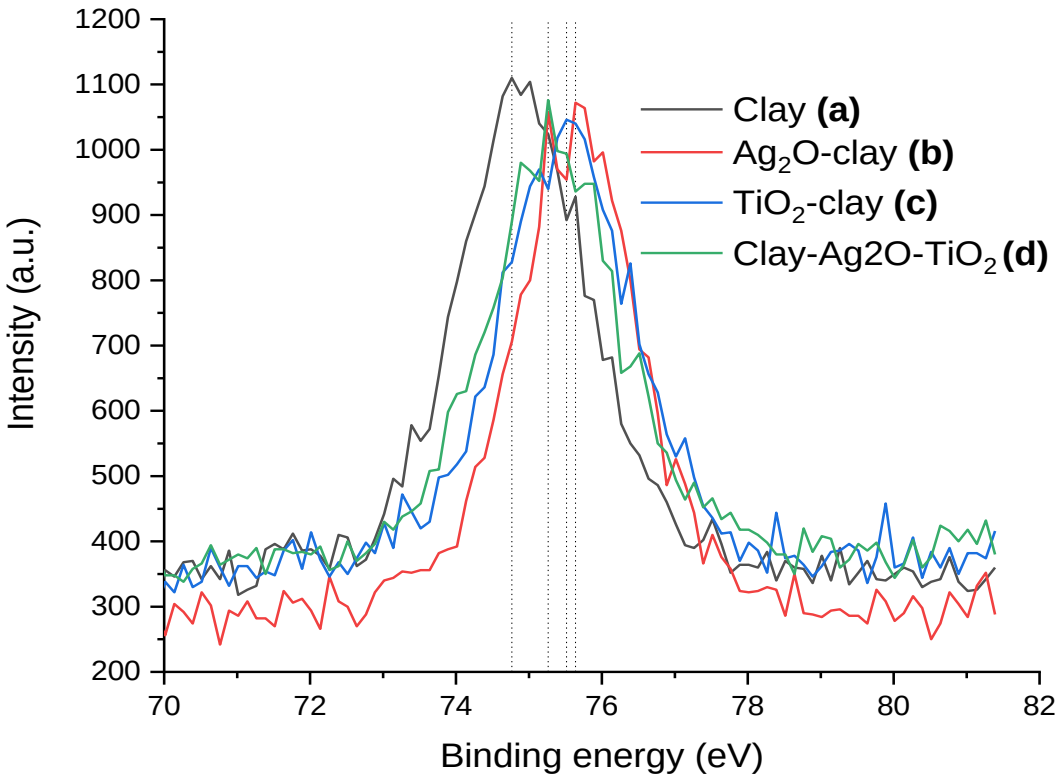

Figure 4.22: High-resolution Al 2p envelope and deconvoluted XPS spectra of Ag in (a) activated clay (b) Ag_2O-clay (c) TiO_2-clay (d) Ag_2O-TiO_2-clay

The reduction in peak intensity of Al 2p orbital in Ag_2O-clay, TiO_2-clay and Ag_2O-TiO_2-clay may be attributed to the deposition of Ag^+ and Ti^{4+} on the Al 2p orbital. This is because both Ag (0.115 nm), and Ti (0.061 nm) have ionic radii that are larger compared to that of aluminium (0.0535 nm).

Figure 4.22 shows the deconvoluted spectra of Si (2p). The binding energy at 103.14 eV shows a peak deconvoluted for Si 2p on clay (Figure 4.23a) which is similar to 103 eV reported for Si 2p orbital by Krishnan and Mahalingam (2017) for bentonite clay. With the gradual intercalation of the nanoparticles, a slight depletion of peaks occurred with a shift in binding energies to 102.97 eV in Ag_2O-clay, 102.33 eV in TiO_2-clay and 102.09 eV in Ag_2O/TiO_2- clay composites as shown in Figure 4.23(b, c and d), respectively. This peak shift and reduction in the peak intensity may be linked to the substitution and diffusion of the dominant elements onto each other. Figures 4.24 (a-e) show the deconvoluted XPS spectra for O 1s in Ag_2O, TiO_2, Ag_2O/TiO_2, Ag_2O-clay, TiO_2-clay, and Ag_2O/TiO_2-clay, respectively.

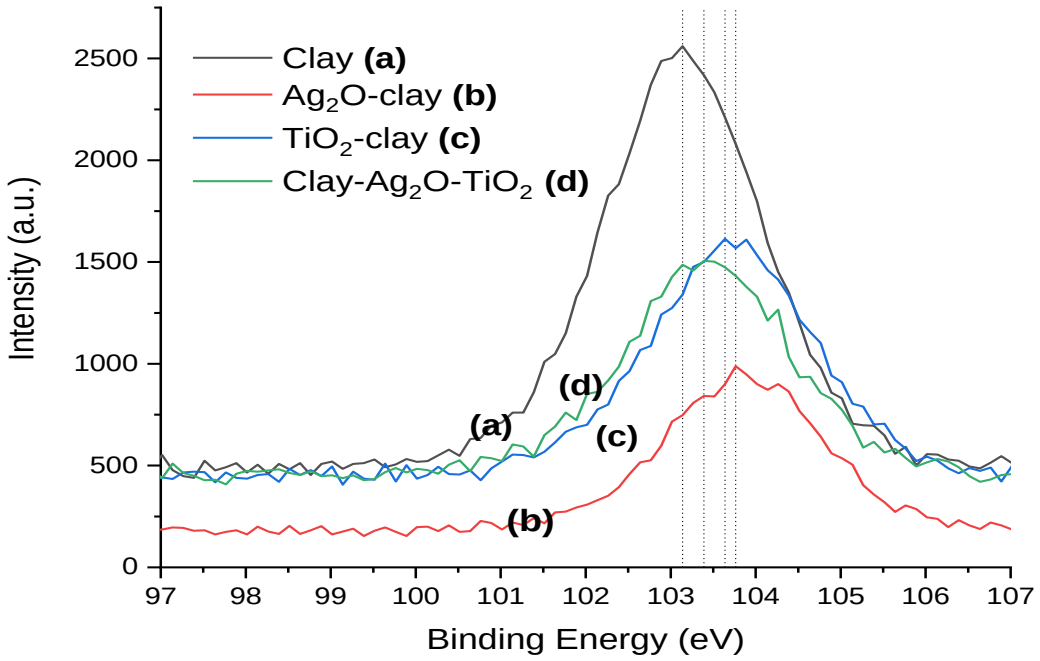

Figure 4.23: High-resolution Si 2p Envelope and deconvoluted XPS spectra of Ag in (a) activated clay (b) Ag_2O-clay (c) TiO_2-clay (d) Ag_2O/TiO_2-clay

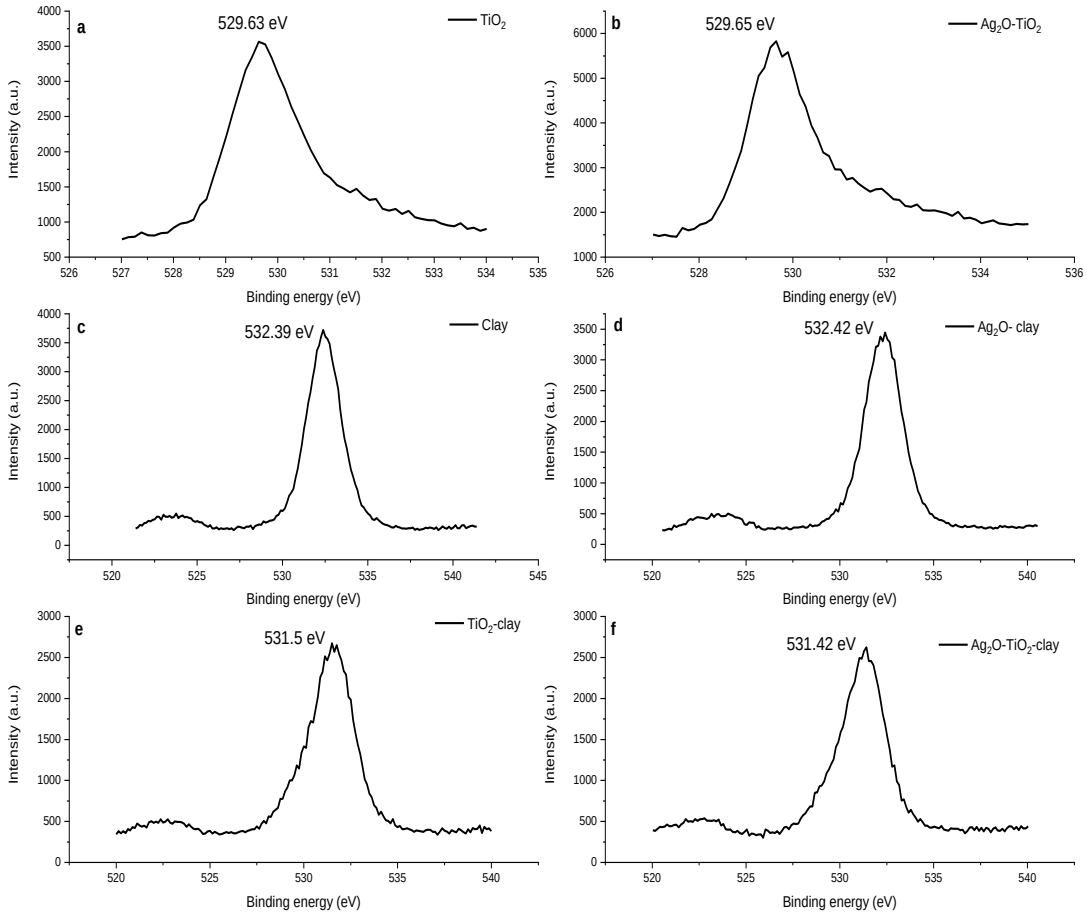

Figure 4.24: High-resolution O 1s envelope and deconvoluted XPS spectra of Ag in (a) Ag_2O (b) TiO_2 (c) activated clay (d) Ag_2O-clay (e) TiO_2-clay (f) Ag_2O/TiO_2-clay Oxygen

A single peak was observed at 530 eV on TiO_2, and 530 eV on Ag_2O/TiO_2 suggesting the formation of O-Ti-O and Ag-O bonding respectively which agrees with the literature (Djebaili *et al.*, 2015; Krishnan and Mahalingam, 2017). However, a single peak which corresponds to the oxygen bonded with silicon (Si-O-Si) was found at binding energy 532 eV in clay, 532 eV (Ag-O-Si) in Ag_2O-clay, 532 eV in the TiO_2-clay and 531 eV in Ag_2O-TiO_2-clay. All the binding energies demonstrated the presence of lattice oxygen (Jlassi *et al.*, 2013) in all six samples. Comparatively, the binding energy of O 1s in the nanocomposites of Ag_2O, TiO_2, Ag_2O/TiO_2, Ag_2O-clay, TiO_2-clay, and Ag_2O/TiO_2-clay did not change significantly. This implies the absence of oxygen vacancies and defects in the prepared composite materials.

Figure 4.25 (a-d) presents the deconvoluted XPS spectra of adventitious C 1s in activated clay, Ag_2O-clay, TiO_2-clay, and Ag_2O/TiO_2-clay nanocomposites respectively.

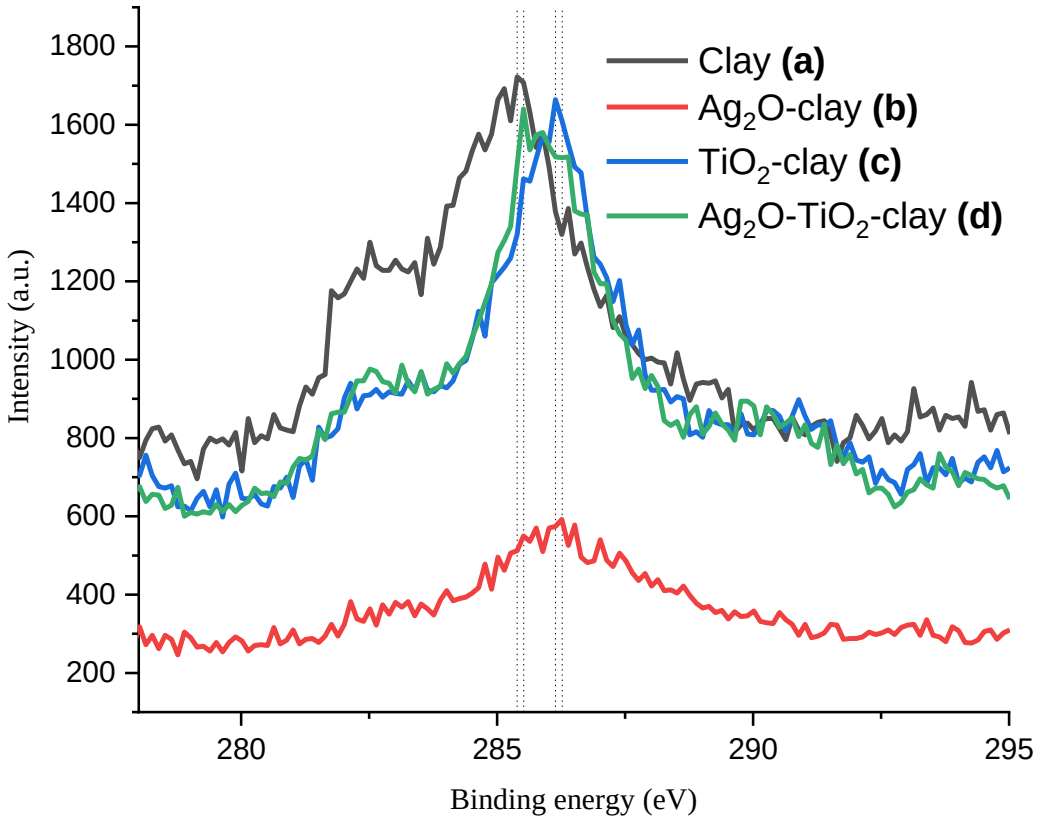

Figure 4.25: High-resolution C 1s envelope and deconvoluted XPS spectra of (a) Activated clay (b) Ag_2O-clay (c) TiO_2-clay (d) Ag_2O/TiO_2-clay Carbon

All the samples show similar binding energy in their spectra for the C 1s region. The peaks located at 284.8 and 285.27 eV indicate oxygen-bonded species C-O on the nanocomposites. The C (1 s) peak observed at 285.27 eV originated probably from the *Parkia biglobossa* leaf extract used during the synthesis of Ag_2O and TiO_2 nanoparticles. The elements detected are major constituents in the samples and no other forms of contamination are present. Therefore, the XPS analysis revealed that silver and silicon have different interactions with the TiO_2 nanoparticles. In the case of Ag, there was evidence of chemical bonds of Ag^o or Ag_2O to TiO_2, implying that either Ag^o or Ag_2O was anchored onto the superficial surface of TiO_2.

Hence, the incorporation of Ag, Si and Al did not change the electronic state of Ti from Ti^{4+} to Ti^{3+}. This implies that the phase structure of TiO_2 was still rutile irrespective of the dopants as evident in the XRD result. Thus, the entire analytical tool employed confirmed the successful formation of Ag_2O-TiO_2, Ag_2O-Clay, TiO_2-Clay, and Ag_2O/TiO_2-Clay.

4.6 Physico-chemical Characterization of Mine Site Wastewater

The wastewater collected from the artisanal gold mining site in *Chanchaga* area of Minna, Niger state, Nigeria was analysed for its physicochemical properties before the treatment using the established standard procedure of the environmental protection agency (EPA) and the result is presented in Table 4.14. The mining wastewater was turbid, containing phosphate, nitrate, coliform, and heavy metals (Fe, Mn, Cu, Ni and Pb), and are also characterised by their respective BOD, COD, DO and pH. These physico-chemical parameters were evaluated in triplicates and the values obtained are presented in Table 4.14.

Turbidity is a key test for water quality which indicates the cloudiness or haziness of a fluid caused by the presence of dissolved organic and inorganic pollutants in water. The permissible turbidity in water is 1 to 5 NTU according to WHO/EPA (2017) and NIS (2015). A turbidity value of 14.54 NTU was obtained in the present study of mining wastewater while a higher 560 NTU turbidity value was obtained from iron mining wastewater in Algeria by Touahria *et al.* (2016). The variation in the turbidity values may be linked to the deposition of other wastes in the mining wastewater resulting from the abandonment of the mining site, types of mineral resources mined and other geographical reasons (Touahria *et al.*, 2016). Increased turbidity affects the growth rate of algae and other aquatic plants in streams and lakes. Values higher than 2 NTU (14.54 NTU in the present study) are undesirable.

Table 4.14: Physico-chemical Parameters of Mine Site Wastewater

Parameter	Initial values	WHO/EPA (2017)	NIS (2015)
Turbidity (NTU)	14.54 ± 0.51	1.00-5.00	5
Phosphate (mg/L)	11.25 ± 0.63	0.10	0.10
Carbonate (mg/L)	BDL	100-500	100-500
Nitrate (mg/L)	33.01 ± 0.55	50.00	50
Sulphate (mg/L)	38.83 ± 0.15	100	100
BOD (mg/L)	1.04 ± 0.18	Not specified	
COD (mg/L)	274.00 ± 6.00	<120	
DO (mg/L)	3.27 ± 0.01	>6.50-8.00	>6.50-8.00
pH	5.97 ± 0.05	6.50-8.50	6.50-8.50
Total coliform (Cfu/100 mL)	$1.12x10^3$ ± 25.17	10	10
Conductivity (μS/cm)	750.66 ± 53.42	<500	<500
Fe (mg/L)	20.25 ± 0.20	1.00-3.00	0.3
Cu (mg/L)	0.31 ± 0.01	0.05	1
Mn (mg/L)	4.29 ± 0.01	0.05	0.2
Cd (mg/L)	ND	0.005	0.003
Ni (mg/L)	0.33 ± 0.01	3.00	0.02
Pb (mg/L)	0.98 ± 0.01	0.015	0.01
Cr (mg/L)	0.10 ± 0.01	0.10	0.05
Colour	Dark	Clear	Clear
Odour	Offensive	Odourless	Odourless

(WHO, 2017), (NIS, 2015), BDL=Below Detection Limit

This is because, they could lead to wastewater treatment problems, and health risks to humans (Kjelland *et al.*, 2015). A turbidity value between 150 and 600 NTU was recorded in similar research (Efimov *et al.*, 2019), which generates more concern than the one obtained in the present research. As the increased turbidity causes a decrease in the amount of light for photosynthesis in water, which further implies depletion in oxygen level in the water.

The suspended particles also absorb heat, thereby raising the water temperature, which is deleterious to the existence of aquatic animals. This can lead to suffocation and the eventual death of fish and other aquatic animals (Kjelland *et al.*, 2015). Increased turbidity is therefore associated with the presence of heavy metals and other toxic compounds (Chapman *et al.*, 2014). In addition, higher values of turbidity may be attributed to the migration of elements from high-chelated complex compounds as a result of changes in external hydrochemical conditions from the mined environment (Efimov *et al.*, 2019). A high level of phosphate and nitrate in wastewater leads to eutrophication (Ganesh *et al.*, 2012). Eutrophication causes an algal bloom in the wastewater, which in turn decreases the dissolved oxygen in the water, thereby making water uninhabitable to freshwater organisms.

Therefore, the level of phosphate indicated as 11.60 mg/L which is more than 100 times higher than the amount recommended by WHO for drinking water could be due to run-offs from agricultural soil in the vicinity where the wastewater was collected. The differences in the level of phosphate may be ascribed to the acidification process (Bunce *et al.*, 2018). A high concentration of nitrate in drinking water can be harmful to children; it is responsible for an increased risk of spontaneous abortion and certain birth defects in pregnant women if it exceeds 10 mg/L (Kurniawati *et al.*, 2017). Other effects of high nitrate concentration are; ovarian and bladder cancer, cardiovascular disease, stomach cancer, miscarriage, high blood pressure, the formation of nitrosamine and nervous system disruptions (Kurniawati *et al.*, 2017). A nitrate level of 33.60 mg/L and 0.00 mg/L carbonate obtained is lower than the specified permissible limit, and thus not considered as targeted pollutants to be removed.

The low value of nitrate implies less acidity of the mining wastewater while higher values would lead to high acidity due to the COD and BOD indicating the presence of toxic recalcitrant organic constituents in water bodies. The level of BOD is indirectly proportional to the level of Dissolved Oxygen (DO) while COD measures the relative depletion of oxygen in wastewater. The COD value of 274 mg/L is above the permissible limit, which suggests that the mining wastewater contains diverse organic constituents. Good quality water is considered to have DO (dissolved oxygen) concentrations above 6.50 to 8.00 mg/L. The value of 3.27 mg/L obtained suggests the unhealthy state of the mining wastewater.

The pH is a parameter that indicates the acidity or basicity of water and by extension pollution status (Cai *et al.*, 2019). It is an extremely important and simple parameter that determines most chemical reactions in aquatic media. Too high or too low a pH value can be harmful to aquatic life. The pH of the mining wastewater is acidic due to the oxidation of metal sulphide contained in it (Acheampong and Ansa, 2017). This acidic water can cause different skin diseases and the eventual death of aquatic organisms as a result of toxicity (Masindi and Muedi, 2018). Moreover, the presence of heavy metals such as Fe, Cu, Mn, Cd, Ni, Pb and Cr in wastewater have been reported to cause serious health challenges. These are mental retardation (Pb), skin rashes, respiratory problems (Cr), acute renal failure (Mn), weakened immune systems, kidney and liver damage(Cd), cancer, chest pain, rapid respiration (Ni) (Lakherwal, 2014).

Other health effects of heavy metals concentration above the permissible limit in body interaction are cirrhosis of the liver, thyroid dysfunction, skin peels, diarrhoea, stunted growth, and a lower reproduction rate. From Table 4.14, the wastewater is rich in Fe (20.02 mg/L). This value is greater than the WHO standard of 3 mg/L but less than 384 mg/L reported by Kamal and Gooyong (2019) from mining wastewater.

The level of Ni was determined to be 0.326 mg/L, which is below WHO permissible limit concentrations of 3.0, therefore not considered a priority pollutant to be removed. From the literature, a low Ni concentration of 2.97 mg/L was reported from coal mining wastewater by Masindi and Muedi (2018) while 1 mg/L of Ni was reported by Esmaeili *et al.* (2019) for gold mining wastewater. The Cd was below the detectable limit (BDL) in the wastewater as presented. Previous studies documented varied concentrations of heavy metal pollutants in mining wastewater and its surrounding. For instance, 4-100 μg/L of Cu, 0.1- 50 μg/L Pb, 0.6-100 μg/L Ni, 4-32 μg/L Mn, 0.6-100 Ni and 0.03-1 mg/L Fe were obtained by Gabrielyan *et al.* (2018) from their characterisation of mining wastewater of *Voghji* River basin (Armenia).

Also, high levels of heavy metal ions of Mn^{2+} (63.45 mg/L), Pb^{2+} (11.42 mg/L), Cr^{3+} (14.60 mg/L), Ni^{2+} (1.260), Cd^{2+} (15.67 mg/L) were observed in the mining communities of Abakaliki, Southeast Nigeria (Obasi and Akudinobi, 2020). The obtained values of heavy metals from a lead-zinc mining site in Southeast, Nigeria are slightly higher than those obtained from *Chanchaga* mining wastewater, except Cu^{2+} (0.00-0.341) whose ranges coincide with the value obtained in the present study. Other values reported for the *Abare* artisanal gold mining wastewater site in Zamfara, Nigeria are; 0.832 mg/L (Pb^{2+}), 7.278 mg/L (Hg), 0.004 mg/L (Cd), 0.0001 mg/L (Cr), 0.062 mg/L (Cu), 7.770 mg/L (Fe) respectively (Muhammad *et al.*, 2013).

On the other hand, Xie *et al.* (2018) reported 0.008 to 3.355 mg/L of Cu, 0.058 to 0.349 mg/L of Pb, 0.035 to 0.476 mg/L of Ni, and 0.006 to 0.022 mg/L of Cr from *Dabaoshan* Mine in South China. The values of heavy metal concentrations reported in Dabaoshan Mine, South China are all lower than the values obtained in this study (*Chanchaga* mining wastewater).

Also, the mobility, bioavailability and toxicity of the heavy metals are variable, an indication of the chemical reactions which take place at the water interface. Furthermore, the presence of a dark colour (coloured water) of low oxygen content and foul odour of the mining wastewater suggests a series of oxidation-reduction reactions (Kefeni *et al.*, 2017; Seo *et al.*, 2016). This implies that the wastewater needs to be treated to get rid of the colour to increase the oxygen and make life easier for aquatic species. The results of the physicochemical parameters revealed that the mining wastewater cannot be directly discharged into the environment without proper treatment and therefore some of the possible contaminants which pose a threat to living things need to be removed from the mining wastewater.

4.7 Adsorption Studies

4.7.1 Batch adsorptions studies of the developed adsorbents

The results of batch experiments for the removal of Mn, Fe, Pb and Cu ions from mining wastewater using beneficiated and activated clay, TiO_2, Ag_2O/TiO_2, Ag_2O-clay, TiO_2-clay, Ag_2O/TiO_2-clay nano adsorbents are shown in Figure 4.26(a-g). In each case, 0.5 g adsorbent dosage, 100 mL volume of wastewater, 180 mins contact time and 30°C were used. The quantity of each metal ion adsorbed was found to increase with increased time for the seven adsorbents. From Figure 4.26a, it can be observed that adsorption was rapid for the first 60 mins, especially the uptake of Fe (III) and Mn (II) and continued up until the first 120 mins. The beneficiated clay (4.26a) removed up to 40.76% Mn (II), 55.95% Fe (III), 36.22% Cu (II) and 19.10% Pb (II) ions while the activated clay (Figure 4.26b) removed 57.00% Mn (II), 58.93% Fe (III), 40.76% Cu (II), 20.42% Pb (II) ions. The maximum amount of each of the metal ions removed by activated clay is a little more than that removed by beneficiated clay comparably, at an equilibrium time of 140 mins.

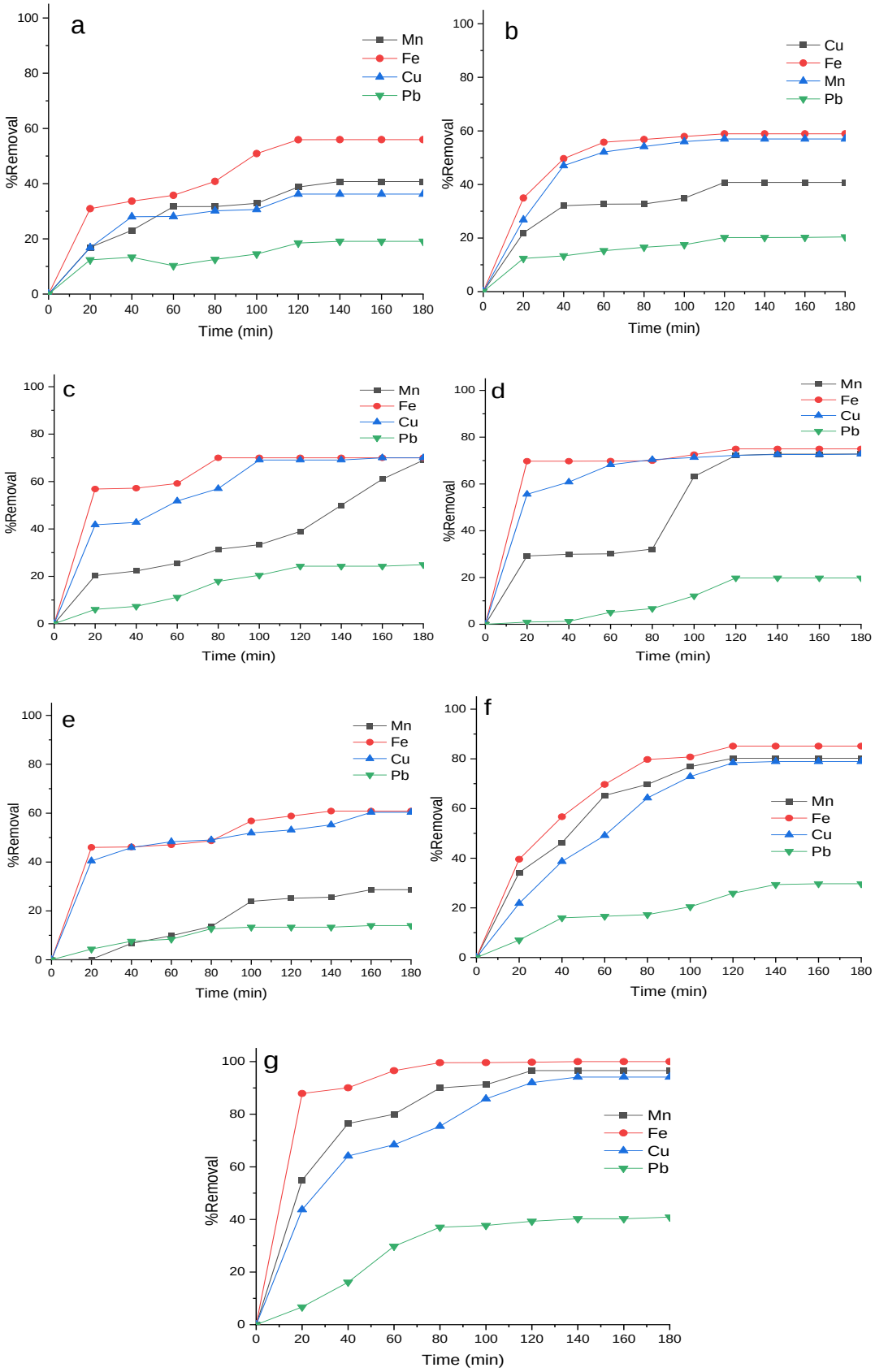

Figure 4.26: Removal of metal ions with (a) Beneficiated clay (b) Activated clay (c)TiO_2 (d) Ag_2O/TiO_2 (e) Ag_2O-clay (f)TiO_2-clay (g) Ag_2O/TiO_2-clay

Figure 4.26c shows that the TiO_2 nano adsorbent removed 68.98% Mn (II), 70.00% Fe (III), 70.00% Cu (II), 24.28% Pb (II) ions as single component adsorbent at 120 mins contact time. Also, Figure 4.26d reveals that the Ag_2O/TiO_2 was able to remove 72.58% Mn (II), 72.76% Fe (III), 60.33% Cu (II) and 19.80% Pb (II) ions with equilibrium also attained at 140 min. From Figures 4.26e and f, Ag_2O-clay removed a maximum of 72.58% Mn (II), 72.76% Fe (III), 60.33% Cu (II) and 13.99% Pb (II) ions. While TiO_2-clay was able to remove 80.22% Mn (II), 85.13% Fe (III), 78.42% Cu (II) and 29.71% Pb (II) ions each.

The result showed that the TiO_2-clay removed a higher percentage of metal ions than the Ag_2O/TiO_2 and Ag_2O-clay nanocomposite which are also binary component adsorbents. The Ag_2O/TiO_2-clay composite performance on the heavy metal ions removal from the mining wastewater is presented in Figure 4.26g. It was observed that 96.59% Mn (II), 100.00 Fe (III), 94.13% Cu (II) and 40.89% Pb (II) ions respectively were removed. The result shows that the Ag_2O/TiO_2-clay was more favourable for the removal of Mn (II), Fe (III), Cu (II) and Pb (II) ions than the other nanoparticles/nanocomposites (Figure 4.26 a-f). The observed trend of percentage increase by the Ag_2O/TiO_2-clay may be attributed to the synergistic relationship between the components of the ternary adsorbent. Also, the Ag_2O/TiO_2-clay adsorbent performed well with a Fe (III) removal percentage of 99% efficiency. The Ag_2O-clay composites was not efficient for the removal of Mn (II) as only 28.69% of the ion was sequestered. This may be due to the repulsion between the Si-Ag_2O framework in the nano adsorbent composite (Ag_2O-clay) and the manganese ion (Gupta *et al.*, 2021). All the nano adsorbents had an affinity for the Cu (II) ions from the mining wastewater. This is due to the increased rate of Cu (II) ion adhesion to the nano adsorbents, which is due to its small ionic radii.

The removal percentages are; 36.22, 40.76, 70.00, 72.58, 60.33, 78.42 and 94.13% for the beneficiated and activated clay, TiO_2, Ag_2O/TiO_2, Ag_2O-clay, TiO_2-clay, Ag_2O/TiO_2-clay respectively. The adsorption of Cu (II) ions onto the adsorbent was considered better with TiO_2-clay and Ag_2O/TiO_2-clay due to the synergetic effects of the binary and the ternary composites.

The favourable adsorption of Fe (III), Mn (II) and Cu (II) ions shown in Figures 4.26 (a-g) indicates that nanocomposites of clay, TiO_2, Ag_2O/TiO_2, Ag_2O-clay, TiO_2-clay and Ag_2O/TiO_2-clay are viable materials for the adsorption of the heavy metals in the mining wastewater. The adsorption of Pb (II) ions from mine wastewater onto the nano adsorbents was not favourable which may be due to its large ionic radius of 119 pm (1.19Å). As it is bigger than that of Fe (III), 60 pm and Mn (II), 70 pm and Cu (II) having 73 pm ionic radius.

Out of the four metal ions adsorbed, Fe (III) was the most adsorbed as a result of its small ionic radius, which is responsible for its highest removal percentage by the adsorbents. The selectivity of Fe (III) ions amidst the competing cations by the Ag-TiO_2-clay adsorbent is also adjudged responsible for its uptake over other metal ions in the solution (Zendelska *et al.*, 2018). The removal efficiency of Cu (II) ion by the nano clays is comparable, 36.22% for beneficiated clay and 40.76% for activated clay under the applied conditions. The later performance may be due to increased surface area by the activation of the kaolinite clay. The removal efficiency for Cu (II) ion by other adsorbents is in the order Ag_2O/TiO_2-clay>TiO_2-clay>Ag_2O/TiO_2>TiO_2>Ag_2O-clay respectively. This performance may be due to their relative porosity when compared with one another. It was found that Ag_2O/TiO_2-clay nano adsorbents had a better affinity for Pb (II) ions with up to 40.89% removal capacity.

Generally, the six adsorbents' performance revealed that the amount of Pb (II) ions adsorbed was affected due to other competing ions for the surface of the adsorbents from the multicomponent adsorbate solution. Fe (III) ions present in the mining wastewater were better removed, due to their tendency to saturate and diffuse into the adsorbent medium surface faster than others. This is based on the mechanism of the smaller ionic radius when compared with Mn (II), Pb (II) and Cu(II) ions which in turn, enhance its diffusion and attachment into the pores of the adsorbents considered (Wei *et al.*, 2017).

Figure 4.26 (a-g) also shows a gradual enhancement of the percentage removal from the single components (beneficiated clay, activated clay and TiO_2) to binary (Ag_2O/TiO_2, Ag_2O-clay and TiO_2-clay). Then, the ternary composite (Ag_2O/TiO_2-clay) exhibited significant removal efficiency for Fe (III), Cu (II), Mn (II) and Pb (II) metals ions. The enhanced adsorption by the Ag_2O/TiO_2-clay can be ascribed to higher surface area and more functional groups on the ternary composites compared to the single and binary component adsorbents. This may be due to the existence of a synergistic effect among the three anchored adsorbents (Ag_2O/TiO_2-clay composite).

Therefore, from this preliminary study, a conclusion can be made that Ag_2O/TiO_2-clay nanocomposites had the maximum removal efficiency for the four metal ions in the mining wastewater followed by TiO_2-AAC. Hence, Ag_2O/TiO_2-clay was chosen for further study on adsorption isotherms, kinetics and thermodynamics process.

4.7.2 Adsorption effects with Ag_2O/TiO_2-Clay

4.7.2.1 Effect of contact time

The result of the effect of variation of contact time on the removal of Mn (II), Fe(III), Pb (II) and Cu (II) ions by Ag_2O/TiO_2-clay nano adsorbent is shown in Figure 4.27.

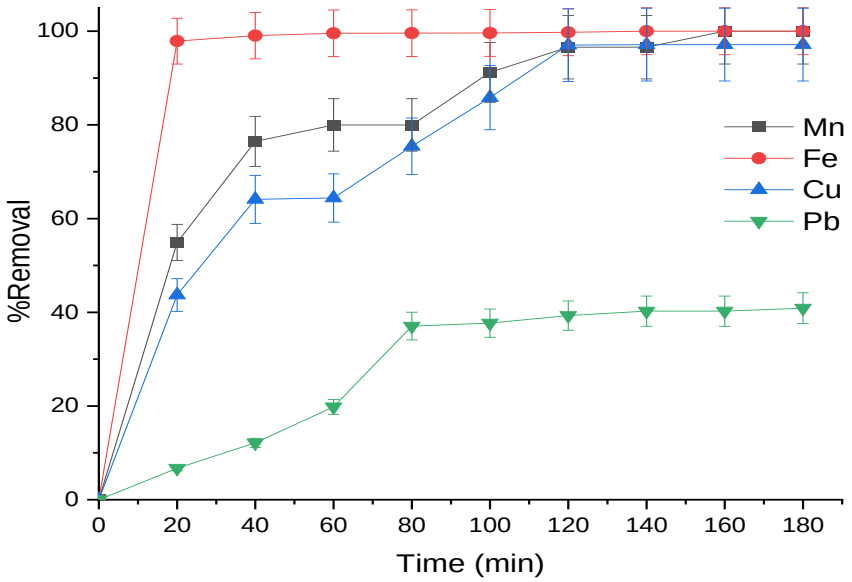

Figure 4.27: Effect of contact time on percentage removal of the metal ions

It can be noticed that the adsorption of Fe (III) ions from mine wastewater was rapid at the first 10 min of the process. Mn (II), and Cu (II)) ions adsorption from mine wastewater also increased drastically within the first 60 minutes then became gradual from 80 to 120 minutes and thereafter the adsorption became constant for all the metal ions considered in this study. The rapid increase in the percentage removal of the metal ions at the onset of the adsorption process was ascribed to the high number of vacant adsorptive surfaces on Ag_2O-TiO_2-clay and this resulted in a higher solute concentration gradient (Mnasri-Ghnimi and Frini-Srasra, 2019). The high solute concentration gradient results in a faster diffusion of metal ions onto the adsorbent surface, which was occasioned by the resultant stronger driving force. As time progresses between 80 to 120 mins, the adsorptive surfaces became saturated with metal ions and further adsorption became difficult (Kazak *et al.*, 2018). This results from the repulsion between the adsorbed ions on the adsorbent material and those in the bulk solution signifying equilibrium attainment. Therefore, after 120 mins of average equilibrium time, the vacant adsorptive surfaces become highly populated with adsorbed metal ions.

This causes the repellent of the oncoming metal ions that intend to move onto the adsorbent surface and hence hindering adsorption (Inyinbor *et al.*, 2016). Also, the difference in equilibrium time of adsorption of each ion may be attributed to ionic radii, selectivity of the heavy metal by the adsorbents, the surface charge of adsorbent and difference in hydration energy; Cu (II) (-2010 kJ mol^{-1}), Mn (II) (-1760 $kJmol^{-1}$) and Pb (II)ions (-1481 $kJmol^{-1}$). The higher the hydration energy, the faster the ease of adsorption (Zendelska *et al.*, 2018). The order of removal is Fe (III) > Mn (II)> Cu (II) > Pb (II). As time progresses from 80 to 120 mins, the adsorptive surfaces on Ag_2O/TiO_2-clay were saturated with metal ions, resulting in the repulsion between the adsorbed ions on the adsorbent material. While those in the bulk solution signify the attainment of equilibrium for the four ions (Abunah *et al.*, 2019).

4.7.2.2 Effect of Ag_2O/TiO_2-clay adsorbent dosage

The effect of adsorbent dosage on Mn (II), Fe (III), Pb (II) and Cu (II) ions adsorption from mining wastewater onto Ag_2O/TiO_2-clay was investigated and the results presented in Figure 4.28. From the Figure, it was noticed that the uptake level of Mn (II), Fe (III) and Cu (II) ions increase as the dosage increased from 0.1 to 0.5 g.

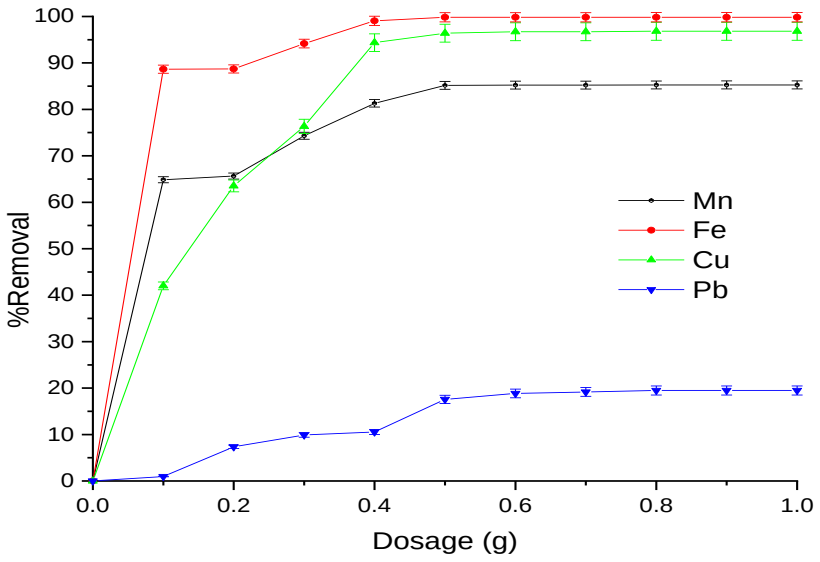

Figure 4.28: Effect of adsorbent dosage on percentage removal of the metal ions

The percentages up to 81.3, 99 and 94% were removed for the Mn (II), Fe (III) and Cu (II) ions respectively, using 0.5 g adsorbent dosage, 120 mins and adsorbate concentrations of 20.25 mg/L Fe (III), 4.29 mg/L Mn (II), 0.98 mg/L Pb (II) and 0.31 mg/L Cu (II). However, Pb (II) ions percentage removal was only 17.5% using 0.4 g adsorbent dosage. There was no desirable change in the percentage removal of Pb (II) ions even at maximum adsorbent dosage. The maximum percentage removal of Mn (II), Fe (III) and Cu (II) ions are 85.1, 99.00 and 96.00% when 0.5 g adsorbent dosage was employed. The low removal efficiency at low adsorbent mass may be attributed to the saturation of the few nano adsorbent sites present (lower mass) by the metal ions. However, as the nano adsorbent dose increases, the number of active sites and the bulk surface area available for adsorption increases. Thus, this is the reason for the higher percentage of removal of metal ions (Khalil *et al.*, 2018).

The percentage of metal ions removal became constant as the adsorbent mass increased from 0.6 to 1.0 g for the four ions studied. The constant percentage removal was because large surfaces of the adsorbent are left unoccupied by the adsorbate, whose volume used is constant (50 mL) irrespective of the mass/dosage of the adsorbent employed. The percentage removal of metal ions when the adsorbent dosage varied between 0.5 and 1.0 g was almost constant.

The consistency observed in the uptake of the metal ions at higher adsorbent mass was linked to possible accumulation and overlapping of saturation of the vacant adsorptive sites by the metal ions. Thus, making the dosage higher than 0.5 g of the Ag_2O-TiO_2-clay to be prevented further adsorption of the metal ions (Adebayo *et al.*, 2020). A similar trend was reported by Abunah *et al.* (2019), who investigated the adsorption of Cu and Cd ions but, using montmorillonite-cellulose nanocomposite.

Comparatively, the adsorption of Cu (II) ions by the ternary composite in this study is adjudged better than the research of Ouyang *et al.* (2019), who had 82% removal using a multi-component composite, (which comprise silicate tailings, bauxite, bentonite, iron, magnesium and sodium salts) which is lesser than 97% removed in the present work. Mungondori *et al.* (2017) also used ternary composites to remove Fe(III), Cu(II) and others but with a lesser adsorbate concentration of 10 mg/L Fe ion. This shows the better suitability of the nanocomposite synthesised in this study compared to that used by the previous researchers.

4.7.2.3 Effect of temperature

The percentage removal of Mn (II), Fe (III), Pb (II) and Cu (II) ions by Ag_2O/TiO_2-clay nano adsorbent was studied as a function of temperature at a constant contact time of 120 mins and 0.5 g adsorbent dosage. The temperature was varied between 30 and 70ºC at a step of 10ºC and the result is presented in Figure 4.29. The percentage removal of the ions increased steadily as the temperature increased for the ions.

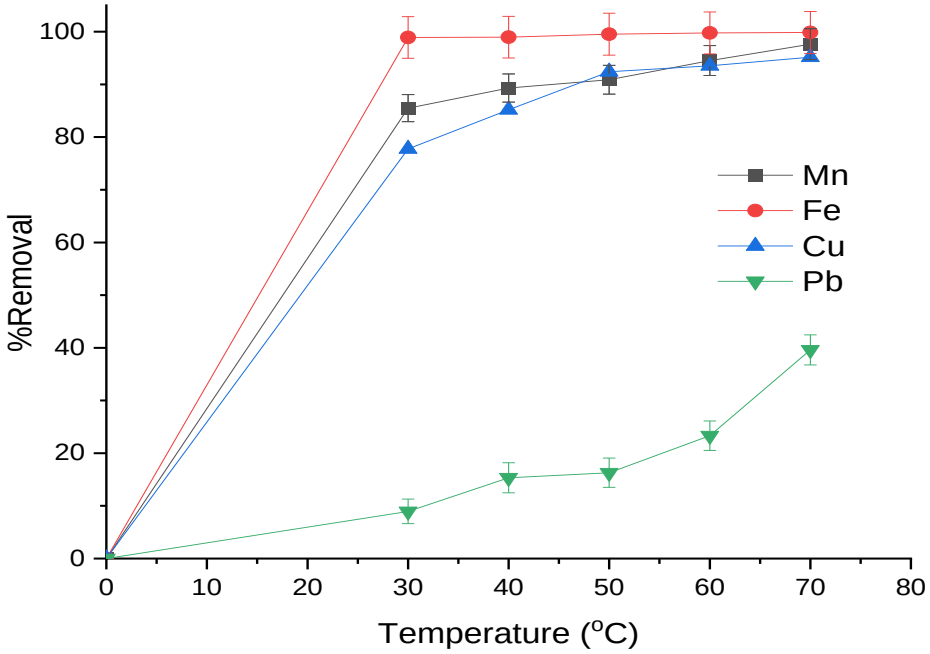

Figure 4.29: Effect of temperature on the percentage removal of the metal ions

Percentage removals were 85.48% for Mn (II), 98.90% for Fe (III), 77.74% for Cu (II) and 8.95% for Pb (II) ions at 30ºC. As the temperature was increased from 40ºC to 70ºC, the amount of the Mn (II) metal ions adsorbed also increased to 89.30%, while that of Fe (II) increased to 89.30%. The percentage removal of Cu (II) ion increased to 85.17% at 40ºC. Similar stepwise incremental results were obtained at 50 and 60ºC, with the maximum percentage removal obtained at 70ºC, having 97.64% Mn (II), 99.85% Fe (III), 95.18% Cu (II) and 39.62% Pb (II). There is no increase in the percentage removal of the metal ions at temperatures beyond 70ºC. This implies a direct relationship between the solution temperature and the percentage of heavy metals removed, which is evidence of an increase in the distribution coefficient of the metal ions between the outer and inner pores of the nano-adsorbent molecules.

This further supports the enlargement of surface pores behaviour of the nano-adsorbents in the solution as temperature increases. A researcher has shown that cations in solution move faster when temperature increases due to the weakness in the electrostatic force of attraction which decreases solvation, causing ions to be smaller thereby, enhancing mobility and adsorption rate (Adebayo *et al.*, 2020).

Also, in the present study, the direct relationship trend was observed as the percentage removal of the heavy metals by the nanocomposite increased with increasing temperature from 30 to 70 ºC due to the strengthening of the bonds, binding the four metal ions onto the surfaces of the Ag_2O/TiO_2-clay. The highest % removal of Fe (III) can be attributed to its smallest ionic radius, which increased its rate of diffusion and adhesion onto the Ag_2O/TiO_2-clay surface. Furthermore, the highest concentration of Fe (III) in the multicomponent mine site wastewater has resulted in stronger competition by Fe (III) ions among heavy metal ions in the multi-metal adsorbate solution (Zacaroni *et al.*, 2015).

This finding is in close agreement with Bankole *et al.* (2019), who utilised purified and functionalised CNT to remove heavy metals from electroplating wastewater. Hence, the adsorption process of Mn (II), Fe (III), Pb (II) and Cu (II) was optimally achieved, as temperature increased. This could mean insignificant temperature effects on the adsorbent, which is similar to research by Chaudhry *et al.* (2016) in which higher and lower temperatures favoured the adsorption of Zn (II) and Pb (II) ions onto manganese oxide-coated sand.

4.7.2.4 Competitive adsorption among the selected heavy metal ions

The selectivity of each metal ion to a particular nano adsorbent is based on the interaction between heavy metal ions and the different adsorbents used. The six nano adsorbents considered were selective to Fe (III) ions, this was attributed to their highest concentration in the wastewater, its small ionic radii and ease of diffusion. The next adsorbed heavy metal ions by the Ag_2O/TiO_2-clay was Mn (II) ion due to its ionic radius and small atomic weight. Other reasons for metal ion selectivity may be related to the hydration energy and hydrated ionic radius of heavy metals, as lower hydration energy enhances the selectiveness for the adsorption. The order of selectivity of the heavy metal ions removal by Ag_2O/TiO_2-clay may be attributed to their ionic radii and hydration energy, the higher the hydration energy, the faster the ease of adsorption (Zendelska *et al.*, 2018). Based on their hydration energy given as; Fe (-4429 kJ mol^{-1}), Cu (-2010 kJ mol^{-1}), Mn (-1760 $kJmol^{-1}$) and Pb ions (-1481 $kJmol^{-1}$), the order of adsorption was Fe (III) >Mn (II) > Cu (II) respectively (Zendelska *et al.*, 2018). The variations in the selectivity for heavy metal ions by other adsorbents may also, be due to the adsorbent surface charge and adsorbent crystallite sizes as compared with the heavy metal ionic radii. Ions with a smaller ionic radius diffused faster (onto the adsorbent surface) than those with a larger ionic radius.

Except for Pb (II) ions 0.119 nm (0.00119 Angstrom), which is heavy and has high ionic radii, therefore retarding its diffusion capability onto the pores of the adsorbent, this is in the migration order of Fe (III) 0.06 nm> Mn (II) 0.072 nm> Cu (II) 0.073 nm. Mobasherpour *et al.* (2012) investigated the comparative adsorption of Pb (II), Cd (II), and Ni (II) from aqueous solution onto nano crystallite hydroxyapatite and discovered that the competing metal ions' ionic radii affect the rate of their adsorption from the aqueous solution. The selectivity for the seven adsorbents (beneficiated clay, activated clay, TiO_2, Ag_2O/TiO_2, Ag_2O-clay, TiO_2-clay, and Ag_2O/TiO_2-clay according to Figure 4.26(a-g) are in the order; Fe (III) >Mn (II) > Cu (II) >Pb (II).

4.7.3 Adsorption isotherm

Langmuir, Freundlich, Temkin, Dubinin-Radushkevic, Harkin-Jura and Jovanovich isotherm models were used to investigate the adsorption mechanism of the removal of Mn (II), Fe (III), Pb (II) and Cu (II) ions from mining wastewater onto the Ag_2O/TiO_2-clay adsorbent and the corresponding plots (Appendix C) gave the estimated parameters presented in Tables 4.15a and b. The quality of fitness of data to Langmuir, Freundlich, Temkin, Dubinin-Radushkevic, Harkin-Jura and Jovanovich isotherms were compared using the correlation coefficient R^2, SSE and X^2.

The R^2 values for each adsorbed metals ions (Mn (II), Fe (III), Cu (II) and Pb (II)) with respect to the studied isotherms are; 0.987, 1, 0.944, 0.841(Langmuir), 0.844, 0.927, 0.774, 0.950 (Freundlich), 0.882, 0.928, 0.857, 0.998 (Temkin), 0.686, 0.818, 0.621, 0.939 (D-R), 0.756, 0.925, 0.586, 0.653 (Harkin-Jura) and 0.997, 0.999, 0.986 and 0.965 (Jovanovic) respectively. The R^2 values alone could not be used to justify the suitability of any model as the values are comparative, especially; Langmuir, Freundlich and Jovanovic isotherms.

Table 4.15a: Parameters of isotherm models for Mn (II), Fe (III), Cu (II) and Pb (II) adsorption onto Ag_2O/TiO_2-clay

Isotherm Parameters	Parameters	Mn	Fe	Cu	Pb
Langmuir	q_m (mg/g)	0.600	3.920	0.094	0.202
	K_L ($Lmin^{-1}$)	33.668	1306.740	17.961	5.683
	R_L	0.031	3.90×10^{-5}	0.031	1.285
	R^2	0.987	1	0.944	0.841
	SSE	0.052	3.71×10^{-7}	0.010	0.001
	X^2	0.007	5.29×10^{-8}	0.108	0.243
	ARE	0.751	0.019	0.581	13.924
	RMSE	0.059	0.021	0.025	0.044
	F-value	529.994	1.78×10^5	117.340	37.113
	p-value	<0.001	<0.001	<0.001	<0.001
Freudlich	N	9.680	113.638	4.669	0.2846
	K_f (mg/g)	0.672	3.897	0.095	7.34×10^{-5}
	R^2	0.844	0.927	0.774	0.950
	SSE	0.017	1.87×10^{-5}	0.113	0.174
	X^2	0.002	4.66×10^{-6}	0.023	0.025
	ARE	0.367	0.094	1.706	0.828
	RMSE	0.042	0.027	0.025	0.006
	F-value	37.801	50.608	17.457	133.294
	p-value	<0.001	0.002	0.009	<0.001
Temkin	b_T (kJ/mol)	3.31×10^4	-7.229×10^4	-8.372×10^4	-5.440×10^4
	A_T (L/g)	1.43×10^{-4}	2.762 x10-^{49}	0.049	3.092
	R^2	0.882	0.928	0.857	0.998
	SSE	0.007	2.874×10^{-4}	0.0013	9.030×10^{-7}
	X^2	9.49×10^{-4}	7.185×10^{-5}	2.604×10^{-4}	1.300×10^{-7}
	ARE	N/A	N/A	N/A	N/A
	F-value	52.092	51.406	29.899	4474.056
	p-value	<0.001	0.002	0.003	4.387×10^{-11}
D-R	K_{ad} (mol^2/kJ^2)	-0.386	1.366	-2.183	-7.992
	q_α (mg/g)	1.00	1.00	1.00	1.00
	E	1.137	0.605	0.479	0.250

Table 4.15b: Parameters of isotherm models for Mn (II), Fe (III), Cu (II) and Pb (II) adsorption onto Ag_2O/TiO_2-clay

Isotherm Parameters	Parameters	Mn	Fe	Cu	Pb
	R^2	0.686	0.818	0.621	0.939
	SSE	0.034	$4.637x10^{-5}$	0.192	0.214
	X^2	0.005	$1.159 x10^{-5}$	0.038	0.031
	ARE	0.348	75.094	N/A	N/A
	RMSE	0.041	0.750	0.201	0.244
	F-value	15.299	17.962	8.191	107.538
	p-value	0.006	0.013	0.035	<0.001
Harkin-Jura	A	1.105	386.100	0.017	$5.400x10^{-6}$
	B	2.488	25.417	1.827	0.723
	R^2	0.756	0.925	0.586	0.653
	SSE	0.426	$3.14x10^{-7}$	3807.508	$9.240x10^{8}$
	X^2	0.061	$7.85x10^{-8}$	761.502	$1.320x10^{8}$
	ARE	N/A	N/A	N/A	N/A
	F-value	21.708	49.067	7.072	13.164
	p-value	0.002	0.002	0.045	0.008
Jovanovic	q_{max} (mg/g)	0.865	4.003	0.458	0.199
	K_J	-0.277	$5.976x10^{-5}$	0.064	-15.281
	R^2	0.997	0.999	0.986	0.965
	SSE	$3.524x10^{-4}$	$3.635x10^{-9}$	0.009	0.122
	X^2	$5.035x10^{-5}$	$5.193x10^{-10}$	0.001	3.375
	ARE	0.009	0	0.003	N/A
	RMSE	0.007	0	0.001	0.108
	F-value	$2.142x10^{3}$	$7.138x10^{5}$	508.660	194.350
	p-value	<0.001	<0.001	<0.001	<0.001

Considering the importance of each isotherm, it was noticed that Mn (II), Fe (III) and Cu (II) ions adsorption on the Ag_2O/TiO_2-clay was better described by the Langmuir model (Tables 4.15a and b). The Langmuir model may also describe the adsorption mechanism of Pb (II) although with little percentage removal. Besides the R^2 value, the fitness of Langmuir isotherm can also be expressed by the dimensionless constant called equilibrium parameter, (R_L), (R_L = 0) is considered an irreversible process, favourable (0< R_L< 1), and unfavourable (R_L >1) (Miyah *et al.*, 2017). The results in Table 4.15 shows that the adsorption of Mn (II), Fe (III) and Cu (II) ions onto the Ag_2O/TiO_2-clay was favourable because the R_L values fall between 0 and 1 except for Pb, which is unfavourable, with 1.27 R_L value.

For Freundlich isotherm, the essential parameter K_F which represents the adsorption capacity of the Ag_2O/TiO_2-clay composites was much higher for Fe ion. This implies that Fe (III) was the most adsorbed out of the four heavy metal ions considered and can be attributed to its high rate of saturation of the multicomponent adsorbate solution (Zendelska *et al.*, 2018). The value of N, which is related to the distribution of bonded ions on the sorbent surface was found to be greater than 1 for Mn (II), Fe (III) and Cu (II) ions, indicating that the adsorption process is favourable except for Pb (II) ions with the value less than 1.

This depicts that the adsorption of Pb (II) by Ag_2O/TiO_2-clay was not so favourable. The adsorption data fitted into Temkin isotherm revealed that the constant 'b_T' related to the heat of sorption varied from -3.31 x 10^4 to -8.372 x 10^4 kJ/mol for Fe (III) Mn (II) and Cu (II) ions. Negative values of the constant for each of the metal ions are indicative of the endothermic nature of the adsorption process. Furthermore, the 'b_T' values obtained lie between 1 to 20 Kcal/mol which implies the involvement of both physical and chemical processes in the adsorption (Ajala *et al.*, 2022a; Amin *et al.*, 2015b).

Temkin equilibrium binding constant A_T was found to be highest for Pb (II) suggesting the least adsorbed ion. The essential parameter of the D-R model, the mean free energy (E) value obtained from K_{ad} is useful to predict the adsorption mechanisms, interpreted as physical ($E < 8$ kJmol^{-1}); chemical or ion exchange ($8 \leq E \leq 16$ kJmol^{-1}) (Ogunleye *et al.*, 2014). The calculated values of E in this study are all below 8 kJmol^{-1} signifying that the phenomenon governing the process may be a physical process.

According to the Harkin-Jura isotherm, the B and A values obtained for Fe ions were the highest (25.417 and 386.1 Jmol^{-1}). This indicates that the adsorbent has more affinity for Fe ions; an indication of multilayer adsorption on the surface of Ag_2O/TiO_2-clay due to likely heterogeneous pore distribution. The Jovanovic model is essentially like the Langmuir model except that allowance is made in the Jovanovic isotherm for the surface binding vibrations of an adsorbed species. The model represents another approximation for monolayer localised adsorption without lateral interactions (Ayawei *et al.*, 2017). The maximum monolayer adsorption capacities of 0.865, 4.003, 0.199 and 0.965 mg/g were obtained for Mn (II), Fe (III), Cu (II) and Pb (II) ions respectively.

Since the regression coefficients alone are not sufficient to adjudge the most fitted isotherm, the probability value (p-value) as a function of F-values and different error functions such as the (a) sum of squares error (SSE), (b) Chi-square (X^2), (c) average relative error (ARE), (d) root mean square error (RMSE) were calculated for the four ions. The six isotherms have high F-values and low *p*-values. Lower *p*-values<0.004 imply a more significant model (Ajala *et al.*, 2022a). From Table 4.15, the F-values of the Langmuir and Jovanovic Isotherms are far higher than that of others in the order Temkin > Freudlich > Harkin-Jura > D-R. The *p*-values were not consistently lower than 0.001 for the four ions fitted with Freundlich, Temkin, D-R and Harkin-Jura.

But for Langmuir and Jovanovic the *p*-values were < 0.001 for all the four ions considered which means the two models are significant. The smallest value of error functions was taken as the criteria for selecting the best model as it has the minimum error distribution between the experimental and predicted values (Khandelwal *et al.*, 2020). Averagely, the SSE of each model value is in the order Harkin-Jura >Temkin> Freudlich>D-R>Langmuir>Jovanovic while ARE follows a similar pattern. The values ARE for the Jovanovic model were consistently closer to zero than that of Langmuir isotherm in the ionic order of Fe (III)>Mn (II)>Cu (II). The ARE model cannot perfectly justify the suitability of Langmuir and Jovanovic models for Pb (II) adsorption as the error value is analysed as either higher or not applicable (N/A) as presented in Table 4.15.

Considering the root mean square error (RMSE) values analysed, both Langmuir and Jovanovic values have low values and have good fits for all the four ions adsorbed. But the entire values obtained for Jovanovic were lower compared to the Langmuir RMSE values. These results validate the suitability of two isotherms (Langmuir and Jovanovic isotherm model) for the heavy metal adsorption similar to the fittings of adsorption of Cu^{2+}, Cd^{2+} and Pb^{2+} on synthesised silicate porous material/composite (Ouyang *et al.*, 2019).

Therefore, it can be affirmed that the Ag_2O/TiO_2-clay surface is more of being homogeneous than heterogeneous, and there is monolayer coverage of the metal ions molecule. Among the six applied equations for the isotherm fitting, the Langmuir and Jovanovic isotherms could be identified as the most consistent and suitable, but the Jovanovic Isotherm is the best fit for modelling the equilibrium sorption behaviour of the Mn (II), Fe (III), Cu (II) and Pb (II) ions onto Ag_2O/TiO_2-clay nanocomposite covering all the heavy metal ions in the mine wastewater used in this study.

This suggests that the surface adsorption was homogeneous with mono-layer coverage of adsorbate molecule enhanced by some mechanical energy.

4.7.4. Adsorption kinetics of Mn (II), Fe (III), Cu (II) and Pb (II) ions onto Ag_2O/TiO_2-clay

The results of the kinetics of Mn (II), Fe (III), Cu (II) and Pb (II) ions adsorption onto Ag_2O/TiO_2-clay nano adsorbent analysed using Pseudo-First Order (PFO), Pseudo-Second Order (PSO), Intra-particle Diffusion (IPD) and Elovich Kinetics models plots (appendix D) are presented in Table 4.16. From the table, the Pseudo-first-Order model correlation coefficients (R^2) values are 0.884, 0.687, 0.936 and 0.902 for Mn (II), Fe (III), Cu (II) and Pb (II) ions respectively which indicates a good fit, except for Fe ions. While R^2 values for the Pseudo-second-order model are 0.996, 1, 0.965 and 0.545 for the four ions indicating a better fit by the PSO. The obtained R^2 from the Pseudo-second-order model for Mn (II), Fe (III) and Cu (II) ions had a high linear regression coefficient (closer to unity) when compared to R^2 values for the Pseudo-First-Order model.

The R^2 coefficients obtained from the Intraparticle diffusion kinetic model are; 0.882, 0.808, 0.933 and 0.957, which are lesser than those obtained from the Pseudo-First-Order model, while that of the Elovic model are; 0.939, 0.907, 0.968 and 0.900 for Mn (II), Fe (III), Cu (II) and Pb (II) ions respectively, which are not comparative (lesser) with those of the Pseudo second order kinetics model. The Elovich model had good fitness for the Pb (II) ions judging by only the R^2 value, but that is not sufficient. The rate constant for PFO (K_1) is of a small order of magnitude, given as 0.0280 min^{-1}, 0.040 min^{-1}, 0.026 min^{-1} and 0.033 min^{-1} for Mn (II), Fe (III), Cu (II) and Pb (II) (Table 4.16). This suggests a deprived affinity between the mine site wastewater and the Ag_2O/TiO_2-clay nanocomposite with the model (López-Luna *et al.*, 2019). For the PSO rate constant K_2, the values diminish compared with the increased initial concentration.

Table 4.16: Kinetics parameters for Mn (II), Fe (III), Cu (II) and Pb (II) adsorption onto Ag_2O/TiO_2-clay

Pseudo First Order					**Pseudo Second Order**				
Ions	**Mn (II)**	**Fe (III)**	**Cu (II)**	**Pb (II)**	**Ions**	**Mn (II)**	**Fe (III)**	**Cu (II)**	**Pb (II)**
R^2	0.888	0.687	0.936	0.902	**R^2**	0.996	1	0.965	0.545
K_1(g/mg/min)	0.028	0.040	0.026	0.033	**K_2(g/mg/min)**	0.096	0.478	0.099	0.044
$q_{e(exp)}$(mg/g)	0.852	4.003	0.195	0.015	**$q_{e\ (exp)}$(mg/g)**	0.838	4.0026	0.195	0.015
q_e(cal)(mg/g)	0.556	0.522	0.216	0.043	**$q_{e\ (cal)}$(mg/g)**	0.898	4.014	0.243	0.077
SSE	0.669	8.109	0.763	1.339	**SSE**	0.004	$1.33x10^{-4}$	$2.33x10^{-4}$	$2.65\ x10^{-3}$
X^2	0.167	1.622	0.127	0.268	**X^2**	$3.97x10^{-3}$	$3.31x10^{-5}$	0.003	0.007
F-value	31.849	10.994	87.532	45.816	**F-value**	$3.41x10^{3}$	$2.68x10^{6}$	$4.76x10^{2}$	5.14
***p*-value**	0.005	0.021	$8.46x10^{-5}$	0.001	***p*-value**	<0.001	<0.001	<0.001	0.058
Intraparticle Diffusion Model					**Elovich**				
R^2	0.882	0.808	0.933	0.957	**R^2**	0.939	0.907	0.958	0.900
Kint	0.055	0.026	0.015	0.002	**α(g/mg/min^2)**	1.280	$1.21x10^{45}$	$1.28x10^{-2}$	$7.06x10^{-4}$
C(mg/g)	0.217	1.631	0.016	0.003	**β (g/mg/min)**	8.863	28.011	18.769	89.206
$q_{e\ (exp)}$(mg/g)	0.852	4.003	0.195	0.015	**$q_{e\ (exp)}$(mg/g)**	0.852	4.003	0.195	0.015
$q_{e\ (cal)}$(mg/g)	0.217	1.631	0.016	0.003	**$q_{e\ (cal)}$(mg/g)**	0.274	3.825	0.076	0.031
SSE	0.007	0.001	$8.23x10^{-4}$	$8.24x10^{-5}$	**SSE**	0.003	$5.43x10^{-4}$	$5.21x10^{-4}$	$5.78x10^{-5}$
X^2	$9.44x10^{-4}$	$1.59x10^{-4}$	$1.18x10^{-4}$	$1.18x10^{-5}$	**X^2**	$4.87x10^{-4}$	$7.75x10^{-5}$	$7.45x^{-5}$	$8.25x10^{-6}$
F-value	52.43	29.62	97.33	42.09	**F-value**	108.210	68.018	157.76	63.030
***p*-value**	$1.71x10^{-4}$	$9.63x10^{-4}$	$2.34x10^{-5}$	$3.38x10^{-4}$	***p*-value**	<0.001	<0.001	<0.001	<0.001

Therefore, the adsorption mechanism of the Mn (II), Fe (III), Cu (II) and Pb (II) onto Ag_2O/TiO_2-clay surface involves valence forces through the sharing or exchange of electrons between the adsorbate and the adsorbent as covalent forces and ion exchange (Ho, 2006). From the results, the rate constants for IPD (K_{int}), was not having a consistent increase with increased metal ions concentration, this means there is no film diffusion from the adsorbate bulk solution to the adsorbent layer. Also, the value of $q_{e(exp)}$ and $q_{e(cal)}$ for the IPD had great disparity, which shows the inconsistency of the model for fitting the kinetics of the metal ions adsorption onto the Ag_2O-TiO_2-clay adsorbent.

The C values between 0.003 and 1.63 signify a low boundary layer resistance by the adsorbent because, higher C values signify an intense effect of the boundary layer resistance between the adsorbent and the adsorbed (Kajjumba *et al.*, 2018). It is important to note that, if intraparticle diffusion is the mechanism underlying the adsorption process, the plot q_t against $t_{1/2}$ would be linear (Table 4.16). If the plot passes through the origin, the rate-limiting process would solely be due to intraparticle diffusion (Abesekara *et al.*, 2020; Hasani *et al.*, 2022). Otherwise, some other process is involved in addition to intraparticle diffusion.

Therefore, since the intraparticle diffusion model plot has a low regression coefficient when compared with the previous models and the intercept is not equal to zero (Table 4.16), it is unlikely that intraparticle diffusion was the only rate-limiting step. Other parameters obtained from the analysis of the IPD model are presented in Table 4.16. Considering the Elovich model desorption constant (β) which relates to the extent of surface coverage and activation energy. The values are unevenly distributed as concentration increases from Fe (III) to Mn (II) to Cu (II) and then to Pb (II) 8.86-89.26 g/mg/min (Table 4.16). This implies that there is no heterogeneous distribution of sites having activation energies that vary with surface coverage (Pintor *et al.*, 2018).

The low α values may imply the absence of chemical bonding, while the high suggests otherwise (Abdullah *et al.,* 2022). Considering the error functions, SSE and (X^2) error values closer to zero depict a significant agreement between the experimental ($qe_{,exp}$) and the calculated ($qe_{,exp}$). The Chi-square (X^2) error values obtained for PSO varied between 0.167 and 1.622 while that of Pseudo Second Order varied between $3.31x10^{-5}$ and $3.97x10^{-3}$. The Sum Square Error (SSE) values obtained for Pseudo-first-order also lie between 0.669 and 8.109 while the PSO model SSE values are between $1.33x10^{-4}$ and $4.00x10^{-3}$ which are far lesser than PFO error values.

The results obtained therefore suggest that the mechanism of adsorption of Mn (II), Fe (III), Cu (II) and Pb (II) ions from the mine wastewater was Pseudo-Second Order Kinetics controlled. This implies chemisorption phenomenon driven which is similar to the arsenic removal result using manganese ferrite nanoparticles reported by Lopez-Luna *et al*., (2019). This means the chemical reaction was significant in the rate-controlling step, which involves valency forces through the sharing or exchange of electrons between the Ag_2O-TiO_2-clay and mine wastewater (Ogbu *et al.*, 2019).

The Intraparticle and Elovich kinetic models comparatively explain the adsorption kinetics, especially for the Cu ion removal as demonstrated by the Chi-square test and SSE values. For the two models, F-values are high up to 108.21 for Elovich and 52.43 for Intra-Particle Diffusion (IPD). The p-values (probability values) for both IPD and Elovich are less than 0.001, but the Elovich error values are lesser than that of the Intraparticle diffusion model. This result implies that the chemical adsorption process is the rate controlling with homogeneous adsorbing surfaces, thus describing the multicomponent heavy metal adsorption system in the present study. The obtained Pseudo second order kinetics model agrees with some other adsorption studies on different clay composites (Mnasri-Ghnimi and Frini-Srasra, 2019; Nouh *et al.,* 2019).

4.6.5 Adsorption thermodynamics

The thermodynamic parameters of Mn (II), Fe (III), Cu (II) and Pb (II) ions onto the Ag_2O-TiO_2-clay, as obtained from the thermodynamics plots, are shown in Table 4.17. From the table, the negative values of Gibbs free energy change (ΔG°) at all temperatures for Mn, and Fe ions show that the adsorption of these two ions was feasible and spontaneous (Abunah *et al.,* 2019).

Nevertheless, the adsorption of Cu (II) and Pb (II) ions from wastewater was only feasible and spontaneous at the experimented temperatures of 303 K and 313K. The positive values of Enthalpy change (ΔH°), shows that the adsorption of the heavy metal ions was endothermic. More so, the magnitude of the enthalpy change provides information about the type of sorption. The heat evolved during physisorption generally lies in the range of 2.1–20.9 kJ/mol, while the heat of chemisorption generally falls in the range of 80–200 kJ/mol (Ogbu *et al.*, 2019). The values obtained for Mn (II), Fe (III), and Cu (II) ions fall between 1 and 60 kJ/mol, which implies that the reaction between the nano adsorbent and the adsorbate solution was more of being physically controlled than chemically controlled. The negative values obtained for entropy change (ΔS) for the adsorption of Mn. Fe, Pb and Cu onto the Ag_2O/TiO_2-clay reveal a reduction of randomness experienced at the adsorbent/adsorbate interface during the adsorption process (Mnasri-Ghnimi and Frini-Srasra, 2019).

4.7.6 Comparison of adsorption parameters of Ag_2O/TiO_2-clay with literature

Tables 4.18a and b show the comparison of adsorption parameters of Ag_2O/TiO_2-clay for Pb (II), Cu (II), Mn (II) and Fe (III) ions, with the available data in the literature. For the adsorption of the Mn (II) ion, it was observed that Ag_2O/TiO_2-clay (96.59%) performed better than the MnO-Zeolite (42%) reported by Rubio (2010).

Table 4.17: Thermodynamics parameters for Mn (II), Fe (III), Cu (II) and Pb (II) adsorption onto Ag_2O/TiO_2-clay nanocomposites

	Mn (II)			Fe (III)			Cu (II)			Pb (II)		
Temp. (K)	ΔG° (kJ/mol)	ΔH° (kJ/mol)	ΔS° (J/mol)	ΔG° (kJ/mol)	ΔH° (kJ/mol)	ΔS° (J/mol)	ΔG° (kJ/mol)	ΔH° (kJ/mol)	ΔS° (J/mol)	ΔG° (kJ/mol)	ΔH° (kJ/mol)	ΔS° (J/mol
303	-5.330	15.683	-0.535	-20.895	33.532	-73.013	-19.084	5.196	-166.255	-0.967	30.832	-119.056
313	-3.331			-11.451			-0.257			10.548		
323	-3.267			-10.090			0.621			8.485		
333	-3.110			-8.401			1.209			8.298		
343	-3.169			-8.241			6.915			8.109		
353	-3.033			-8.155			7.250			7.984		

Table 4.18a: Comparison of Ag_2O/TiO_2-clay adsorption parameters with other adsorbents in the literature

Adsorbents	Ag_2O/TiO_2 Precursors	TiO_2 Phase	Initial conc. C_o (mg/L)	Contact Time (min)	Adsorbent Dosage (g)	Surface area m^2/g	Crystallite size (nm)	Efficiency (%)	References
				Mn (II)					
MnO-Zeolite	-	-	100	150	1	-	3000	42	Rubio (2010)
Graphene-ZnO Nps	-	-	10.5	20	25.06	-	-	34.10	Leiva *et al.* (2021)
White rice husk	Organic	-	100	480	2.5	-	50000	26.60	Tavlieva *et al.* (2015)
AAC	-	-	0.943	120	0.5	14.15	8.10	83.12	Ajala *et al.* (2022b)
TiO_2-AAC	TTIP	Rutile	0.943	120	0.5	32.98	6.11	89.34	Ajala *et al.* (2022b)
Zeolite	Clinoptilolite	-	400	360	3.7	-	-	95.20	Motsi *et al.* (2009)
Ag_2O /TiO_2/Clay	TTIP	Rutile	0.943	120	0.5	48.07	6.29	96.59	**This study**
				Fe (III)					
Zeolite	Clinoptilolite	-	400	360	3.7	-	-	59.50	Motsi *et al.* (2009)
Ha-TiO_2	$TiCl_4$	Anatase	300	15	0.05	449	-	14.80	Kanna *et al.* (2005)
CBK/TiO_2	$Ti(SO_4)_2$	Anatase	50	60	1	118.0	-	87	Han *et al.* (2019)
Cellulosic waste	Organic materials	-	4000	1440	2	2.66	-	8.70	Genty *et al.* (2017)
AAC	-		20.02	120	0.5	14.15	8.10	86.45	Ajala *et al.* (2022b)
TiO_2-AAC	-		20.02	120	0.5	32.98	6.11	91.99	Ajala *et al.* (2022b)
Ag_2O/TiO_2/Clay	TTIP	Rutile	20.02	120	0.5	48.07	6.29	99.66	**This study**
				Cu (II)					
Ag/TiO_2/clay	$AgNO_3/TiO_2$	Anatase	1100	720	0.125	-	-	91.50	Ajenifuja *et al.* (2016)
Clay- TiO_2	TiO_2	A-R	100	240	0.1	50	30	91.19	Guillaume *et al.* (2018)
Raw clay	-	-	1000	60	1	17.84	-	3.07	Sdiri *et al.* (2014)
Bentonite	-		10	60	0.5	-	-	76.88	Hussain and Ali (2021)
TiO_2	TIO_2	A-R	1.28	30	0.5	50	30	99.90	Georgaka and Spanos (2010)

Table 4.18b: Comparison of Ag_2O/TiO_2-clay adsorption parameters with other adsorbents in the literature

Adsorbents	Ag_2O/TiO_2 Precursors	TiO_2 Phase	Initial conc. C_o (mg/L)	Contact Time (min)	Adsorbent Dosage (g)	Surface area m^2/g	Crystallite size (nm)	Efficiency (%)	References
Raw clay	Bentonite	-	2000	864	1	47	-	25.40	Budsaereechai *et al.* (2012)
Activated clay	-		2000	864	1	74	-	29.97	Budsaereechai *et al.* (2012)
AAC	-		0.943	120	0.5	14.15	8.10	68.47	Ajala *et al.* (2022b)
TiO_2-AAC	-		0.943	120	0.5	32.98	6.11	81.94	Ajala *et al.* (2022b)
Clay-$BTiO_2$	TTIP	Rutile	100	90	1	-	-	88.27	Ajala *et al.* (2022c)
Ag_2O/TiO_2/Clay	TTIP	Rutile	0.943	120	0.5	48.07	6.29	96.12	**This study**
				Pb (II)					
LAO-TiO_2	$TiCl_4$		50.00	1440	0.25	-	-	4.40	Bijang 2020
Bentonite	Local		10	60	0.5	-	-	75.76	Hussain and Ali (2021)
Raw clay	Bentonite	-	2000	864	1	47	-	76.50	Budsaereechai *et al.* (2012)
Activated clay	-		2000	864	1	74	-	84.00	Budsaereechai *et al.* (2012)
AAC	Kaolin		0.94	120	0.5	32.98	8.10	29.48	Ajala *et al.* (2022b)
TiO_2		Anatase		240	0.15	-	-	82.5	Poursani *et al.* (2016)
TiO_2-AAC	TTIP		0.94	120	0.5	32.98	6.11	32.39	Ajala *et al.* (2022b)
Clay-$BTiO_2$	TTIP	Rutile	100	90	1	-	-	92.51	Ajala *et al.* (2022c)
Ag_2O/TiO_2/Clay	TTIP	Rutile	0.943	120	0.5	48.07	6.29	40.26	**This study**

Also, the Ag_2O/TiO_2-clay performed better than the acid-activated clay (AAC) (83.12%), TiO_2-AAC (89.34%) reported by Ajala *et al.* (2022b) and Graphene-Zinc oxide (34.10%) reported by Leiva *et al.* (2021).This may be due to the modification of the clay by Ag_2O/TiO_2 nanoparticles. However, Motsi *et al.* (2009) found that Zeolite removes Mn (II) (95.20%) at almost the same magnitude as the Ag_2O/TiO_2-clay (96.59%) but at a longer contact time of 360 min. This corroborates the findings of Tavlieva *et al.* (2015) which revealed that manganese removal increased with the increase in contact time until it reaches equilibrium. As shown in the table, all other adsorbents have a low efficiency of below 50% for Mn (II) ion removal.

This justifies that the adsorbents in this study were efficient for the removal of Mn (II) ion at a lesser contact time of 120 mins than that of the Zeolite (360 mins). Also, the Ag_2O/TiO_2-clay adsorbent effectively removes Fe (III) ion from the mining wastewater than CBK-TiO_2, AAC and TiO_2-AAC at 87.00%, 86.45% and 91.99%, respectively. Other adsorbents shown in the table such as zeolite, Ha-TiO_2 and cellulosic waste gave adsorbent efficiency of 59.5%, 14.80% and 8.70% respectively, for Fe (III) ion removal, which are below the values obtained for Ag_2O/TiO_2-clay (96.12%) in Figure 4.27. The adsorption efficiency of Cu (II) unto AAC and TiO_2-AAC as presented in the table was 68.47% and 81.94%, respectively.

However, a similar adsorbent, though the anatase phase of TiO_2 reported by Ajenifuja *et al.* (2016) removed 91.50% of Cu (II). The 91.50% of Cu (II) removal was achieved at a much longer contact time of 720 mins. This shows that the Ag_2O/TiO_2-clay removed Cu (II) ions from the wastewater more efficiently than some adsorbents reported in the literature (Budsaereechai *et al.*, 2012; Sdiri *et al.*, 2014). Some other adsorbents such as anatase-rutile TiO_2 (Georgaka and Spanos, 2010) and anatase-rutile TiO_2-clay (Guillaume *et al.*, 2018) performed comparatively with the Ag_2O/TiO_2-clay

investigated. This may be due to the surface area of respective adsorbents obtained from different clay sources. In addition, the contact time of the adsorption process could also be responsible for the increase in the removal percentage of Cu (II) ion as Guillaume *et al.* (2018) attained the percentage removal of 91.19% Cu (II) ion at 240 min as against 120 mins in this study. Therefore, the shorter contact time to remove Cu (II) ion indicates the efficacy of the adsorbent investigated in this study.

As contact time plays a vital role in the adsorption process, which implies that a shorter interaction time in attaining equilibrium adsorption reduces the operational cost and the operating time (Rudi *et al.*, 2020). From the table, Pb (II) ion was the least adsorbed compared to other heavy metals, as the Ag_2O-TiO_2-clay removed only 40.26% of the Pb (II) ion. This is due to the ionic radii of Pb (II) ion (0.119 nm) which is more than those of Fe (III) (0.060 nm), Mn (II) (0.070nm) and Cu (II) (0.073 nm) ions. As the Pb (II) ion has the least chance to be incorporated into AAC and TiO_2-AAS structures compared with cations with smaller ionic radii (Mobasherpour *et al.*, 2012).

Generally, the Ag_2O/TiO_2-clay adsorbent revealed greater efficiency for the adsorption process as it was able to sequester multi ions from the mining wastewater in the order of Fe (III) > Mn (II) > Cu (II) > Pb (II). This is made feasible by the Ag_2O and rutile-TiO_2 nanoparticle's increased surface area of the Ag_2O/TiO_2-clay adsorbent. Therefore, the Ag_2O/TiO_2-clay adsorbent effectively removed several ions from the mine wastewater when compared to other comparable adsorbents shown in the table; this is what makes this study novel.

4.7.7. Adsorption mechanism of Ag_2O/TiO_2-clay nanocomposites

Usually, the mechanism of adsorption of the heavy metal ions onto the nano adsorbent is greatly influenced by the surface chemistry of the adsorbent, the ionic charge on the metal ions and the adsorbate interactions (Miyah *et al.*, 2017).

From this research, the adsorption of Mn (II), Fe (III), Pb (II) and Cu (II) ions onto Ag_2O/TiO_2-clay was dependent on the pH and ionic strength. Figure 4.30 provides information about the mechanism of the metal ions' adsorption onto the Ag_2O/TiO_2-clay nano adsorbent. It can be observed that the adsorption of heavy metal ions onto Ag_2O/TiO_2-clay was favoured by high pH ($pH > pH_{PZC}$) values above 8.20 points of zero charge, which resulted in a high amount of Mn (II), Fe (III), and Cu (II) ions adsorbed.

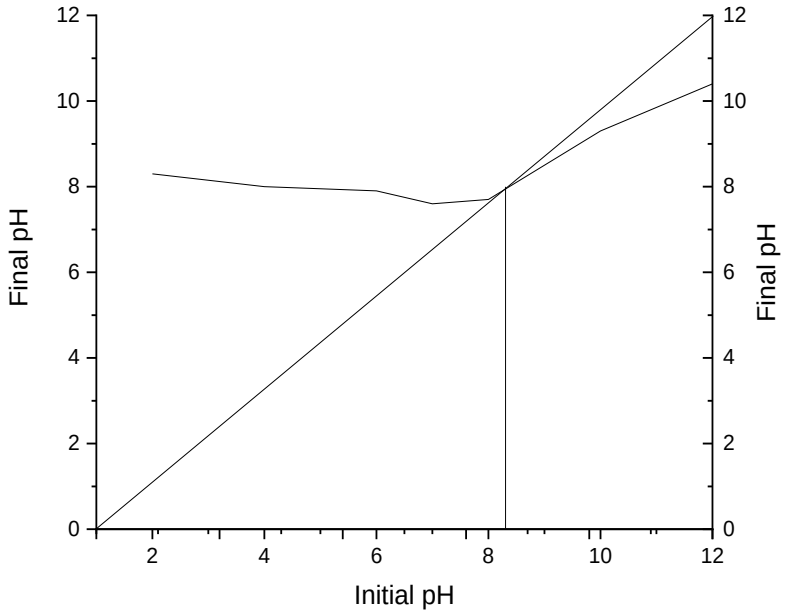

Figure 4.30: Ag_2O/TiO_2-clay point of zero charges (pH_{PZC}) determined by pH drift method

This was ascribed to the strong intermolecular electrostatic attraction between the negatively charged adsorbate in mine wastewater and the positively charged Ag_2O/TiO_2-clay surface. However, at higher pH than 8.2 ($pH > pH_{PZC}$), a small number of metal ions was adsorbed by Ag_2O/TiO_2-clay. This is due to the increased electronegativity (pH) of the adsorbate solution at the surface of the adsorbent. This reduces the susceptibility of the positive metal ions (Mn (II), Fe (III), Pb (II) and Cu (II)) adsorption due to electrostatic repulsion (Egbosiuba *et al.*, 2019). Other adsorption mechanisms such as; ion exchange or hydrophobic bonding instead of electrostatic interactions may also be responsible for the heavy metal adsorption onto the Ag_2O/TiO_2-clay surface.

4.7 Determination of Optimal Mixing Ratio for Ag_2O/TiO_2 and Clay for Composite Filter Fabrication

Clay and the Ag_2O/TiO_2 nanoparticle composite were prepared in the ratios of; 1:3, 1:1 and 3:1 (25:75, 50:50 and 75:25) for adequate comparison of their efficiency as adsorbents. These were tested for the removal of Mn (II), Fe (III), Pb (II) and Cu (II) ions from the mining wastewater as a function of contact time and the results are shown in Figure 4.31 (a-c).

The three composites were efficient in the removal of the Mn (II), Fe (III), Pb (II) and Cu (II) ions from mine wastewater under the applied conditions. The composite with 75% clay and 25% Ag_2O/TiO_2 (3:1) was able to remove; 92.22% Mn (II) ion, 99.53% Fe (III), 94.10% Cu (II) and 40.25% Pb (II) ions, at equilibrium time of 140 mins (Figure 4.31a). In the same vein, the composite with an equal mixing ratio (1:1) removed 96.58% of Mn (II) ion at 100 mins, almost 100% of Fe (III) ion at 40 mins, and 40.26% Pb (II) ion at 120 mins. While 40.89% of Cu (II) ion was removed at an equilibrium time of 120 mins (Figure 4.31b).

The composite with 1:3 (Figure 4.31c) removal efficiency for Cu (II) ion was the least, however, it removed other heavy metal ions satisfactorily. Comparatively, the 1:1 (50:50) (Figure 4.31b) composite performed better than the other two (1:3 and 3:1) composites in the removal of heavy metal ions per time. Meanwhile, the third composite (clay-Ag_2O/TiO_2) with a mixing ratio (1:3) was able to remove; 97.22% Mn (II) ion in 120 minutes, 99.52% Fe (III) ion in 120 mins, 38.20% Cu (II) ion in 80 mins and 30.89% Pb (II) ion in 120 mins (Figure 4.31c). From Figure 4.32, the percentage removal for the 75 clay:25 Ag_2O/TiO_2 composites (at 120 mins) compares relatively well with that of the 50:50, except it took a long time to attain equilibrium. The 25-75 clay-Ag_2O/TiO_2 composite could not remove more than 53.62% Cu (II) ion, even at elongated contact time (140 mins) of the process.

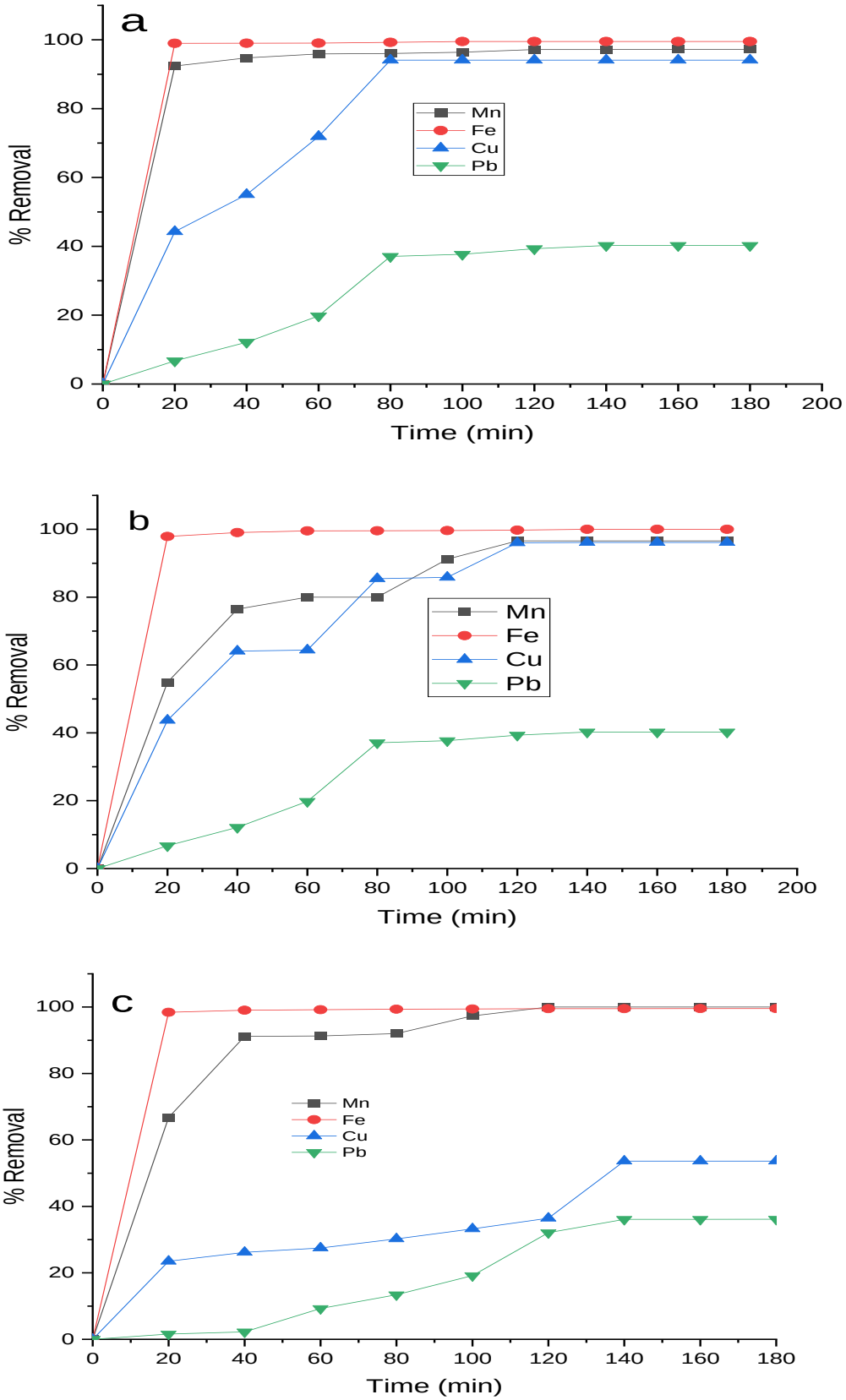

Figure 4.31: Effect of (a) 75 clay- 25 Ag_2OTiO_2 (3:1) (b) 50 clay- 50 Ag_2OTiO_2 (1:1) and (c) 25 clay- 75 Ag_2O-TiO_2 (1:3) compositions on the percentage adsorption of heavy metals

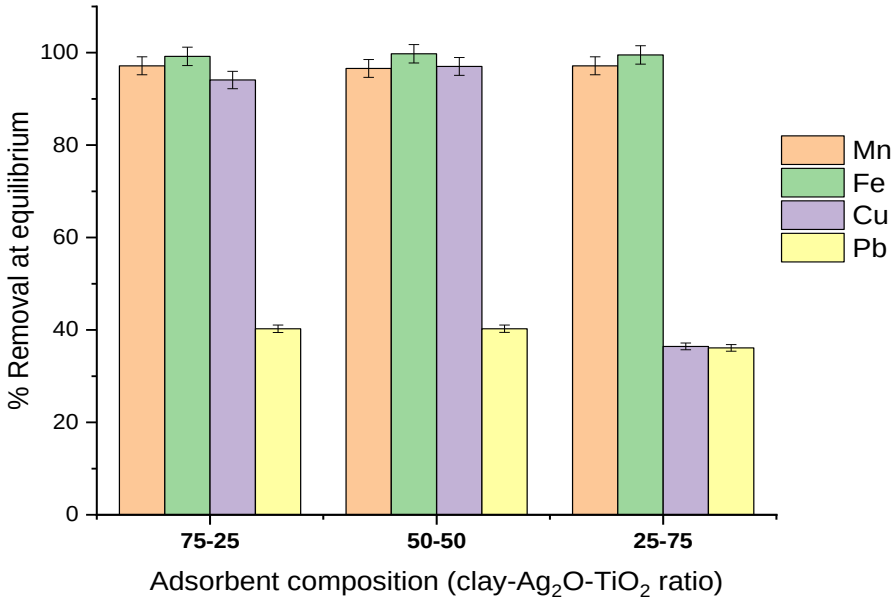

Figure 4.32: Comparative effect of clay ratio Ag_2O/TiO_2 composition on the percentage adsorption of heavy metals at equilibrium time

This inability may be due to a lack of proper interaction between the excess Ag_2O/TiO_2 to a small percentage of the clay and likely deposition of the Ag_2O/TiO_2 on the pores of the available clay. Therefore, the 50 clay: 50 Ag_2O/TiO_2 and 25 Ag_2O/TiO_2:75 clay composites were adjudged better as observed in Figure 4.31.

In addition, the crystallite size of the 25-75 clay-Ag_2O/TiO_2 being 8.75 nm predicts a smaller surface area when compared with 7.24 nm and 6.29 nm (for 25-75 clay-Ag_2O/TiO_2 and 50:50 clay-Ag_2O/TiO_2 composites). Smaller crystallite size may be linked to a wider surface area, which was responsible for a better adsorption process. Also, the HRSEM micrograph of the three micrographs shows that the 50:50 clay/nanoparticles ratio composition is more porous with a smaller size assemblage than others. The bigger crystallite sizes and lesser performance of the 75:25 composite may be linked to the clogging of the adsorptive surface by the excess quantity of TiO_2 and Ag_2O in the composite. Also, the moderate presence of Ag and Ti in 50:50 and 25:75 composites may have informed their higher rate of adsorption and affinity for the metal ions in the wastewater.

Therefore, the 50:50 composite performed better and was considered for the fabrication of the filter due to its high crystallinity and porosity, as well as increased functional group and more binding sites for the adsorption process.

4.9 Production of Ceramic Water Filter

The focus of this research is the fabrication of a filter for mining wastewater treatment. Before the fabrication, several compositions of clay-sawdust mixtures were constituted for filter test-bar production (a representation of the filter pot).

These were subjected to different tests such as shrinkage tests, water absorption/porosity tests and flow rate tests. These characterisations were carried out to determine the most suitable composition for an efficient nanocomposite filter fabrication.

4. 9.1 Effect of sample composition on the percentage shrinkage of samples

The different compositions of clay and combustible (sawdust) used for the filter bar and their shrinkage results are presented in Table 4.19a and the composition is in Table 3.8. The table presents the result of the rate of wet-to-dry shrinkage, dry-to-fired shrinkage and total shrinkage of samples for different nanoclay and sawdust compositions. The shrinkage tests were conducted to determine the extent of collapse in the structure of the clay, a determinant of the stability and porosity in filters, when subjected to different temperature ranges.

Table 4.19a: Shrinkage test for Ceramic Water Filter Test Samples Production

S/No	Sample Name	Clay (%)	Sawdust (%)	Wet-to-Dry Shrinkage (%)	Dry-to-Fired Shrinkage (%)	Total Shrinkage (%)
1.	FC0	100	0	13.10	10.53	23.63
2.	FC1	90	10	12.00	7.80	19.80
3.	FC2	80	20	11.25	7.70	18.95
4.	FC3	70	30	11.25	7.68	18.93
5.	FC4	60	40	11.25	7.67	18.92
6.	FC5	50	50	11.15	7.70	18.85
7.	FC6	40	60	11.25	5.67	16.92
8.	FC7	20	80	9.75	5.35	15.10

From the results obtained, it was observed that the shrinkage values of test samples FC0 were the highest with 13.10% wet-to-dry, 10.53% dry-to-fired and 23.63% total shrinkage. The values obtained are attributed to the high rate of evaporation of physically bonded water from the surface of pure clay by the drying and firing process (Gu *et al.*, 2019). From the table, the wet-to-dry shrinkage values of the test bars decreased from FC1 to FC7 as shown in Plate XV with values ranging from 12.00% to 9.75%.

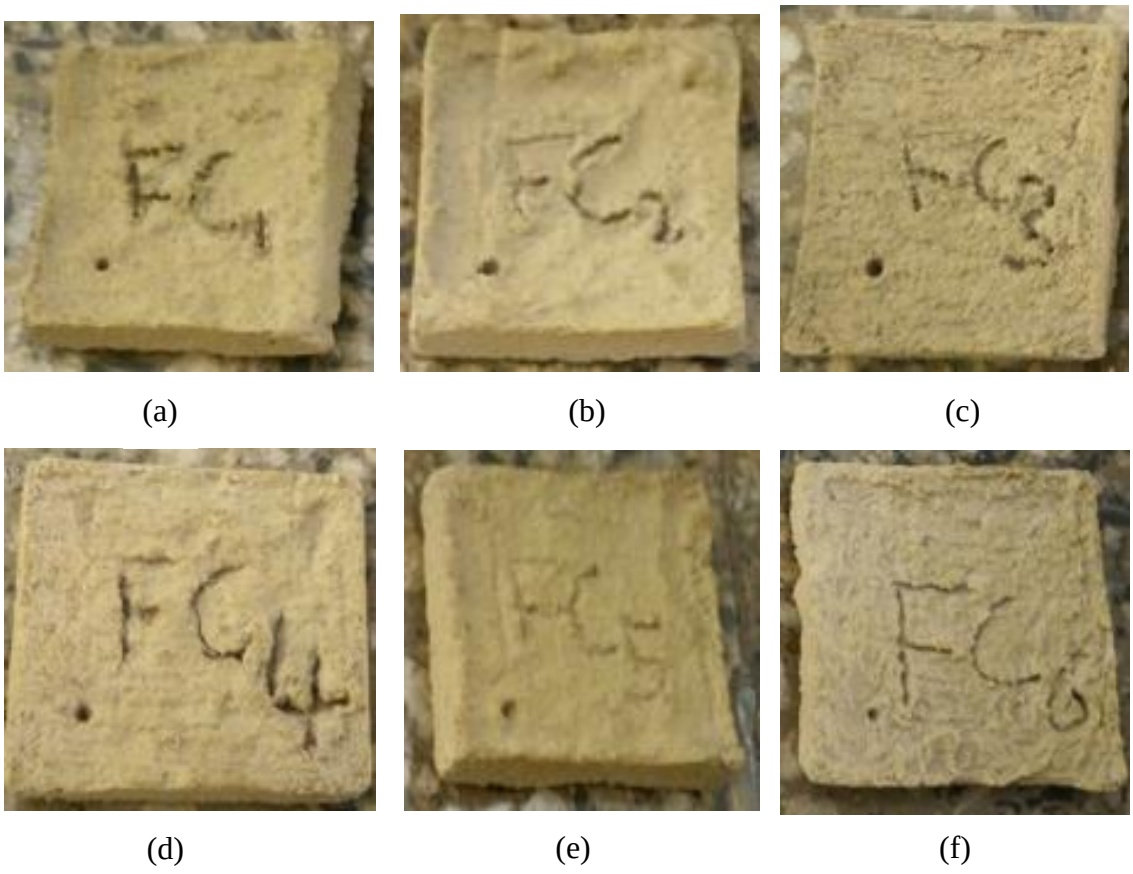

(a) (b) (c)

(d) (e) (f)

Plate XV: Nano filters test sample without grog as in (a) FC1 (b) FC2 (c) FC3 (d) FC4 (e) FC5 (f) FC6

The dry-to-fired shrinkage was also observed to follow a similar trend as a result of water loss by firing linked to the dehydroxylation water loss phenomena (El-Gaidoumi *et al.*, 2018). Following pure clay FC0, FC1 has the higher value of dry-to-fired shrinkages (7.80%) and FC7 has the least value of 5.67% dry-to-fired shrinkages. These results (FC1-FC7) are attributed to the densification of the test samples with higher clay volume.

Since the higher the clay volume, the higher the percentage shrinkage due to the bonding together of the clay particles (Zereffa and Desalegn, 2019). The reduction in dry-to-fired shrinkage, when compared with green-to-dry shrinkage, can be linked to the gradual development of crystalline phases. This is with an excess of glassy phase and an increase in voids formed at elevated drying temperature, which in turn causes a reduction in the dry-to-fired shrinkage values (Andreola *et al.*, 2013).

The percentage of total shrinkage obtained for the samples FC1 to FC7 is between 19.80% to 15.10%, with FC7 (20% clay, 80% sawdust) having the lowest percentage of total shrinkage. This may also be linked to the dehydroxylation of the kaolinite clay, causing a release of the OH group and further transformation of the filter sample into metakaolin (Bukalo *et al.*, 2017; Olaremu, 2015). Thereby resulting in excessive weight loss in samples FC1 to FC7. These values are higher than the acceptable shrinkage values in filters by the ASTM standard (ASTM, 2010), as it will increase the breakage rate of the filter during sintering or transportation.

Also, by physical examination, the final fired samples were observed to have warped, therefore the need for further experiments. Table 4.19b presents, the results of further experiments conducted on the test samples (modified test samples) with the introduction of grog. The grog is a vitrified amorphous clay, which reduces the degree of collapse of the bonded structures in moulded filters. Grog enhances also, the filtration performance of filters (Abiriga and Kinyera, 2014). The reduction in the collapse of structure may be enhanced by the grog's stability and reduced plasticity, which is a result of heat treatment imposed on the clay. From the table, the percentage of wet-to-dry shrinkage reduces from 8.92 to 6.80 in the three composites FC8, FC9 and FC10. These were considered a drastic reduction in comparison to those obtained in the Table 4.19a.

Table 4.19b: Shrinkage test for Ceramic Water Filter Test Samples Production

S/No	Sample Name	Wet-to-Dry Shrinkage (%)	Dry-to-Fired Shrinkage (%)	Total Shrinkage (%)
1	FC7	5.02	3.90	8.92
2	FC8	5.00	2.63	7.63
3	FC9	4.80	2.00	6.80

The reduction in percentage shrinkages and stability of the filter bars were attributed to the introduction of the grog-clay material. As the grog is in a shrunk state due to the thermal treatment imposed on it. Also, the mixtures already fused before usage in filter samples FC8, FC9 and FC10, leading to a reduction in linear shrinkage before and after sintering at high temperatures (Bories *et al.*, 2014). The ordinary clay test sample has the highest shrinkage value of 23.63% while, the sample with 40% grog has higher wet-to-dry, dry-to-fired and total shrinkage values (5.02, 3.90 and 8.92%) and the test sample with 50% grog introduction has the low shrinkage values (5.00, 2.63 and 7.63%). These samples shown in Plate XVI depict good stability of the filter test samples. This result agrees well with the shrinkage values of Baosaree *et al.* (2018) who obtained values between 5.67-12.68% total shrinkage per cent.

(a) (b) (c)

Plate XVI: Nano filter test samples (a) FC8, 40% (b) FC9, 50% (c) FC10, 60% grog

Summarily, the addition of 40, 50, and 60% grog to the nanoclay reduced the final shrinkages to 8.92%, 7.63% , 6.80% respectively. These values falls within the ASTM standard. Hence, sample FC9 (50% nanoclay, 50% grog) with the smallest shrinkage composition was adopted for further studies as FC10 may increase brittleness.

4.9.2 Effect of sawdust ratio on shrinkage ratio of filters

Sample composites NC1 to NC17 were formulated with FC9 (50% grog, 50% nanoclay) composition. This was ascertained earlier with the varied ratio of sawdust (nanoclay-grog/sawdust), to further determine shrinkage ratios, water absorption and porosity when sawdust is introduced. The result of the shrinkage test is presented in Table 4.20 and the images are shown on Plate XVII.

Table 4.20: Shrinkage test for Ceramic Water Filter test samples with Grog, Nanoclay and Sawdust

S/No	Sample Name	L_o (mm)	L_i (mm)	L_f (mm)	Wet-to-Dry Shrinkage (%)	Dry-to-Fired Shrinkage (%)	Total shrinkage (%)
1.	NC1	100	93.0	90.0	7.00	3.23	10.23
2.	NC2	100	94.0	91.0	6.00	3.30	9.30
3.	NC3	100	95.0	91.5	5.00	3.68	8.68
4.	NC4	100	94.0	92.0	6.00	2.13	8.13
5.	NC5	100	93.5	92.0	6.50	1.60	8.10
6.	NC6	100	95.0	93.0	6.00	1.11	7.11
7.	NC7	100	94.0	93.0	6.00	1.06	7.06
8.	NC8	100	95.0	94.0	5.00	1.05	6.05
9.	NC9	100	95.0	94.0	5.00	1.05	6.05
10.	NC10	100	97.0	95.0	4.01	1.05	5.06
11.	NC11	100	97.0	95.5	3.00	1.55	4.55
12.	NC12	100	98.0	96.0	2.00	2.04	4.04
13.	NC13	100	98.0	B	2.00	NA	NA
14.	NC14	100	99.0	B	1.00	NA	NA
15.	NC15	100	NM	NM	NM	NA	NA
16.	NC16	100	NM	NM	NM	NA	NA
17.	NC17	100	NM	NM	NM	NA	NA

Lo= Original length, Li= length after drying, Lf= Length after firing, B= Breakage NA=Not Available, NM= Not mouldable, DS= Drying Shrinkage, FS= Dried-to-Fired shrinkage, Green-to-Fired shrinkage TS= (DS+FS).

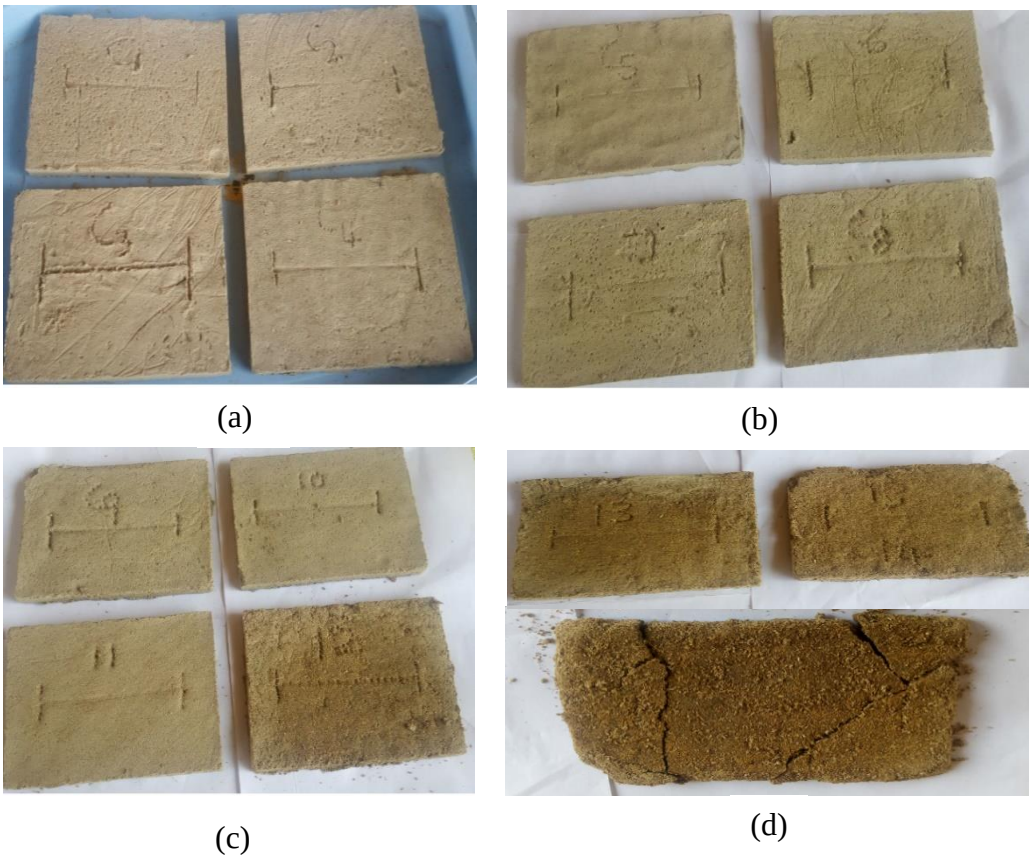

(a) (b)

(c) (d)

Plate XVII: Nano filter test samples with grog (a) NC1-NC4, (b) NC5-NC8, (c) NC9-NC12 and (d) NC13-NC17

From the table, it was observed that as the volume of clay reduces and sawdust increases from NC1 to NC14, length after drying (L_i) was reduced compared to the original length (L_o) as a result of evaporation of mechanically bonded water (mixing water) from the surface of the ceramic test filters. Length after firing also reduced as a result of in-depth drying at increased temperature, compared with length after drying and original length. The length, after open surface drying (L_i) increased non-uniformly with increasing saw dust ratio. This may be attributed to non-uniform temperature distribution in the open laboratory and non-uniform heat interaction to which the samples were exposed. This is contrary to length after firing (L_f), which increased uniformly between 90.00 to 96.00 mm due to constant heat supplied from the oven, with increased sawdust ratio composition from NC1- NC12. The resultant wet-to-dry shrinkage reduced from (7.00% to 2.00%).

This is due to a reduction in the volume of clay (lower volume) and stability of sawdust (high volume) because sawdust does not shrink. The nanoclay-grog/sawdust was stable and without warp, however, it became unmouldable and started to break away, as the sawdust content exceeds 65% (NC13- NC17). The absence of warp and stability of the composites NC1- NC12 achieved was because the grog used in the composite's composition is thermally stable at 700^{o}C and thus, reduces shrinkage in the ceramics (Abiriga and Kinyera, 2014). The addition of grog to the nanoclay/sawdust mixture also removed the warp in the mouldable samples as presented in Plate XVII. The result of the shrinkage test conducted on the samples as shown in Table 4.20 reveals that a smaller amount of sawdust corresponds to an increased shrinkage percentage, not minding the addition of 50% grog with 50% nanoclay.

Meanwhile, as the percentage of sawdust added increases, dried-to-fired shrinkage also reduces. This is because the clay-sawdust mixture already created a stable filter structure, a porous cake, having a stable length, thereby maintaining almost the length after the burning off, of the sawdust by firing at an elevated temperature of 850^{o}C. The total shrinkage, being an aggregate of wet-to-dried and dried-to-fired, reduces sharply from 10.23 (NC1) to 4.04 (NC12) until the filters break (B) and became unmouldable (NM) from C13-C17 by the presence of more sawdust. This may be linked to low adhesion between the fewer particles of the nanoclay and more sawdust as seen on Plate XVI.

4.9.3 Effect of sample composition on the water absorption and apparent porosity of samples

The water absorption test was carried out to determine the water flow within the samples using the standard methods and Archimedes' principle. The results of water absorption and apparent porosity of samples are presented in Table 4.21. From the table, it was observed that the water absorption capacity of samples NC1 to NC12 increased with an increase in the volume of sawdust mixed with clay.

This observation may be due to an increase in the pores spaces created by more sawdust as the samples were fired (Majid *et al.*, 2018; Tsao *et al.*, 2015; Yakub *et al.*, 2013). The water absorption results of samples NC13 to NC17 could not be presented in Table 4.21 due to the cracking and breaking away of the moulded composite, because of excess sawdust. The addition of the beneficiated kaolin to the grog created a more compact and rigid mixture due to the heat treatment imposed on the grog (sintered clay) used.

Table 4.21: Water absorption and apparent porosity of test samples

S/No	Sample	Water absorption (A)%	Apparent Porosity (P)%
1.	NC1	25.81	41.18
2.	NC2	30.24	42.18
3.	NC3	32.00	42.83
4.	NC4	34.60	44.17
5.	NC5	35.50	48.87
6.	NC6	49.65	58.68
7.	NC7	51.11	62.86
8.	NC8	60.71	73.40
9.	NC9	62.86	76.00
10.	NC10	67.88	77.27
11.	NC11	83.82	85.50
12.	NC12	91.80	86.92

The apparent porosity values of samples NC1 to NC12 observed follows the same pattern with water absorption capacity, with values ranging from 41.18 to 86.92%. The increase in the values depicts an increase in the porosity of the composites as the increased volume of sawdust increased because of the presence of more spaces created by the sawdust, which allowed more water to pass. These values are higher than that obtained in the literature between 39.90- 42.80% (Baosaree *et al.*, 2018), but with a similar pattern of less shrinkage, although a different type of clay was used.

Other differences in results may be attributed to natural modifications in the raw clay to geographical locations (Zereffa and Desalegn (2019). From the water absorption and apparent porosity results obtained, three samples were chosen due to their low total shrinkage (7.11, 7.06 and 6.06%), higher water absorption capacity (49.65, 51.11, 60.71%) and apparent porosity (58.68, 62.86 and 73.40%).

According to literature, efficient ceramic water filter formulations are expected to have performance parameters of linear shrinkage, water absorption rate, and apparent porosity in the ranges of ≤10%, >40%, and >50%, respectively (ASTM, 2010; Ibeh and Nwadinobi, 2021). Although, Yakub *et al.* (2013) reported 47% porosity in their fabricated ceramic water filter while 30.4% porosity was reported in another research (Ibeh and Nwadinobi, 2021). As a result, NC6, NC7 and NC8 with linear shrinkages of 7.11, 7.06, and 6.05%, water absorption rates; 49.65, 51.11, 60.71%, porosity; 58.68, 62.86 and 73.40%, respectively were employed for the filters' fabrication process (Appendix E). These values are in agreement with the literature and were chosen for further experiments. The three test samples NC6, NC7 and NC8 made from the clay (50% nanoclay/50% grog) and sawdust in vol/vol (13:7, 12:6 and 11:9) with 50% vol of water, were used to manufacture small filters NC6, NC7 and NC8 as shown in Plate XVIII.

(a) (b)

(c)

Plate XVIII: Small-size moulded filter of (a) NC6, (b) NC7 and (c) NC8

4.9.4 Water flow rate of samples

A water flow rate test was carried out as an important quality assurance step to indicate the rate at which water passes through the filter. The results of the water flow rate of the filters shown in Plate XIX are presented in Table 4.22.

Plate XIX: Flowrate test of ceramic filters of (a) NC6, (b) NC7 and (c) NC8

Sample NC8 has the highest flow rate of 0.170 L/hr, followed by sample NC7 with a water flow rate of 0.122 L/hr and the least was 0.086 L/hr for NC6. The results obtained revealed an increase in water flow rates with an increase in the apparent porosity and absorption capacity of the fabricated samples. The lowest flow rate in sample NC6 could be attributed to the low volume sawdust content of 25% when compared with 40% and 45% in samples NC7 and NC8 with higher flow rates respectively. The clay ratio of 75% to sawdust ratio of 35% may be linked to the densification of the NC6 sample, causing fewer pore spaces and pore networks for the free flow of water in the NC6 filter. The NC7 flow rate of 0.122 L/h, higher than the NC6 is attributed to an increase in the combustible ratio, which created a better tortuous pathway for the flow of water through the pores of the NC7.

Also, NC8 with a 0.178 L/h flow rate, implies larger interconnected pores due to the highest combustible volume, which is responsible for pores created in the NC8 filter. This filter was not considered for further studies because, large pores (a function of material ratios) may discourage bacteria and other microorganisms removal, which is by size exclusion (Venis and Basu, 2020).

Table 4.22 Water flow rate of filter samples

Sample	Water flowrate (L/h)
NC6	0.086±0.005
NC7	0.122±0.005
NC8	0.178±0.003
$NC7_S$	0.123±0.003
$NC7_B$	1.700±0.01

Therefore, NC7 filter composition was adopted in the fabrication of small and big filters having Ag_2O/TiO_2 nanoparticles embedded in them, which was denoted as $NC7_S$ and $NC7_B$ shown in Plate XX. The new small and big filters containing 2 g of Ag_2O/TiO_2 per 800 g of clay fabricated with the NC7 composition denoted as $NC7_S$ and $NC7_B$. The $NC7_S$ and $NC7_B$ were also evaluated for their flow rate and the result obtained is presented in Table 4.22 alongside the other small filters. The flow rates of 0.123 L/hr and 1.70 L/hr were obtained from the $NC7_S$ and $NC7_B$ as shown in Table 4.22. The result obtained showed that the addition of the nanoparticles does not hurt the fabricated filter as the flow rate of the filter without nanoparticles (NC7) flowrate compares well with the filter with the Ag_2O-TiO_2 nanoparticles (NC7s), as there was no significant difference in the flowrate values obtained (0.122 L/hr and 0.123 L/hr).

Plate XX: Fabricated small (NC7s) and big ($NC7_B$) filters with Ag_2O-TiO_2

This may be due to Ag_2O-TiO_2 nanoparticles bonding well with the structure of the kaolinite clay. The flow rate value of the big filter fabricated with ($NC7_B$) is higher compared with the result obtained by (Yakub *et al.*, 2013), who reported a 1.3-2.0 L/h from 50:50 volume ratio of clay to sawdust employed, different from 60:40 and 65:35 used in this study. The disparity may be due to the type of clay and the sawdust tree (*Anogeissus Leiocarpus*) employed in this study. The flow rate result of the filters with Ag_2O-TiO_2 $NC7_S$ shows that, there is no significant difference in the flow rates of the filter without nanoparticles (0.122 L/h) and that with Ag_2O-TiO_2 nanoparticles, having 0.123 L/h flow rate. The higher flow rate of the big filter NC7B, 1.70 L/h may be attributed to its large surface area (where increased gravitational force can act), this implies more pores available on the surface of the filter.

4.10 Testing of Filter Assembly

The performance of fabricated filter assembly as shown in Plate XXI for the mining wastewater treatment was conducted using a ceramic water filter made from sample NC7s (nano clay: grog: kaolin of 2:1:1 with 40 % sawdust and 0.0025 g Ag_2O-TiO_2/g clay) for the removal of heavy metals. The results obtained for the inlet concentration of heavy metals in wastewater before adsorption and the permissible limits set by WHO and EPA are presented in Table 4.23a. Table 4.23b shows the results of the heavy metals concentration (outlet concentration) and percentage removal of the metal ions after the adsorption treatment for 5 h using the ceramic filter.

Plate XXI: The performance evaluation of fabricated filter assembly

The performance evaluation of the filter for each metal ion studied showed that Fe(III) ions were completely removed by the filter from 20 minutes of contact up to the 5^{th} hour, with 100.00% removal of ions, which falls within the acceptable limit by WHO, EPA and NIS (Bankole *et al.,* 2019; WHO, 2017).

Table 4.23a: Inlet Concentration and Effluent Limit by WHO and Environmental Protection Agency (EPA)

Ions	**Fe (III)**	**Mn (II)**	**Pb(II)**	**Cu(II)**	**References**
Inlet concentration (mg/L)	20.019	4.291	0.943	0.313	**This study**
WHO limit (mg/L)	0.300	0.050	0.050	2.000	WHO (2017)
EPA limit (mg/L)	0.200	2.000	0.050	0.050	Bankole *et al.* (2019)

Table 4.23b: Concentration of the Treated Mining Wastewater with the Filter

Adsorption time (h)	**Fe(III) (mg/L)**	**%Removal Fe (III)**	**Mn(II) (mg/L)**	**%Removal Mn (II)**	**Pb(II) (mg/L)**	**%Removal Pb(II)**	**Cu(II) (mg/L)**	**%Removal Cu(II)**
0	20.02	-	4.29	-	0.94	-	0.31	-
0.33	0.00	100.00	0.00	100.00	0.00	100.00	0.00	100.00
0.67	0.00	100.00	0.00	100.00	0.00	100.00	0.00	100.00
1.00	0.00	100.00	0.01	99.74	0.00	100.00	0.00	100.00
2.00	0.00	100.00	0.02	99.65	0.00	100.00	0.00	100.00
3.00	0.00	100.00	0.02	99.63	0.00	100.00	0.00	100.00
4.00	0.00	100.00	0.02	99.58	0.00	100.00	0.00	100.00
5.00	0.00	100.00	0.02	99.58	0.00	100.00	0.00	100.00

Table 4.24: Physicochemical Parameters Performance Evaluation by the Filter

Parameter	Initial values	Final values	%Removal	WHO/EPA (2017)	NIS (2015)
Turbidity (NTU)	14.54 ± 0.51	1.86±0.04	87.27	1.00-5.00	5
Phosphate (mg/L)	11.60 ± 0.63	5.09±0.01	56.21	0.10	0.10
Carbonate (mg/L)	BDL	-	-	100-500	100-500
Nitrate (mg/L)	33.01 ± 0.55	5.15±0.01	84.67	50.00	50
Sulphate (mg/L)	38.83 ± 0.15	2.30±0.1	94.08	100	100
BOD (mg/L)	1.04 ± 0.18	1.00±0.00	78.12	Not specified	
COD (mg/L)	274.00 ± 6.00	28.00±0.58	89.78	<120	
DO (mg/L)	3.27 ± 0.01	7.00±0.02	-	>6.50-8.00	>6.50-8.00
pH	5.97 ± 0.05	7.80±0.08	24.10	6.50-8.50	6.50-8.50
Total coliform (Cfu/100 mL)	$1.12x10^3$ ± 25.17	$2.78x10^2$ ±2.08	74.55	10	10
Conductivity (µS/cm)	750.66 ±53.42	425.00±1.63	45.51	<500	<500
Fe (mg/L)	20.02±0.20	0.00±0.01	100	1.00-3.00	0.3
Cu (mg/L)	0.31±0.01	0.00±0.01	100	0.05	1
Mn (mg/L)	4.29±0.01	0.01±0.01	99.74	0.05	0.2
Cd (mg/L)	ND	-	-	0.005	0.003
Ni (mg/L)	0.33±0.01	-	-	3.00	0.02
Pb (mg/L)	0.98±0.01	0.00±0.01	100	0.015	0.01
Cr (mg/L)	0.10±0.01	-	-	0.10	0.05
Colour	Dark	Clear	100	Clear	Clear
Odour	Offensive	Odourless	100	Odourless	Odourless

The Cu (II) and Pb (II) ions were also completely removed, while 99.58% of the Mn (II) ion was removed and agrees with the permissible limit as approved by the standard organisations. Comparatively, the results of the outlet concentration of the metal ions as shown in Table 4.23b is far lesser than those of the inlet concentration as shown in Table 4.23a. Therefore, the performance evaluation study specifies that each of the heavy metals in the mining wastewater after treatment conformed to the permissible limit of outlet concentration at different times.

The physicochemical parameters of the treated mining wastewater at 1 hr of a test are presented in Table 4.24. From the Table, the turbidity of the wastewater decreased from 14.614 NTU to 1.8 NTU, depicting clear water free of suspended particles, the phosphate concentration decreased from 11.6 mg/L to 5.08 mg/L, a decrease also, but higher than the 0.5 mg/L stated by WHO. The nitrate concentration decreased from 33.6 mg/L to 5.15 mg/L which is within the acceptable limits by standard organisations reported by Bankole *et al.* (2019) for electroplating wastewater. The values of BOD obtained after treatment of the mining wastewater by the fabricated filter (NC7) indicate that the treated water can be suitable for living organism survival. Dissolved oxygen (DO) values increased from 3.27 mg/L to 7.00 mg/L, which implies that treated water can support life. The obtained final pH (7.80) shows non-acidic water, suitable for human consumption and other usages which agree with WHO/EPA and NIS standards of quality water. The total coliform count was reduced by 75%, but the remaining value was still higher than the permissible total coliform in drinking water. Therefore, the treated water is recommended for irrigation purposes. The reduced conductivity from 750.66 to 45.51 μS/cm shows the water is devoid of excess hydrogen ions thus, reduced acidity. The selected heavy metal ions targeted were all removed to acceptable levels which buttress the efficacy of the fabricated filter.

The mining wastewater treated (physical appearance), changed from being dark to colourless with the odour completely adsorbed by the composite filter. The Mn (II), Fe (III), Pb (II) and Cu (II) metal ions targeted were removed in conformity with the WHO and EPA standards. The performance evaluation results, therefore, show the efficiency and suitability of the ceramic-silver-titanium nanocomposite filter in removing undesirable physicochemical parameters from the mining wastewater.

4.11 Mechanical Properties of the Fabricated Filter

The average compressive strength, tensile strength and flexural strength results of the fabricated $NC7_B$ filter made of Ag_2O-TiO_2-clay composite and sawdust performed in three cycles are presented in Table 4.25.

Table 4.25: Mechanical test results of Ag_2O-TiO_2-clay filter (NC7B)

Filter	Compressive strength		Tensile strength		Flexural strength	
	Young Modulus (MPa)	Stress at peak (MPa)	Young Modulus (MPa)	Stress at peak (MPa)	Stress at peak (MPa)	Deflection at peak (m)
NC7	1.78±0.10	54.06±0.1	873.61±1.8	51±0.04	1.85±0.44	1.23±0.15

From the table, it was observed that the compressive strength of the NC7B filter with tensile stress 54.06 MPa and Young Modulus 1.78 MPa compares well with the literature (Ibeh and Nwadinobi, 2021). The Tensile strength has its Young Modulus at 873.61 MPa while the flexural strength stress at the peak is 1.85 MPa. This may be due to the presence of sufficient combustible material in the clay mixture, causing the proper distribution of load within the available pore sites in the filter. The values of the tensile strength obtained further buttress the rigidity and toughness of the fabricated filter. The Young Modulus value obtained agrees with the recommended standard values of compressive strength in the filter generally, expected not to be below 700±10 kN/m^2 ($7x10^{-4}$MPa) (Sooksaen and Karawatthanaworrakul, 2015).

The values obtained in the present research are higher than that reported by Baosaree *et al.* (2018), who used rice husk charcoal as a pore-forming agent in their clay filter composite. The tensile strength Young modulus obtained in this study is greater (<) than 300 MPa reported when bio-composite of lignocellulose composite films from wood and paper were tested (Chen *et al.*, 2018). The flexural strength of the filters obtained as 1.85 MPa for the NC7B filter implied that the filter can withstand a higher amount of load before rupture, which is attributed to the increased stiffness of the material as indicated by the Young modulus of the composite filter. From the study, it was observed that increased porosity is commensurate with increased flexural strength but low tensile strength, this agrees with previous report (Mustapha *et al.*, 2021). These results highlights the efficacy and the efficiency of the fabricated NC7B filter, as it can withstand suitable loads.

4.12 Post-analysis of the Fabricated NC7$_B$ Filter

4.12.1 XRD of the composite

Figure 4.33 (a) and (b) depict the X-ray diffraction (XRD) spectra of the fabricated filter, (a) before use and (b) after use. The two figures showed the presence of Anordite, Albite, Labrodorite and Quartz peaks which are alumino-silicate transformations related to the kaolinite clay structure compositions.

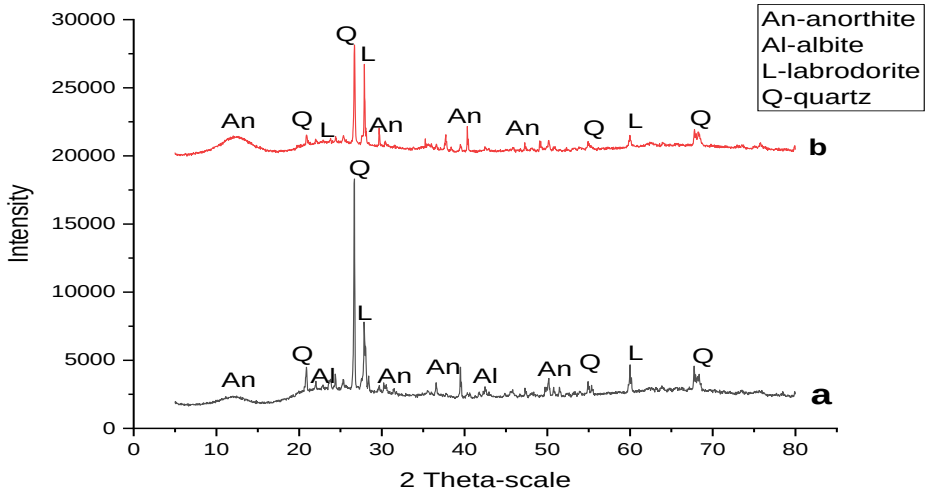

Figure 4.33: XRD pattern of (a) Unused filter (b) Used filter composites, SC

Figure 4.33 (b) are Anorthite, Labrodorite and Quartz peaks also, with the disappearance of Albite peak transformations. In Figure 4.33a the diffraction peaks at 2Ɵ values of 13.63° which corresponds with Miller indices (-110) and agrees with the Anorthite (JCP 00-018-1202) library. At 2Ɵ value of 22.02°(-201) is the Albite peak corresponding with JCP 01-076-0927, while the 2Ɵ values of 23.83° (-130), 27.83° (040) and 60.95° (024) are Labrodorite peaks corresponding with JCP 01-083-1371 respectively.

The peaks at 2Ɵ values and Miller indices of 20.92°(100), 26.59° (101), 50.51°(400) and 67.61° (212) corresponding to quartz peaks were also observed similar to those on the kaolinite clay-base used in the filters' fabrication. The Anorthite spectral on 23.65° indicates a shift from Labrodorite, maintaining the same Miller indices at (-130) on both planes. Also, at 25.64°(-1-1 2) is a shifted peak, from Labrodorite on an unused filter (Figure 4.32a) to Anorthite on a new plane (Figure 4.32b) which depicts the deposit of the heavy metal ions entrapped within the wall of the used filter. Other diffraction peaks and corresponding crystal planes 20.92°(100), 26.59° (101), 50.51°(400) and 67.61° (212), on Figure 4.32b closely matched with that of the Quartz phase of SiO_2 in alumino-silicates respectively. The average crystallite size of the filter increased from 32.49 nm before use to 44.44 nm after use, an indication of adsorption onto the surface of the spent/used filter composites.

4.12.2 SEM of the composites

The SEM in Plate XXII (a) shows the surface microstructure of the filter composite before use. While Plate XXII (b) shows the surface microstructure of the filter composite after use. In terms of the surface morphology and porous structure, there was no significant change in the hemispherical arrangement of the kaolinite plates after the wastewater treatment process, though the surface roughness of the used filter support slightly increased with the hemispherical structure more pronounced.

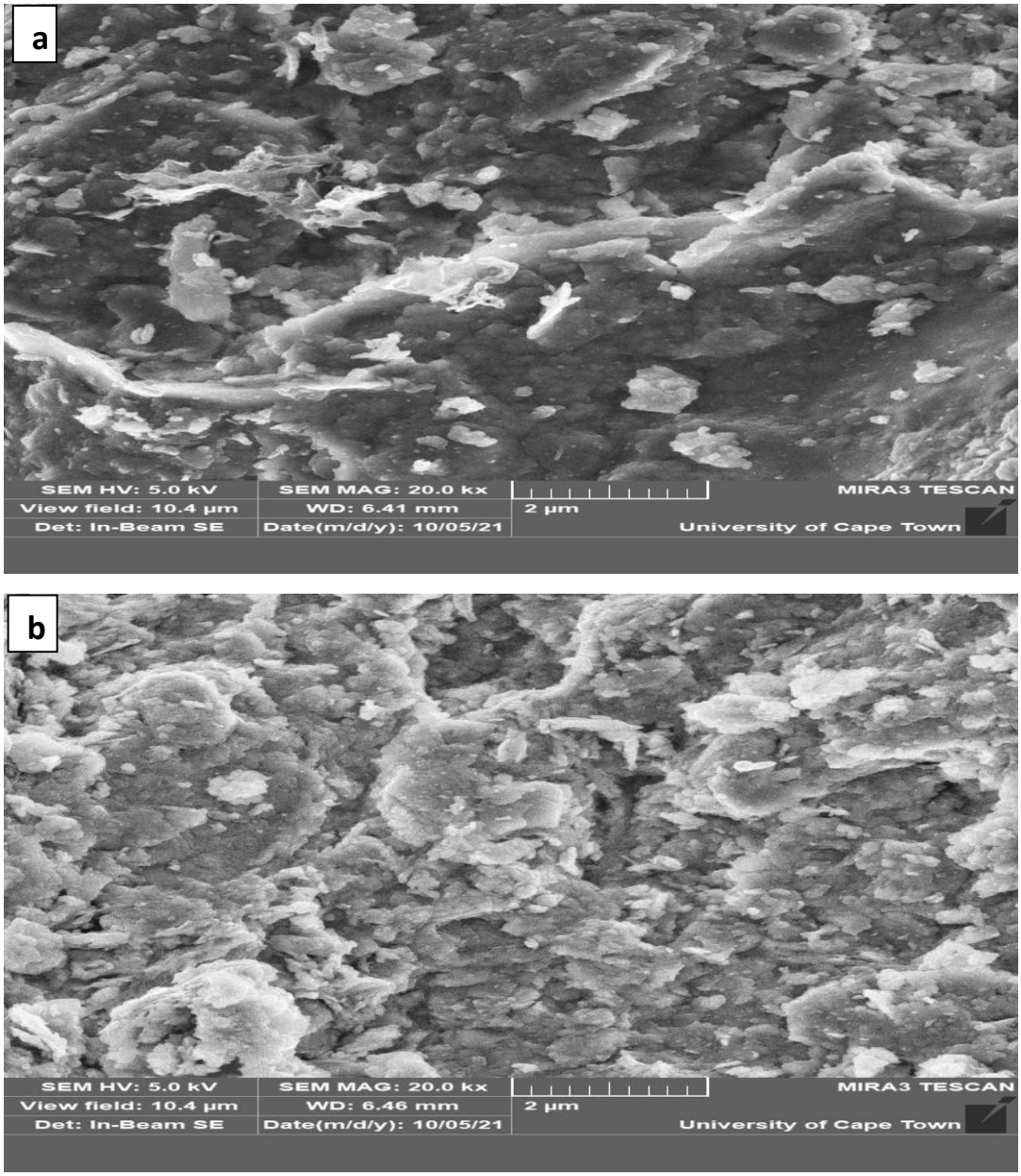

Plate XXII: HRSEM of the Composites Filter (a) before use/NC7 (b) after use

This must be a consequence of filling the pores of the filter with the adsorbed pollutants from the mining wastewater, evidenced by reduced porosity shown in the watershed images (Appendix F). The EDS results of the unused and used filter composites are presented in Plate XXIII (a) and (b). Before use, the filter has the component elemental composition of 19.11% C, 51.02% O, 12.79% Al, 14.68% Si, 0.44% Ca, 0.43% Ti and 1.54% Fe while the used filter has 28.37% C, 48.12% O, 10.33% Al, 11.85% Si, 0.27% and 1.05% Fe.

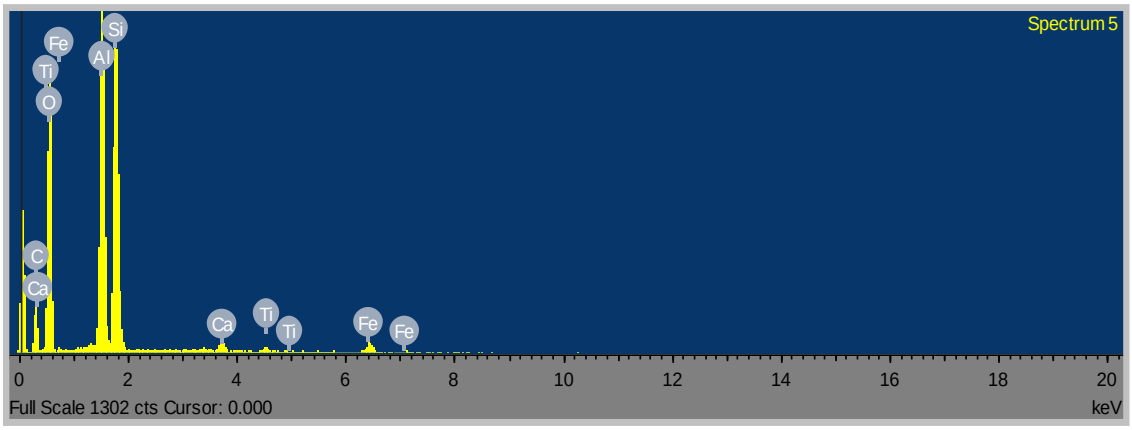

(a) EDS of Filter before use/NC7

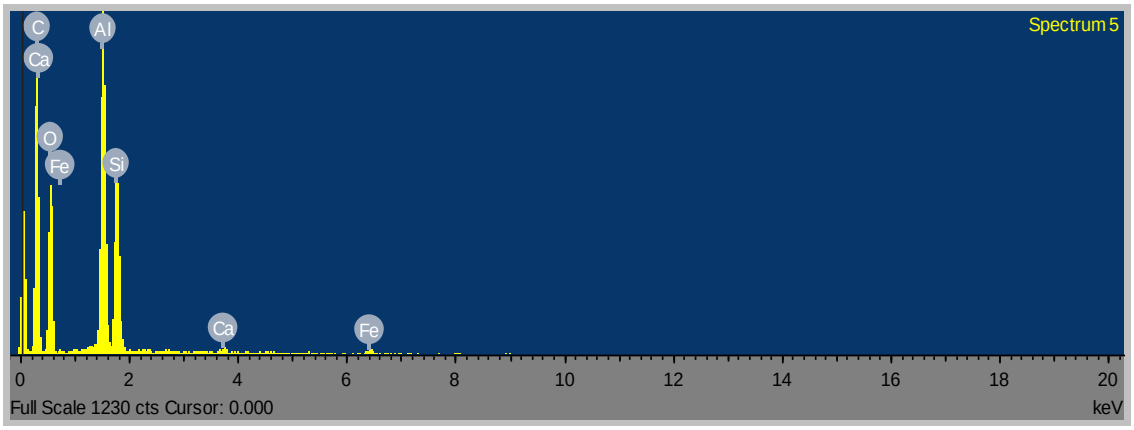

(b) Spent Filter/Composite (after use)

Plate XXIII: EDS of the composites filter (a) before use/NC7 (b) after use

From the result, it was observed that silver embedded in the composite did not show in both composites, probably due to its low concentration of 0.042mg/g of moulded clay. Titanium was observed in the composites before use as evidence of doping of 2.46 mg/g TiO_2 on clay. After the treatment, the percentage of oxygen in the filter decreased from 51.02% to 48.12%, probably as a result of the combination with the adsorbed ions. The non-detection of Ti after usage may be attributed to the several cycles of usage of the filter. Also, added weights of the adsorbed pollutants are another factor, making the titanium composition in the spent filter to be below the detection level in the used filter composite when subjected to EDS analysis.

4.12.3 Chemical stability of the filter

The chemical stability of the filter was analysed by subjecting the filter to acid and basic solutions between the pH of 2 and 14 at 48 h soaking time in ambient temperature. The obtained result is presented in Figure 4.34 which shows that there was no significant weight loss when the filter sample was soaked in an acidic solution from pH 2 to 6. The produced filter exhibited minimal weight loss in strongly acidic solutions compared to the weak regions. The minimal loss in weight in the strongly acidic solution may be due to the dissolution of retained organic material in the filter after sintering or the dissolution of some elements from the kaolinite clay used, which may make the filter become fragile over a long period.

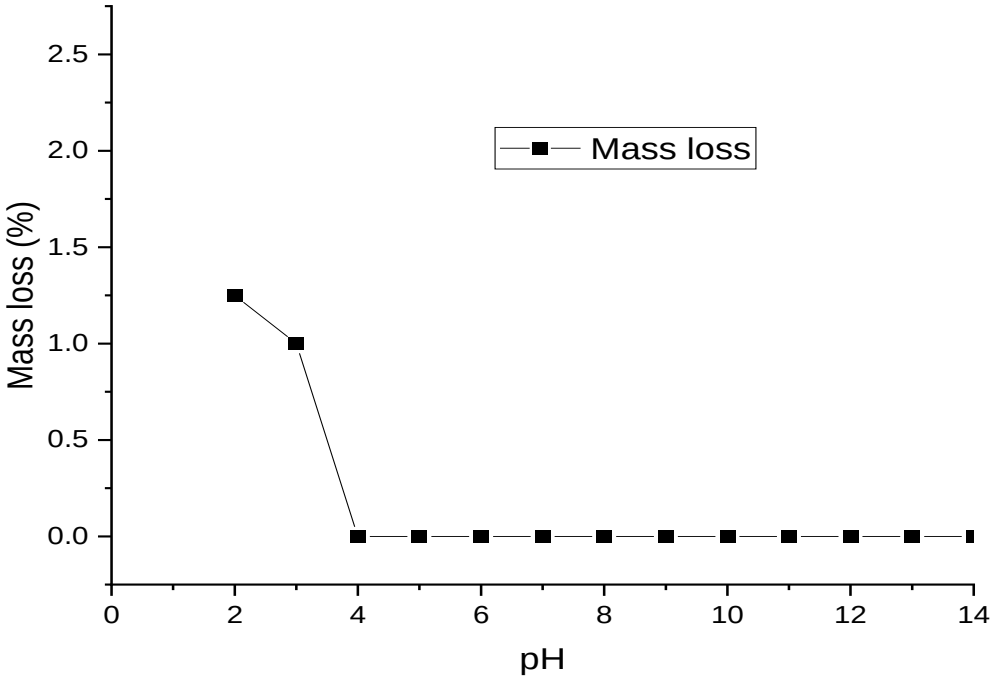

Figure 4.34: Mass loss (%) of sintered Ag_2O-TiO_2-clay/sawdust filter in an acidic and basic medium at room temperature for 48 h

From the figure, there was no weight loss in the filter samples when immersed in aqueous NaOH between pH 8-14. This result may be due to the strong interaction between hydroxide ions and the porous sample, providing sufficient mechanical strength.

There was no mass loss also, for the porous filter made from Mouka's clay and rice husk sintered at 830˚C, the mass loss during the chemical stability/corrosion test showed good chemical corrosion resistance for both acidic and basic mediums (Nguiamba *et al.*, 2019). This shows that the fabricated filter is both acid and alkali resistant and could thus, possess the characteristics of suitable ceramics which is corrosion resistance.

4.12.4 Filters' reusability performance

The ability of the fabricated filter to be recycled or reused in the treatment of mining wastewater is among its most important features. The reusability extent of the NC7 filter to remove heavy metal ions was examined for 10 cycles of 24 hours each, using the mining wastewater. At the end of each heavy metal adsorptive experimental cycle, the sample of the filtrate was retrieved from the container and subjected to AAS analysis. The filter was oven dried at 200˚C for 1h, scrubbed with a brush, re-washed with distilled water using a sponge and then oven-dried the second time at 200˚C for 1 h before the continuation of another cycle of reusability experiment. This was repeated for every cycle of the reusability experiment to reactivate the pores on the filter.

Figure 4.35 shows that a high percentage of Fe (III), Mn(II), Cu (II) and Pb(II) ions were removed from the mining wastewater from the first cycle to the 8th cycle. However, there was a decrease of about 2% in the percentage removal of Pb (II) ions at the 8^{th} cycle, which could be a result of insufficient cleaning of the surface of the filter, thus making the obtained 2% concentration of Pb (II) ion to be present in the treated water. There was an upward improvement in the percentage of BOD, COD and DO remove as the cycle progresses from the 1^{st} to the 8^{th}. The better performance in the removal may be attributed to partially clogged pores of the filter over a long cycle of use.

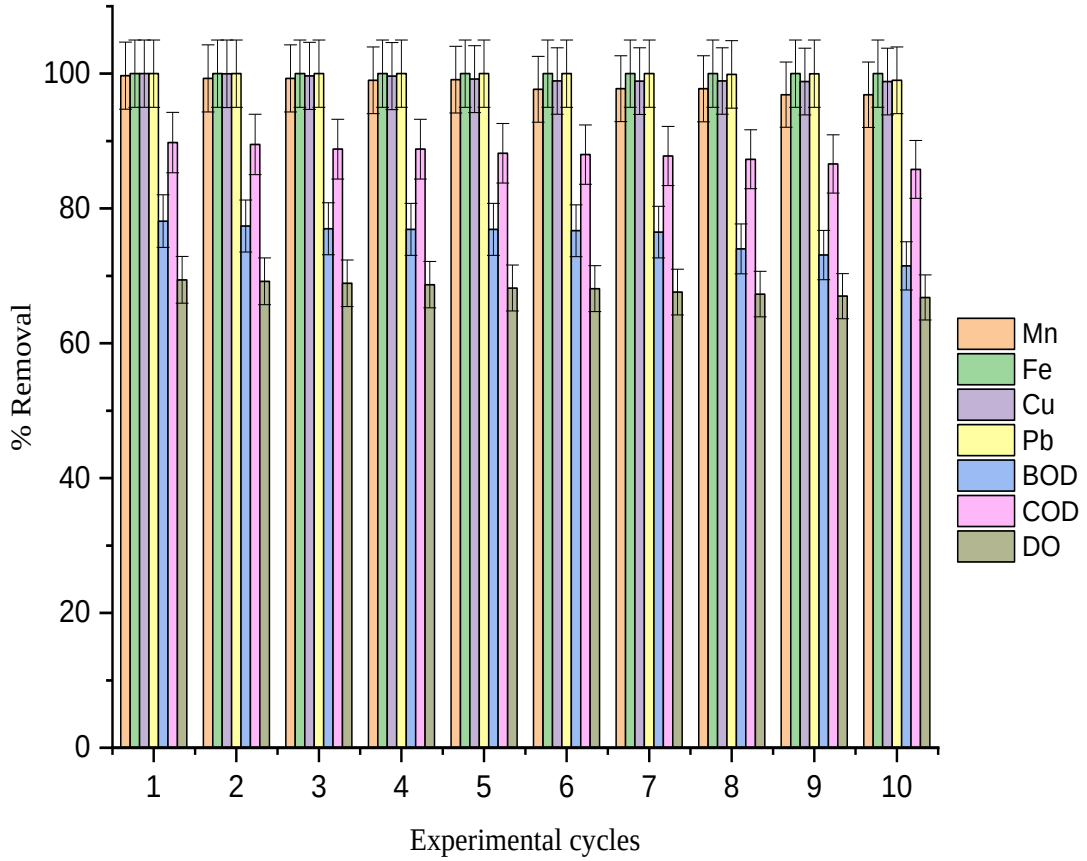

Figure 4.35: Reusability cycle of the filter, showing % heavy metal removal

4.13 Modelling Results

The rate of water discharged versus the time taken to flow from the fabricated water filter $NC7_B$ is presented in Figure 4.36. The rate of flow is determined by the pore size and pore size distribution, coupled with permeability. These in turn quantify the filter's efficacy in removing particulates from wastewater. From the result obtained, it was discovered that the rate of flow of water from the NC7 filter reduces over 12 h, test time in a slow-wise disposition. Comparatively, the NC8 filter tested, being the most porous of the filters studied, exhibited the fastest rate of discharge (which is not desirable for optimum treatment of wastewater and so discarded), followed by the preferred NC7 filter as shown in Figure 4.37.

The NC6 (35% volume sawdust) manufactured filter was linked to the slowest discharge rates in both the short and long term. Therefore, the rate of water discharge by the ceramic filters increases with porosity.

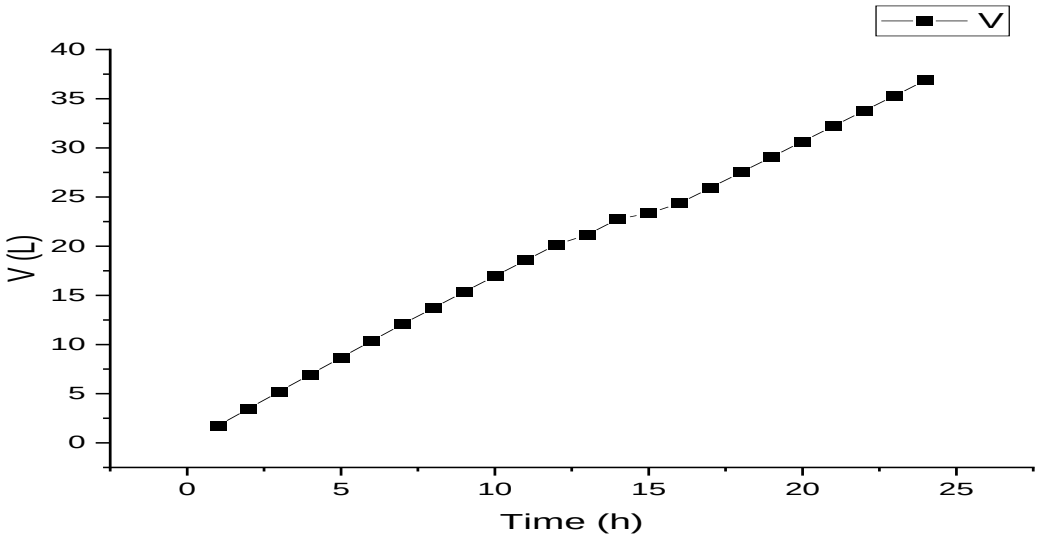

Figure 4.36: Rate of Flow through the NC7B Filter versus Time

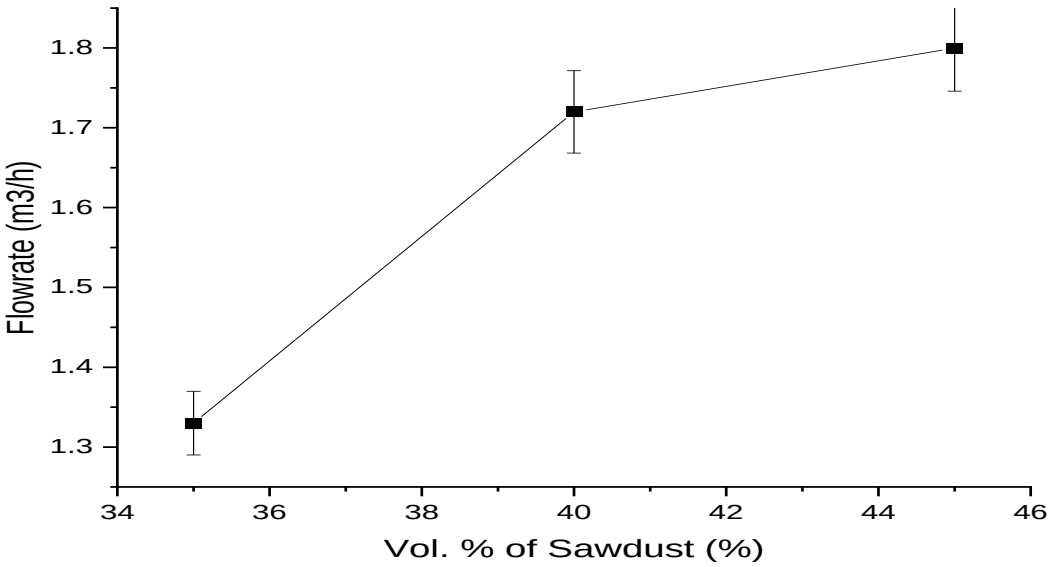

Figure 4.37: Dependence of the Flow Rate on the Volume Percentage of Sawdust

The flow rates obtained for the NC7 (40% volume sawdust) filter were between ~1.6 and 1.75 L/h during the first twelve hours of testing time, which agrees with the range that is typical of Potters for peace ceramic (PFP) filters (Yakub *et al.*, 2013). Whereas, flow rates for the NC6 were well below this level (Figure 4.37).

It is important to note that the amount of water through the NC7 approached an asymptote, as the pressure head decreased with increasing flow. Hence, the flow-time plots became increasingly nonlinear with increasing flow, as also shown in Figure 4.38.

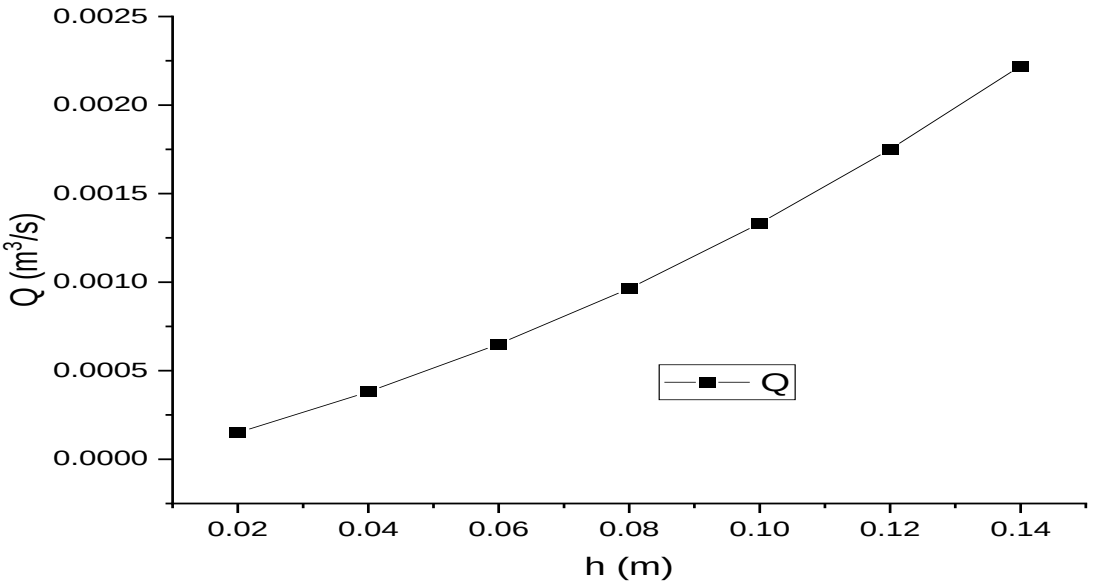

Figure 4.38: Rate of flow through the filter membrane at varying heights

This asymptotic tendency was recently theoretically modelled using a stochastic birth process model (Yakub *et al*., 2013) that was personalised to the amounts of organic raw material utilized in the filter production process as shown in Figure 4.38. The figure presents the variation of flow rate with different heights at the constant experimental time. From the results, it was observed that there was a reduction in flow rate as the height of water in the filter reduces applying constant pressure. At the full height of the filter, the flow rate presents 0.0022 m^3/s, which was reduced to 0.0018 m^3/s at the next hour. At the lowest height obtainable with the NC7B filter, the flow rate of the ceramic filter has dropped to 0.00165 m^3/s. The results imply that decreased height caused a random decrease in the flow rate of water obtained from the ceramic filter. This is a result of the decrease in the force of inertia acting on the surface of the filter at a reduced height.

This implies, for optimum performance of the ceramic filter, the water volume in the filter must be maintained at the maximum possible always, which can be ensured by introducing a sensor in the filter, which will control the inlet valve to make the filter volume maintained at the maximum regularly.

The result obtained from the permeate flux analysis of the filter is presented in Figure 4.39. The figure showed that the quantity of permeate flux generated during the membrane separation process per unit of time is directly proportional to the mass of permeate collected at constant time.

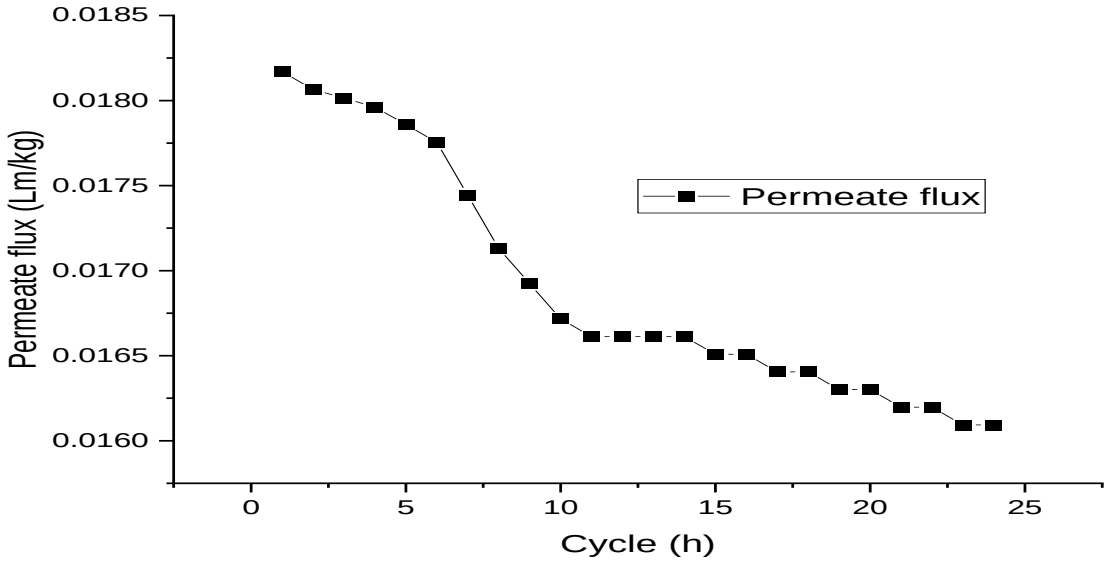

Figure 4.39: Permeate flux of filter per cycle

This shows that the clogs of pollutants filtered over time reduce the number of available pores in the filter. Hence, it is necessary to carry out the regeneration process of the filter after about 24 cycles of use, to increase the quantity of permeate for efficient wastewater treatment. This can be done by washing and scrubbing with a hard brush. Therefore, the filter can be efficiently used over 24 cycles, even at optimum performance, before the need for cleaning or regeneration. The results of the retention of heavy metal ions in the filter per cycle are presented in Table 4.26.

Table 4.26: Percentage of heavy metals retention by the filter

		Cycle						
Metal ions	**Parameters**	**1**	**2**	**3**	**4**	**5**	**6**	**7**
Fe (III)	Cf (mg/L)	20.01	20.01	20.01	20.01	20.01	20.01	20.01
	Cp (mg/L)	0	0	0	0	0	0	0
	Retention (%)	100	100	100	100	100	100	100
Mn (II)	Cf (mg/L)	4.29	4.29	4.29	4.29	4.29	4.29	4.29
	Cp (mg/L)	0	0	0.01	0.02	0.02	0.02	0.02
	Retention (%)	100	100	99.77	99.53	99.53	99.53	99.53
Pb (II)	Cf (mg/L)	0.975	0.975	0.975	0.975	0.975	0.975	0.975
	Cp (mg/L)	0	0	0	0	0	0	0
	Retention (%)	100	100	100	100	100	100	100
Cu (II)	Cf (mg/L)	0.33	0.33	0.33	0.33	0.33	0.33	0.33
	Cp (mg/L)	0	0	0	0	0	0	0
	Retention (%)	100	100	100	100	100	100	100

From the table, the percentage retention of Fe (III), Pb (II) and Cu (II) ions is 100% throughout the seven cycles investigated while Mn (II) was 100% for only the first two cycles of the study and the remaining cycles were 99.53%. The findings revealed that the fabricated filter has a close unity retention rate, which confirms the efficiency of the membrane separation process over the adsorption process.

The results of the cake constitutive relationship show that the pressure drops across the fabricated filter estimated using the Hagen Poiseuille Equation was 4.891×10^{-3} N/m, while the velocity of flow was 0.0285 m/s and the cake specific resistance estimated to be 4.937×10^{-6}. The results indicate that the larger the particles' diameter, the faster the filtration. The larger the pressure drops across the filter unit, the faster the filtration. The larger the initial filtration flow rate, the faster the filtration, and the larger the initial solidosity, the faster the filtration. The results are similar to one of the cases of monosized particles and are comparable to the literature data (Tien, 2012).

CHAPTER FIVE

5.0 CONCLUSION AND RECCOMENDATIONS

5.1 Conclusion

This research developed a nano-based filter from silver oxide, titanium (IV) oxide and kaolinite clay as a nanocomposite for the treatment of mining wastewater that was laden with heavy metals such as Mn (II), Fe (III), Pb (III) and Cu (II) ions, and other pollutants. The study concludes that:

A sixty percentage yield of beneficiated clay was achieved when kaolinite clay of 250 g was dissolved in 5000 mL of distilled water. The crystallite size of the clay improved from 16.65 nm to 14.92 nm due to the beneficiation and further reduced to 8.08 nm after activation. This confirmed that the beneficiation and activation improved the crystallite size of the kaolinite clay.

Parkia biglobossa leaves extract was found most suitable among the six leaves studied, for the nanoparticle synthesis of Ag_2O and TiO_2. The optimisation of nanoparticle synthesis for Ag_2O gave the optimal conditions as $10cm^3$ precursor volume, $1cm^3$ aqueous leaves extract, 60^oC temperature and pH of 8 to achieve a particle size of 5.79 nm. Also, the nano synthesis of TiO_2 was achieved at 50 cm^3 leaves extract, 50 cm^3 TTIP, and 200 rpm stirring speed, to yield 3.45 nm crystallite size.

The incorporation of 25%, 50% and 75% w/w of Ag_2O/TiO_2 on the activated clay gave a well-intercalated Ag_2O/TiO_2-clay composite with well-formed hemispherical edges.

The characterisation of nanoparticles confirmed rutile phase TiO_2 in the +4 oxidation states and also the formation of cubic Ag_2O nanoparticles. The Ag_2O/TiO_2-clay nanocomposite characterisation confirmed the presence of functional groups, mesopores and improved morphology that encourages maximum adsorption of heavy metals and other pollutants.

The analysis of the mining wastewater revealed that it was laden with heavy metals; Mn (II), Fe (III), Pb (III) and Cu (II) ions. The mining wastewater has high turbidity (14.54 NTU), low pH (5.97), high BOD (1.04 mg/L), high COD (274.00 mg/L), nitrate (33.01 mg/L), sulphate (38.83 mg/L) and conductivity (750.66 μS/cm) which are above the WHO/NIS permissible limit for drinkable water.

The Ag_2O/TiO_2-clay was found to be the most effective among the nano-adsorbents (TiO_2, Ag_2O/TiO_2, clay, Ag_2O-clay, TiO_2-clay and Ag_2O/TiO_2-clay) investigated, for the removal of the metal ions and other pollutants from the mining wastewater. From among the isotherm models studied, Jovanovic fitted best the experimental adsorption data. Hence, the surface adsorption was homogeneous with mono-layer coverage of the adsorbate molecule. Also, among the kinetic models employed, Psuedo-second-order best fitted the experimental data, thus, the process was multiple adsorption systems. The thermodynamic parameters justified that the adsorption processes were endothermic, feasible and spontaneous.

The fabricated filter was found to have a low shrinkage ratio of 7.06%, an acceptable water absorption percentage of 51.11%, a porosity of 62.86%, and a flow rate of 1.7 L/h. The filter also possessed acceptable mechanical properties such as compressive strength, and tensile strength. The filter was found suitable for the effective removal of heavy metals and other physicochemical parameters in the mining wastewater.

Therefore, Ag_2O/TiO_2-clay is a suitable and efficient nanocomposite for the sequestering of mining wastewater that was laden with Mn (II), Fe (III), Pb (III) and Cu (II) ions, and other pollutants.

5.2 Recommendations

Following the achievements in the research work, these are the recommendations made;

(i) From the study, the nanocomposite was found excellent, research work should be conducted on the regeneration of the spent adsorbents and further re-use ability of ceramic water filter.

(ii) The Ag_2O/TiO_2-clay nanocomposite was tested for the efficient sequestering of heavy metals in mining wastewater. Further study is recommended on the deployment of the nanocomposite for the treatment of other industrial wastewater such as electroplating, battery and textile.

(iii) The leaching of Ag_2O and TiO_2 nanoparticles from the Ag_2O/TiO_2-clay composite filter should be examined by analysing filtrates with the Inductively Coupled Plasma (ICP) technique, to know the exact composition of the treated water.

(iv) This work sintered the filter at 850^oC temperature, although the filter was effective for the mining wastewater treatment. Further investigations on different sintering temperatures are recommended for possible improvement of porosity distribution within the filter element to increase the flow rate.

5.3 Suggestion for further studies

a. The adsorbents developed from this study can be used for the treatment of other industrial wastewater apart from mining wastewater.
b. The nanocomposite can be developed into pellets wherein it can be used for fixed bed adsorption columns for industrial wastewater treatment.
c. The fabricated pots can be arranged in series for the efficient removal of microbes in the wastewater.

5.4 Contributions to Knowledge

This study has developed a nanocomposite filter from kaolin base material with nanocomposite Ag_2O and TiO_2 nanoparticles for the treatment of mining wastewater. Ag_2O/TiO_2-clay nanocomposite in the developed water filter yielded the highest removal of all the metal ions. The developed filter is composed of 60% clay, 40% sawdust and 0.042/2.46 $mg.g^{-1}$ Ag_2O/TiO_2. The percentage removal of 96.59, 99.66, 96.12 and 40.26 for Mn (II), Fe (III), Cu (II) and Pb (II) respectively. Therefore Ag_2O/TiO_2-clay nano-filter developed is suitable and efficient for the sequestration of pollutants from mining wastewater for irrigation and other purposes.

REFERENCES

Abdallah, M. A. M. (2022). Removing two transition metal ions from spiked wastewater by two modified nano-sorbents. *Cogent Engineering, 9*(1). doi:10.1080/23311916.2022.2035133

Abdallah, S. (2019). Remediation of Copper and Zinc from wastewater by modified clay in Asir region southwest of Saudi Arabia. *Open Geoscience, 11*, 505–512. doi:10.1515/geo-2019-0041

Abdullah, N., Adnan, N., Rashidi, N., Yaacob, M., & Salim, N. (2022). Comparing the adsorption isotherms and kinetics of phosphate adsorption on various waste shells as adsorbent. *Water Practice and Technology, 17*. doi:10.2166/wpt.2022.051

Abesekara, M. S., Kosvinna, K. N., & Amarasinghe, P. (2020). *Adsorption and desorption studies of Ni^{2+} ions on to coconut shell char*. Paper presented at the IOP Conf. Series: Earth and Environmental Science, Chennai, India.

Abhishek, L., Abishek, K. R., Deepak, K. K., & Sivakumar, G. (2014). Advanced water treatment using nano-materials. *International Journal of Innovative Research in Science, Engineering and Technology, 3*(11).

Abiriga, F., & Kinyera, S. O. (2014). Effect of Grogs on in the Performance of Ceramic Water Filters. *Science Journal of Physics, 2014*, 1-10. doi:10.7237/sjp/252

Abu-Dalo, M., Jaradat, A., Albiss, B. A., & Al-Rawashdeh, N. A. F. (2019). Green synthesis of TiO2 NPs/pristine pomegranate peel extract nanocomposite and its antimicrobial activity for water disinfection. *Journal of Environmental Chemical Engineering, 7*(103370). doi:10.1016/j.jece.2019.103370

Abunah, D., Onindo, C., Andala, D., & Ochoti, E. (2019). Physico-chemical removal of heavy metals from contaminated water using recyclable montmorillonite cellulose nanocomposite. *Journal of Materials and Environmental Sciences, 10*(12), 1349-1361.

Acheampong, M. A., & Ansa, E. D. O. (2017). Low-Cost Technologies for Mining Wastewater Treatment. *Journal of Environmental Science and Engineering, B*(6), 391-405. doi:10.17265/2162-5263/2017.08.001

Acosta, F. A., Castillejos, A. H., Almanza, J. M., & Flores, A. (1995). Analysis of Liquid Flow through Ceramic Porous Media Used for Molten Metal Filtration. *Metallurgical and Materials Transactions B, 26B*(February), 159-171.

Addy, M., Losey, B., Mohseni, R., Zlotnikov, E., & Vasiliev, A. (2012). Adsorption of heavy metal ions on mesoporous silica-modified montmorillonite containing a grafted chelate ligand. *Applied Clay Science, 59*, 115-120.

Adebayo, G. B., Adegoke, H. I., & Sidiq, F. (2020). Adsorption of Cr(VI) ions onto goethite, activated carbon and their composite: kinetic and thermodynamic studies. *Applied Water Science, 10*, 213-231. doi:10.1007/s13201-020-01295-z

Aguiar, A. O., Andrade, L. H., Ricci, B. C., Pires, W. L., Miranda, G. A., & Amaral, M. C. S. (2016). Gold Acid Mine Drainage Treatment by Membrane Separation Processes: An Evaluation of the Main Operational Conditions. *Separation and Purification Technology*. doi: http://dx.doi.org/10.1016/j.seppur.2016.07.003

Aguiar, J. E., Cecilia, J. A., Tavares, P. A. S., Azevedo, D. C. S., Castellón, E. R., Lucena, S. M. P., & Silva-Junior, I. J. (2017). Adsorption study of reactive dyes onto porous clay heterostructures *Applied Clay Science, 135*, 36-44.

Ahmad, A., Hamidah Mohd Setapar, S., Ali Yaqoob, A., & Nasir Mohamad Ibrahim, M. (2021a). Synthesis and characterization of GO-Ag nanocomposite for removal of malachite dye from aqueous solution. *Materials Today: Proceedings, 47*, 1359-1365. doi:https://doi.org/10.1016/j.matpr.2021.03.643

Ahmad, W., Singh, A., Jaiswal, K. K., & Gupta, P. (2021b). Green Synthesis of Photocatalytic TiO2 Nanoparticles for Potential Application in Photochemical Degradation of Ornidazole. *Journal of Inorganic and Organometallic Polymers and Materials, 31*(2), 614-623.

Ahmed, S., Ahmad, M., Swami, B. L., & Ikram, S. (2016). A review on plants extract mediated synthesis of silver nanoparticles for antimicrobial applications: A green expertise. . *Journal of Advanced Research, 7*, 17-28.

Ajala, E. O., Ajala, M. A., & Saka, H. B. (2021). Titanium dioxide-based nanocatalyst in biodeisel production. In A. P. Ingle (Ed.), *Nano- and biocatalysts for biodiesel production* (pp. 115-142). Hoboken, New Jersey, USA: John Wiley & Sons Ltd.

Ajala, E. O., Ayanshola, A. M., Obodo, C. I., Ajala, M. A., & Ajala, O. J. (2022a). Simultaneous removal of Zn(II) ions and pathogens from pharmaceutical wastewater using modified sugarcane bagasse as biosorbents. *Results in Engineering, 15*, 100493. doi:https://doi.org/10.1016/j.rineng.2022.100493

Ajala, M. A., Abdulkareem, A. S., Tijani, J. O., & Kovo, A. S. (2022b). Adsorptive behaviour of rutile phased titania nanoparticles supported on acid-modifed kaolinite clay for the removal of selected heavy metal ions from mining wastewater. *Applied Water Science, 12*(19), 1-24. doi:10.1007/s13201-021-01561-8

Ajala, M. A., Ajala, E. O., Tayo-Alabi, A., Sodiq, H. K., Abdulkareem, A. S., Kovo, A. S., & Tijani, J. O. (2022c). Development of Titanium Dioxide Pillared Clay Adsorbent for Removal of Lead (II), Zinc (II), and Copper (II) ions from Aqueous Solution. *UNIOSUN Journal of Engineering and Environmental Sciences, 4*(1), 264-280. doi:10.36108/ujees/2202.40.0172

Ajenifuja, E., Ajao, J. A., & Ajayi, E. O. B. (2016). Equilibrium adsorption isotherm studies of Cu (II) and Co (II) in high concentration aqueous solutions on Ag-TiO2-modified kaolinite ceramic adsorbents. *Applied Water Science*. doi:10.1007/s13201-016-0403-6

Akinnawo, S. (2019). Synthesis, Modification, Applications and Challenges of Titanium Dioxide Nanoparticles. *Research Journal of Nanoscience and Engineering, 3*(14), 10-22.

Al-Naib, U. M. B. (2018). *Introductory Chapter: A Brief Introduction to Porous Ceramic* (U. Basheer Ed.). London, SW7 2QJ, United Kingdom: IntechOpen.

Al-Qahtani, K. M. (2017). Cadmium removal from aqueous solution by green synthesis zero valent silver nanoparticles with Benjamina leaves extract. *Egyptian Journal of Aquatic Research, 43*(4), 269-274. doi:10.1016/j.ejar.2017.10.003

Alandis, N. M., Mekhamer, W., Aldayel, O., Hefne, J. A. A., & Alam, M. (2019). Adsorptive Applications of Montmorillonite Clay for the Removal of Ag(I) and Cu(II) from Aqueous Medium. *Journal of Chemistry, 2019*, 7129014. doi:10.1155/2019/7129014

Alaqad, K., & Saleh, T. A. (2016). Gold and Silver Nanoparticles: Synthesis Methods, Characterization Routes and Applications towards Drugs. *Journal of Environmental & Analytical Toxicology, 6*(4). doi:10.4172/2161-0525.1000384

Alaya-Ibrahim, S., Kovo, A. S., Abdulkareem, A. S., Adeniyi, O. D., & Yahya, M. D. (2019). Development of nano-silver doped zeolite Asynthesized from Nigerian Ahoko kaolin for treatment of wastewater of a typical textile company. *Chemical Engineering Communications, 9*, 1-25. doi:10.1080/00986445.2019.1641490

Albukhaty, S., Al-Bayati, L., Al-Karagoly, H., & Al-Musawi, S. (2020). Preparation and characterization of titanium dioxide nanoparticles and in vitro investigation of their cytotoxicity and antibacterial activity against Staphylococcus aureus and Escherichia coli. *Animal Biotechnology*, 1-7.

Ali, A. F., Abdullahi, A. S., & Zangina, A. S. (2018). Environmental Issues and the Prospects of Mining in Nigeria. *Dutse Journal of Pure and Applied Sciences, 4*(2), 531-539.

Aljlil, S. A., & Alsewailem, F. D. (2014). Adsorption of Cu & Ni on Bentonite Clay from Waste Water. *Athens Journal of Sciences, 1*(1), 21-30. doi:10.30958/ajs.1-1-2

Álvarez, S., Riera, F., Álvarez, R., & Coca, J. (2001). Prediction of flux and aroma compounds rejection in a reverse osmosis concentration of apple juice model solutions. *Industrial & engineering chemistry research, 40*(22), 4925-4934.

Amin, M., Alazba, P., & Shafiq, M. (2015a). Adsorptive Removal of Reactive Black 5 from Wastewater Using Bentonite Clay: Isotherms, Kinetics and Thermodynamics. *Sustainability, 7*, 15302-15318. doi:10.3390/su71115302

Amin, M. T., Alazba, A. A., & Shafiq, M. (2015b). Adsorptive Removal of Reactive Black 5 from Wastewater Using Bentonite Clay: Isotherms, Kinetics and Thermodynamics. *Sustainability, 7*, 15302-15318. doi:10.3390/su71115302

Ampitan, T. A. (2013). Ethnobotanical survey of medicinal plants in Biu local government area of Borno state, Nigeria. *Comprehensive Journal of Herbs and Medicinal Plants, 2*(1), 7-11.

Anawar, H. M. (2015). Sustainable rehabilitation of mining waste and acid mine drainage using geochemistry, mine type, mineralogy, texture, ore extraction and climate knowledge. *Journal of Environmental Management, 158*, 111-121. doi:10.1016/j.jenvman.2015.04.045

Andreola, F., Martín, M. I., Ferrari, A. M., Lancellotti, I., Bondioli, F., Rincón, J. M., . . . Barbieri, L. (2013). Technological properties of glass-ceramic tiles obtained using rice husk ash as silica precursor. *Ceramics International, 39*(5), 5427–5435.

Ani, I. J., Akpan, U. G., Olutoye, M. A., & Hameed, B. H. (2018). Photocatalytic degradation of pollutants in petroleum refinery wastewater by TiO_2 and ZnO-based photocatalysts: Recent development. *Journal of Cleaner Production*. doi:10.1016/j.jclepro.2018.08.189

Anirudh, K. V. S., Bottu, M. M. V., & D., S. (2018). Production of TiO2 nanoparticles by green and chemical synthesis-A short review. *International Journal of Scientific & Engineering Research, 9*(11), 1634-1649.

Anju, K., Anitha, J. L., & Nagendra, G. N. (2018). Optimisation of green synthesized silver nanoparticles from *Caralluma umbellata*. *International Journal of Applied Pharmaceutics, 10*, 103-110.

Annan, E., Agyei-Tuffour, B., Bensah, Y. D., Konadu, D. S., Yaya, A., Onwona-Agyeman, B., & Nyankson, E. (2018). Application of clay ceramics and nanotechnology in water treatment: A review. *Cogent Engineering, 5*(1), 1476017. doi:10.1080/23311916.2018.1476017

Annan, E., Kan-Dapaah, K., Azeko, S. T., Mustapha, K., Asare, J., Zebaze, K. M. G., & Soboyejo, W. (2016). Clay Mixtures and the Mechanical Properties of Microporous and Nanoporous Ceramic Water Filters. *Journal of Materials in Civil Engineering, 04016105*, 1-11. doi:10.1061/(ASCE)MT.1943-5533.0001596

Anwar, M. S., Kumar, S., F., A., Arshi, N., Lee, C. G., & H, K. B. (2012). One step synthesis of rutile TiO2 nanoparticles at low temperature. *Journal of Nanoscience and Nanotechnology, 12*, 1555-1558.

APHA. (2017). *Standard Methods for the Examination of Water and Wastewater* (23rd ed). Retrieved from Washington DC:

Aritonang, H. F., Koleangan, H., & Wuntu, A. D. (2019). Synthesis of silver nanoparticles using aqueous extract of medicinal plants' (*Impatiens balsamina and lantana camara*) fresh leaves and analysis of antimicrobial activity. *International Journal of Microbiology*, 1-8. doi:10.1155/2019/8642303

Arya, G., Kumari, R. M., Gupta, N., Kumar, A., Chandra, R., & Nimesh, S. (2018). Green synthesis of silver nanoparticles using Prosopis juliflora bark extract: reaction optimization, antimicrobial and catalytic activities. *Artificial Cells, Nanomedicine, and Biotechnology, 46*(4), 985-993. doi:10.1080/21691401.2017.1354302

Asamoah, R. B., Yaya, A., Nbelayim, P., Annan, E., & Onwona-Agyeman, B. (2020). Development and Characterization of Clay-Nanocomposites for Water Purification. *Materials (Basel, Switzerland), 13*(17), 3793. doi:10.3390/ma13173793

ASTM. (2010). ASTM Standard. In *Standard Test Methods for Apparent Porosity, Water Absorption, Apparent Specific Gravity, and Bulk Density of Burned Refractory Brick and Shapes by Boiling Water 1* (pp. 1-3). West Conshohocken, PA 19428-2959. United States: ASTM International.

Awaleh, M. O., & Soubaneh, Y. D. (2014). Waste Water Treatment in Chemical Industries: The Concept and Current Technologies. . *Hydrol Current Res, 5*(1). doi:10.4172/2157-7587.1000164

Awasthi, A., Jadhao, P., & Kumari, K. (2019). Clay nano-adsorbent: structures, applications and mechanism for water treatment. *SN Applied Sciences, 1*(1076), 1-21. doi:10.1007/s42452-019-0858-9

Ayawei, N., Ebelegi, A. N., & Wankasi, D. (2017). Modelling and Interpretation of Adsorption Isotherms. *Journal of Chemistry, 2017*, 3039817. doi:10.1155/2017/3039817

Azeez, L., Lateef, A., & Adebisi, S. A. (2017). Silver nanoparticles (AgNPs) biosynthesized using pod extract of Cola nitida enhances antioxidant activity and phytochemical composition of Amaranthus caudatus Linn. *Applied Nanoscience, 7*(1), 59-66. doi:10.1007/s13204-017-0546-2

Aziz, W. J., & Jassim, H. A. (2018). A novel study of pH influence on Ag nanoparticles size with antibacterial and antifungal activity using green synthesis. *World Scient i f ic News, 97*, 139-152.

Bagheri, S., Shameli, K., & Hamid, S. B. A. (2013). Synthesis and characterisation of anatase titanium dioxide nanoparticles using egg white solution via sol-gel method. *Journal of Chemistry*, 1-5. doi:http://dx.doi.org/10.1155/2013/848205

Bagheri, S. B., Ramimoghadam, D., Yousefi, A. T., & Hamid, S. A. (2015). Synthesis, Characterization and Electrocatalytic Activity of Silver Doped-Titanium Dioxide Nanoparticles. *International Journal of Electrochemical Science, 10*, 3088 - 3097.

Bahjat, H. H., Ismail, R. A., Sulaiman, G. M., & Jabir, M. S. (2021). Magnetic field-assisted laser ablation of titanium dioxide nanoparticles in water for anti-bacterial applications. *Journal of Inorganic and Organometallic Polymers and Materials, 31*(9), 3649-3656.

Balali-Mood, M., Naseri, K., Tahergorabi, Z., Khazdair, M. R., & Sadeghi, M. (2021). Toxic Mechanisms of Five Heavy Metals: Mercury, Lead, Chromium, Cadmium, and Arsenic. *12*(227). doi:10.3389/fphar.2021.643972

Baluch, M. A., & Hashmi, H. N. (2019). Investigating the Impact of Anthropogenic and Natural Sources of Pollution on Quality of Water in Upper Indus Basin (UIB) by Using Multivariate Statistical Analysis. *Hindawi Journal of Chemistry, 2019*, 1-13. doi:10.1155/2019/4307251

Banerjee, P., Sau, S., Das, P., & Mukhopadhyah, A. (2014). Green Synthesis of Silver nanocomposite for Treatment of Textile dye. . *Nanoscience and Technology, 1*(2), 1-6.

Bankole, M. T., Abdulkareem, A. S., Mohammed, I. A., Ochigbo, S. S., Tijani, J. O., Abubakre, O. K., & Roos, W. D. (2019). Selected heavymetals removal from electroplating wastewater by purifiedand polyhydroxylbutyrate functionalized carbon nanotubesadsorbents. . *Scientific Report, 9*, 1-19. doi:10.1038/s41598-018-37899-4.

Bao, Y., He, J., Song, K., Guo, J., Zhou, X., & Liu, S. (2021). Plant-Extract-Mediated Synthesis of Metal Nanoparticles. *Journal of Chemistry, 2021*, 6562687. doi:10.1155/2021/6562687

Baosaree, J., Rakharn, N., Kammee, D., Pengpajon, P., Sriaphai, S., Sittijanda, S., . . . Mopoung, S. (2018). The Effect of Rice Husk Charcoal and Sintering Temperature on Porosity of Sintered Mixture of Clay and Zeolite. *Indian Journal of Science and Technology, 11*(8). doi:10.17485/ijst/2018/v11i8/104310

Barbato, M., & Bruno, C. (1996). Heterogeneous Catalysis: Theory, Models and Applications. In (pp. 139-160).

Barkhade, T., Indoliya, A., Poddar, R., Mahapatra, S. K., & Banerjee, I. (2021). Iron content titanium dioxide nanoparticles as exogenous contrast agent for tissue imaging using swept-source optical coherence tomography. *AIP Advances, 11*(1), 015023.

Baset, S., Akbari, H., Zeynali, H., & Shafie, M. (2011). Size measurement of metal and semiconductor nanoparticles via uv-vis absorption spectra. *Digest Journal of Nanomaterials and Biostructure, 6*(2), 709-716.

Bashir, A., Malik, L. A., Ahad, S., Manzoor, T., Bhat, M. A., Dar, G. N., & Pandith, A. H. (2019). Removal of heavy metal ions from aqueous system by ion-exchange and biosorption methods. *Environmental Chemistry Letters, 17*(2), 729-754. doi:10.1007/s10311-018-00828-y

Batool, F., Akbar, J., Iqbal, S., Noreen, S., & Bukhari, S. N. A. (2018). Study of Isothermal, kinetic, and thermodynamic parameters for adsorption of cadmium: An Overview of linear and non-linear approach and error analysis. *Bioinorganic Chemistry and Applications, 2018*, 3463724-3463724. doi:10.1155/2018/3463724

Bayan, E. M., Lupeiko, T. G., Pustovaya, L. E., Volkova, M. G., Butova, V. V., & Guda, A. A. (2020). Zn–F co-doped TiO_2 nanomaterials: Synthesis, structure and photocatalytic activity. *Journal of Alloys and Compounds, 822*, 153662.

Bel'chinskaya, L. I., Khodosova, N. A., Novikova, L. A., Strel'nikova, O. Y., Roessner, F., Petukhova, G. A., & Zhabin, A. V. (2016). Regulation of sorption processes in natural nanoporous aluminosilicates and determination of the ratio between active sites. *Protection of Metals and Physical Chemistry of Surfaces, 52*(4), 599-606. doi:10.1134/S2070205116040055

Belaiche, Y., Khelef, A., Laouini, S. E., Bouafia, A., Tedjani, M. L., & Barhoum, A. (2021). Green synthesis and characterization of silver/silver oxide nanoparticles using aqueous leaves extract of Artemisia Herba – Alba as reducing and capping agents *Romanian Journal of Materials, 51*(3), 342 - 352.

Belver, C., Ponce, S., Carpio, E., Salazar, G., García, P., Bedia, J., . . . Rodríguez, J. M. (2020). TiO_2:Cex onto Al clays for photocatalytic solar water dis-infection. *International Journal of Photoenergy, 2020*, 8881259. doi:10.1155/2020/8881259

Ben, C. K., & Baghour, M. (2013). The role of algae in phytoremediation of heavy metals:a review. *Journal of Material Environmental Science., 4*(6), 873-880.

Bharti, B., Kumar, S., Lee, H., & Kumar, R. (2016). Formation of oxygen vacancies and Ti^{3+} state in TiO_2 thin film and enhanced optical properties by air plasma treatment. *Scientific Report, 6*, 1-12. doi:DOI: 10.1038/srep32355

Bijang, C. M., Nurdin, M., Azis, T., Sekewael, S. J., & Wattimena, H. (2020). Ouw Natural Clay-Titanium Oksida ($LaO\text{-}TiO_2$) Composite Adsorption Ability On Lead (Pb) Metal. *Journal of Physics: Conference Series, 1463*(012011). doi:1088/1742-6596/1463/1/012011

Bisht, N. S., Tripathi, A. H., Kumar, S., Mehta, S. P. S., & Dandapat, A. (2021). Silver oxide-bismuth oxybromide nanocomposites as an excellent weapon to combat with opportunistic human pathogens. *Journal of photochemistry and photobiology, 6*(100031), 10. doi:https://doi.org/10.1016/j.jpap.2021.100031

Bodrud-Dozaa, M. D., Towfiqul Islamb, A. R. M., Ahmeda, F., Dasd, S., Sahae, N., & Safiur, R. M. (2016). Characterization of groundwater quality using water evaluation indices, multivariate statistics and geostatistics in central Bangladesh. . *Water Science and Technology, 30*, 19-40.

Bories, C., Borredon, M. E., Vedrenne, E., & Vilarem, G. (2014). Development of eco-friendly porous fired clay bricks using pore-forming agents: A review. *Journal of Environmental Management, 143*, 186-196.

Borodina, V. G., & Mirgorod, Y. A. (2014). Kinetics and mechanism of the interaction between HAuCl4 and rutin. *Kinetics and Catalysis, 55*, 683-687.

Budsaereechai, S., Kamwialisak, K., & Ngernyen, Y. (2012). Adsorption of lead, cadmium and copper on natural and acid activated bentonite clay. *KKU Research Journal, 17*(5), 800-810.

Bukalo, N. N., Ekosse, G. E., Odiyo, J. O., & Ogola, J. S. (2017). Fourier transform infrared spectroscopy of clay size fraction of cretaceous-tertiary kaolins in the Douala Sub-Basin, Cameroon. *Open Geoscience, 9*, 407–418. doi:10.1515/geo-2017-0031

Bulta, A. L., & Micheal, G. A. W. (2019). Evaluation of the efficiency of ceramic filters for water treatment in Kambata Tabaro zone, southern Ethiopia. *Enviromental Systems Research, 8*(1), 1-15. doi:10.1186/s40068-018-0129-6

Bunce, J. T., Ndam, E., Ofiteru, I. D., Moore, A., & Graham, D. W. (2018). A review of phosphorus removal technologies and their applicability to small-scale domestic wastewater treatment systems. *Frontiers in Environmental Science, 6*. doi:10.3389/fenvs.2018.00008

Bwapa, J. K., Jaiyeola, A. T., & Chetty, R. (2017). Bioremediation of acid mine drainage using algae strains: A review. *South African Journal of Chemical Engineering, 24*, 62-70.

Cai, Y., Ben, T., Zaidi, A. A., Shi, Y., Zhang, K., Lin, A., & Liu, C. (2019). Effect of pH on pollutants removal of ship sewage treatment in an innovative aerobic-anaerobic micro-sludge MBR system. *Water, Air, & Soil Pollution, 230*(7), 163. doi:10.1007/s11270-019-4211-0

Cao, J., Cao, H., Zhu, Y., Wang, S., Qian, D., Chen, G., . . . Huang, W. (2017). Rapid and effective removal of Cu^{2+} from aqueous solution using novel chitosan and laponite-based nanocomposite as adsorbent. *Polymers, 9*(1), 5. doi:10.3390/polym9010005

Chapman, J. M., Proulx, C. L., Veilleux, M. A. N., Levert, C., Bliss, S., Andre, M. E., . . . Cooke, S. J. (2014). Clear as mud: a meta-analysis on the effects of sedimentation on freshwater fish and the effectiveness of sediment-control measures. *Water research, 56*, 190-202.

Chaudhry, S. A., Khan, T. A., & Ali, I. (2016). Adsorptive removal of Pb(II) and Zn(II) from water onto manganese oxide-coated sand: Isotherm, thermodynamic and kinetic studies. *Egyptian journal of b a s i c and a p p l i e d s c i e n c e s 3 (2 0 1 6) 287–300, 3*(2016), 287–300. doi:10.1016/j.ejbas.2016.06.002

Chen, D., Zhu, H., & Wang, X. (2014). A facile method to synthesize the photocatalytic TiO_2/montmorillonite nanocomposites with enhanced photoactivity. *Applied Surface Science, 319*, 158-166. doi:https://doi.org/10.1016/j.apsusc.2014.05.085

Chen, R., Xu, Y., Xu, C., Shu, Y., Ma, S., Lu, C., & Mo, X. (2019). Associations between mercury exposure and the risk of nonalcoholic fatty liver disease (NAFLD) in US adolescents *Environmental Science and Pollution Research, 26*(30), 31384–31391. doi:10.1007/s11356-019-06224-5

Chen, Y., Dang, B., & Jin, C. (2018). Processing Lignocellulose-Based Composites into an Ultrastrong Structural Material. *ACS Nano, 13*. doi:10.1021/acsnano.8b06409

Chetty, S., & Pillay, L. (2019). Assessing the influence of human activities on river health: a case for two South African rivers with differing pollutant sources. *Environmental Monitoring and Assessment, 191*(3). doi:10.1007/s10661-019-7308-4

Chinnasamy, C., Tamilselvam, P., Karthik, V., & Karthick, B. (2017). Optimization and characterization studies on green synthesis of silver nanoparticles using response surface methodology. *Advances in Natural and Applied Sciences, 11*(4), 214-221.

Chinthalapudi, N., Kommaraju, V., Kannan, M., Nalluri, C., & Varanasi, S. (2021). Composites of cellulose nanofibers and silver nanoparticles for malachite green dye removal from water. *Carbohydrate Polymer Technologies and Applications, 2*, 100098. doi:https://doi.org/10.1016/j.carpta.2021.100098

Choudhary, N., Yadav, V. K., Yadav, K. K., Almohana, A. I., Almojil, S. F., Gnanamoorthy, G., . . . Jeon, B. H. (2021). Application of green synthesized MMT/Ag nanocomposite for removal of methylene blue from aqueous solution. *Water, 13*(3206). doi:10.3390/w13223206

Chowdhury, S., Yusof, F., Faruck, M. O., & Sulaiman, N. (2016). Process optimization of silver nanoparticle synthesis using response surface methodology. *Procedia Engineering, 148*(2016), 992-999. doi:10.1016/j.proeng.2016.06.552.

Christopher, J. D., Saswati, B., & Ezilrani, P. S. (2015). Optimization of parameters for biosynthesis of silver nanoparticles using leaf extract of *Aegle marmelos*. *Brazilian Archives of Biology and Technology, 58*(5), 702-710. doi:10.1590/S1516-89132015050106

Cobbina, S. J., Duwiejuah, A. B., Quansah, R., Obiri, S., & Bakobie, N. (2015). Comparative assessment of heavy metals in drinking water sources in two small-scale mining communities in Northern Ghana. *International Journal of environmental Research and Public Health, 12*, 10620-10634. doi:10.3390/ijerph120910620

Dada, A. O., Adekola, F. A., Adeyemi, O. S., Bello, O. M., Oluwaseun, A. C., Awakan, J. O., & Grace, F. A. (2018). Exploring the effect of operational factors and characterization imperative to the synthesis of silver nanoparticles. In K. Maaz (Ed.), *Silver nanoparticles - Fabrication, Characterization and Applications* (pp. 165-184). London: IntechOpen.

Darroudi, M., Ahmad, M. B., Abdullah, A. H., Ibrahim, N. A., & Shameli, K. (2010). Effect of accelerator in green synthesis of silver nanoparticles. *International Journal of Molecular Sciences, 11*(10), 3898–3905.

Das, R., Sarkar, S., Chakraborty, S., Choi, H., & Bhattacharjee, C. (2014). Remediationof antiseptic components in wastewater by photocatalysis using TiO_2 nano-particles. *Industrial Engineering Chemical Resources., 53*(3), 3012–3020.

Dawodu, F. A., & Akpomie, K. G. (2014). Simultaneous adsorption of Ni(II) and Mn(II) ions from aqueous solution unto a Nigerian kaolinite clay. *Journal of Material Research and Technology, 3*(2), 129–141. doi:10.1016/j.jmrt.2014.03.002

De Silva, G. O., Abeysundara, A. T., & Apons, M. M. W. (2017). Extraction methods, qualitative and quantitative techniques for screening of phytochemicals from plants. *American Journal of Essential Oils and Natural Products, 5*(2), 29-32.

Dedehou, V. F., Olounladé, P. A., Adenilé, D. A., Alowanou, G., Azando, E. V., & Hounzangbé-Adoté, M. S. (2016). A review on medicinal plants of Parkia Biglobosa (Mimosaceae -Fabaceae) and Pterocarpus Erinaceus (Leguminosae – Papilionoidea). *Journal of Medicinal Plants, 4*(6), 132-137.

Demirci, S., Dikici, T., Yurddaskal, M., Gultekin, S., Toparli, M., & Celik, E. (2016). Synthesis and characterization of Ag doped TiO_2 heterojunction films and their photocatalytic performances. *Applied Surface Science, 390*, 591-601. doi:https://doi.org/10.1016/j.apsusc.2016.08.145

Desimoni, E., & Brunetti, B., 3 : 70. . (2015). X-ray photoelectron spectroscopic characterization of chemically modified electrodes used as chemical sensors and biosensors. *Chemosensors, 3*, 70-82.

Dewi, R., Agusnar, H., & Alfian, Z. (2018). Characterization of technical kaolin using XRF, SEM, XRD, FTIR and its potentials as industrial raw materials. Paper presented at the Journal of Physics: Conference Series.

Dhand, V., Soumya, L., Bharadwaj, S., Chakra, S., Bhatt, D., Sreedhar, B. J. M. S., & C, E. (2016). Green synthesis of silver nanoparticles using Coffea arabica seed extract and its antibacterial activity. *58*, 36-43.

Diko, M., Ekosse, G., & Ogola, J. (2016). Fourier transform infrared spectroscopy and thermal analyses of kaolinitic clays from South Africa and Cameroon *Acta Geodyn. Geomater., 13*(182), 149–158. doi:10.13168/AGG.2015.0052

Djebaili, K., Kekhalif, Z., Boumaza, A., & Djelloul, A. (2015). XPS, FTIR, EDX and XRD analysis of Al_2O_3 scales grown on PM2000 alloy. *Journal of Spectroscopy, 2015*, 1-16. doi:10.1155/2015/868109

Dobrucka, R. (2017). Synthesis of titanium dioxide nanoparticles using *Echinacea purpurea herba*. *Iranian Journal of Pharmaceutical Research, 16*(2), 756-762.

Dodoo-Arhin, D., Buabeng, F. P., Mwabora, J. M., Amaniampong, P. N., Agbe, H., Nyankson, E., . . . Asiedu, N. Y. (2018). The effect of titanium dioxide synthesis technique and its photocatalytic degradation of organic dye pollutants. *Heliyon, 4*, 1-23. doi:10.1016/j.heliyon.2018.e00681

Dontala, S. P., Reddy, T. B., & Vadde, R. (2015). Environmental aspects and impacts its mitigation measures of corporate coal mining. *Procedia Earth and Planetary Science, 11*, 2-7. doi:10.1016/j.proeps.2015.06.002

Dontsova, T. A., Kutuzova, A. S., Bila, K. O., Kyrii, S. O., Kosogina, I. V., & Nechyporuk, D. O. (2020). Enhanced photocatalytic activity of TiO_2/SnO_2 binary nanocomposites. *Journal of Nanomaterials, 2020*.

Dubey, R. S., Krishnamurthy, K. V., & Singh, S. (2019). Experimental studies of TiO_2 nanoparticles synthesized by sol-gel and solvothermal routes for DSSCs application. *Results in Physics, 14*, 102390. doi:https://doi.org/10.1016/j.rinp.2019.102390

Durgalakshmi, D., Rajendran, S., & Naushad, M. (2019). Current Role of Nanomaterials in Environmental Remediation. In M. Naushad (Ed.), *Advanced Nanostructured Materials for Environmental Remediation, Environmental Chemistry for a Sustainable World* (Vol. 25, pp. 2-17). Switzerland: Springer Nature.

Edmunson, S. J., & Wilkie, A. C. (2013). Landfill leachate – a water and nutrient resource for algae-based biofuels. *Environmental Technology., 34*(13-14), 1849-1857.

Efeovbokhan, V. E., Olurotimi, O. O., Yusuf, E. O., Abatan, O. G., & Alagbe, E. E. (2019). Production of Clay Filters for Waste Water Treatment. *Journal of Physics: Conference Series, 1378*, 2-11. doi:10.1088/1742-6596/1378/3/032028

Efimov, V. A., Chalov, S. R., Efimova, E., Ivanov, V. A., Jarsjö, J., Fisherrsjö, S., & Fisher, S. (2019). Impact of mining activities on the surface water quality (case study of Khibiny mountains, Russia). *Earth and Environmental Science, 263*(012008). doi:doi:10.1088/1755-1315/263/1/012008

Egbosiuba, T. C., Abdulkareem, A. S., Kovo, A. S., Afolabi, E. A., Tijani, J. O., Auta, M., & Roos, W. D. (2019). Ultrasonic enhanced adsorption of methylene blue onto the optimized surface area of activated carbon: Adsorption isotherm, kinetics and thermodynamics. *Chemical Engineering Research and Design, 153*, 315-336. doi:10.106/j.cherd.2019.10.016

Eksangsri, T., Sapcharoenkun, C., & Phromma, S. (2021). Synthesis of silver doped titanium dioxide by wet-ball milling sol–gel method for antibacterial application. *MATEC Web of Conferences, 333*, 11002. doi:10.1051/matecconf/202133311002

El-Gaidoumi, A., Benabdallah, A. C., El-Bali, B., & Kherbeche, A. (2018). Synthesis and characterisation of zeolite hs using natural pyrophyllite as new clay source. *Arabian Journal of Science and Engineering, 43*, 191-197. doi:doi.org/10.1007/s13369-017-2768-8

El-Ghmari, B., Farah, H., & Ech-Chahad, A. (2021). A new approach for the green biosynthesis of silver oxide nanoparticles Ag_2O, characterization and catalytic application. *2021, 16*(3), 651-660. doi:10.9767/bcrec.16.3.11577.651-660

El-Rafie, M. H., Ahmed, H. B., & Zahran, M. K. (2014). Facile precursor for synthesis of silver nanoparticles using alkali treated maize starch. *International Scholarly Research Notices, 2014*, 702396. doi:10.1155/2014/702396

El-Sherbiny, S., Morsy, F. A., Hassan, M. S., & Mohamed, H. F. (2015). Enhancing Egyptian kaolinite via calcination and dealumination for application in paper coating. *Journal of Coatings Technology and Research, 12*(4), 739-749. doi:10.1007/s11998-015-9672-5

Eldebany, N., Abd El-Kodous, M., Tohamy, H., Abdelwahed, R., Elkammar, M., Abu-Ahmed, H., & Elkhenany, H. (2021). Gelatin loaded titanium dioxide and silver oxide nanoparticles: implication for skin tissue regeneration. *Biological trace element research, 199*. doi:10.1007/s12011-020-02489-x

Esmaeili, A., Mobini, M., & Eslami, H. (2019). Removal of heavy metals from acid mine drainage by native natural clay minerals, batch and continuous studies. *Applied Water Science, 9*(97), 1-6. doi:10.1007/s13201-019-0977-x

Esmaeili, H., & Foroutan, R. (2015). Investigation into ion exchange and adsorption methods for removing heavy metals from aqueous solutions. *International Journal of Biology, Pharmacy and Allied Sciences, 4*(12), 620-629.

Falk, G. S., Borlaf, M., López-Muñoz, M. J., Fariñas, J. C., Rodrigues Neto, J. B., & Moreno, R. (2018). Microwave-assisted synthesis of TiO_2 nanoparticles: Photocatalytic activity of powders and thin films. *Journal of Nanoparticles Resources, 20*(23).

Falyouna, O., Maamoun, I., Bensaida, K., Tahara, A., Sugihara, Y., & Eljamal, O. (2021). Chemical deposition of iron nanoparticles (Fe^0) on titanium nanowires for efficient adsorption of ciprofloxacin from water. *Water Practice and Technology, 17*, 1-22. doi:10.2166/wpt.2021.091

Foo, K. Y., & Hameed, B. H. (2010). Insights into the modeling of adsorption isotherm systems. *Chemical Engineering Journal, 156*(2010), 2-10. doi:10.1016/j.cej.2009.09.013

Foroutan, R., Mohammadi, R., Adeleye, A. S., Farjadfard, S., Esvandi, Z., Arfaeinia, H., . . Sahebi, S. (2019). Efficient arsenic(V) removal from contaminated water using natural clay and clay composite adsorbents. *Environmental Science and Pollution Research, 19*(5), 1-15. doi:10.1007/s11356-019-06070-5

Freitas, E. D., Carmo, A. C. R., Almeida Neto, A. F., & Vieira, M. G. A. (2017). Binary adsorption of silver and copper on Verde-lodo bentonite: Kinetic and equilibrium study. *Applied Clay Science, 137*, 69-76. doi:10.1016/j.clay.2016.12.016

Gabrielyan, A. V., Shahnazaryan, G. A., & Minasyan, S. H. (2018). Distribution and identification of sources of heavy metals in the Voghji River Basin impacted by mining activities (Armenia). *Journal of Chemistry, 2018*, 7172426. doi:10.1155/2018/7172426

Ganesh, S., Khan, F., Ahmed, M. K., Velavendan, P., Pandey, N. K., & Kamachi Mudali, U. (2012). Spectrophotometric determination of trace amounts of phosphate in water and soil. *Water Sci Technol, 66*(12), 2653-2658. doi:10.2166/wst.2012.468

García-Gil, Á., García-Muñoz, R. A., McGuigan, K. G., & Marugán, J. (2021). Solar water disinfection to produce safe drinking water: A review of parameters, enhancements, and modelling approaches to make SODIS faster and safer. *Molecules, 26*(2021), 3431-3456. doi:10.3390/molecules26113431

Genty, T., Bussière, B., Benzaazoua, M., Neculita, C. M., & Zagury, G. J. (2017). Iron removal in highly contaminated acid mine drainage using passive biochemical reactors. *Water Science and Technology, 76*(7), 1833-1843. doi:10.2166/wst.2017.362

Georgaka, A., & Spanos, N. (2010). Study of the Cu (II) removal from aqueous solutions by adsorption on titania. *Global NEST Journal, 12*(3), 239-247.

Ghernaout, D., Alghamdi, A., & Ghernaout, B. (2019). Microorganisms killing: Chemical disinfection vs. electrodisinfection. *Applied Engineering, 3*(1), 13-19. doi:10.11648/j.ae.20190301.12

Ghotekar, S., Dabhane, H., Pansambal, S., Oza, R., Tambade, P., & Medhane, V. (2020). A review on biomimetic synthesis of Ag_2O nanoparticles using plant extract, characterization and its recent applications. *Advance Journal of Chemistry: Section B, 2*(3), 102-111. doi:10.33945/SAMI/AJCB.2020.3.2

Gontijo, L. A. P., Raphael, E., Ferrari, D. P. S., Ferrari, J. L., Lyon, J. L., & Schiavon, M. A. (2020). pH effect on the synthesis of different size silver nanoparticles evaluated by DLS and their size-dependent antimicrobial activity. *Matéria, 25*(4), 1-10. doi:10.1590/S1517-707620200004.1145.

Goutam, S. P., Saxena, G., Singh, V. K., Yadav, A. K., Bharagava, R. N., & Thapa, K. B. (2017). Green synthesis of TiO_2 nanoparticles using leaf extracts of *Jatropha curcas L*. for photocatalytic degradation of tannery wastewater. *Chemical Engineering Journal*. doi:10.1016/j.cej.2017.12.029

Grema, A. S., Idriss, I. M., Alkali, A. N., Ahmed, M. M., & Iyodo, H. M. (2021). Production of clay-based ceramic filter for water purification. *European Journal of Engineering and Technology Research, 6*(7), 140-143. doi:10.2'4018/ejers.2021.6.7.2623

Gu, S., Kang, X., Wang, L., Lichtfouse, E., & Wang, C. (2019). Clay mineral adsorbents for heavy metal removal from wastewater: a review. *Environmental Chemistry Letters, 17*(2), 629-654. doi:10.1007/s10311-018-0813-9

Guan, Z., Jin, P., Liu, Q., Wang, X., Chen, L., Xu, H., . . . Du, R. (2019). Carbon quantum dots/Ag sensitized TiO_2 nanotube film for applications in photocathodic protection. *Journal of Alloys and Compounds, 797*, 912-921. doi:https://doi.org/10.1016/j.jallcom.2019.05.199

Guillaume, P. L. A., Chelaru, A., Visa, M., & Lassiné, O. (2018). Titanium oxide-clay" as adsorbent and photocatalysts for wastewater treatment. *Journal of Membrane Science and Technology, 8*(1), 176-186. doi:10.4172/2155-9589.1000176

Gunanto, Y., Sinaga, K., & Pratala, Y. (2018). The effect of stirring techniques on TiO_2 nanoparticle size by usinga wet chemical method. *Jurnal Sains Materi Indonesia, 18*, 30. doi:10.17146/jsmi.2016.18.1.4184

Gunputh, U. F., Le, H., Besinis, A., Tredwin, C., & Handy, R. D. (2019). Multilayered composite coatings of titanium dioxide nanotubes decorated with zinc oxide and hydroxyapatite nanoparticles: Controlled release of Zn and antimicrobial properties against Staphylococcus aureus. *International Journal of Nanomedicine, 14*, 3583-3600. doi:10.2147/IJN.S199219

Gupta, A., Kushwah, K. K., Mahobia, S. K., Soni, P., & Murty, V. V. S. (2019). Synthesis and characterization of TiO_2 nanoparticles for solar cell applications. *International Journal of Innovative Technology and Exploring Engineering (IJITEE), 8*(9), 2462 - 2465. doi:10.35940/ijitee.I8739.078919

Gupta, A., Sharma, V., Sharma, K., Kumar, V., Choudhary, S., Mankotia, P., . . . Mishra, P. K. (2021). A review of adsorbents for heavy metal decontamination: growing approach to wastewater treatment. *Materials (Basel, Switzerland), 14*(16). doi:10.3390/ma14164702

Gurreri, L., Tamburini, A., Cipollina, A., & Micale, G. (2020). Electrodialysis applications in wastewater treatment for environmental protection and resources recovery: A Systematic Review on Progress and Perspectives. *Membranes (Basel), 10*(7). doi:10.3390/membranes10070146

Hadjltaief, H. B., Zina, M. B., Galvez, M. E., & Da Costa, P. (2016). Photocatalytic degradation of methyl green dye in aqueous solution over natural clay-supported ZnO–TiO2 catalysts. *Journal of photochemistry and photobiology, 315*, 25-33.

Haiyang, Y., Min, X., Xu, S., Bender, J., & Wang, Y. (2020). Development of effective and fast-flow ceramic porous media for point-of-use water treatment: effect of pore size distribution. *ACS Sustainable Chemistry & Engineering, 8*(2020), 2531−2539. doi:10.1021/acssuschemeng.9b07177

Hajjaji, W., Andrejkovičová, S., Pullar, R. C., Tobaldi, D. M., Lopez-Galindo, A., Jammousi, F., . . . Labrincha, J. A. (2018). Effective removal of anionic and cationic dyes by kaolinite and TiO_2/kaolinite composites. *Clay Minerals, 51*(1), 19-27. doi:10.1180/claymin.2016.051.1.02

Han, Y., Zhao, S., Wu, H., & Asuha, S. (2019). Functionalizing naturally occurring kaolinite by anatase nanoparticles and its effects on the adsorption of fluoride. *Desalination and Water Treatment, 160*(2019), 240–249. doi:10.5004/dwt.2019.24250

Hari, N., & Vandana, P. N. (2018). FTIR Spectroscopic Analysis of Leaf Extract in Hexane in Jasminum Azoricum L. *International Journal of Scientific Research in Science and Technology, 4*(8), 170-172.

Harifi, T., & Montazer, M. (2014). Photo-, bio-, and magneto-active colored polyester fabric with hydrophobic/hydrophilic and enhanced mechanical properties through synthesis of TiO_2/Fe_3O_4/Ag nanocomposite, . *Industrial Engineering and Chemical Resources, 53*, 1119–1129.

Hasani, N., Selimi, T., Mele, A., Thaçi, V., Halili, J., Berisha, A., & Sadiku, M. (2022). Theoretical, equilibrium, kinetics and thermodynamic investigations of methylene blue adsorption onto lignite coal. *Molecules, 27*(1856), 1-19. doi:10.3390/molecules27061856

Hashemian, S., & Shahedi, M. R. (2013). Novel Ag/kaolin nanocomposite as adsorbent for removal of acid cyanine 5R from aqueous solution. *Journal of Chemistry, 2013*, 285671. doi:10.1155/2013/285671

Hassan, S. B., Aigbodion, V. S., & Dikko, D. A. (2019). Economic sustainability and diversification through solid minerals development in Nigeria. Paper presented at the 18th Annual International Conference of Nigerian International Materials Congress, University of Ilorin, Kwara State.

Heydari, A., Khoshnood, H., Sheibania, H., & Doostan, F. (2016). Polymerization of β-cyclodextrin in the presence of bentonite clay to produce polymer nanocomposites for removal of heavy metals from drinking water. *Polymers Advanced Technologies*, 1-9. doi:10.1002/pat.3951

Hızal, J., & Yılmazoğlu, M. (2021). Montmorillonite Clay Composite for Heavy Metal Removal from Water. In Inamuddin, M. I. Ahamed, E. Lichtfouse, & A. M. Asiri (Eds.), *Green Adsorbents to Remove Metals, Dyes and Boron from Polluted Water* (pp. 93-112). Cham: Springer International Publishing.

Ho, Y. S. (2006). Review of second-order models for adsorption systems. *Journal of Hazardous Materials, 136*, 681–689. doi:10.1016/j.jhazm at.2005.12.043

Hussain, S. T., & Ali, S. A. K. (2021). Removal of heavy metal by ion exchange using bentonite clay. *Journal of Ecological Engineering, 22*(1), 104–111. doi:10.12911/22998993/128865

Ibeh, M. I., & Nwadinobi, P. C. (2021). Design and development of ceramic candle filter from Ohiya clay. *Scientific Research Journal, 9*(10), 96-100. doi:10.31364/SCIRJ/v9.i10.2021.P1021894

Ihekweme, G. O., Shondo, J. N., Orisekeh, K. I., Kalu-Uka, G. M., Nwuzor, I. C., & Onwualu, A. P. (2020). Characterization of certain Nigerian clay minerals for water purification and other industrial applications. *Heliyon, 6*(4), e03783. doi:https://doi.org/10.1016/j.heliyon.2020.e03783

Ijaz, I., Gilani, E., Nazir, A., & Bukhari, A. (2020). Detail review on chemical, physical and green synthesis, classification, characterizations and applications of nanoparticles. *Green Chemistry Letters and Reviews, 13*(3), 223-245. doi:10.1080/17518253.2020.1802517

Inyinbor, A. A., Adekola, F. A., & Olatunji, G. A. (2016). Kinetics,isotherms and thermodynamic modeling of liquid phase adsorption of Rhodamine B dye onto *Raphia hookeriem* fruit epicarp. *Water Resources and Industry, 15*, 14-27. doi:10.1016/j.wri.2016.06.001

Islam, S., Nagpure, S., Kim, D., & Rankin, S. (2017). Synthesis and catalytic applications of non-metal doped mesoporous titania. *Inorganics, 5*(1), 15.

Ismail, I., Balachandran, S., & Devi, M. G. (2018). Synthesis, characterization and application of nanoparticles in wastewater treatment. *Indian Chemical Engineer, 18*(1), 1-11. doi:10.1080/00194506.2018.1469099

Jain, S., & Mehata, M. S. (2017). Medicinal plant leaf extract and pure flavonoid mediated green synthesis of silver nanoparticles and their enhanced antibacterial property. *Scientific Reports, 7*(1), 15867. doi:10.1038/s41598-017-15724-8

Jalees, M., Lawrence, R. S., Chhattree, A., Yadav, M., & Sailus, N. (2018). Green synthesis of silver oxide nanoparticles prepared from waste part of mango peels *International Journal of Pure and Applied Bioscience, 6*(3), 502-508. doi:10.18782/2320-7051.6740

Jayapriya, E., & Lalitha, P. (2013). Synthesis of silver nanoparticles using leaf aqueous extract of Ocimum basilicum (L.). *International Journal of ChemTech Research, 5*, 2985-2992.

Jerlin, B. S., & Beula, J. M. (2017). Biosynthesis of silver nanoparticles from the mangrove avicennia marina and its applications. *International Journal of Development Research,, 7*(11), 16895-16905.

Jiao, T., Guo, H., Zhang, Q., Peng, Q., Tang, Y., Yan, X., & Li, B. (2015). Reduced graphene oxide-based silver nanoparticle-containing composite hydrogel as highly efficient dye catalysts for wastewater treatment. *Scientific Reports, 5*(1), 11873. doi:10.1038/srep11873

Jlassi, K., Singh, A., & Aswal, D. K. (2013). Novel, ternary clay/polypyrrole/silver hybrid materials through in situ photopolymerization. *Colloids and Surfaces A: Physicochemical and Engineering Aspects . 439*, 193-199.

Ju, Q. L., Zhong, L. X., Zan, D., Lu, Z., Hao, Y., & Rong, C. (2018). Enhanced antibacterial activity and mechanism studies of Ag/Bi_2O_3 nanocomposites. *Advance Powder Technology, 29*(9), 2082–2090.

Kajjumba, G., Serkan, E., Atakan, Ö., Kurtulus, Ö., & Serdar, A. (2018). Modelling of adsorption kinetic processes—errors, theory and application. In E. Serpil (Ed.), *Advanced Sorption Process Applications* (pp. Ch. 10). Rijeka: IntechOpen.

Kalaki, Z. A., SafaeiJavan, R., & Faraji, H. (2018). Procedure optimisation for green synthesis of silver nanoparticles by Taguchi method. *Micro and Nano Letters*, 1-4. doi:10.1049/mnl.2017.0308

Kalyanasundharam, S., & Prakash, M. J. (2015). Biosynthesis and characterization of titanium dioxide nanoparticles using pithecellobium dulce and lagenaria siceraria aqueous leaf extract and screening their free radical scavenging and antibacterial properties. *International Letters of Chemistry, Physics and Astronomy, 50*, 80-95. doi:10.18052/www.scipress.com/ILCPA.50.80

Kamal, N. A., & Gooyong, L. (2019). Removal of selected heavy metals in acid mine drainage using chemical precipitation method. *Journal of Advanced Research in Fluid Mechanics and Thermal Sciences, 57*(1), 121-130.

Kanna, M., Wongnawa, W., Sherdshoopongse, P., & Boonsin, P. (2005). Adsorption behavior of some metal ions on hydrated amorphous titanium dioxide surface. *Songklanakarin Journal of Science and Technology, 27*(5), 1017-1026.

Kar, B., Sahoo, H., Rath, S. S., Rao, D. S., & Das, B. (2013). Characterization and beneficiation studies for the removal of iron from a china clay from India. *Clay Minerals, 48,* 759-769. doi:10.1180/claymin.2013.048.5.08

Karimi, L., & Salem, A. (2011). The role of bentonite particle size distribution on kinetic of cation exchange capacity. *Journal of Industrial and Engineering Chemistry, 17*(1), 90-95. doi:https://doi.org/10.1016/j.jiec.2010.12.002

Karunakaran, G., Jagathambal, M., Gusev, A., Minh, N. V., Kolesnikov, E., Mandal, A. R., & Kuznetsov, D. (2016). Nitrobacter sp. extract mediated biosynthesis of Ag_2O NPs with excellent antioxidant and antibacterial potential for biomedical application. *IET Nanobiotechnology, 10*(6), 425–430. doi:10.1049/iet-nbt.2015.0097

Kavitha, K. S., Baker, S., Rakshith, D., Kavitha, H. U., Yashwantha-Rao, H. C., Harini, B. P., & Satish, S. (2013). Plants as green source towards synthesis of nanoparticles. *International Resource Journal of Biological Science, 2*(6), 66-76.

Kazak, O., Eker, Y. R., Bingol, H., & Tor, A. (2018). Preparation of chemically-activated high surface area carbon from waste vinasse and its efficiency as adsorbent material. *Journal of Molecular Liquids, 272,* 189-197. doi:10.1016/j.molliq.2018.09.085.

Kefeni, K. K., Msagati, T. A. M., & Mamba, B. B. (2017). Acid mine drainage: Prevention, treatment options, and resource recovery: A review. *Journal of Cleaner Production, 151*(2017), 475-493.

Kenne-Diffo, B., Elimbi, A., Cyr, M., Dika-Manga, J., & Tchakoute, K. H. (2015). Effect of the rate of calcination of kaolin on the properties of metakaolin-based geopolymers. *Journal of Asian Ceramic Society, 3*(1), 130-138.

Khalil, A., Sergeevich, N., & Borisova, V. (2018). Removal of ammonium from fish farms by biochar obtained from rice straw: Isotherm and kinetic studies for ammonium adsorption. *Adsorption Science & Technology, 36*(5-6), 1294-1309. doi:10.1177/0263617418768944

Khan, M., Aa, H. R., & Venkatachalam, G. (2018). Removal of Cadmium from Aqueous Solution using Bentonite Clay. *International Journal of Applied Environmental Sciences, 13*(4), 353-364.

Khan, M. I., Almesfer, M. K., Danish, M., Ali, I. H., Shoukry, H., Patel, R., . . . Rehan, M. (2019). Potential of Saudi natural clay as an effective adsorbent in heavy metals removal from wastewater. *Desalination and Water Treatment, 158,* 140-151. doi:10.5004/dwt.2019.24270

Khandelwal, A., Narayanan, N., Varghese, E., & Gupta, S. (2020). Linear and nonlinear isotherm models and error analysis for the sorption of kresoxim-methyl in agricultural soils of india. *Bulletin of Environmental Contamination and Toxicology, 20,* 1-8. doi:10.1007/s00128-020-02803-2

Khatun, Z., Lawrence, R. S., Jalees, M., & Lawerence, K. (2015). Green synthesis and anti-bacterial activity of silver oxide nanoparticles prepared from *Pinuslongifolia* leaves extract. *International Journal of Advanced Research, 3*(11), 337 - 343.

Kjelland, M. E., Woodley, C. M., Swannack, T. M., & Smith, D. L. (2015). A review of the potential effects of suspended sediment on fishes: potential dredging-related physiological, behavioral,and transgenerational implications. *Environ System Decision, 35*, 334–350. doi:10.1007/s10669-015-9557-2

Kobayashi, M., Kato, H., & Kakihana, M. (2013). Synthesis of titanium dioxide nanocrystals with controlled crystal- and micro-structures from titanium complexes. *Nanomaterials and Nanotechnology*, *3*(23), 1-10.

Konduri, M. K. R., & Fatehi, P. (2017). Influence of pH and ionic strength on flocculation of clay suspensions with cationic xylan copolymer. *Colloids and Surfaces, 1*(530), 20-32.

Korolkova, S. V., Volovicheva, N. A., Vezentsev, A. I., Gorbunova, N. M., & Nurasyl, T. E. (2020). Sorption of Cu^{2+} ions and Fe^{3+} with alkaline forms of montmorillonite containing clay. *European Journal of Molecular & Clinical Medicine, 7*(2), 5586-5597.

Krishnan, B., & Mahalingam, S. (2017). Ag/TiO_2/bentonite nanocomposite for biological applications: Synthesis, characterization, antibacterial and cytotoxic investigations. *Advanced Powder Technology*, *28*, 2265–2280. doi:http://dx.doi.org/10.1016/j.apt.2017.06.007

Kulkarni, R. M., Malladi, R. S., Hanagadakar, M. S., Doddamani, M. Y. R., & Bhat, U. K. (2016). Ag-TiO_2 nanoparticles for photocatalytic degradation of lomefloxacin. *Desalination and Water Treatment, 57*(34), 16111-16118. doi:10.1080/19443994.2015.1076352

Kumar, K. P., Keizer, K., Burggraaf, A. J., Okubo, T., & Nagamoto, H. (1993). Synthesis and textural properties of unsupported and supported rutile (TiO,) membranes. *Journal of Material Chemistry, 3*(9), 923-929.

Kumari, N., & Mohan, C. (2021). Basics of clay minerals and their characteristic properties. In G. M. D. Nascimento (Ed.), Clay and clay minerals: *IntechOpen*.

Kumari, S., & Mishra, A. (2021). Heavy metal contamination. *Intechopen*, 1-15. http://dx.doi.org/10.5772/intechopen.93412

Kurniawati, P., Gusrianti, R., Dwisiwi, B. B., Purbaningtias, T. E., & Wiyantoko, B. (2017). Verification of spectrophotometric method for nitrate analysis in water samples. Paper presented at the AIP Conference Indonesia.

Kyomuhimbo, H. D., Michira, I. N., Mwaura, F. B., Derese, S., Feleni, U., & Iwuoha, E. I. (2019). Silver–zinc oxide nanocomposite antiseptic from the extract of Bidens pilosa. *SN Applied Sciences, 1*(681), 1-17. doi:10.1007/s42452-019-0722-y

Lakherwal, D. (2014). Adsorption of heavy metals: a review. *International journal of environmental research and development, 4*(1), 41-48.

Lam, B., Déon, S., Morin-Crini, N., Crini, G., & Fievet, P. (2018). Polymer enhanced ultrafiltration for heavy metal removal: influence of chitosan and carboxymethyl cellulose on filtration performances. *Journal Cleaner Production, 171*, 927-933. doi:10.1016/j.jclepro.2017.10.090

Landage, K. S., Arbade, G. K., Khanna, P., & Bhongale, C. J. (2020). Biological approach to synthesize TiO_2 nanoparticles using *Staphylococcus aureus* for antibacterial and anti-biofilm applications. *Journal of Microbiology and Experimentation, 8*(1), 36–43. doi:10.15406/jmen.2020.08.00283

Lateef, A., Oladejo, S. M., Akinola, P.O., Aina, D. A., Beukes, L. S., Folarin, B. I., & Gueguim-Kana, E. B. (2020). *Facile synthesis of silver nanoparticles using leaf extract of Hyptis suaveolens (L.) Poit for environmental and biomedical applications.* Paper presented at the IOP Conf. Series: Materials Science and Engineering.

Laysandra, L., Sari, M. W., Soetaredjo, F. E., Foe, K., Putro, J. N., Kurniawan, A., . . . Ismadji, S. (2017). Adsorption andphotocatalytic performance of bentonite-titanium dioxide composites formethyleneblue and rhodamine B decoloration. *Heliyon, 3*, 1-22. doi:10.1016/j.heliyon.2017.e00488

Leiva, E., Tapia, C., & Rodríguez, C. (2021). Removal of Mn(II) from acidic wastewaters using graphene oxide–ZnO nanocomposites. *Molecules, 26*(2713), 1-18. doi:10.3390/molecules26092713

Leyssens, L., Vinck, B., Van Der Straeten, C., Wuyts, F., & Maes, L. (2017). Cobalt toxicity in humans.A review of the potential sources and systemic health effects. *Toxicology 5*(15), 3-57. doi:10.1016/j.tox.2017.05.015

Li, L., Yan, J., Wang, T., Zhao, Z., Gong, J., & Guan, N. (2015). Sub-10 nm rutile titanium nanoparticles for efficient visible-light-driven photocatalytic hydrogen production. *Nature Communications, 6*. doi:10.1038/ncomms6881

Li, X., Wu, S., Kan, C., Zhang, Y., Liang, Y., Cui, G., . . . Yang, S. (2021). Application of ion exchange resin in the advanced treatment of condensate water. Paper presented at the E3S Web of Conferences, China.

Liley, J. R., Thomas, R. K., Penfold, J., Tucker, I. M., Petkov, J. T., Stevenson, P., & Webster, J. R. (2017). Surface adsorption in ternary surfactant mixtures above the critical micelle concentration: effects of asymmetry on the composition dependence of the excess free energy. *J Phys Chem B, 121*(13), 2825-2838. doi:10.1021/acs.jpcb.7b01337

Liu, H., Zhang, H., Wang, J., & Wei, J. (2020). Effect of temperature on the size of biosynthesized silver nanoparticle: Deep insight into microscopic kinetics analysis. *Arabian Journal of Chemistry, 13*(1), 1011-1019. doi:https://doi.org/10.1016/j.arabjc.2017.09.004

Liu, J., Li, X., Zuo, S., & Yu, Y. (2007). Preparation and photocatalytic activity of silver and TiO_2 nanoparticles/montmorillonite composites. *Applied Clay Science, 37*(3), 275-280. doi:https://doi.org/10.1016/j.clay.2007.01.008

Liu, Q., Liu, E., Li, J., Qiu, Y., & Chen, R. (2019). Rapid ultrasonic-microwave assisted synthesis of spindle-like Ag/ZnO nanostructures and their enhanced visible-light photocatalytic and antibacterial activities. *Catalysts Today., 2019*. doi:10.1016/j.cattod.2019.01.017

Liu, S., Zhu, D., Zhu, J., Yang, Q., & Wu, H. (2017). Preparation of Ag@AgCl-doped TiO2/sepiolite and its photocatalytic mechanism under visible light. *Journal of Environmental Sciences, 60*, 43-52. doi:https://doi.org/10.1016/j.jes.2016.12.026

Liu, X. (2019). Research progress on treatment technology of produced water by adsorption method. *Materials Science and Engineering, 472*(2019), 2-6. doi:10.1088/1757-899X/472/1/012082

Lopes, J., Rodrigues, W., Oliveira, V., Braga, A., da Silva, R., França, A., . . . da Silva Filho, E. (2019). Modification of kaolinite from Pará/Brazil region applied in the anionic dye photocatalytic discoloration. *Applied Clay Science, 168*, 295-303. doi:https://doi.org/10.1016/j.clay.2018.11.028

López-Luna, J., Ramírez-Montes, L. E., Martinez-Vargas, S., Martínez, A. I., Mijangos-Ricardez, O. F., González-Chávez, M. A., . . . Vázquez-Hipólito, V. (2019). Linear and nonlinear kinetic and isotherm adsorption models for arsenic removal by manganese ferrite nanoparticles. *SN Applied Sciences, 1*(950), 1-19. doi:10.1007/s42452-019-0977-3

Lu, Z., Gao, J., He, Q., Wu, J., Liang, D., Yang, H., & Chen, R. (2017). Enhanced antibacterial and wound healing activities of microporouschitosan-Ag/ZnO composite dressing. *Carbohydrate Polymers, 156*, 460-469.

Lukong, V. T., Ukoba, K., & Jen, T. (2022). Review of self-cleaning TiO_2 thin films deposited with spin coating. *The International Journal of Advanced Manufacturing Technology, 122*, 1-22. doi:10.1007/s00170-022-10043-3

Luo, L., Wang, B., Jiang, J., Huang, Q., Yu, Z., & Li, H. (2020). Heavy metal contaminations in herbal medicines: Determination, comprehensive risk assessments. . *Frontiers in Pharmacology, 11*(59). doi:10.3389/fphar.2020.595335

Madadi, Z., Soltanieh, M., Lotfabad, T. B., & Nazari, B. S. (2020). Green synthesis of titanium dioxide nanoparticles with Glycyrrhiza glabra and their photocatalytic activity. *Asian Journal of Green Chemistry, 4*(3), 256-268. doi:10.33945/SAMI/AJGC.2020.3.3

Mahmood, W. K., Rawa, K. I., & Naje, A. N. (2021). Surface Plasmon Resonance study of Ag nanoparticles colloidal. *Iraqi Journal of Science, 58*(4B), 2090-2097. doi:10.24996/ijs.2017.58.4B.12

Majid, M. S., Mohsin, A. A., & Saba, M. B. (2018). Effects of Sawdust and Rice husk Additives on Physical Properties of Ceramic Filter. *Journal of University of Babylon, Engineering Sciences, 26*(1), 221-228.

Malima, N., Lugwisha, E., & Mwakaboko, A. (2018). The efficacy of raw Malangali kaolin clay in the adsorptive removal of cadmium and cobalt ions from water. *Tanzania Journal of Science, 44*(2), 64-30.

Manikandan, V., Velmurugan, P., Park, J., Chang, W., Park, Y., Jayanthi, P., . . . Oh, B. (2017). Green synthesis of silver oxide nanoparticles and its antibacterial activity against dental pathogens *3 Biotech, 7*(72). doi:10.1007/s13205-017-0670-4

Marsooli, M., nasrabadi, M., fasihi-ramandi, M., Adib, K., Eghbali-Arani, M., Pourmasoud, S., . . . Ganjali, M. (2019). Preparation of $Fe_3O_4/SiO_2/TiO_2/PrVO_4$ nanocomposite in various molar ratios: Investigation on photocatalytic performance on organic contaminate and bacterial environments, and anti-cancer properties. *Polyhedron, 176*, 114239. doi:10.1016/j.poly.2019.114239

Masindi, V., & Muedi, K. L. (2018). *Heavy Metals*. In H. E.-D. M. Saleh & R. F. Aglan (Eds.), *Environmental Contamination by Heavy Metals*. Retrieved from https://www.intechopen.com/books/heavy-metals/environmental-contamination-by-heavy-metals doi:10.5772/intechopen.76082

Memarian, N., Mohammadi, M., & Neirameh, A. (2020). Effect of synthesis conditions and calcination on structural properties of TiO2 nanoparticles prepared by sol-gel method. *NANOSCALE, 6*(4), 102-109.

Merem, E. C., Twumasi, Y., Wesley, J., Isokpeh, P., Shenge, M., Fageir, S., . . . Nwagboso, E. (2017). Assessing the Ecological Effects of Mining in West Africa: The Case of Nigeria. *International Journal of Mining Engineering and Mineral Processing, 6*(1), 1-19. doi:10.5923/j.mining.20170601.01

Mgbemena, C. O., Ibekwe, N. O., Sukumar, R., & Menon, A. R. (2013). Characterization of kaolin intercalates of oleochemicals derived from rubber seed (Hevea brasiliensis) and tea seed (Camelia sinensis) oils. *Journal of King Saud University – Science, 25,* 149–155. doi:10.1016/j.jksus.2012.11.004

Mishra, A., Mehta, A., & Basu, S. (2018). Clay Supported TiO2 Nanoparticles for Photocatalytic Degradation of Environmental Pollutants: A Review. *Journal of Environmental Chemical Engineering volume 2018, 6*(6), 6088-6107. doi:10.1016/j.jece.2018.09.029

Mitko, K., Noszczyk, A., Dydo, P., & Turek, M. (2021). Electrodialysis of coal mine water. *Water Resources and Industry, 25*, 100143. doi:https://doi.org/10.1016/j.wri.2021.100143

Miyah, Y., Lahrichi, A., Idrissi, M., Boujraf, S., Taouda, H., & Zerrouq, F. (2017). Assessment of adsorption kinetics for removal potential of Crystal Violet dye from aqueous solutions using Moroccan pyrophyllite. *Journal of the Association of Arab Universities for Basic and Applied Sciences, 23*, 20-28. doi:10.1016/j.jaubas.2016.06.001

Mnasri-Ghnimi, S., & Frini-Srasra, N. (2019). Removal of heavy metals from aqueous solutions by adsorption using single and mixed pillared clays. *Applied Clay Science, 179*(2019), 3-19. doi:10.1016/j.clay.2019.105151

Mobasherpour, I., Salahi, E., & Pazouki, M. (2012). Comparative of the removal of Pb^{2+}, Cd^{2+} and Ni^{2+} by nano crystallite hydroxyapatite from aqueous solutions: Adsorption isotherm study. *Arabian Journal of Chemistry, 5*, 439–446. doi:10.1016/j.arabjc.2010.12.022

Mohd-Noor, S. F., Ahmad, N., Khattak, M. A., Mukhtar, A., Badshah, S., & Khan, R. U. (2019). Removal of heavy metal from wastewater: A review of current treatment processes. *Journal of Advanced Research in Materials Science, 58*(1), 1-9.

Motazedian, F., Wu, Z., Zhang, J., Samsam-Shariat, B., Jiang, D., Martyniuk, M., . . . Yang, H. (2019). Determining intrinsic stress and strain state of fibre-textured thin films by X-ray diffraction measurements using combined asymmetrical and Bragg-Brentano configurations. *Materials & Design, 181*, 108063. doi:https://doi.org/10.1016/j.matdes.2019.108063

Motsi, T., Rowson, N. A., & Simmons, M. J. H. (2009). Adsorption of heavy metals from acid mine drainage by natural zeolite. *International Journal of Mineral Processing, 92 (2009)* (2009), 42–48. doi:10.1016/j.minpro.2009.02.005

Muhammad, I., Ashiru, S., Ibrahim, D., Salawu, K., Muhammad, T., & Muhammad, A. (2013). Determination of some heavy metals in wastewater and sediment of artisanal gold local mining site of Abare area in Nigeria. *Journal of Environmental Treatment Techniques, 1* (3), 174-182.

Mukul, B., Yogesh, U., Suresh, G., Parita, B., Van-Huy, N., Shreyas, P., . . . Vanita, K. (2022). Plant-mediated biological synthesis of Ag-Ago-Ag_2O nanocomposites using leaf extracts of *Solanum elaeagnifolium* for antioxidant, anticancer, and DNA cleavage activities. *Research Square, 11*(1). doi:10.21203/rs.3.rs-973781/v1

Munasir, M., Supardi, Z., Mashadi, P., Nisa, Z., Kusumawati, D., Putri, N., . . . Darminto, D. (2018). Phase transition of SiO_2 nanoparticles prepared from natural sand: The calcination temperature effect. *Journal of Physics: Conference Series, 1093*, 012025. doi:10.1088/1742-6596/1093/1/012025

Munasir, M., Triwikantoro, T., Zainuri, M., & Darminto, D. (2015). Synthesis of SiO_2 nanopowders containing quartz and cristobalite phases from silica sands. *MATERIALS SCIENCE-POLAND, 33*, 47-55. doi:10.1515/msp-2015-0008

Mungondori, H. H., Mtetwa, S., Tichagwa, L., Katwire, T. M., & Nyamukamba, P. (2017). Synthesis and application of a ternary composite of clay, saw-dust and peanut husks in heavy metal adsorption. *Water Science Technology, 12*(3), 1-11. doi:10.2166/wst.2017.123

Murali, V. S., Meena Devi, V. N., Parvathy, P., & Murugan, M. (2021). Phytochemical screening, FTIR spectral analysis, antioxidant and antibacterial activity of leaf extract of Pimenta dioica Linn. *Materials Today: Proceedings, 45*, 2166-2170. doi:https://doi.org/10.1016/j.matpr.2020.10.038

Musial, J., Krakowiak, R., Mlynarczyk, D. T., Goslinski, T., & Stanisz, B. J. (2020). Titanium dioxide nanoparticles in food and personal care products—What do we know about their safety? *Nanomaterials, 10*(6), 1110-1121.

Mustapha, S., Ndamitso, M. M., Abdulkareem, A. S., Tijani, J. O., Mohammed, A. K., & Shuaib, D. T. (2019). Potential of using kaolin as a natural adsorbent for the removal of pollutants from tannery wastewater. *Heliyon, 5*(e02923), 1-17. doi:10.1016/j.heliyon.2019.e02923

Mustapha, S., Ndamitso, M. M., Abdulkareem, A. S., Tijani, J. O., Shuaib, D. T., Ajala, A. O., & Mohammed, A. K. (2020). Application of TiO_2 and ZnO nanoparticles immobilized on clay in wastewater treatment: a review. *Applied Water Science, 10*(49), 1-36. doi:10.1007/s13201-019-1138-y

Mustapha, S., Tijani, J. O., Ndamitso, M. M., Abdulkareem, S. A., Shuaib, D. T., Mohammed, A. K., & Sumaila, A. (2020b). The role of kaolin and kaolin/ZnO nanoadsorbents in adsorption studies for tannery wastewater treatment. *Scientific Reports*. doi:10.1038/s41598-020-69808-z

Mustapha, S. I., Aderibigbe, F. A., Adewoye, T. L., Mohammed, I. A., & Odey, T. O. (2021). Silver and titanium oxides for the removal of phenols from pharmaceutical wastewater. *Materials Today: Proceedings, 38*, 816-822.

Myilsamy, M., Murugesan, V., & Mani, D. M. (2015). The effect of synthesis conditions on mesoporous structure and the photocatalytic activity of TiO_2 nanoparticles. *Journal of Nanoscience and Nanotechnology, 15*, 4664-4675. doi:10.1166/jnn.2015.9772

Nadeem, M., Tungmunnithum, D., Hano, C., Abbasi, B. H., Hashmi, S. S., Ahmad, W., & Zahir, A. (2018). The current trends in the green syntheses of titanium oxide nanoparticles and their applications. *Green Chemistry Letters and Reviews, 11*(4), 492-502. doi:10.1080/17518253.2018.1538430

Naghibi, S., Sani, M. A. F., & Hosseini, H. R. M. (2013). Application of the statistical Taguchi method to optimize TiO_2 nanoparticles synthesis by the hydrothermal assisted sol–gel technique. *Ceramics International, 8*. doi:10.1016/j.ceramint.2013.08.077

Narayanan, M., Devi, P. G., Natarajan, D., Kandasamy, S., Devarayan, K., Alsehli, M., . . . Pugazhendhi, A. (2021). Green synthesis and characterization of titanium dioxide nanoparticles using leaf extract of Pouteria campechiana and larvicidal and pupicidal activity on Aedes aegypti. *Environmental Research, 200*, 111333. doi:https://doi.org/10.1016/j.envres.2021.111333

Ndikau, M., Noah, N. M., Andala, M. D., & Masika, E. (2017). Green synthesis and characterization of silver nanoparticles using *Citrullus lanatus* fruit rind extract. *International Journal of Analytical Chemistry*, 1-9. doi:https://doi.org/10.1155/2017/8108504

Nersisyan, H. H., Lee, J. H., Son, H. T., Won, C. W., & Maeng, D. Y. (2003). A new and effective chemical reduction method for preparation of nanosized silver powder and colloid dispersion. *Materials Research Bulletin, 38*(6), 949-956. doi:https://doi.org/10.1016/S0025-5408(03)00078-3

Nguiamba, N., Belibi, P. D. B., Sieliechi, J. M., & Ngassoum, M. B. (2019). Physico-chemical characterization and stability study in acidic and basic solution of ceramic filters from Mouka's clay (Cameroon). *Journal of Materials Science and Chemical Engineering, 7*(11), 42-53. doi:10.4236/msce.2019.711005

Nimibofa, A., & Bennett, V. (2022). Investigation of Biochemical Oxygen Demand (BOD) in Ntanwoba Creek Using Dilution Method.

NIS. (2015). *Nigerian standard for drinking water quality*. Retrieved from Abuja,Nigeria: https://africacheck.org/wp-content/uploads/2018/06/Nigerian-Standard-for-Drinking-Water-Quality-NIS-554-2015.pdf

Nishijo, M., Nakagawa, H., Suwazono, Y., Nogawa, K., & Kido, T. (2017). Causes of death in patients with Itai-itai disease suffering from severe chronic cadmium poisoning: a nested case–control analysis of a follow-up study in Japan. *BMJ. Open, 7*(7), 1-18. doi:10.1136/bmjopen-2016-015694

Nouh, E. A., Lasheen, T. A., El-sherif, R. M., & Abdel-Ghany, N. A. (2019). CeO_2–$TiFe_2O_4$ nanocomposite for efective removal of uranium ions from aqueous waste solutions. *Springer Nature Applied Sciences, 1*(159), 1-13. doi:10:1007/s42452-019-0176-2

Nyamukamba, P., Okoh, O., Tichagwa, L., & Greyling, C. (2016). Preparation of titanium dioxide nanoparticles immobilized on polyacrylonitrile nanofibres for the photodegradation of methyl orange. *International Journal of Photoenergy, 2016*, 1-9.

Obasi, P. N., & Akudinobi, B. B. (2020). Potential health risk and levels of heavy metals in water resources of lead–zinc mining communities of Abakaliki, southeast Nigeria. *Applied Water Science, 10*(7), 184. doi:10.1007/s13201-020-01233-z

Ogbu, I. C., Akpomie, K. G., Osunkunle, A. A., & Eze, S. I. (2019). Sawdust-kaolinite composite as efficient sorbent for heavy metal ions. *Bangladesh Journal of Scientiofic and Industrial Research, 54*(1), 99-110. doi:10.3329/bjsir.v54i1.40736

Ogunleye, O. O., Ajala, M. A., & Agarry, S. E. (2014). Evaluation of biosorptive capacity of banana (*Musa paradisiaca*) stalk for lead(II) removal from aqueous solution. *Journal of Environmental Protection., 5*, 1451-1465. doi:10.4236/jep.2014.515138

Oguzhan, A., Yildiz, B., Semih, G., & Ozge, K. (2016). Ag doped TiO_2 nanoparticles prepared by hydrothermal method and coating of the nanoparticles on the ceramic pellets for photocatalytic study: Surface properties and photoactivity. *Journal of Engineering Technology and Applied Sciences, 1*(1), 1-12.

Oi, L. E., Choo, M., Lee, H. V., Ong, H. C., Hamida, S. B. A., & Juan, J. C. (2016). Recent advances of titanium dioxide (TiO_2) for green organic synthesis. *RSC Advances, 6*(2016), 108741–108754.

Ojonimi, T., Asuke, F., Onimisi, M., & Onuh, C. (2019). Acid Mine Drainage (AMD): an environmental concern generated by coal mining. *Journal of Degraded and Mining Lands Management, 6*, 1875-1881. doi:10.15243/jdmlm.2019.064.1875

Okhovat, N., Hashemi, M., & Golpayegani, A. A. (2015). Photocatalytic decomposition of metranidazolein aqueous solutions using titanium dioxide nanoparticles. *J. Mater. Environ. Sci., 6*(3), 792-799.

Okolo, C. C., Oyedotun, T. D. T., & Akamigbo, F. O. R. (2018). Open cast mining: threat to water quality in rural community of Enyigba in south-eastern Nigeria. *Applied Water Science, 8*(204), 1-12. doi:10.1007/s13201-018-0849-9

Olaremu, A. G. (2015). Physico-chemical characterization of Akoko mined kaolin clay. *Journal of Minerals and Materials Characterization and Engineering, 3*, 353-361. doi:http://dx.doi.org/10.4236/jmmce.2015.35038

Oliveira, W. V., Morais, A. I. S., Honorio, L. M. C., Trigueiro, P. A., Almeida, L. C., Garcia, R. R. P., . . . Osajima, J. A. (2020). TiO_2 Immobilized on Fibrous Clay as Strategies to Photocatalytic Activity. *Materials Research, 23*(1). doi:10.1590/1980-5373-MR-2019-0463

Oncel, M. S., Muhcu, A., Demirbas, E., & Kobya, M. (2013). A comparative study of chemical precipitation and electrocoagulation for treatment of coal acid drainage wastewater. *Journal of Environmental Chemical Engineering, 1*(4), 989–995. doi:10.1016/j.jece.2013.08.008

Ortega-Dıaz, D., Fernandez, D., Sepulveda, S., Lindeke, R. R., Perez-Bueno, J. J., Pelaez-Abella, E., & Manrıquez, J. (2020). Preparation of nanoparticulate TiO_2 containing nanocrystalline phases of anatase and brookite by electrochemical dissolution of remelted titanium components. *Arabian Journal of Chemistry, 13*, 2858-2864. doi:10.1016/j.arabjc.2018.07.015

Ostovar, F., Ansari, R., & Moafi, H. F. (2017). Preparation and application of silver oxide/sawdust nanocomposite for Chromium (VI) ion removal from aqueous solutions using column system,. *Global NEST Journal, 19*(3), 412-422.

Ouyang, D., Zhuo, Y., Hu, L., Zeng, Q., Hu, Y., & He, Z. (2019). Research on the Adsorption behavior of heavy metal ions by porous material prepared with silicate tailings. *Minerals, 9*(291), 1-16. doi:10.3390/min9050291

Pardha-Saradhi, P., Yamal, G., Peddisetty, T., Sharmila, P., Nagar, S., Singh, J., . . . Rao, K. S. (2014). Reducing strength prevailing at root surface of plants promotes reduction of Ag+ and generation of Ag0/Ag_2O nanoparticles exogenously in aqueous phase. *PLoS ONE, 9*(9). doi:10.1371/journal.pone.0106715

Park, Y. T., Lee, H., Yun, H., Song, K., Yeom, S., & Choi, H. (2013). Removal of metal from acid mine drainage using a hybrid system including a pipes inserted microalgae reactor. *Bioresource Technology., 150*, 242-248. .

Patidar, V., & Jain, P. (2017). Green Synthesis of TiO2 Nanoparticle Using Moringa Oleifera Leaf Extract. *International Research Journal of Engineering and Technology, 4*(3), 1-4.

Pavesi, T., & Moreira, J. C. (2020). Mechanisms and individuality in chromium toxicity in humans. *Journal of Applied Toxicology, 40*, 1183–1197. doi:10.1002/jat.3965

Pessanha, N. F., Kawase, K. Y., & Coelho, G. L. (2014). Preparation and Characterization of Silver/Organo-clay Nanocomposites *Chemical and Materials Engineering., 2*(8), 173-178. doi:10.13189/cme.2014.020802

Petrik, L., Missengue, R., Fatoba, O., Tuffin, M., & Sachs, J. (2012). *Silver/ Zeolite Nano Composite-Based Clay filters for water disinfection*. Retrieved from Gezina, South Africa.:

Petrinic, I., Korenak, J., Povodnik, D., & Hélix-Nielsen, C. (2015). A feasibility study of ultrafiltration/reverse osmosis (UF/RO)-based wastewater treatment and reuse in the metal finishing industry. *Journal of Cleaner Production, 101*, 292-300. doi:https://doi.org/10.1016/j.jclepro.2015.04.022

Pham, T., & Lee, B. (2014). Feasibility of silver doped TiO_2/glass fiber photocatalyst under visible irradiation as an indoor air germicide. *International Journal of environmental Research and Public Health, 11*, 3271-3288.

Pintor, A. M. A., Vieira, B. R. C., Santos, S. C. R., Boaventura, R. A. R., & Botelho, C. M. S. (2018). Arsenate and arsenite adsorption onto iron-coated cork granulates. *Science of Total Environment, 642*, 1075–1089. doi:10.1016/j.scito tenv.2018.06.170

Pohl, A. (2020). Removal of heavy metal ions from water and wastewaters by sulfur-containing precipitation agents. *Water, Air, & Soil Pollution, 231*(10), 503. doi:10.1007/s11270-020-04863-w

Politova-Brinkova, N., Tsibranska, S., Tcholakova, S., Denkov, N., & Danner, T. (2020). Preparation of TiO_2 nanoparticle aggregates and capsules by the 'two-emulsion method'. *Colloids and Interfaces, 4*, 57. doi:10.3390/colloids4040057

Ponka, P., Tenenbein, M., & Eaton, J. W. (2015). Chapter 41 - Iron. In G. F. Nordberg, B. A. Fowler, & M. Nordberg (Eds.), *Handbook on the Toxicology of Metals (Fourth Edition)* (pp. 879-902). San Diego: Academic Press.

Poursani, S. K., Nilchi, A., Hassani, A., Shariat, S. M., & Nouri, J. (2016). The synthesis of nano TiO_2 and its use for removal of lead ions from aqueous solution. *Journal of Water Resource and Protection, 8*(2019), 438-448. doi:10.4236/jwarp.2016.84037

Prakash, N. B., Sockan, V., & Jayakaran, P. (2014). Wastewater treatment by coagulation and flocculation. *International Journal of Engineering Science and Innovative Technology, 3*(2), 479.

Prasse, C., Stalter, D., Schulte-Oehlmann, U., Oehlmann, J., & Ternes, T. (2015). Spoilt for choice: A critical review on the chemical and biological assessment of current wastewater treatment technologies. *Water research, 87*, 237-270.

Pretty, M. M., & Odeku, K. O. (2017). Harmful mining activities, environmental impacts and effects in the mining communities in South Africa: a critical perspective. *Environmental Economics, 8*(4), 14-24. doi:10.21511/ee.08(4).2017.02

Qisti, N., Indrasti, N. S., & Suprihatin. (2016). Optimization of process condition of nanosilica production by hydrothermal method. *IOP Conference Series: Materials Science and Engineering, 162*(1), 012036. doi:10.1088/1757-899x/162/1/012036

Quezada, C., Estay, H., Cassano, A., Troconso, E., & Ruby-Figueroa, R. (2021). Prediction of Permeate Flux in Ultrafiltration Processes: A Review of Modeling Approaches. *Membranes, 11*(5), 368-456. doi:10.3390/membranes11050368

Rajabi, A., Ghazali, M. J., Mahmoudi, E., Baghdadi, A. H., Mohammad, A. W., Mustafah, N. M., . . . Naicker, A. S. (2019). Synthesis, characterization, and antibacterial activity of Ag_2O-loaded polyethylene terephthalate fabric via ultrasonic method. *9*(3), 450.

Ramesh, A., Rajesh, D., Shanthi, K., Bhargav, P. B., & Nguyen-Le, M.-T. (2021). Catalytic conversion of glucose to 5-hydroxymethylfurfural productions over sulphated Ti-Al2O3 catalysts. *Biomass and Bioenergy, 154*, 106261. doi:https://doi.org/10.1016/j.biombioe.2021.106261

Rania, F., & Yousef, N. S. (2015). Equilibrium and Kinetics studies of adsorption of copper (II) on natural Biosorbent. *International Journal of Chemical/Engineering and Applications, 6*(5).

Rashmi, B. N., Harlapur, S. F., Avinash, B., Ravikumar, C. R., Nagaswarupa, H. P., Kumar, M. R. A., . . . Santosh, M. S. (2020). Facile green synthesis of silver oxide nanoparticles and their electrochemical, photocatalytic and biological studies. *Inorganic Chemistry Communications, 111*(107580). doi:10.1016/j.inoche.2019.107580

Ravichandran, S., Paluri, V., Kumar, G., Loganathan, K., & R., K. V. B. (2016a). A novel approach for the biosynthesis of silver oxide nanoparticles using aqueous leaf extract of Callistemon lanceolatus (Myrtaceae) and their therapeutic potential. *Journal of Experimental Nanoscience, 11*(6), 445-458. doi:10.1080/17458080.2015.1077534

Ravichandran, S., Paluri, V., Kumar, G., Loganathan, K., & Venkata, B. R. K. (2016b). A novel approach for the biosynthesis of silver oxide nanoparticles using aqueous leaf extract of Callistemon lanceolatus (Myrtaceae) and their therapeutic potential *Journal of Experimental Nanoscience, 11*(6), 445-458. doi:10.1080/17458080.2015.1077534

Reidy, B., Haase, A., Luch, A., Dawson, K. A., & Lynch, I. (2013). Mechanisms of Silver Nanoparticle Release, Transformation and Toxicity: A Critical Review of Current Knowledge and Recommendations for Future Studies and Applications. *Materials, 6* 2295-2350. doi:doi:10.3390/ma6062295

Ren, Y., Kong, J., Xue, J., Shi, X., Li, H., Qiao, J., & lu, Y. (2019). Effects of ozonation on the activity of endotoxin and its inhalation toxicity in reclaimed water. *Water research, 154*(2019), 153-161. doi:10.1016/j.watres.2019.01.051

Roberts, J., Power, A., Chapman, J., Chandra, S., & Cozzolino, D. (2018). The use of UV-vis spectroscopy in bioprocess and fermentation monitoring. *Fermentation, 4*(1), 18. doi:10.3390/fermentation4010018

Roghini, R., & Vijayalakshmi, K. (2018). Phytochemical screening, quantitative analysis of flavonoids and minerals in ethanolic extract of citrus paradisi r. . *International Journal of Pharmaceutical Science and Research, 9*(11), 4859-4864. doi:10.13040/IJPSR.0975-8232.9(11).4859-64

Roos, W. D. (2017). A preliminary report on nanoparticle powders of TiO_2 doped with silver and boron. *Department of Physics, University of Free State, South Africa, 4*, 18-22.

Rubio, S. R. T. J. (2010). Removal of Mn^{2+} from aqueous solution by manganese oxide coated zeolite. *Minerals Engineering, 23*(2010), 1131–1138. doi:10.1016/j.mineng.2010.07.007

Rudi, N. N., Muhamad, M. S., Chuan, L. T., Alipal, J., Omar, S., Hamidon, N., . . . Harun, H. (2020). Evolution of adsorption process for manganese removal in water via agricultural waste adsorbents. *Heliyon, 6*(e05049). doi:https://doi.org/10.1016/j.heliyon.2020.e05049

Russo, V., Hmoudah, M., Broccoli, F., Lesce, M., Jung, O., & Di_serio, M. (2020). Applications of MOFs in wastewater treatment: A review on adsorption and photodegradation. *Frontiers in Chemical Engineering, 2*(15). doi:0.3389/fceng.2020.581487

Sadasivam, S., & Rao, S. (2016). Characterization of silver—kaolinite (AgK): An adsorbent for long–lived 129I species. *SpringerPlus, 5*. doi:10.1186/s40064-016-1855-8

Salahudeen, N. (2018). Metakaolinisation effect on the thermal and physicochemical properties of Kankara kaolin. *KMUTNB International Journal of Applied Science Technology, 11*(2), 127-135.

Salahudeen, N., Nasiru, A., Ahmed, A. S., Dauda, M., Waziri, S. M., Okonkwo, P. C., & Isa, M. T. (2015). Chemical and physical comparative study of the effect of wet and dry beneficiation of kankara kaolin. *Nigerian Journal of Technology (NIJOTECH), 34*(2). doi:http://dx.doi.org/10.4314/njt.v34i2.13

Samy, M., Mossad, M., & Eletriby, H. (2019). Synthesized nano titanium for methylene blue removal under various operational conditions. *Desalination and Water Treatment, 165*, 374-381. doi:10.5004/dwt.2019.24510

Santhoshkumar, T., Rahuman, A. A., Jayaseelan, C., Rajakumar, G., Marimuthu, S., Kirthi, A. V., . . . Kim, S. (2014). Green synthesis of titanium dioxide nanoparticles using Psidium guajava extract and its antibacterial and antioxidant properties. *Asian Pacific Journal of Tropical Medicine, 14*, 968-976. doi:10.1016/S1995-7645(14)60171-1

Sarma, G. K., Gupta, S. S., & Bhattacharyya, K. G. (2019). Nanomaterials as versatile adsorbents for heavy metal ions in water: a review. *Environmental Science and Pollution Research, 26*, 6245-6278. doi:https://doi.org/10.1007/s11356-018-04093-y

Satti, S., Raja, N., Javed, B., Akram, A., Mashwani, Z., Ahmad, M., & Ikram, M. (2021). Titanium dioxide nanoparticles elicited agro-morphological and physicochemical modifications in wheat plants to control Bipolaris sorokiniana. *PLoS ONE, 16*, e0246880. doi:10.1371/journal.pone.0246880

Satyanarayana, T., & Reddy, S. (2018). A review on chemical and physical synthesis methods of nanomaterials. *International Journal for Research in Applied Science and Engineering Technology, 6*, 2321-9653. doi:10.22214/ijraset.2018.1396

Sdiri, A., Higashi, T., Chaabouni, R., & Jamoussi, F. (2012). Competitive removal of heavy metals from aqueous solutions by montmorillonitic and calcareous clays. *Water, Air, & Soil Pollution, 223*(3), 1191-1204.

Sdiri, A. T., Higashi, T., & Jamoussi, F. (2014). Adsorption of copper and zinc onto natural clay in single and binary systems. *International Journal of Environmental Science and Technology, 11*, 1081-1092. doi:10.1007/s13762-013-0305-1

Seo, E. Y., Cheong, Y. W., Yimb, G. J., Mina, K. W., & Geroni, J. W. (2016). Recovery of Fe, Al and Mn in acid coal mine drainage by sequential selective precipitation with control of pH. *Catena, 148*, 11-16. doi:10.1016/j.catena.2016.07.022

Sethy, N., Arif, Z., Mishra, P., & Kumar, P. (2020). Green synthesis of TiO_2 nanoparticles from Syzygium cumini extract for photo-catalytic removal of lead (Pb) in explosive industrial wastewater. *Green Processing and Synthesis, 9*(1), 171-181. doi:10.1515/gps-2020-0018

Shah, A., Haq, S., Rehman, W., Waseem, M., Shoukat, S., & Rehman, M. (2019). Photocatalytic and antibacterial activities of paeonia emodi mediated silver oxide nanoparticles. *Materials Research Express, 6*(4), 045045. doi:10.1088/2053-1591/aafd42

Shah, M., Fawcett, D., Sharma, S., Tripathy, S. K., & Poinern, G. E. J. (2015). Green synthesis of metallic nanoparticles via biological entities. *Materials, 8*, 7278–7308. doi:10.3390/ma8115377

Shameli, K., Ahmad, M. B., Yunus, W. M., & Ibrahim, N. A. (2011). Fabrication of silver Nanoparticles doped in the zeolite framework and antibacterial activity. *International Journal of Nanomedicine, 6*, 331-341.

Sharififard, H., Ghorbanpour, M., & Hosseinirad, S. (2018). Cadmium removal from wastewater using nano-clay/TiO_2 composite: kinetics, equilibrium and thermodynamic study. *Advances in Environmental Technology, 4*(4), 203-209. doi:10.22104/aet.2019.3029.1149

Sharma, G. K., & Khan, M. I. (2013). Bioremediation of sewage wastewater using selective algae for manure production. *International Journal of Environmental Engineering Management, 4*, 573-580.

Sharma, S. N., & Srivastava, R. (2020). Silver oxide nanoparticles synthesized by green method from Artocarpus Hetrophyllus for antibacterial and antimicrobial applications. *Materials Today: Proceedings*. doi:10.1016/j.matpr.2020.02.233

Sheeba, G. D., & Viswanathan, P. (2014). GC-MS analysis of phytocomponents in Spermacoce articularis L. f. leaf. *Research in Pharmacy, 4*(4), 01-07.

Shittu, K. O., & Ihebunna, O. (2017a). Purification of simulated wastewater using green synthesised silver nanoparticles of Piliostigma thonningi aqueous leave extract. *Nanoscience and Nanotechnology, 8*, 1-9. doi:10.1088/2043-6254/aa8536

Shittu, K. O., & Ihebunna, O. (2017b). Purification of simulated wastewater using green synthesised silver nanoparticles of *Piliostigma thonningi* aqueous leave extract. . *Advances in Natural Science : Nanoscience and Nanotechnology, 8*, 1-9. doi:https://doi.org/10.1088/2043-6254/aa8536

Shivaraju, H. P., Egumbo, H., Madhusudan, P., Anil Kumar, K. M., & Midhun, G. (2018). Preparation of affordable and multi-functional clay-based ceramic filter matrix for treatment of drinking water. *Environmental Technology,*, 1-30. doi:10.1080/09593330.2018.1430853

Shooto, N., Dikio, C., Wankasi, D., Sikhwivhilu, L., Mtunzi, F., & Dikio, E. (2016). Novel PVA/MOF nanofibres: fabrication, evaluation and adsorption of lead ions from aqueous solution. *Nanoscale research letters, 11*, 1-13.

Shukla, S. K., Mushaiqri, N. R., Subhi, H. M. A., Yoo, K., & Sadeq, H. A. (2020). Low-cost activated carbon production from organic waste and its utilization for wastewater treatment. *Applied Water Science, 10*(62). doi:10.1007/s13201-020-1145-z

Sibiya, N. P., Rathilal, S., & E.K., T. (2021). Coagulation Treatment of Wastewater: Kinetics and Natural Coagulant Evaluation. *Molecules, 26*(3), 698-708. doi:10.3390/molecules26030698.

Singh, A., Gaud, B., & Jaybhaye, S. (2020). Optimization of synthesis parameters of silver nanoparticles and its antimicrobial activity. *Materials Science for Energy Technologies, 3*, 232-236. doi:10.1016/j.mset.2019.08.004

Singh, J., Dutta, T., Kim, K., Rawat, M., Samddar, P., & Kumar, P. (2018). 'Green' synthesis of metals and their oxide nanoparticles: applications for environmental remediation. *Journal of Nanobiotechnology, 16*(1), 84. doi:10.1186/s12951-018-0408-4

Singh, J., Kaur, G., Kaur, P., Bajaj, R., & Rawat, M. (2016). A review on green synthesis and characterization of silver nanoparticles and their applications: A green nanoworld. *World Journal Of Pharmacy And Pharmaceutical Sciences, 5*(7), 730-762. doi:10.20959/wjpps20167-7227

Singh, T., Pal, D. B., Almalki, A., Althobaiti, Y., Alkhanani, M., Haque, S., . . . Srivastava, N. (2022). Green synthesis of TiO_2 bionanocomposite using waste leaves of water hyacinth: Application in antibacterial activity of toilet bacteria Serratia marcescens. *Materials Letters, 316*, 132012. doi:https://doi.org/10.1016/j.matlet.2022.132012

Sirichokthavasarp, J., Dang, T. T., Channei, D., Chansaenpak, K., Khanitchaidecha, W., & Nakaruk, A. (2020). Influence of preparation methods of TiO_2 nanoparticle on photodegradation of methylene blue. *Materials Science Forum, 998*, 84-89. doi:10.4028/www.scientific.net/MSF.998.84

Soliman, M. Y. M., Halema, D., & Medema, G. (2020). Virus removal by ceramic pot filter disks: Effect of biofilm growth and surface cleaning. *International Journal of Hygiene and Environmental Health, 224*(2020), 1-8. doi:10.1016/j.ijheh.2019.113438

Sooksaen, P., & Karawatthanaworrakul, S. (2015). The properties of Southern Thailand clay-based porous ceramics fabricated from different pore size templates. *Applied Clay Science, 104*, 295-302. doi:10.1016/j.clay.2014.12.009

Sotomayor, F. J., Cychosz, K. A., & Thommes, M. (2018). Characterization of Micro/Mesoporous Materials by Physisorption: Concepts and Case Studies. *Accounts of Material and Surface Research, 3* (2), 34-50.

Souri, M., Hoseinpour, V., Shakeri, A., & Ghaemi, N. (2018). Optimisation of green synthesis of MnO nanoparticles via utilising response surface methodology. *IET Nanobiotechnology, 12*(6), 822-827. doi:10.1049/iet-nbt.2017.0145

Stavinskaya, O., Laguta, I., Fesenko, T., & Krumova, M. (2019). Effect of temperature on green synthesis of silver nanoparticles using *Vitex agnus-castus* extract. *Chemistry Journal of Moldova, 14*(2), 117-121. doi:10.19261/cjm.2019.636

Subhapriya, S., & Gomathipriya, P. (2018). Green synthesis of titanium dioxide (TiO_2) nanoparticles by Trigonella foenum-graecum extract and its antimicrobial properties. *Microbial Pathogenesis, 116*, 215-220. doi:https://doi.org/10.1016/j.micpath.2018.01.027

Sumi, L., & Gestring, B. (2013). Polluting the future: How mining companies are contaminating our nation's waters in perpetuity. *Earthworks*, 1-51.

Suresh, S., Pradheesh, G., & Ramani, V. A. (2018). Biosynthesis and characterization of CuO, MgO and Ag_2O nanoparticles, anti inflammatory activity and phytochemical screening of the ethanolic extract of the medicinal plant *Pavetta indica Linn*. *Journal of Pharmacognosy and Phytochemistry, 7*(4), 1984-1990.

Sushman, D., & Richa, S. (2015). Use of nanoparticles in water treatment: A review. *International Research Journal of Environment Sciences, 4*(10), 103-106.

Swathi, N., Sandhiya, D., Rajeshkumar, S., & Lakshmi, T. (2019). Green synthesis of titanium dioxide nanoparticles using Cassia fistula and its antibacterial activity. *International Journal of Research In Pharmaceutical Sciences, 10*(2), 856-860. doi:https://doi.org/10.26452/ijrps.v10i2.261

Szczepanik, B. (2017). Photocatalytic degradation of organic contaminants over clay-TiO_2 nanocomposites: A review. *Applied Clay Science, 141*, 227-239. doi:https://doi.org/10.1016/j.clay.2017.02.029

Taha, A., Ben Aissa, M., & Da'na, E. (2020). Green synthesis of an activated carbon-supported Ag and ZnO nanocomposite for photocatalytic degradation and its antibacterial activities. *25*(7), 1586.

Taufiq, A., Nikmah, A., Hidayat, A., Sunaryono, S., Mufti, N., Hidayat, N., & Susanto, H. (2020). Synthesis of magnetite/silica nanocomposites from natural sand to create a drug delivery vehicle. *Heliyon, 6*(4), 10. doi:10.1016/j.heliyon.2020.e03784

Tavlieva, M. P., Genieva, S. D., Georgieva, V. G., & Vlaev, L. T. (2015). Thermodynamics and kinetics of the removal of manganese(II) ions from aqueous solutions by white rice husk ash. *Journal of Molecular Liquids, 211*, 938–947.

Taylor, A. A., Tsuji, J. S., Garry, M. R., McArdle, M. E., Goodfellow, W. L., Adams, W. J., & Menzie, C. A. (2020). Critical review of exposure and effects: implications for setting regulatory health criteria for ingested copper. *Environmental Management (2020) 65:, 65*(2020), 131–159. doi:10.1007/s00267-019-01234-y

Tetteh, E., Rathilal, S., & Chollom, M. (2017). Treatment of industrial mineral oil wastewater-optimisation of coagulation flotation process using response surface methodology (RSM). *International Journal of Applied Engineering Research, 12*, 13084-13091.

Thakur, B. K., Kumar, A., & Kumar, D. (2019). Green synthesis of titanium dioxide nanoparticles using *Azadirachta indica* leaf extract and evaluation of their antibacterial activity. *South African Journal of Botany, 124*, 223–227.

Thilagavathi, T., Renuka, R., & Priya, R. (2016). Bio-synthesis of silver nanoparticles using Punica granatum (pomegranate) peel extract: a novel approach toward waste utilization. *Internaional Journal of Advance Science and Engineering, 3*(1), 234-236.

Tien, C. (2006). *Introduction to Cake Filtration*.

Tien, C. (2012). Principles of Filtration. *Principles of Filtration*, 1-334.

Tijani, J. O., Totito, T. C., Fatoba, O. O., Babajide, O. O., & Petrik, L. F. (2017). Synthesis, characterization and photocatalytic activity of ag metallic particles deposited carbon-doped TiO_2 nanocomposites supported on stainless steel mesh. *Journal of Sol-Gel Science Technology,, 83*, 207-222.

Touahria, S., Hazourli, S., Touahria, K., Eulmi, A., & Aitbara, A. (2016). Clarification of Industrial Mining Wastewater Using Electrocoagulation. *International Journal of Electrochemical Science, 11*, 5710-5723. doi:10.20964/2016.07.51

Traiwatcharanon, P., Timsorn, K., & Wongchoosuk, C. (2017). Flexible room-temperature resistive humidity sensor based on silver nanoparticles. *Material Research Express, 4*(2017), 2-11. doi:10.1088/2053-1591/aa85b6

Trinh, V. T., Nguyen, T. M., Van, H. T., Hoang, L. P., Nguyen, T. V., Ha, L. T., . . . Nguyen, X. C. (2020). Phosphate Adsorption by Silver Nanoparticles-Loaded Activated Carbon derived from Tea Residue. *Scientific Reports, 10*(3634), 1-13. doi:10.1038/s41598-020-60542-0

Tsao, N. H., Malatesta, K. A., Anuku, N. E., & Soboyejo, W. O. (2015). Virus filtration in porous iron (III) oxide doped ceramic water filters. *Advance Material Resources, 1132*, 284-294. doi:10.4028/www.scientific.net/AMR.1132.284

Uddin, M. K. (2017). A review on the adsorption of heavy metals by clay minerals, with special focus on the past decade. *Chemical Engineering Journal, 308*, 438-462.

Udobi, C. E., & Onaolapo, J. A. (2009). Phytochemical analysis and antibacterial evaluation of the leaf stem bark and root of the African locust bean (*Parkia biglobosa*). *Journal of Medicinal Plants Research, 3*(5), 338-344.

UNESCO. (2020). *The United Nations world water development report 2020: Water and climate change* (A. Azoulay & G. F. Houngbo Eds. Vol. 2020). Paris, France: UNESCO.

van Halem, D., van der Laan, H., Soppe, A. I. A., & Heijman, S. G. J. (2017). High flow ceramic pot filters. *Water research, 124*, 398-406. doi:https://doi.org/10.1016/j.watres.2017.07.045

Venis, R. A., & Basu, O. D. (2020). Mechanisms and efficacy of disinfection in ceramic water filters: A critical review. *Critical Reviews in Environmental Science and Technology*, 1-41. doi:10.1080/10643389.2020.1806685

Verma, D., Patel, S., & Kushwah, K. (2020). Synthesis of Titanium dioxide (TiO_2) nanoparticles and impact on morphological changes, seeds yield and phytotoxicity of Phaseolus vulgaris L. *Tropical Plant Research, 7*. doi:10.22271/tpr.2020.v7.i1.021

Wang, Z., Bao, J., Wang, T., Moryani, H. T., Kang, W., Zheng, J., . . . Xiao, W. (2021). Hazardous heavy metals accumulation and health risk assessment of different vegetable species in contaminated soils from a typical mining city, Central China. *18*(5), 2617.

Wazwaz, A., Al-Salaymeh, A., & Khan, M. S. (2019). Removing heavy metals through different types of soils and marble powder found in Oman. *20*(4), 136-142. doi:10.12911/22998993/102798

Wei, L., Li, Y., Noguera, D., Zhao, N., Song, Y., Ding, J., . . . Cui, F. (2017). Adsorption of Cu2+ and Zn2+ by extracellular polymeric substances (EPS) in different sludges: Effect of EPS fractional polarity on binding mechanism. *Journal of Hazardous Materials*, *321*, 473-483. doi:https://doi.org/10.1016/j.jhazmat.2016.05.016

WHO. (2017). *Guidelines for Drinking-water Quality: Fourth Edition Incorporating the First Addendum.* Retrieved from Geneva.:

WHO. (2019). WHO Guidelines for Drinking Water Quality: First Addendum to the Fourth Edition. In J. A. Cotruvo (Ed.), (Vol. 109, pp. 44-51). Washington, DC, USA: American Water Works Association.

Wu, A., Wang, D., Wei, C., Zhang, X., Liu, Z., Feng, P., . . . Niu, J. (2019). A comparative photocatalytic study of TiO2 loaded on three natural clays with different morphologies. *Applied Clay Science*, *183*, 105352. doi:https://doi.org/10.1016/j.clay.2019.105352

Xiang, Q., Ma, X., Zhang, D., Zhou, H., Liao, Y., Zhang, H., & Bazaka, K. (2019). Interfacial modification of titanium dioxide to enhance photocatalytic efficiency towards H_2 production. *Journal of colloid and interface science*, *556*, 376-385.

Xie, Y., Lu, G., Yang, C., Qu, L., Chen, M., Guo, C., & Dang, Z. (2018). Mineralogical characteristics of sediments and heavy metal mobilization along a river watershed affected by acid mine drainage. *PLoS ONE*, *13*(1), 1-17. doi:10.1371/journal.pone.0190010

Xu, Z., Wei, C., Jin, J., Xu, W., Wu, Q., Gu, J., . . . Xu, X. (2018). Development of a novel mixed titanium, silver oxide polyacrylonitrile nanofiber as a superior adsorbent and its application for MB removal in wastewater treatment. *Journal of the Brazilian Chemical Society*, *29*(3), 560-571. doi:10.21577/0103-5053.20170168

Yadav, K. K., Singh, J. K., Gupta, N., & Kumar, V. (2017). A review of nanobioremediation technologies for environmental cleanup: a novel biological approach. *Journal of Materials and Environmental Science*, *8*(2), 740-757.

Yakub, I., Du, J., & Soboyejo, W. O. (2012). Mechanical properties, modeling and design of porous clay ceramics. *Materials Science & Engineering A*, *558*, 21-29. doi:10.1016/j.msea.2012.07.038

Yakub, I., Plappally, A., Leftwich, M., Malatesta, K., Friedman, K. C., Obwoya, S., . . . Soboyejo, W. O. (2013). porosity, flow, and filtration characteristics of frustum-shaped ceramic water filters. *Journal Of Environmental Engineering*, *139*(7), 987-994.

Yari, A., Yari, M., Sedaghat, S., & Delbari, A. S. (2021). Facile green preparation of nano-scale silver particles using *Chenopodium botrys* water extract for the removal of dyes from aqueous solution. *Journal of Nanostructure in Chemistry*, *11*, 423+.

Younas, F., Mustafa, A., Farooqi, Z. U. R., Wang, X., Younas, S., Mohy-Ud-Din, W., . . . Hussain, M. M. (2021). Current and emerging adsorbent technologies for wastewater treatment: Trends, limitations, and environmental implications. *Water*, *13*(215), 1-25. doi:10.3390/w13020215

Youssef, H. F., Hegazy, W. H., Abo-almaged, H. H., & El-Bassyouni, G. T. (2015). Novel synthesis method of micronized Ti-Zeolite Na-A and Cytotoxic activity of its silver exchanged form. *Bioinorganic Chemistry and Applications*, *2015*, 1-12. doi:10.1155/2015/428121

Yusof, K. N., Alias, S. S., Harun, Z., Basri, H., & Azhar, F. H. (2018). *Parkia speciosa* as reduction agent in green synthesis of silver nanoparticles. . *Chemistry select, 3*, 1-6.

Zacaroni, L. M., Magriotis, Z. M., das Graças Cardoso, M., Santiago, W. D., Mendonça, J. G., Vieira, S. S., & Nelson, D. L. (2015). Natural clay and commercial activated charcoal: Properties and application for the removal of copper from cachaça. *Food Control, 47*, 536–544.

Zahir, A. A., Chauhan, I., Bagavan, A., Kamaraj, C., Elango, G., Shankar, J., . . . Singh, N. (2015a). Green synthesis of silver and titanium dioxide nanoparticles using *Euphorbia prostrata*. *Antimicrobial Agents and Chemotherapy, 59*(8), 4782-4799. doi:doi:10.1128/AAC.00098-15

Zahir, A. A., I.S., C., & A., B. (2015b). Green synthesis of silver and titanium dioxide nanoparticles using *Euphorbia Prostata* Extract. *Antimicrobial agents and chemotherapy, 59*(8), 4782-4799.

Zekić, E., Vuković, Z., & Halkijević, I. (2018). Application of nanotechnology in wastewater treatment. *GRAĐEVINAR, 70* (4), 315-323. doi:10.14256/JCE.2165.2017

Zelepukin, I. V., Popov, A. A., Shipunova, V. O., Tikhonowski, G. V., Mirkasymov, A. B., Popova-Kuznetsova, E. A., . . . Deyev, S. M. (2021). Laser-synthesized TiN nanoparticles for biomedical applications: Evaluation of safety, biodistribution and pharmacokinetics. *Materials Science and Engineering: C, 120*, 111717. doi:https://doi.org/10.1016/j.msec.2020.111717

Zendelska, A., Golomeova, M., Golomeov, B., & Krstev, B. (2018). Effect of competing cations (Cu, Zn, Mn, Pb) adsorbed by zeolite bearing tuff from Macedonia. *Nature Environment and Pollution Technology, 17*(1), 21-23.

Zereffa, E. A., & Bekalo, T. B. (2017). Clay ceramic filter for water treatment. *Materials Science and Applied Chemistry, 34*, 69–74. doi:10.1515/msac-2017-0011

Zereffa, E. A., & Desalegn, T. (2019). Preparation and characterization of sintered clay ceramic membranes water filters. *Open Material Science, 5*, 24-33. doi:10.1515/oms-2019-0005

Zhang, S., Chen, W., Liu, Y., Luo, P., & Gu, H. (2018). A modified method for the accurate determination of chemical oxygen demand (COD) in high chloride oilfield wastewater. *Open Journal of Yangtze Oil and Gas, 3*, 263-277. doi:10.4236/ojogas.2018.34023

Zhang, X., Li, Z., Xu, S., & Ruan, Y. (2021). Carbon quantum dot-sensitized hollow TiO2 spheres for high-performance visible light photocatalysis. *New Journal of Chemistry, 45*(19), 8693-8700. doi:10.1039/D1NJ00501D

APPENDICES

A Preparation of reagents

A1: Preparation of NaOH (2 M)

About 80 g of NaOH pellets were measured into a volumetric flask and initially dissolved with 200 cm^3 of distilled water and made up to 1000 L to give a 2 M aqueous NaOH solution. Equations A1 –A3 were used to determine the amount of NaOH pellets needed to obtain the desired concentration:

$$Mass\ of\ NaOH = Molar\ mass\ X\ Number\ of\ moles \quad (A1)$$

$$Number\ of\ moles = \frac{Volume\ (cm^3)}{1000}\ X\ Molarity \quad (A2)$$

Where; Molar Mass = 40 g/mol

A2: Preparation of HCl (2 M)

A known volume of 167.2 cm^3 concentrated HCl was measured into a beaker and slowly added to 200 cm^3 of distilled water in a 1 L volumetric flask. The total volume was made up to 1000 cm^3. Equation A3 was used to obtain the desired molarity:

$$Molarity = \frac{SG \times \%\ Purity \times 10}{MolarMass} \quad (A3)$$

Where; Specific Gravity (SG) = 1.18,

% Purity = 37, and Molar Mass = 36.5 g/mol.

A3: Preparation of silver trioxonitrate (V) ($AgNO_3$) solutions

The various concentrations of 0.01, 0.02 and 0.05 M of $AgNO_3$ solution were prepared by dissolving mass of 0.086, 0.172, or 0.43 g, respectively into 50 cm^3 of deionized water. The standard was obtained using Equation A4:

$$C = \frac{mass}{molarmass\ x\ volume\ (L)} \quad (A4)$$

Where; C = concentration of $AgNO_3$ and molar mass of $AgNO_3$ = 169.89 g/mol.

B XPS Spectal of the Composites

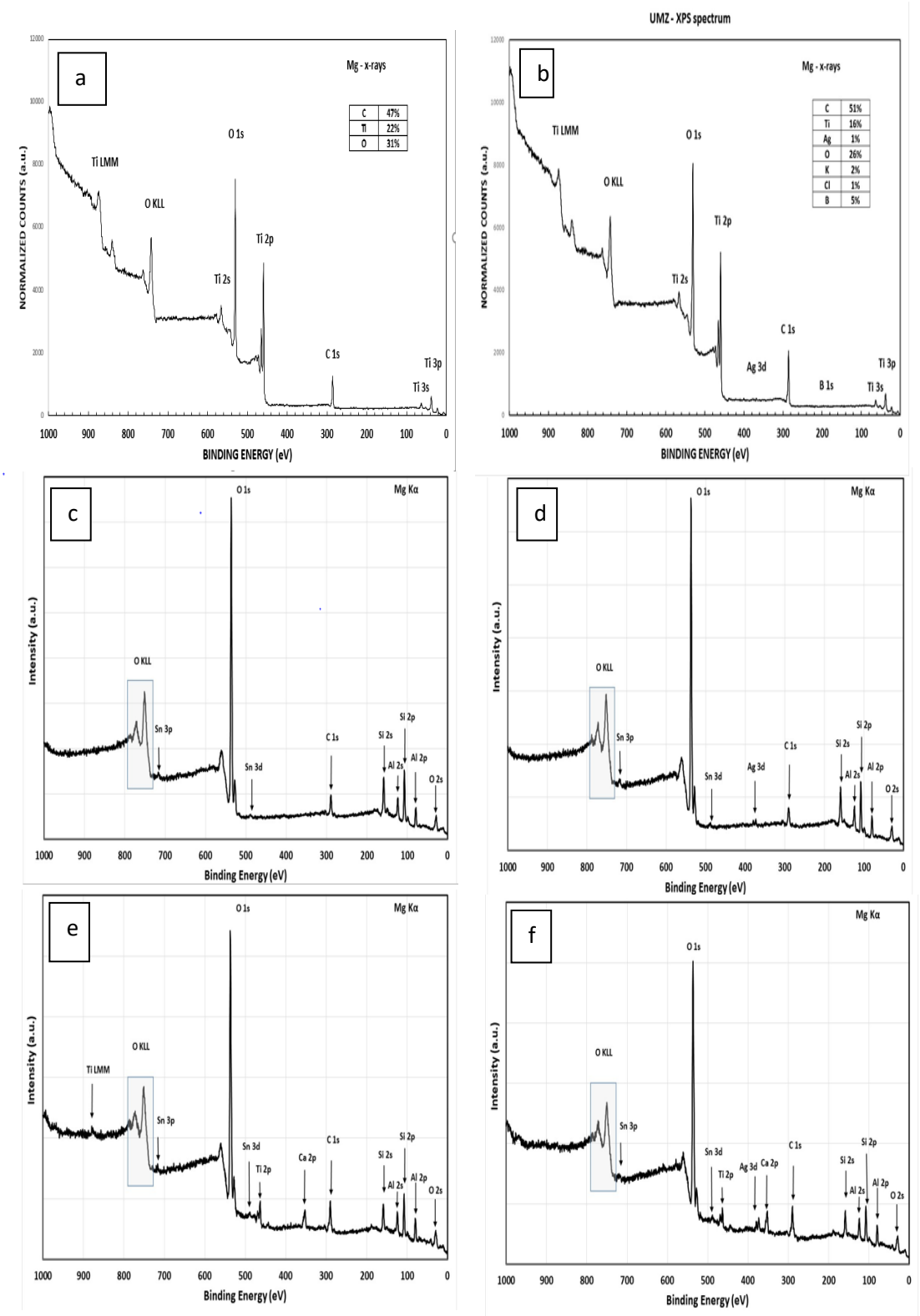

Figure B1: XPS spectrals of; (a) TiO_2 (b) Ag_2O/TiO_2 (c) Clay (d) Ag_2O-clay (e) TiO_2-clay (f) Ag_2O/TiO_2-clay

C: Isotherm Plots of the Metal Ions Adsorption onto Ag_2O/TiO_2-clay

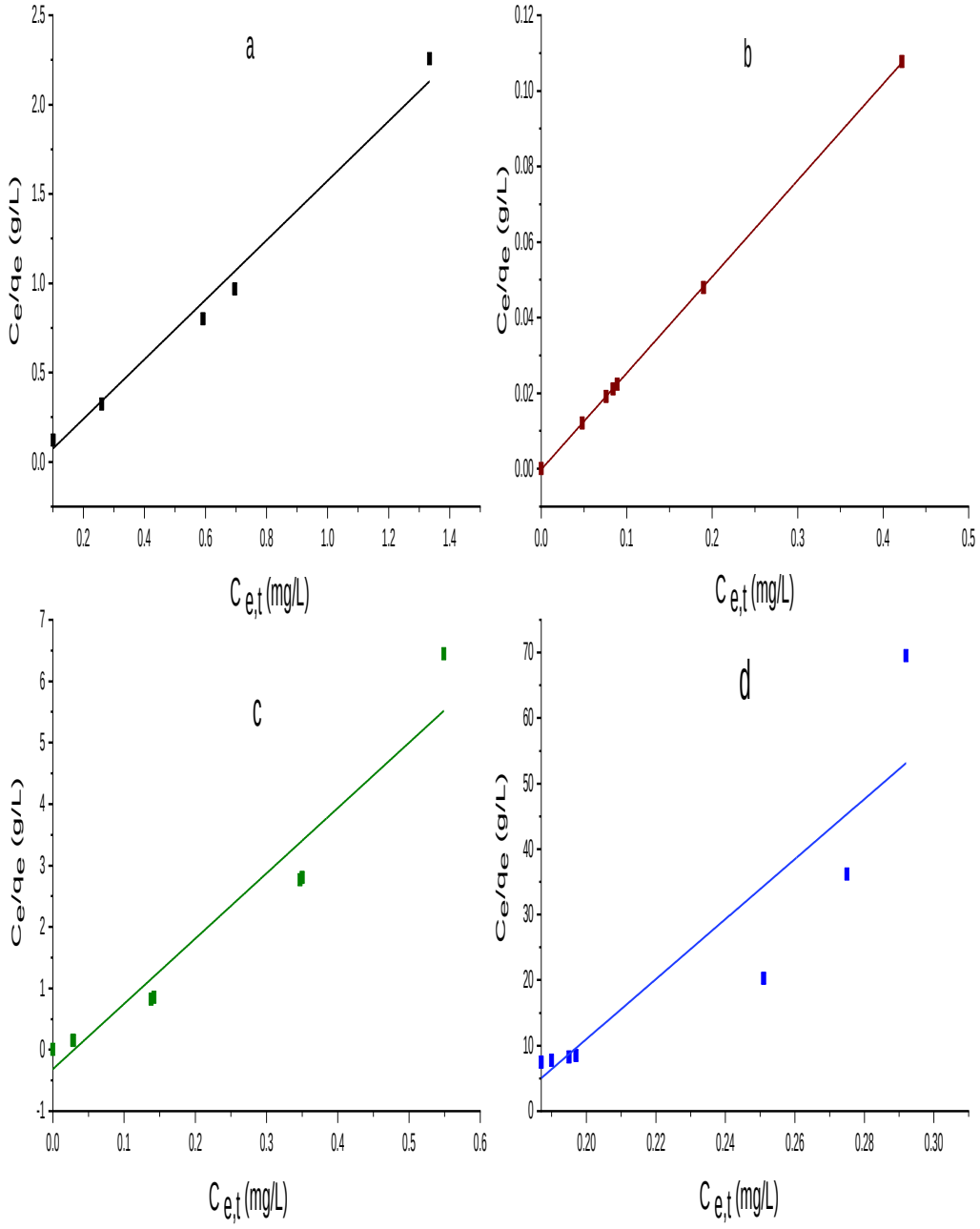

Figure C1: Langmuir plots for the adsorption of (a) Mn (II), (b) Fe (III), (c) Cu (II) and (d) Pb (II) ions onto Ag_2O/TiO_2-clay

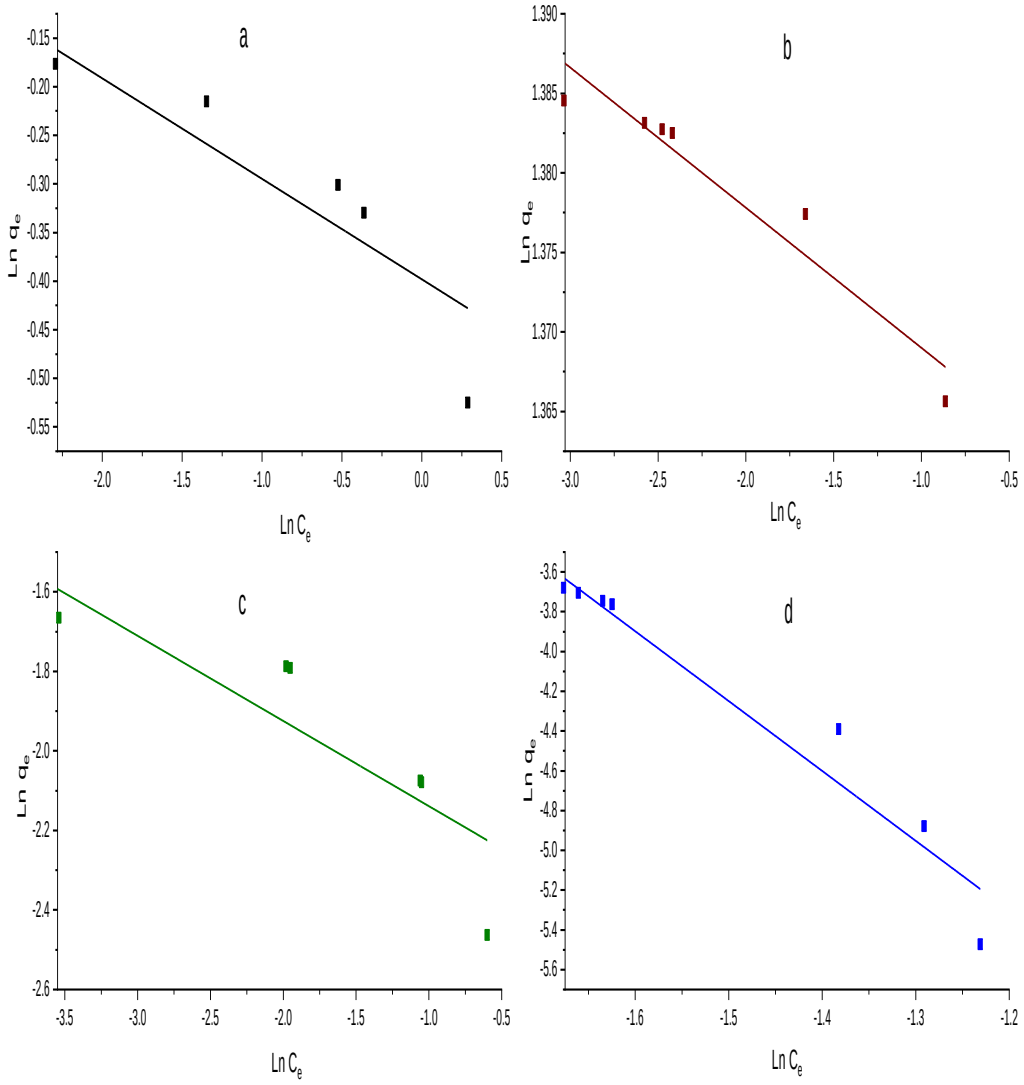

Figure C2: Freudlich plots for the adsorption of (a) Mn (II) (b) Fe (III), (c) Cu (II) and (d) Pb (II) ions onto Ag_2O/TiO_2-clay nanocomposites

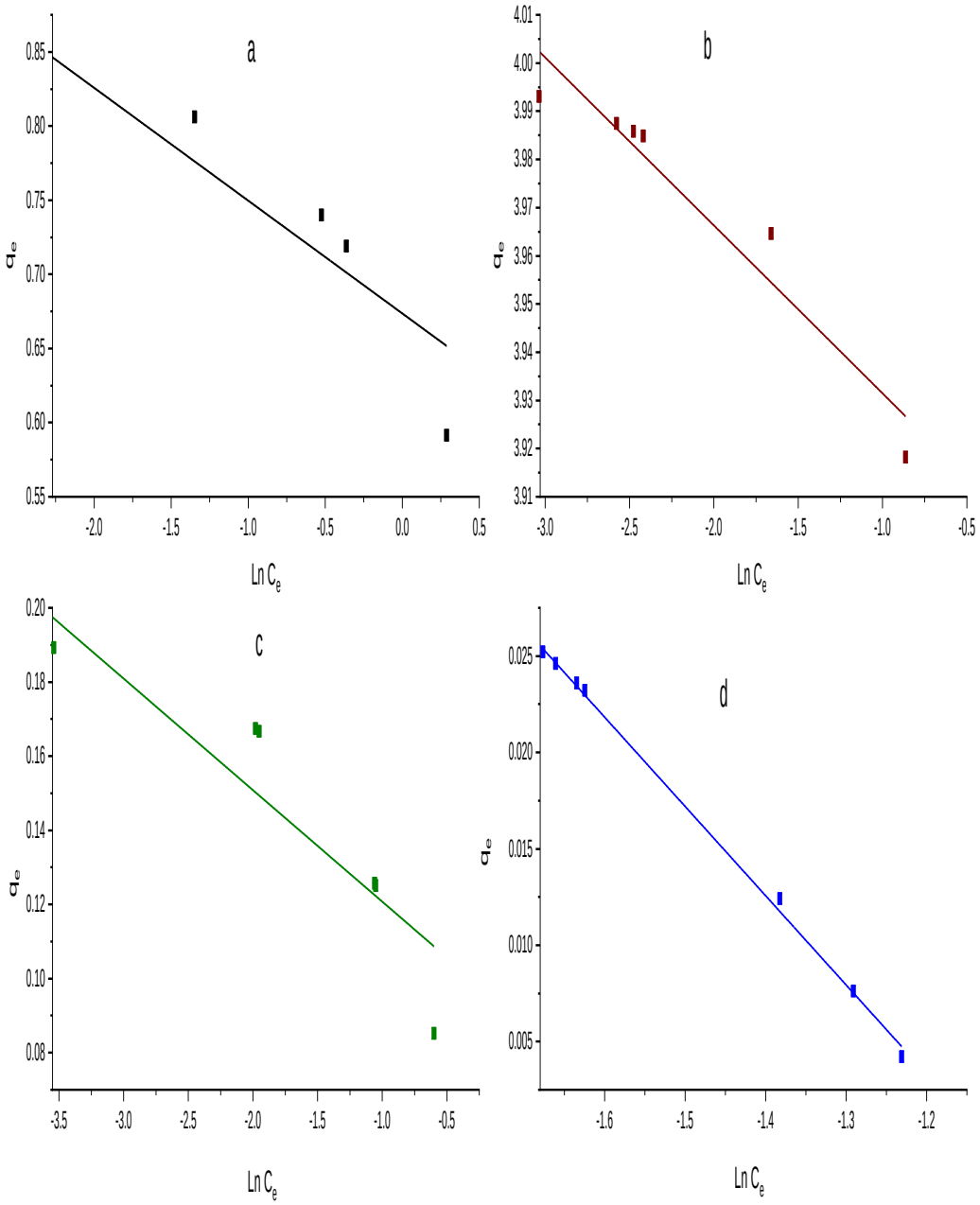

Figure C3: Temkin plots for the adsorption of (a) Mn (II), (b) Fe (III), (c) Cu (II) and (d) Pb (II) ions onto Ag_2O/TiO_2-clay

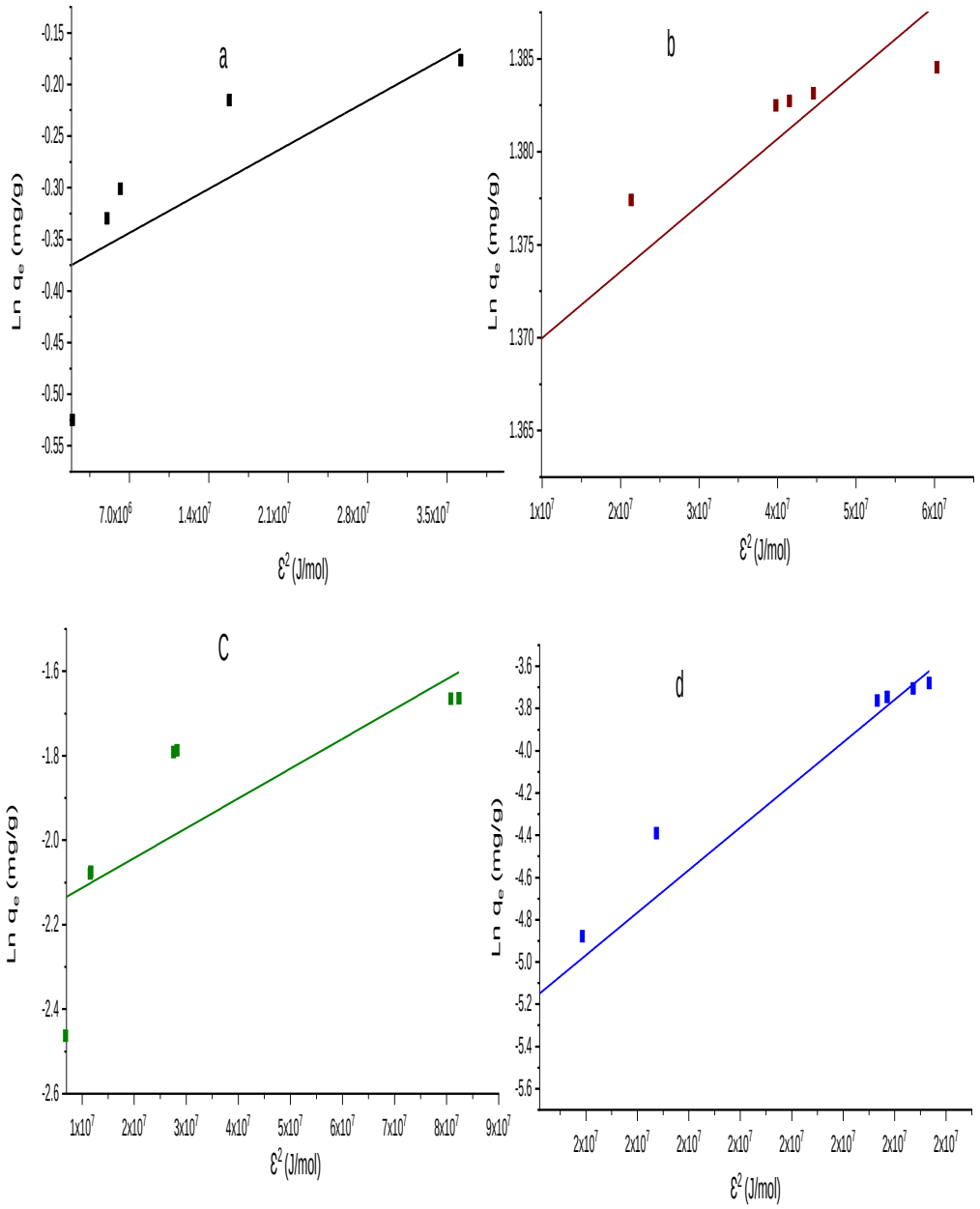

Figure C4: D-R plots for the adsorption of (a) Mn (II), (b) Fe (III), (c) Cu (II) and (d) Pb (II) ions onto Ag_2O/TiO_2-clay

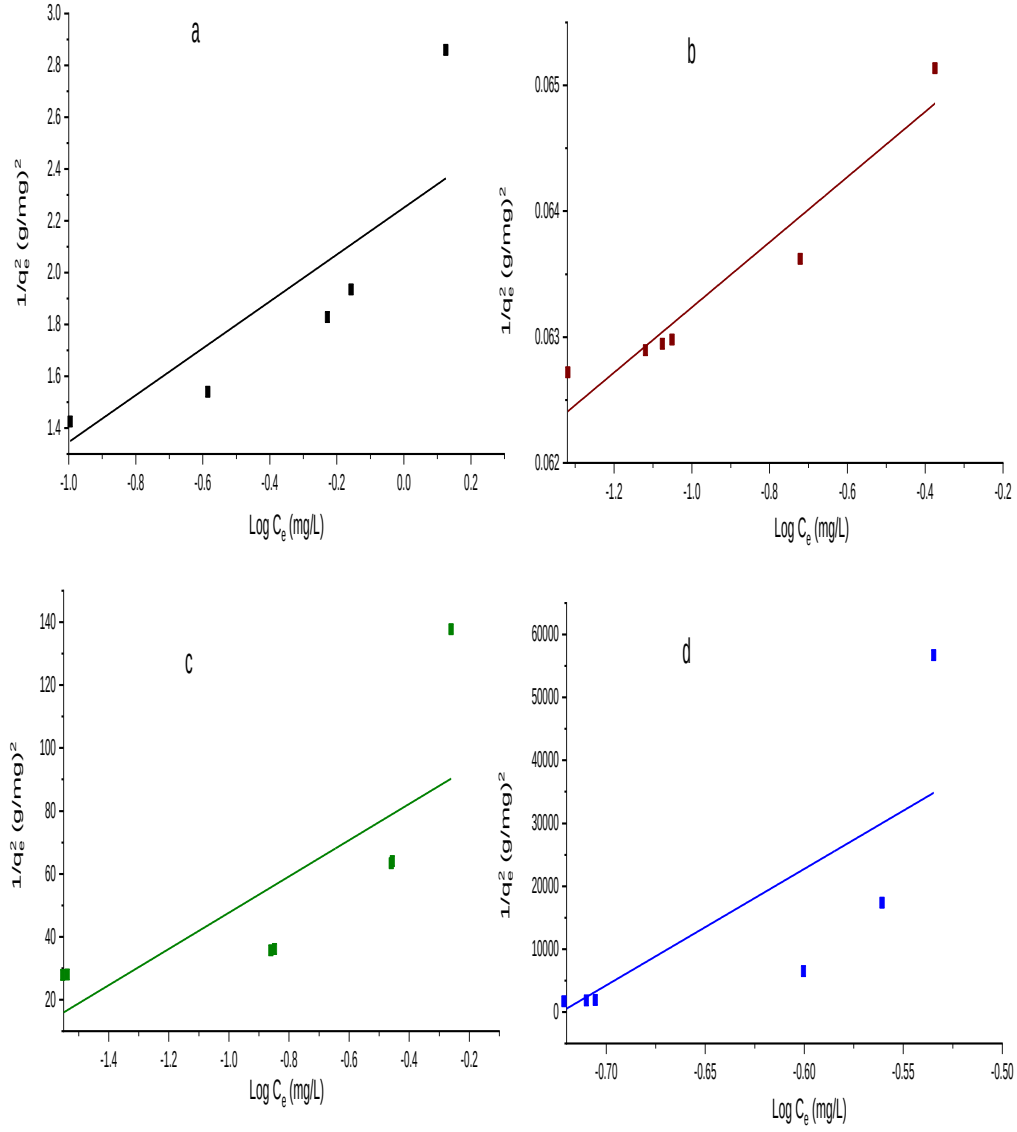

Figure C4: Harkin-Jura plots for the adsorption of (a) Mn (II), (b) Fe (III), (c) Cu (II) and (d) Pb (II) ions onto Ag_2O/TiO_2-clay

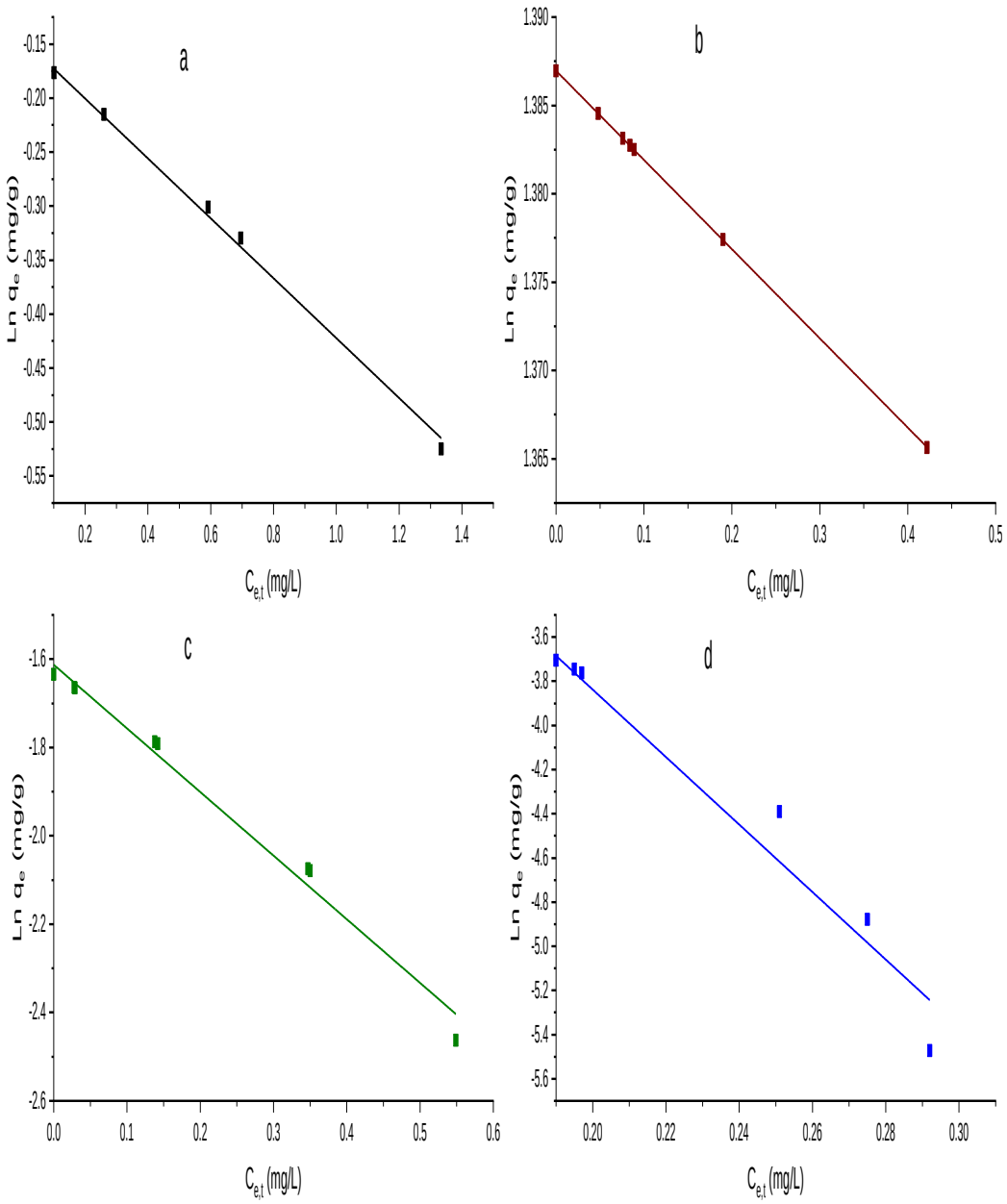

Figure C6: Jovanovic plots for the adsorption of (a) Mn (II), (b) Fe (III), (c) Cu (II) and (d) Pb (II) ions onto Ag_2O/TiO_2-clay

D: Kinetics Plot of the Metal Ions Adsorption

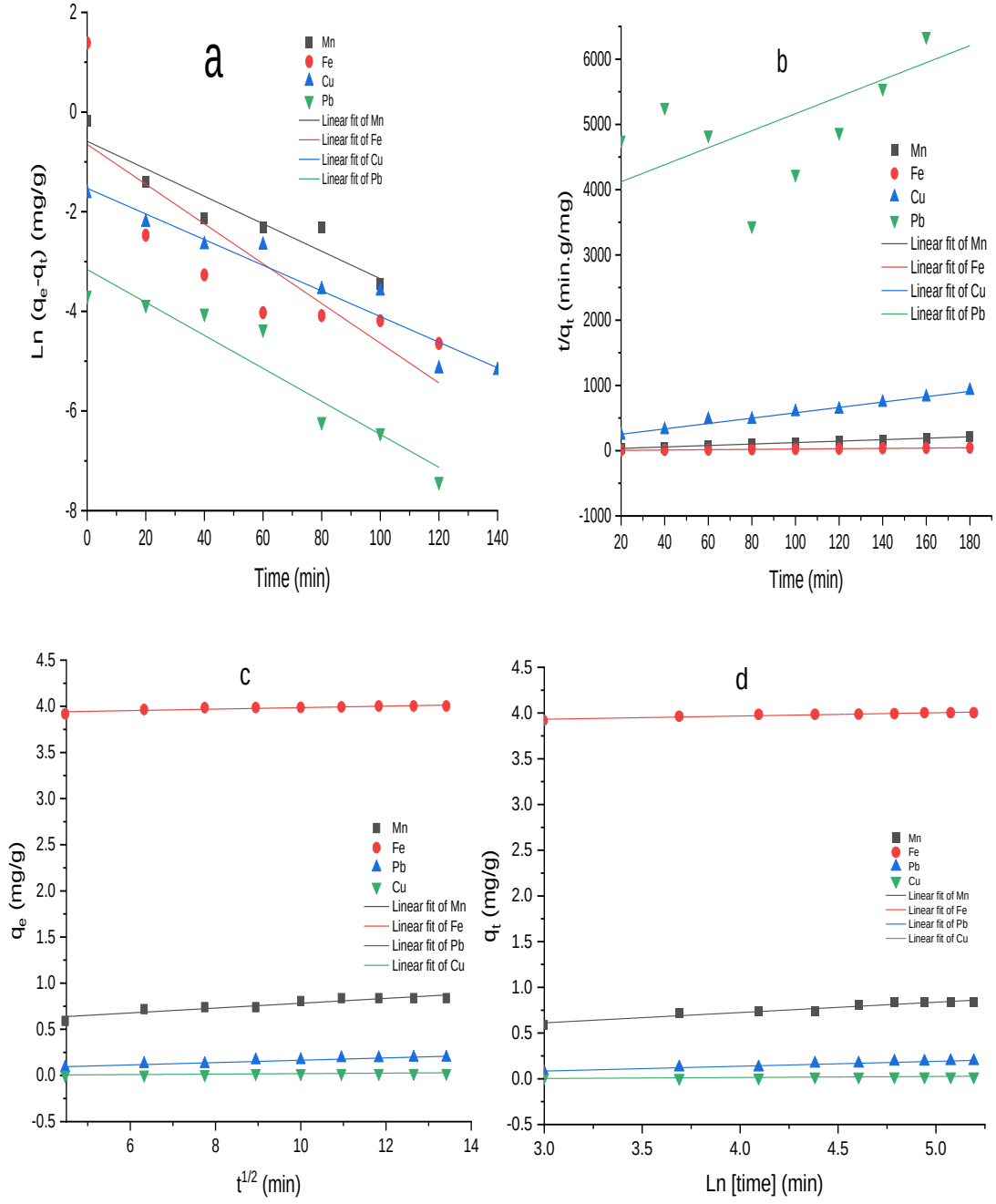

Figure D1: Kinetics plots for the adsorption of the metal ions onto Ag_2O/TiO_2-clay for (a) Pseudo first order (b) Pseudo second order (c) Intraparticle diffusion (d) Elovich models

E: Fabrication Process of the Filters

Plate E1: Fabrication process images of the filters (a) Jigle jolly moulding (b) Gas kiln sintering (c) Sintered small filters (d) Saturation process (e) The hydraulic press (e) Big filter pressing process

Plate E2: Fabrication process images of the filters (a) Kiln sealing (b) Greenware (c) Greenware drying (d) Sintered filters

F: SEM Water Shed Images of Fabricated Filter

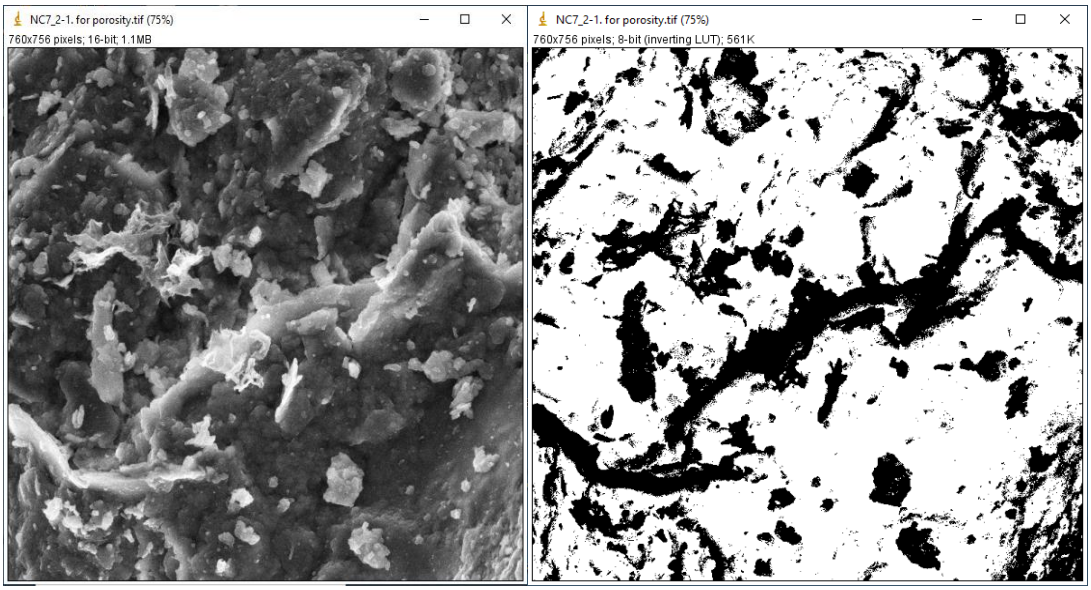

(a) **NC7** Original image (b) **NC7** Binary image

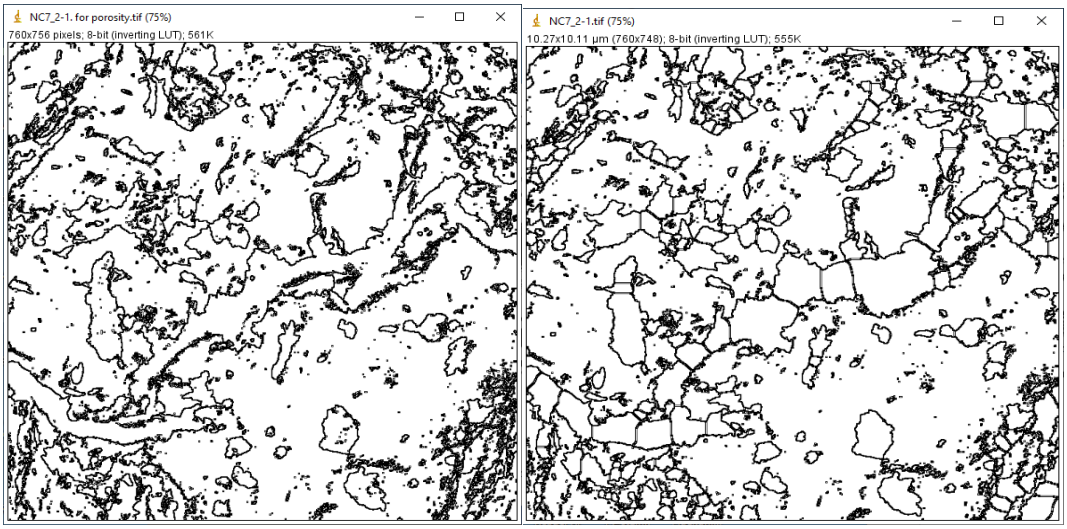

(c) Binary image fill holes (d) Image after watershed

Plate F1: SEM water shed images of fabricated filter before use (SC7)

	Area	Mean	StdDev	Min	Max	%Area
1	574560	46.43	98.41	0	255	18.21
2	574560	46.43	98.41	0	255	18.21
3	103.81	45.9	97.97	0	255	18.00

Porosity = 18.14% Note; % Area = porosity

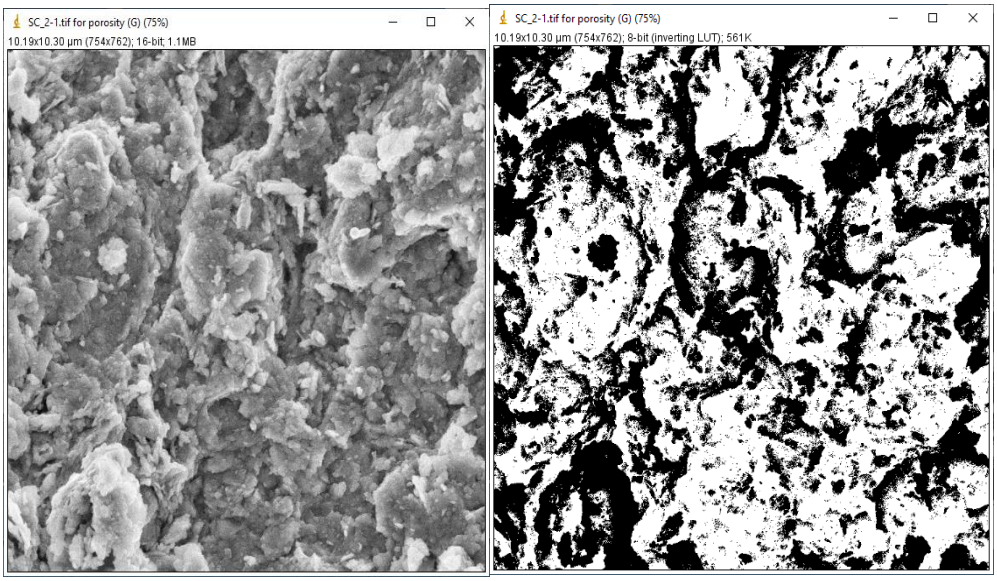

(a) SC2 original image (b) SC2 Binary Image

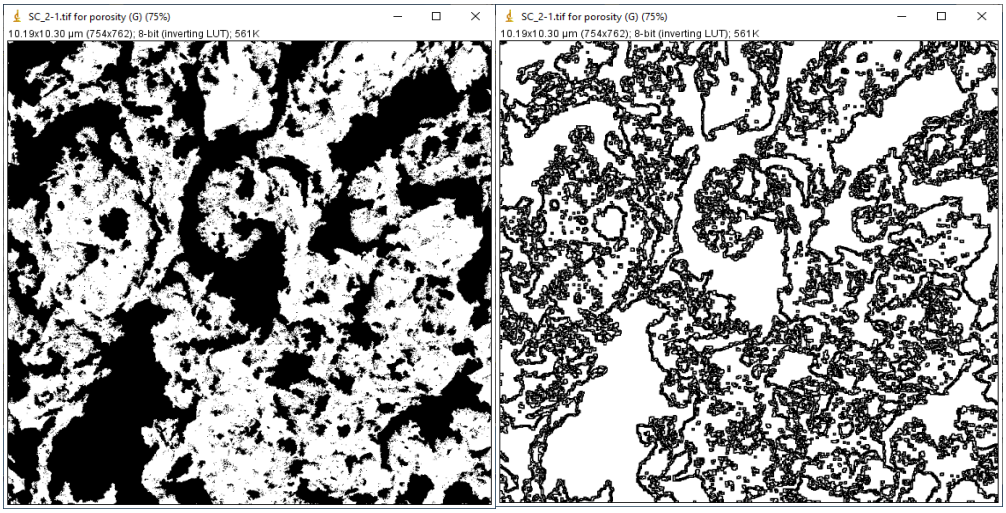

(c) SC2 Image fill holes (d) SC2 Image after the watershed

Plate F2: SEM water shed images of fabricated filter after use (SC2)

	Area (um^2)	Mean	Std. Dev.	Min	Max	%Area
1.	104.90	97.23	123.85	0	255	38.13
2.	104.90	97.23	123.85	0	255	38.13
3.	104.90	97.23	123.85	0	255	38.13

Porosity (%): 38.13

G: IUPAC classificaion of BET pore size (Sotomayor *et al.*, 2018)

S. No	Pore size (nm)	Classification
1.	< 2	Microporous
2.	>2 <50	Mesoporous
3.	> 50	Macroporous